

ABSTRACT

KOO, JUNE MO Computational Nanofluid Flow and Heat Transfer Analyses Applied to Micro-systems. (Under the direction of Professor C. Kleinstreuer).

The compactness and high surface-to-volume ratios of microscale liquid flow devices make them attractive alternatives to conventional flow systems for heat transfer augmentation, chemical reactor or combustor miniaturization, aerospace technology implementations, as well as biomedical applications, such as drug delivery, DNA sequencing, and bio-MEMS, to name a few. While experimental evidence indicates that fluid flow in microchannels, especially in terms of wall friction and heat transfer performance, differs from macrochannel flow behavior, laboratory observations are often inconsistent and contradictory. Some researchers attributed the deviations to *unknown microscale* effects, which often turned out to originate from inappropriate approaches to analyze the new phenomena. Specifically, system parameters were neglected, which are not important on the macroscale but play important roles in microscale analyses.

The main objectives of the study are *to identify important parameters for microscale liquid flows and nanoparticle suspensions, to find a physically sound way to analyze the new phenomena, and to provide mathematical models to simulate them.*

Scale analysis was found to be a valuable tool to determine which forces become important on the microscale. With increasing system miniaturization surface forces, such as surface tension and van der Waals forces, take over the control from body forces like gravity and pressure. Furthermore, surface roughness, viscous dissipation, and entrance region effects are very important liquid flow parameters in microscale conduits. In summary, for liquid

flow in microchannels with a characteristic width or height of $L \geq 10$ [μm], the continuum approach, in conjunction with appropriate closure models, is appropriate to analyze *microscale* effects.

Employing the porous medium layer (PML) idea, surface roughness effects on momentum- and heat-transfer in micro-conduits were numerically investigated and verified with experimental data. The friction factor and Nusselt number either increase or decrease depending on the PML model parameters, expressed in terms of the relative surface roughness, Darcy number, Reynolds number, and effective thermal conductivity. Variations in the viscous dissipation effect were found to increasingly affect the friction factor and Nusselt number with decreasing system size. Variations in entrance geometry may cause early laminar-to-turbulent transition resulting in higher friction factor values.

When nanoparticles are added to liquid flow systems, scalar transport properties can be significantly enhanced. Specifically, nanofluids, i.e., dilute suspensions of nanoparticles in liquids, are used to enhance heat transfer performance or to maximize drug delivery. Focusing on micro-scale heat transfer, it was found that the particle Brownian motion and the induced surrounding liquid motion are key mechanisms for the experimentally observed high increase of the effective thermal conductivity of nanofluids. A new, experimentally validated effective thermal conductivity model has been developed based on kinetic theory. The model predicts both the effective thermal conductivity and dynamic viscosity of nanofluids in terms of nanoparticle concentration, size, density and their interaction potential as well as the density, thermal capacity and dielectric constant of the base liquid.

Nanofluid flow applications were tested for micro heat-exchangers and a drug delivery sys-

tem. Concerning micro heat-exchangers, it was found that a base fluid of high Prandtl number together with nanoparticles of high thermal conductivity in a channel of high aspect ratio, form a desirable combination for optimal performance. In order to minimize the problem of non-uniform suspensions, the selection of materials for the carrier fluid, nanoparticles and conduit wall was found to be very important. For example, the dielectric constants difference should be kept small, and appropriate surface treatment, by creating either electrostatic or steric forces to maintain enough repulsion potential, should be provided.

In the case of nanotherapeutics, radial diffusion turns out to be the controlling mechanism for drug delivery. Specifically, the time scale for radial diffusion should be kept small enough to ensure efficient delivery. A shallow channel design together with a pressure chamber to switch between drug delivery- and purging-process, is suggested over the alternative multi-stream design or the fluid-guiding system proposed by others.

**Computational Nanofluid Flow and Heat Transfer Analyses Applied to
Micro-systems**

by

JUNEMO KOO

A dissertation submitted to the Graduate Faculty of
North Carolina State University
in partial satisfaction of the
requirements for the Degree of
Doctor of Philosophy

MECHANICAL AND AEROSPACE ENGINEERING

Raleigh, NC

2005

Approved By:

Dr. C. Kleinstreuer
Chair of Advisory Committee

Dr. J. P. Archie

Dr. T. Echehki

Dr. S. McRae

To my considerate wife, Jungeun,
our lovely son, Daeone, and
devoting parents and parents-in-law.

Biography

The author was born on October 22, 1970 in Seoul.

After graduating from high school, he was admitted to the Korea Advanced Institute of Science and Technology (KAIST) in 1990 and studied in the Department of Mechanical Engineering. He continued his graduate study in the same department concentrating on internal combustion engines and earned his Master of Science degree in 1996.

Afterwards the author was employed as an engineer by POSCO Engineering and Construction Co., Ltd. in Seoul, Korea. He worked in the Oversea Sales Department for two years. Afterwards, he stayed at KAIST for three and a half years as a PhD student.

The author enrolled as a doctoral student August, 2001 in the Department of Mechanical and Aerospace Engineering at North Carolina State University in Raleigh, NC. His dissertation research focused on computational nanofluid flow and heat transfer analyses applied to micro-systems. He has been a McDonald-Kleinstreuer Fellow for three years and is proud to be a member of Phi-Kappa-Phi honor society.

The author wed the former Jungeun Yeo in 2000. They have a lovely son, Daeone, born in 2001.

Acknowledgments

I would like to express a great deal of appreciation for Dr. C. Kleinstreuer, Chairman of my advisory committee. His physical insight, guidance and encouragement have been the impetus for me to keep working hard and to succeed. He has proven to be a very considerate and patient advisor who serves as a role model for professional excellence and integrity.

I would like to express the greatest gratitude to Dr. J. P. Archie, Jr. and his wife Sarah for the generous endowment of the McDonald-Kleinstreuer Fellowship and to him serving as a committee member. Continuation of the McDonald-Kleinstreuer Fellowship over the years was made possible via a commitment by the former Department Head, Professor M. Noori. Without the financial support, I could not even have dreamt of coming to the United States to pursue the degree.

Appreciation is also extended to Dr. S. McRae and Dr. T. Echehki for serving as committee members, and offering superb computational fluid dynamics and combustion classes. Many ideas in this dissertation were obtained from their classes.

Special thanks goes to Dr. S. Hyun (Mercer University, Macon, GA) for his considerate care when I first arrived here. The author appreciates Dr. T. Lee in Duke University for providing the background information on nano-drug delivery systems and Dr. J. Chang in Intel for providing background information on micro heat-sinks. The author was happy to be with all the members in our Computation Fluid-Particle Dynamics Laboratory, including Dr. Z. Zhang, Dr. P. W. Longest, Dr. S. Hyun, Mr. Z. Li, Mr. H. Shi, Mr. Z. Li, and Mr. B. W. Kennedy.

I feel indebted to professors in KAIST including Dr. C. Bae, Dr. H. Shin, Dr. S. Lee, Dr. S. Choi, and Dr. S. Kim. Their teachings set a solid base to climb up to the top.

A special debt of gratitude should go to my wife and son, who spent most of their days and nights without their husband and father, and to my parents and parents-in-law, who supported me in every way to concentrate only on my studies. I should confess that I could not have achieved anything without their thoughtfulness.

Contents

List of Figures	viii
List of Tables	xv
1 INTRODUCTION and LITERATURE REVIEW	1
1.1 Motivation	2
1.2 Research Objectives	3
1.3 Nanofluid Flow and Heat Transfer in Microchannels	4
1.3.1 Characteristics of Nanofluids	4
1.3.2 Driving forces for Microchannel flow	15
1.3.3 Momentum and Heat Transfer in Microchannels	29
1.4 Numerical Solution Techniques	32
1.4.1 Molecular Dynamics (all Knudsen numbers)	32
1.4.2 Direct Simulation Monte Carlo ($0.1 \leq \text{Kn} \leq 10$)	37
1.4.3 Direct Numerical Simulation ($\text{Kn} \leq 0.1$)	47
1.4.4 Approximate Methods ($\text{Kn} \leq 0.5$)	51
1.4.5 Summary	53
2 THEORY and METHODS	54
2.1 Introduction	55

2.2	Governing Equations for Microchannel Flow	56
2.3	Nanofluid Property Models	59
2.3.1	Effective Thermal Conductivity Model	59
2.3.2	Thermal conductivity due to thermo-phoresis	69
2.3.3	Thermal conductivity due to the osmo-phoresis	71
2.3.4	Comparisons	72
2.3.5	Effective Dynamic Viscosity Model	74
2.3.6	The effect of particle-wall interaction	75
3	LIQUID FLOW in MICROCHANNELS	78
3.1	Introduction	79
3.2	Friction Factor Analysis	83
3.3	Surface Roughness Effect	85
3.3.1	Effects on momentum transfer	85
3.3.2	Effects on energy Transfer	92
3.3.3	Summary	104
3.4	Viscous Heating Effect	106
3.4.1	Viscous dissipation effect	106
3.4.2	Governing equations and scale analyses in tubes	107
3.4.3	Numerical solution for rectangular ducts	111
3.4.4	Model validations	112
3.4.5	Results and Discussion	115
3.4.6	Summary	120
3.5	Entrance and other Microchannel Effects	122
3.5.1	Entrance effect	122
3.5.2	Non-Newtonian fluid effects	122
3.5.3	Wall slip effects	124
3.5.4	Channel entry geometry effect	124

3.5.5	Summary	129
3.6	Nanofluids Properties Model	130
3.6.1	Higher thermal conductivities due to Brownian motion effect.	130
3.6.2	Interparticle interactions at high concentrations ($\alpha_d > 1\%$)	133
3.6.3	Examples of heat conduction in nanofluids.	134
3.6.4	Brownian motion effect on momentum transfer	141
3.6.5	Particle non-sphericity effect on the thermal conductivity	142
3.6.6	Summary	146
4	NANOFLUID FLOW APPLICATIONS	148
4.1	Introduction	149
4.2	Micro Heat-Sinks	149
4.2.1	Introduction	149
4.2.2	Theory	152
4.2.3	Results and Discussion	169
4.2.4	Summary	185
4.3	BioMEMS	186
4.3.1	Introduction	186
4.3.2	Theory	186
4.3.3	Results	188
4.3.4	Summary	201
5	CONCLUSIONS and FUTURE WORK	203
5.1	Conclusions and Novel Contributions	204
5.2	Future Work	207
	Bibliography	208

List of Figures

1.1	Schematic of the operation principle with electronic ink.	18
1.2	A schematic for 2D gel electrophoresis on a microchip. The first dimension of separation operates by isoelectric focussing. From this level, the separated groups of molecules are conducted to the second dimension of separation. The separation of molecules occurs by electrophoresis.	20
1.3	Continuous electro-wetting (CEW) effect	23
1.4	Schematic drawing of the nozzle-diffuser based bubble pump (Tsai & Lin, 2002)	24
1.5	Schematic drawing of the exemplary integrated system of a micropump and a mixing channel.	25
1.6	Principle of bubble valve for micro-injector (Kim, 1999)	26
1.7	DSMC flowchart	43
1.8	System sketch of shear-driven flow; U_0 is the moving wall velocity.	44
1.9	Comparison of velocity profiles obtained with DSMC and conventional laminar flow theory. The velocity differences at the walls show the slip velocity, which increases with Kn . The slower flows show higher velocity fluctuations.	45
1.10	Two-dimensional axial velocity contours for the pressure-driven flow case with an inlet velocity of 1,000 m/sec	45
1.11	Axial velocities at the entrance, mid-point, and exit of a two-dimensional channel for the pressure-driven flow case with an inlet velocity of 1,000 m/sec	46

1.12	Two-dimensional number density contours for pressure-driven flow with an inlet velocity of 1,000 m/sec	46
1.13	Unstructured grid for the ALE method	49
1.14	Fixed triangular grid used in DLM computation. The same grid covers the fluid and solid. The fluid in the circles is bordered by Lagrange multipliers to move the particles (circles) as a rigid bodies.	50
1.15	Porous medium layer equivalent to surface roughness and simple microchannel geometry: a) real surface roughness; b) homogeneous distribution of identical roughness elements; and c) mid-plane view of conduit with idealized roughness layer, or porous medium layer (PML)	52
2.1	Illustrative schematic explaining the particles' Brownian-motion effect on micro-mixing	61
2.2	A traveling particle carries fluid around it due to viscous effect. For a low Reynolds number flow, the amount of fluid travel with a particle could be obtained by using Eq. (2.9).	64
2.3	Expectation for a particle to travel in the x -direction	67
2.4	The particle size effect on k_{eff}	70
2.5	Comparison of three different particle dynamics effects on the thermal conductivity enhancement	73
2.6	The particle-liquid-wall interaction effect on nanoparticle distribution near the wall	76
3.1	Effect of the Darcy number on steady 2-D fully-developed flows (Brinkman term only): (a) parallel-plate case and (b) circular tube case.	88
3.2	Effect of the Darcy number on steady 2-D fully-developed flows (Brinkman term only): (a) parallel-plate case and (b) circular tube case.	89
3.3	Comparisons of porous medium layer (PML) model predictions with experimental data: (a) Mala and Li (1999) and (b) Guo and Li (2003)	91

3.4	PML thermal conductivity effect on the temperature profiles between parallel plates ($Da=10^{-3}$, $SR = 2$ [%])	97
3.5	Darcy number effect on the temperature profiles between parallel plates ($SR = 2$ [%])	97
3.6	Effects of PML Darcy number and thermal conductivity on the Nusselt number for parallel plates ($Re = 1000$, $SR = 2$ [%])	98
3.7	Effect of the Reynolds number on the Nusselt number for different Darcy numbers and the conductivity ratios ($SR = 2$ [%])	100
3.8	Effects of PML thickness on the Nusselt number ($Re = 1000$)	100
3.9	Effects of PML Darcy number and thermal conductivity on the Nusselt number ($Re = 1000$, $SR = 2$ [%])	101
3.10	Effect of the Reynolds number on the Nusselt number ($SR = 2$ [%])	102
3.11	Effect of PML thickness on the Nusselt number ($Re = 1000$)	103
3.12	Effects of viscosity changes for different radial temperature distributions ΔT on tubular velocity profiles	108
3.13	Working fluid effect on mean temperature rise ($L/D=1500$, $Re=300$)	112
3.14	Comparison of temperature rises in rectangular channels (Pfhaler et al., 1991). Note : the experimental trapezoidal channels of hydraulic diameter 30 and 40 μm were modeled as rectangular channels of the same hydraulic diameters and the same aspect ratio	114
3.15	Comparison between experimental data (Pfhaler et al., 1991) and computational results	114
3.16	Tube size effect on temperature change, i.e., viscous dissipation (water, $Re=2,000$): a) adiabatic wall case; b) constant wall temperature case	116
3.17	Effect of channel aspect ratio on temperature change due to viscous dissipation for iso-propanol flows in channels of $D_h = 6\mu\text{m}$ with $Re=0.2$	116
3.18	Reynolds number effect on mean temperature rise (water, $D_h=74\mu\text{m}$)	117

3.19	Comparison of heat source term impact due to viscous dissipation, S_v , and thermal boundary, S_h , for $100 \leq Re \leq 2000$: a) in a $74 \mu\text{m}$ square channel; and b) Fractions of source terms in $40 \mu\text{m}$ and $74 \mu\text{m}$ square channels . . .	120
3.20	Comparison of friction factor deviations in a channel entrance ($h/w=1.0$) based on experimental observations (Eq. (3.4)) and computer simulation results for various Reynolds numbers	123
3.21	Effect of height-to-width ratio on apparent friction factor for $Re=1,000$. . .	123
3.22	Effect of non-Newtonian fluid behavior on the friction factor	127
3.23	Schematic diagram of the geometry used in computing the effect of sudden contraction on laminar-to-turbulent flow transition.	127
3.24	Evolution of velocity components, turbulent kinetic energy, apparent viscosity and pressure in a microchannel (50 % contraction, $Re = 2000$): (a) evolution of axial velocity profile, (b) evolution of radial velocity profile, (c) evolution of turbulent kinetic energy and (d) pressure profile in axial direction.	128
3.25	Experimental data sets	131
3.26	Comparison of model predictions with experimental data sets	131
3.27	Comparison of β -functions obtained from experimental data	132
3.28	Comparison of effect of the exponent in the intermolecular potential on impact distance	134
3.29	The particle size effect on the effective thermal conductivity at $T = 300$ [K]; $f(T, \alpha_d) \equiv 1$	135
3.30	The particle type effect on the effective thermal conductivity at $T = 300$ [K]; $f(T, \alpha_d) \equiv 1$	136
3.31	Comparisons of temperature, temperature gradient, and effective thermal conductivity profiles	138
3.32	Volume fraction profiles	139
3.33	Effect of volume fraction change on temperature-, temperature gradient-, and effective thermal conductivity-profiles	140

3.34	The particle size effect on the effective viscosity for water-CuO nanofluids at 300 [K]; $f(T, \alpha_d) \equiv 1$	141
3.35	Schematic diagram to explain the effect of particle rotation	144
3.36	Comparison of model constants β among nanotube (Choi et al., 2001), Cu (Eastman et al., 2001), and CuO (Wang et al., 2003) suspensions	145
4.1	Schematic diagrams of (a) 2-D ODE problems and (b) 3-D PDE problems .	153
4.2	Fin efficiency	156
4.3	Porous medium analogy	157
4.4	Comparison between the full partial-differential-equation solution ((a) at $x = 0.0006 [m]$ and (b) at $x = 0.008 [m]$) and (c) the reduced ordinary-differential-equation solution for the water based <i>CuO</i> nanofluid under the heat flux of 100 [W/cm^2]	171
4.5	Comparison between the full partial-differential-equation solution ((a) at $x = 0.0006 [m]$ and (b) at $x = 0.008 [m]$) and (c) the reduced ordinary-differential-equation solution for the Ethylene Glycol based <i>CuO</i> nanofluid under the heat flux of 100 [W/cm^2]	172
4.6	Comparison of the pressure gradient increase, and effective thermal conductivity between ethylene glycol- and water-base <i>CuO</i> nanofluids	173
4.7	Influence of temperature-function f on dimensionless pressure gradient and effective thermal conductivity for water-based <i>CuO</i> nanofluids	174
4.8	The viscous dissipation effect on non-dimensional temperature profiles for ethylene glycol-based <i>CuO</i> nanofluids ($\alpha_d = 4 [\%]$, $y^* = y/H$, $f \equiv 1$);(a) $x = 0.0006 [m]$, and (b) $x = 0.008 [m]$	176
4.9	The viscous dissipation effect on non-dimensional temperature profiles for water-based <i>CuO</i> nanofluids ($\alpha_d = 4 [\%]$, $f \equiv 1$);(a) $x = 0.0006 [m]$, and (b) $x = 0.008 [m]$	177

4.10 Comparison of temperature profiles of pure-fluid cooling and nanofluid cooling cases ($f \equiv 1$)	178
4.11 Nusselt number comparisons for ethylene glycol- and water-based nanofluids with different CuO -volume fractions ($q'' = 100 [W/cm^2]$, $f \equiv 1$)	180
4.12 The effect of function f on temperature profiles	181
4.13 The effect of function f on the Nusselt number	182
4.14 The particle-liquid-wall interaction effect on nanoparticle distribution near the wall	184
4.15 Dispersion by convection; (Top) at $t=0$, (Bottom) at time t (sec) (Probstein, 2003)	188
4.16 Velocity distribution in two-drug-stream system	189
4.17 Concentration distribution at (a) the mid-plane ($Z=0$) and (b) at the wall ($Z=200 [\mu m]$) at $t = 10$ [sec]	190
4.18 Concentration distribution at (a) the mid-plane ($Z=0$) and (b) at the wall ($Z=200 [\mu m]$) at $t = 130$ [sec]	191
4.19 Preliminary schematic sketch of the drug delivery channel (1)	192
4.20 Preliminary schematic sketch of the drug delivery channel (2)	193
4.21 Sketch of the new system	194
4.22 The function of a plenum chamber (top-view); the pressure gradients are uniform for all branches.	195
4.23 The function of a plenum chamber (top-view); the velocity fields are uniform for all branches.	195
4.24 The function of a plenum chamber (side-view)	196
4.25 Snapshots of concentration distributions during purging process; (a) 0.001 [sec]; (b) 0.017 [sec]; (c) 0.041 [sec]	197
4.26 The snapshots of velocity fields during purging process; (a) 0.001 [sec]; (b) 0.003 [sec]; (c) 0.009 [sec]	198

4.27 The snapshots of concentration distributions during drug supply process; (a)
0 [sec]; (b) 0.05 [sec]; (c) 1 [sec] 199

4.28 Effect of particle concentration on mass flow rate supplied to the testing section 201

List of Tables

1.1	Conventional models of effective thermal conductivity of solid/liquid suspensions k_e , thermal conductivity of base fluid k_m , thermal conductivity of particle k_2 , thermal conductivity ratio $\alpha = k_2/k_m$, $\beta = (\alpha - 1)/(\alpha + 2)$, particle shape factor n and particle volume fraction v , Xue (2003)	6
1.2	Experimental data; d : particle diameter, α_d : volume fraction	8
2.1	Particle speed due to the Brownian effect and corresponding particle Reynolds number of Cu-nanoparticle-water suspensions	61
2.2	Parameter values for different materials (see Eq. (4.75))	66
2.3	Comparison of augmented thermal conductivities	67
3.1	Experimental observations of fluid flow characteristics in microchannels . .	80
3.2	Classification of experimental observations	81
3.3	Typical values of relative surface roughness($h/D_h \times 100[\%]$)	86
3.4	Typical PML parameters.	87
3.5	Mechanical and thermodynamic properties of various working fluids at 298K (Zabransky, 1996; MatWeb, 1999)	113
3.6	Magnitude comparisons between convective, diffusion and dissipation terms in tubes	118

Chapter 1

INTRODUCTION and LITERATURE REVIEW

1.1 Motivation

Starting with the automobile airbag sensors, MEMS devices have been developed for applications in engineering heat and mass transfer, biomedical drug delivery, aerospace technology, micro reactors, etc. However, the understanding of microscale phenomena is still in its infancy due to the fact that such devices have different length- and time-scales than those of our everyday life.

As Trimmer and Stroud (2002) reported, different forces rule on different scales, and scaling theory is a valuable tool to determine which force becomes important on the microscale. For example, gravitational forces dominate on an astronomical scale, i.e., the motion of our planet around the sun and our sun around the galaxy is driven mostly by gravitational forces. Yet, on the macroscale of a desk top, the gravitational force between two objects, e.g., a tape dispenser and stapler, is insignificant. Based on scale analysis, they showed that on the microscale surface tension and wall effects becomes more important when compared to electrostatic, pressure, biochemical and magnetic forces which rule on the macroscale. From a literature review, it was found that experimental observations were, sometimes, contradictory among researchers, and it is very important to identify the origin of the discrepancies. In this study, various parameters such as surface roughness, viscous dissipation, and entrance geometry, among others, were examined to explain the diverging experimental observations.

For example, Pfahler et al. (1990) raised pertinent questions concerning microscale flows:

- Is the continuum assumption still valid?
- Whether the Navier-Stokes equations adequately model the fluid flow in very small scales, or they should be modified, if so, how?
- Do phenomena that are typically ignored in large-scale analyses become important in small-scale channels?
- Is the onset of instabilities affected by the small size of the conduits?

To find answers to these questions, it is necessary to test the assumptions of various analysis methods and to select a proper modeling method.

Over a decade, attempts have been made to use dilute nanoparticle suspensions as working fluids in heat exchangers to improve the efficiency. Researchers observed unconventionally high thermal conductivities with nanoparticle suspensions and suggested various *ad-hoc* models to explain the phenomenon. In a conventional approach, the effect of the particle Brownian motion is neglected due to the assumed large particle size. As the particle size scale approaches the nano-meter range, the particle Brownian motion and its effect on surrounding liquids come to play an important role in heat and mass transfer. The inter-particle interaction force which is negligible on the macroscale is found to be very important for nanoparticle suspensions since the force scales are inversely proportional to L^{-2} , while other body forces vary with L^2 . Thus, the design procedure for microscale systems should be different from that for macroscale systems. Nevertheless, actual systems may work on both the microscale and macroscale, and it is important to interface both scales in the design phase.

As indicated, it is important to identify dominant forces and mechanisms for the analysis and design of microscale systems.

1.2 Research Objectives

The objectives of this study are:

- to identify important parameters for microscale liquid flows and nanoparticle suspensions;
- to find a proper way to simulate the phenomena; and
- to provide models to simulate the phenomena related to them.

1.3 Nanofluid Flow and Heat Transfer in Microchannels

1.3.1 Characteristics of Nanofluids

Nanofluids, as coined by Choi (1995), represent a new class of engineered heat transfer fluids, which contain metallic particles with average particle sizes of about 10 nanometers. They could be produced by using a physical gas-phase condensation process or chemical synthesis technique in order to increase the thermal conductivity of working fluids. Low thermal conductivity is a primary limitation in the development of energy-efficient heat transfer fluids that are required in many industrial applications. Despite considerable previous research and development efforts on heat transfer enhancement, major improvements in cooling capabilities have been lacking because of the low thermal conductivities of conventional heat transfer fluids (Choi, 1995). An innovative new class of heat transfer fluids can be engineered by suspending metallic nanoparticles in conventional heat transfer fluids. The resulting “nanofluids” are expected to exhibit high thermal conductivities compared to those of currently used coolants, and they represent a clear possibility for enhancement of heat transfer.

The basic idea is that by using the orders-of-magnitude larger thermal conductivities of metals compared to those of fluids, very high conductivities are expected for nanofluids. For example, the thermal conductivity of copper at room temperature is about 700 times greater than that of water and about 3000 times greater than that of engine oil. Even oxides such as alumina (Al_2O_3), which are insulators compared to metals such as copper, have thermal conductivities more than an order-of-magnitude larger than water.

The most important benefit of the fluids is dramatic reductions in necessary pumping power for heat exchangers, which results in significant energy and cost savings and supports the current industrial trend towards component miniaturization. Heat exchangers are used in vehicular and avionic cooling systems in the transportation industry, hydraulic heating and cooling systems in buildings, and industrial process heating and cooling systems in petrochemical, textile, pulp and paper, chemical, food and other processing plants. Another

advantage of nanofluids over conventional suspensions of coarse-grained particles in fluid systems is in their expected improved abrasion-related properties, since nanofluids will impart little impulse in collisions with component surfaces. For example, Hu and Dong (1998) reported that titanium oxide suspension in oil could enhance the wear resistance because of its deposition on rubbing surface.

In fact, numerous theoretical and experimental studies concerning effective thermal conductivities of mixtures that contain solid particles have been conducted since Maxwell's theoretical work was published more than 100 years ago (see Table 1.1). However, all of the studies on thermal conductivities of suspensions have been confined to millimeter- or micrometer-size particles. Maxwell's model shows that the effective thermal conductivity of suspensions that contain spherical particles increases with the volume fraction of the solid particles. It is also known that the thermal conductivity of suspensions increases with the ratio of the surface area to volume of the particle. One of the problems identified for micrometer-size particles in fluids is that they cause clogging. The influence of particle loading and size on the pressure drop of slurries was reported by Liu et al. (1988). It states that solid-particle suspensions in the 20 % volume fraction range incur little or no penalty in pressure drop as compared to single-phase fluids at comparable flow rates. Therefore, it is reasonable to assume that the nanofluid pressure drop behaves like that of a single phase fluid at volume fractions up to 20 %.

Table 1.1: Conventional models of effective thermal conductivity of solid/liquid suspensions k_e , thermal conductivity of base fluid k_m , thermal conductivity of particle k_2 , thermal conductivity ratio $\alpha = k_2/k_m$, $\beta = (\alpha - 1)/(\alpha + 2)$, particle shape factor n and particle volume fraction v , Xue (2003)

Models	Expressions	Remarks
Maxwell	$\frac{k_{eff}}{k_m} = 1 + \frac{3(\alpha-1)v}{(\alpha+2)-(\alpha-1)v}$	Spherical particles are considered
Hamilton-Crosser	$\frac{k_{eff}}{k_m} = \frac{\alpha+(n-1)-(n-1)(1-\alpha)v}{\alpha+(n-1)+(1-\alpha)v}$	Spherical and nonspherical particles are considered: $n=3$ for spheres, $n=6$ for cylinders
Jeffrey	$\frac{k_{eff}}{k_m} = 1 + 3\beta v + \left(3\beta^2 + \frac{3\beta^2}{4} + \frac{9\beta^3}{16} \frac{\alpha+2}{2\alpha+3} \dots\right) v^2$	Spherical particles are considered
Davis	$\frac{k_{eff}}{k_m} = 1 + \frac{3(\alpha-1)}{(\alpha+2)-(\alpha-1)v} [v + f(\alpha)v^2 + \mathcal{O}(v^3)]$	High-order terms represent pair interaction of randomly dispersed spheres.
Lu-Lin	$\frac{k_{eff}}{k_m} = 1 + \alpha v + bv^2$	Spherical and nonspherical particles are considered.
Bonnecaze-Brady	Numerical Simulation	Near- and far-field interactions among two or more particles are considered.

Experimental data

In the ideal mode of the transient hot-wire (THW) apparatus, an infinitely long, vertical, heat line source of zero heat capacity and infinite thermal conductivity is immersed at time $t=0$ in an sample fluid in thermodynamic equilibrium. When a stepwise heat flux q per unit length is imposed, the energy is entirely conducted from the line source to the fluid. For the heat line source of radius r_0 and a uniform initial temperature, the solution for the temporal temperature rise of the wire can be obtained with a transient lumped-parameter equation as:

$$\Delta T(r_0, t) = \frac{q}{4\pi k} \ln \left(\frac{4at}{r_0^2 C} \right) \quad (1.1)$$

The slope of the line ΔT vs $\ln t$ determines the thermal conductivity of the fluid.

The important experimental observations are presented in Table 1.2. For example, Lee et al. (1999) investigated the effect of Al_2O_3 and CuO nano-particle suspensions in *quiescent* water and ethylene glycol. They observed that the thermal conductivities of the suspensions increase linearly with volume fraction, α_d . In case of the 4 % Al_2O_3 suspension in ethylene glycol, they observed about 20 % increase of the thermal conductivity compared to that of single phase ethylene glycol. They confirmed that the mixture conductivity depends not only on the conductivity ratio and volume fraction, but also on the particle shape, as indicated Table 1.2 by comparing their data with data of Masuda et al. (1993). However, they observed an abnormal increase of thermal conductivity compared to the values predicted by the conventional relations. They attributed this to size dependence of the thermal conductivity, which does not exist for mini- and micro-particles. Lee et al. (1999) concluded that any new models of nanofluid thermal conductivity should include the surface area and structure dependent behavior as well as the size effect and boundary resistance.

Xuan and Li (2000) carried out the same experiment with Cu nano-particles in water and transformer oil. They listed the reasons of the heat transfer performance enhancement because of:

- increased surface area and heat capacity

Table 1.2: Experimental data; d : particle diameter, α_d : volume fraction

Author(s)	Material	Liquid	d (nm)	α_d (%)	Findings	
Lee et al. (1999)	Al_2O_3/CuO	Water, Glycol	Ethylene	38.4/23.6	1-5	Al_2O_3 good agreement with H-C model/ CuO :showed higher conductivity than H-C model predicts. Ethylene Glycol based nanofluids showed higher value. Al_2O_3 suspensions showed higher value.
Masuda et al. (1993)	Al_2O_3	Water		13	4.3	showed higher conductivity than H-C model predicts. Considered non-spherical particles.
Pak and Cho (1998)	Al_2O_3 , TiO_2	Water		13/27	1-4.5	both suspensions showed higher effective thermal conductivity than conventional theory predicts. Al_2O_3 suspension showed higher effective thermal conductivity. Effective viscosity increased maximum 200 [%]
Xuan and Li (2000)	Cu	Water		100	0.3-2	the suspension showed higher effective thermal conductivity than Maxwell relation predicts.
Eastman et al. (2001)	Cu , Al_2O_3 , CuO	Water, Glycol	Ethylene	< 10	0.3	anomalously increased effective thermal conductivity (40 %)
Choi et al. (2001)	nanotubes	α -olefin oil		$\sim 25 \times 50 \cdot 10^3$	0-1	anomalously increased effective thermal conductivity (160 %)
Xie et al. (2002)	Al_2O_3	Ethylene Glycol, Water, Pump Oil		12-302	0-5	All suspensions showed higher value than H-C model predicts. $k_{eff,DW} < k_{eff,EG} < k_{eff,DE}$. They observed that pH value and specific surface area of nanoparticles affected the effective thermal conductivity.
Das et al. (2003)	Al_2O_3/CuO	Water		38.4/28.6	1-4	both suspensions showed higher value than Maxwell relation predicts. Al_2O_3 suspension showed higher value. They observed temperature dependence of the effective thermal conductivity.
Patel et al. (2003)	Au – $citrate/Ag$ – $citrate$	Water, Toluene		15/70	0.00013- 0.011	both suspensions showed higher value than Maxwell relation predicts. Both suspensions showed measurable increase even with very small concentrations. They observed temperature dependence.
Xie et al. (2003)	nanotubes	Distilled Ethylene Decene	Water, Glycol,	$15 \times 30 \cdot 10^3$	0.1-1.0	All suspensions showed higher value than H-C model predicts. $k_{eff,DW} < k_{eff,EG} < k_{eff,DE}$

- increased apparent thermal conductivity
- interactions among particles, fluid and the flow passages
- intensified mixing due to velocity fluctuations (and turbulence) of the fluid
- flattened transverse temperature gradient of the fluid

They observed that the heat conductivities of nanofluids (≈ 100 nm) obey the Hamilton-Crosser relationship. They compared the enhancement of the heat transfer characteristic adopting nanofluids as working fluid. They adopted the dispersed model to take the random movement of the particles in the bulk flow into account. The effect of dispersion or backmixing results in flattening the temperature gradient. The contribution of the nanoparticles to convective heat transfer enhancement can be understood from two aspects: The particles increase the thermal conductivity of the fluid mixture and the chaotic movement of the particles strengthens the energy transport process.

On the basis of the dispersion model, the governing differential equation for the heat transfer process between the nanofluid flowing in a tube and the tube surface reads:

$$\frac{\partial T}{\partial t} + u \frac{\partial T}{\partial x} = \left(\alpha_{eff} + \frac{D_x}{(\rho C_p)_{eff}} \right) \frac{\partial^2 T}{\partial x^2} + \frac{1}{r} \frac{\partial}{\partial r} \left[\left(\alpha_{eff} + \frac{D_r}{(\rho C_p)_{eff}} \right) r \frac{\partial T}{\partial r} \right] \quad (1.2)$$

where D_x and D_r are the thermal dispersion coefficients to account for the contribution of hydrodynamic dispersion and the irregular movement of the ultra-fine particles.

In general, the thermal dispersion coefficient should be determined experimentally; although, there exist some analytic correlations for predicting this parameter under a number of assumptions. It is expected that for nanofluid flow in a tube the thermal dispersion coefficient may have the form:

$$\frac{D}{\alpha_f} = f \left(Re, Pr, \alpha, \frac{k_p}{k_f}, \frac{(\rho C_p)_p}{(\rho C_p)_f} \right). \quad (1.3)$$

Xuan and Li (2000) obtained an analytic solution for heat transfer with plug flow and concluded that the enhanced performance results not only from its high thermal conductivity of the mixture, but also from the random movement and dispersion effect of the nanoparticles. More details of the model was represented in their follow-up article (Xuan and Roetzel (2000)) which is summarized in the next section.

Eastman et al. (2001) observed that a nanofluid consisting of copper nanometer-sized particles dispersed in ethylene glycol has a much higher effective thermal conductivity than either pure ethylene glycol or ethylene glycol containing approximately 0.3 vol % of Cu-nanoparticles of mean diameter < 10 nm. Since the surface-area-to-volume ratio is 1000 times larger for particles with a 10 nm diameter than for particles with 10 μm diameter, a much more dramatic improvement in effective thermal conductivity is expected as a result of decreasing the particle size in a suspension than can be obtained by altering the shapes of larger particles. Cu-nanoparticles with little agglomeration and an average diameter of less than 10 nm were used with loadings up to approximately 0.5 vol %. For some samples, a small amount of thioglycolic acid (< 1 vol %) was added to the nanofluid to improve the particle dispersion behavior, for the case they observed most significant increase of the effective heat conductivity. They reported three important points.

- Very significant increases in thermal conductivity were seen for all measured nanofluids, with conductivity enhancement of up to 40 % observed for particle loadings well below one volume per cent.
- Nanofluids containing thioglycolic acid as a dispersion agent show improved behavior compared to non-acid containing nanofluids. It should be noted that fluids containing thioglycolic acid, but no particles, showed no improvement in thermal conductivity.
- Fresh nanofluids tested within two days of preparation exhibited slightly higher conductivities than fluids that were stored up to two months prior to measurements.

Based on the Hamilton-Crosser relation (see Table 1.1), for the case of $\alpha \rightarrow \infty$, $\frac{k_{eff}}{k_m} \rightarrow 1 + \frac{nv}{1-v}$. For small volume fractions, the relation reduces to $\frac{k_{eff}}{k_m} \rightarrow 1 + nv$. Therefore,

for their case, the increase of effective conductivity cannot exceed 1.5 % for spherical particles and 3 % for cylindrical particles, which means that the experimental results cannot be interpreted by way of the conventional theory. They mentioned that the lack of size dependence in conventional formulas.

Choi et al. (2001) produced carbon nanotube-in-oil suspensions and measured their effective thermal conductivity. The measured thermal conductivity is anomalously greater than theoretical predictions and is nonlinear with nanotube loadings. They observed a 160 % increase in thermal conductivity by adding 1 vol % of nanotubes into a synthetic poly (α -olefin) oil. They attributed this to the ballistic nature of the heat conduction in nanotube with the organized liquid layer on the solid surface to avoid the acoustic impedance mismatch, as well as nanotube-nanotube interactions due to the extremely high aspect ratio and the astronomical number of nanotubes in the liquid.

Keblinski et al. (2002) reported that the origin of the remarkable increases in thermal conductivity of nanofluids “eludes theoretical understanding” and explored four possible explanations for the anomalous heat conductivity increase by seeding nano-particles in fluids: *Brownian motion of the particles, molecular-level layering of the liquid at the liquid-particle interface, the nature of heat transport inside the nanoparticles, and the effects of nanoparticle clustering.*

- *Brownian motion*

They compared the time scale of Brownian motion ($\tau_d = \frac{3\pi\eta d^3}{6k_B T}$) and that of heating the particle ($\tau_H = \frac{d^2 C_p \rho}{6k_f}$), and conclude the heating time scale is much smaller than the Brownian motion time scale. This implies that the movement of nanoparticles due to Brownian motion is too slow to transport significant amounts of heat through a nanofluid.

- *Molecular layering at liquid-particle interface*

Contact (Kapitza) resistance decrease the thermal conductivity with decreasing grain

size, contrary to the experimental results. By contrast, an interface effect that could enhance thermal conductivity is the layering of the liquid at the solid-liquid interface, by which the atomic structure of the liquid layer is significantly more ordered than that of the bulk liquid. Given that the crystalline solids (which are obviously ordered) display much better thermal properties than liquids, such ordered liquid layering at the interface would be expected to lead to a higher thermal conductivity. Assuming that the thermal conductivity of the interfacial liquid is the same as that of the solid, the layer works as an extended volume of the solid and, hence, increases the volume fraction, v or α_d . However, the experiments and simulations of others showed that a typical interfacial layer thickness is only on the order of a few atomic distances, i.e., ≈ 1 nm. Thus, although the presence of an interfacial layer may play a role in heat transfer, it is not likely to be solely responsible for an enhancement of the thermal conductivity.

- *Nature of heat transfer in nanoparticles*

Macroscopic theories assume diffusive heat transfer. In crystalline solids, such as those used in nanofluids, heat is carried by phonons, i.e., by propagating lattice vibrations. Such phonons are created at random, propagate in random directions, are scattered by each other or by defects, and thus justify the macroscopic description of heat transport. In metals, the heat is primarily carried by electrons, which also exhibit diffusive motion at the microscopic level. Koblinski et al. (2002) compared the mean free path of a phonon and the particle size, and concluded that the phonon cannot diffuse but move ballistically across the particle. This implies that the assumption of diffusive heat transfer in nanoparticles is invalid; consequently, a macroscopic theory, such as the Hamilton-Crosser theory, does not apply and a theoretical treatment based on ballistic phonon transport is required. If the particles are so close (1 - 2 nm) that the phonon can cross the matrix of the liquid, a major increase in thermal conductivity is expected.

- *Effect of nanoparticle clustering*

By creating paths of lower thermal resistance, clustering of particles into percolating patterns would have a major effect on the effective thermal conductivity. Although percolating structures cannot be set up, local clustering is possible and indeed has been observed experimentally. Since within such clusters, heat can move very rapidly, the volume fraction of the highly conductive phase is larger than the solid volume and may significantly increase the thermal conductivity. They noted that, in general, clustering may exert negative effect on heat transfer enhancement, particularly at low volume fractions, by settling small particles out of the liquid and creating large regions of “particle free” liquid with high thermal resistance.

Kebllinski et al. (2002) asserted the non-effectiveness of Brownian motion and ballistic nature of heat transfer in nanoparticles by using molecular dynamics. However, they mentioned that the ballistic nature of heat transfer does not directly relate to the increase of thermal conductivities.

Xue (2003) as well as Yu and Choi (2003) incorporated the ordered liquid layer around a solid particle, they called it nanolayer, into a modified Maxwell model. They proposed that the nanolayer acts as a thermal bridge between a solid and the bulk liquid and so is key to enhancing the thermal conductivity. The thermal conductivity of the nanolayer on the surface of the nanoparticle is not known. However, because the layered molecules are in an intermediate physical state between a bulk liquid and a solid, the nanolayer of liquid molecules is expected to lead to a higher thermal conductivity than that of the bulk liquid. Based on this assumption, they modified the Maxwell equation for the effective thermal conductivity of solid-liquid suspensions to include the effect of this ordered nanolayer. To show a new connection between the nanolayers and a thermal conductivity increase in nanofluids, they assumed that the thermal energy transport in nanofluids is

diffusive. This is feasible because the average interparticle distance in nanofluids is much greater than the mean free path of the liquid molecules. Under this assumption they used the conventional Maxwell relation as a representative of all other conventional models. In order to include the effect of the liquid layer, they considered a nanoparticle-in-liquid suspension with mono-size spherical particles of radius r and particle volume concentration ϕ . They assumed that the layer of thickness h around the particles is more ordered than that of the bulk liquid and that the thermal conductivity k_{layer} is higher than that of the bulk liquid. To further simplify their analysis, they assumed that the nanolayer around each particle could be combined with the particle to form a larger equivalent particle and that the particle volume concentration is so low that there is no overlap of those equivalent particles. The above assumptions resulted in an equivalent particle radius $r + h$ and an increased volume concentration ϕ_e , which can be calculated as:

$$\phi_e = \frac{4}{3}\pi(r + h)^3 n = \frac{4}{3}\pi r^3 n (1 + h/r)^3 = \phi(1 + \beta)^3 \quad (1.4)$$

where n is the particle number per volume and $\beta = h/r$ is the ratio of the nanolayer thickness to the original particle radius. Based on the effective medium theory (Schwartz et al., 1995), the equivalent thermal conductivity k_{pe} of the equivalent particles can be calculated as:

$$k_{pe} = \frac{[2(1 - \gamma) + (1 + \beta)^3(1 + 2\gamma)]\gamma}{-(1 - \gamma) + (1 + \beta)^3(1 + 2\gamma)} \quad (1.5)$$

where $\gamma = k_{layer}/k_p$ is the ratio of nanolayer thermal conductivity to particle thermal conductivity. Plugging the above relation into the Maxwell relation yields the effective conductivity.

$$k_e = \frac{k_{pe} + 2k_1 + 2(k_{pe} - k_1)(1 + \beta)^3\phi}{k_{pe} + 2k_1 - (k_{pe} - k_1)(1 + \beta)^3\phi} k_1 \quad (1.6)$$

Yu and Choi (2003) observed the following:

- Nanoparticles of under 5 nm in radius are affected measurably by the assumed nanolayer.

- If $k_{layer} > 10k_1$ thermal conductivity enhancement is strongly dependent on the thickness of the nanolayer, but is almost invariant to the thermal conductivity of the nanolayer. Therefore, they concluded that the thickness of the nanolayer is important.

However, Xue (2003) as well as Yu and Choi (2003) adjusted the liquid molecular layer-thickness and its thermal conductivity to match the experimental data, which turned out to be non-physical. For example, Xue (2003) assumed a liquid molecular layer to be 3 [nm] thick and its thermal conductivity to be 2.1 [W/mK]. According to Israelachvili (1992), the thickness of such a structured layer cannot exceed 4 to 5 molecule diameters which is usually below 1 [nm]. Furthermore, the intermolecular potential between particle surface and liquid molecule decreases very fast with distance, so that the molecules of the outer layer region are relatively free to move. Xue (2003) used the thermal conductivity value of ice, i.e., 2.1 [W/mK], for the thermal conductivity value of the molecular layer assuming that water molecule layers on the particle surface would be in a fixed structure just like ice, which is not true. He referred to Ohara and Suzuki (2000) as evidence that such an organized “solid-like” structure of a liquid at the surface is a governing factor in heat conduction from a solid wall to an adjacent liquid. However, Ohara and Suzuki (2000) reported that the liquid molecular structure around a particle actually reduced the macroscopic heat flux. Furthermore, Barrat and Chiaruttini (2003) reported that in the case of normal liquids in contact with a solid, it can be expected that the Kapitza length should be of the order of a few molecular diameters, which is the same order as the liquid molecular layer thickness.

1.3.2 Driving forces for Microchannel flow

The flow in a microchannel could be driven by a net pressure force as it is in a macroscale conduits. However, considering the efficiency degradation of pressure driven pumping with system miniaturization, other forces are considered to replace it. The momen-

tum equations of flows with uncommon driving forces, such as electro-osmosis and surface tension, could be expressed by using a generalized momentum equation.

$$\frac{\partial \rho \mathbf{u}}{\partial t} + \nabla \cdot (\rho \mathbf{u} \otimes \mathbf{u}) - \nabla \cdot (\eta \cdot (\nabla \mathbf{u} + \nabla \mathbf{u}^T)) + \mathbf{S} = 0 \quad (1.7)$$

where \mathbf{u} is the velocity vector, ρ is the fluid density, η is the fluid viscosity, and \mathbf{S} is a source term.

For electro-osmosis driven flows the source term \mathbf{S} can be expressed as $\rho_E \mathbf{E}$, where ρ_E and \mathbf{E} are the electric charge density and electric field, respectively.

To simulate the flows using surface tension as the driving force, the boundary conditions at the interface of the two fluids are changed while there is no source term in the governing equations. At the interfaces, the boundary condition is specified as

$$\mathbf{f}_s^\alpha + \mathbf{f}_s^\beta + \nabla_s \sigma = 0 \quad (1.8)$$

where α and β denote the neighboring two fluids, the \mathbf{f}_s stands for the force at the interface, and σ is the surface tension.

Detailed submodels and limiting case solutions may be found in Probst (2003). Here, application examples are listed.

Electrokinetic forces

Governing equations. The electro-osmotic velocity produced in a smooth circular capillary by a uniform electric field applied along the axis is given as follows. If the surface is assumed to be negatively charged, then the flow will be in the direction of the cathode. With the electric body force per unit volume given by $\mathbf{f}_E = \rho_E \mathbf{E}$ where ρ_E and \mathbf{E} are electric charge density [kg m^{-3}] and electric field [J kg^{-1}], respectively,

the momentum equation can be written

$$\rho \frac{D\mathbf{u}}{Dt} = \nabla \cdot \boldsymbol{\tau}_{ij} + \rho \mathbf{g} + \rho_E \mathbf{E} \quad (1.9)$$

Neglecting gravitational forces and supposing the flow to be an inertia free capillary flow, with no pressure gradient, Eq. 1.9 simply reduces to a balance between viscous and electrical forces:

$$\mu \nabla^2 \mathbf{u} = -\rho_E \mathbf{E} \quad (1.10)$$

Applications. Ehrfeld (2003) listed products based on electrokinetic phenomena. He reported that electrokinetic phenomena are based on the fact that a charge separation occurs at the interface of electrochemical two-phase systems and an electrochemical double-layer where a so-called electrokinetic or Zeta potential is created. This may result from a selective dissolution or a specific adsorption of ions on the surface of the solid phase.

He mentioned that electrophoresis has been widely applied in the life sciences as a separation technique for colloidal species or macromolecules in a suitable gel. *Isoelectric focusing* is a special case of electrophoresis where the pH-dependence of the charge properties of amphoteric charged species is utilized. These species (e.g., proteins, peptides) are migrating in the electrical field along a continuous pH gradient in a gel to the isoelectric point, i.e., a steady-state position where their net charge is zero and the molecule comes to rest. He pointed out that a prerequisite for electro-osmosis is the presence of immobilized surface charges at the capillary wall (typically a negatively charged SiO unit) in contact with an electrolyte.

Electronic ink displays. As a real world applications, Ehrfeld (2003) referred to electronic ink displays. The worldwide development of flat panel displays aims at wafer-thin, flexible, full-color and large area devices which have a low electri-

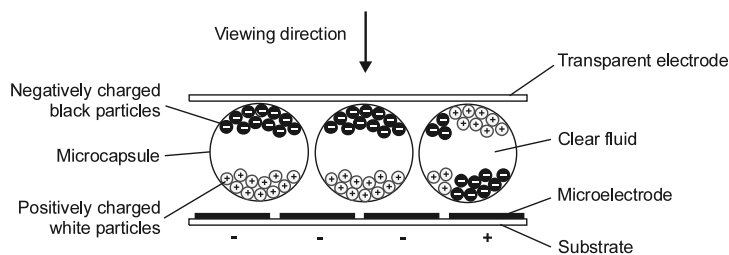


Figure 1.1: Schematic of the operation principle with electronic ink.

cal power consumption and are producible at low cost. Besides advanced liquid crystal displays (LCD) and organic light emitting diode displays (OLED) a novel technology called electronic ink (e-ink) is a very promising approach in this respect. It has been developed by E-Ink Corporation and utilizes electrophoresis in microcapsules for image generation. The microcapsules have a diameter in the order of $50 \mu\text{m}$ and are filled with a clear fluid and a number of white and black particles which are oppositely charged and can be moved in opposite direction by applying an electric field. The principle of image generation is illustrated by Fig. 1.1. When a voltage is applied between the bottom and top electrodes, the oppositely charged black and white particles migrate into the corresponding directions. Compared with transmissive LCDs or emissive technologies like OLEDs, field emitter displays and plasma displays the power consumption of electronic ink displays is very low. Furthermore, it has much more favorable values for reflectance, contrast ratio and viewing angle. Meanwhile, first portable electronic products like PDAs with e-ink displays are coming into the market and a wide variety of further products is under development ranging from eBooks to fashion accessories.

Microfluidic devices. Microfluidic devices can be classified into two main groups. So called micro-arrays mainly aim at high throughput screening of a huge number of substances in drug development using hybridization or other reactions to iden-

tify specific binding of special bio-molecules to other reactants arranged as dots in a large matrix pattern on a small substrate. More complex are so called microfluidic devices where often electrokinetic effects are applied for transport, pumping and dispensing of small amounts of fluids as well as separation of biomolecules like DNA fragments, peptides or proteins. Generally, molecules or reagents are moved in microfluidic devices through a network of microchannels and microchambers comprising several functions on one single chip like sampling, sample treatment including filtration, concentration, mixing, reaction, separation, and detection. The advantages of electrokinetically driven microsystems over, say, pressure-driven microsystems are based in particular on positive scaling effects. Microfluidic devices using electrophoretic separation are superior due to faster speed and smaller sample consumption. In addition, electro-osmosis allows realizing accurate control of transportation and manipulation of liquid samples by means of electrostatic forces without requiring movable mechanical parts.

Recent developments include 2D electrophoresis and free-flow electrophoresis. Figure 1.2 shows a schematic representation of 2D capillary gel electrophoresis on a substrate whose size might be finally only a few square centimeters.

Besides separation, transport and flow control in microchannels on a chip are of major importance. In this respect, electro-osmosis is a powerful tool which allows pumping fluids over a wide range of conductivity, including buffered solutions and organic solvents.

Electrokinetic flow control is carried out on a microscale using pinched valves and gated valves. By that means, a sample can be injected like a plug into a microfluidic T-junction or a sample can be diluted by diffusive mixing of the sample with the buffer solution. Diffusive mixing occurs in tens of seconds and various designs have been reported to reduce the length of the mixing path and corresponding timescale.

The opposite process, increasing the sample concentration can be achieved by

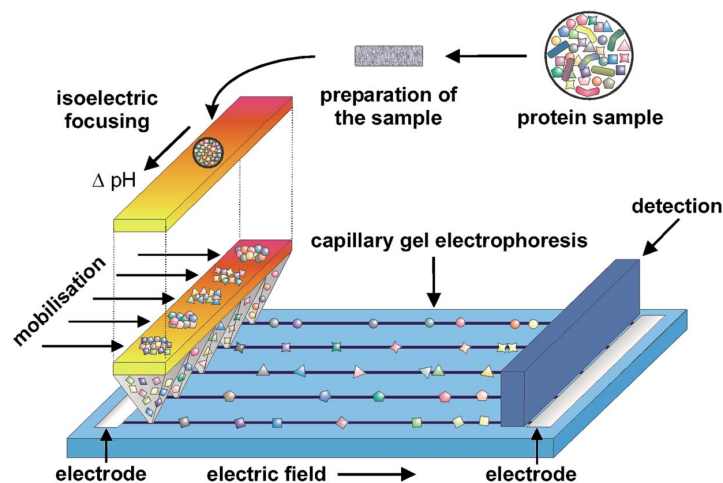


Figure 1.2: A schematic for 2D gel electrophoresis on a microchip. The first dimension of separation operates by isoelectric focussing. From this level, the separated groups of molecules are conducted to the second dimension of separation. The separation of molecules occurs by electrophoresis.

means of semi-permeable membranes which allow withdrawing selected species. Microfluidic devices using electrokinetic effects have made great progress in biochemical analysis and are becoming an indispensable tool for research and development in the life sciences.

Surface tension and phase change (Probstein, 2003)

Boundary conditions As explained, surface tension becomes very important in micro-scale conduits if there is any contact line of different materials. Lee et al. (2004) and Li et al. (2004) investigated experimentally bubble dynamics in microchannels. They reported that the bubble behaves differently from those in macro-scale channels in terms of the growing rate and bubble frequency. They also reported that the surface tension and drag force were the governing forces of the phenomena, where the gravity force plays an important role in macro-scale conduits.

Spatial variations in surface tension at a liquid-gas interface result in added tangential

stresses at the interface and hence a surface attractive force that acts on the adjoining fluid, giving rise to fluid motion in the underlying bulk liquid. The motion induced by tangential gradients of surface tension is usually termed the *Marangoni effect*.

Spatial gradients in surface tension may arise from a variety of causes, surface concentrations of an impurity or additive, or in electric charge or surface potential. The resulting flows are termed, respectively, thermocapillary flows, diffusocapillary flows, and electrocapillary flows. Clearly, then, we must know the concentration, temperature, and charge distributions at the interface in order to define the surface tension variation required to solve the hydrodynamic problem. However, these distributions are themselves coupled to the equations of conservation of mass, energy, and charge through the appropriate interfacial boundary conditions. The boundary conditions are obtained from the requirement that the forces at the interface must balance. This implies that the tangential shear stress must be continuous across the interface, and the net normal force component must balance the interfacial pressure difference due to surface tension.

If the surface tension varies along the interface, a tangential force per unit area will exist on the interface, given by

$$\mathbf{f}_s = \nabla_s \sigma \quad (1.11)$$

where ∇_s denotes the surface gradient and \mathbf{f}_s is the force component in the surface. The positive sign on $\nabla_s \sigma$ indicates that the liquid tends to move in a direction from lower to higher surface tension.

Let us denote the force per unit area exerted on the interface from the viscous stresses and pressures associated with the boundary fluids as \mathbf{f}^α and \mathbf{f}^β . The superscripts α and β refer to the two different fluids on each side of the interface. With \mathbf{n} the unit normal vector into the fluid β , the forces may be written

$$\mathbf{f}^\alpha = \mathbf{n} \cdot \tau_{ij}^\alpha + \mathbf{n} p^\alpha \quad (1.12a)$$

$$\mathbf{f}^\beta = -\mathbf{n} \cdot \boldsymbol{\tau}_{ij}^\beta - \mathbf{n} p^\beta \quad (1.12b)$$

We now can make a tangential and normal force balance. In the tangential direction on the interface the forces \mathbf{f}^α and \mathbf{f}^β are purely viscous, and from Eq. (1.12a) and (1.12b) we have

$$\mathbf{f}_s^\alpha + \mathbf{f}_s^\beta + \nabla_s \sigma = 0 \quad (1.13)$$

Thus the shear stress depends on the local surface tension gradient, in the absence of which Eq. (1.8) simply reduces to the usual fluid dynamic boundary condition that the tangential viscous stress is continuous at the interface of two different fluids. The normal force balance simply gives the scalar equation

$$\mathbf{f}_n^\alpha + \mathbf{f}_n^\beta = \sigma \left(\frac{1}{R_1} + \frac{1}{R_2} \right) \quad (1.14)$$

which is called the Young-Laplace equation. The normal forces \mathbf{f}_n include both the thermodynamic pressures as well as the normal viscous stresses.

Applications

Pumping. Kim (1999) reported that surface-tension-induced motion is possible by creating surface tension difference in fluid-fluid or fluid-solid interface. There are several ways to control the surface tension, such as chemical (i.e., use of surfactant), thermal (e.g. Marangoni force), and electrocapillary. Among them use of electrocapillary appears most promising due to the energy efficiency (vs. thermal) and potentially simple and long-lasting operation (vs. chemical), as well as the simplicity in realizing by microfabrication.

While the electro-capillary, in general, refers to a relationship between surface tension change of liquid metal due to applied voltage, continuous electro wetting (CEW) refers to a principle of moving a lump of liquid metal using electric

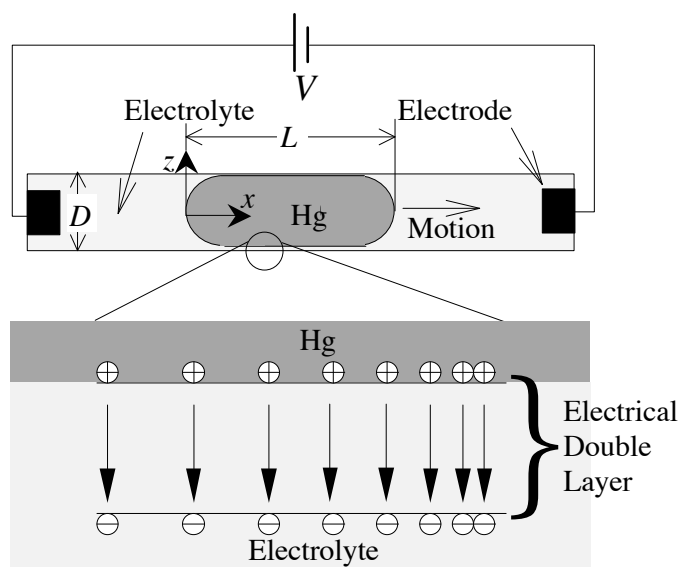


Figure 1.3: Continuous electro-wetting (CEW) effect

potential. A drop of liquid metal travels along an electrolyte-filled channel or tube when electric potential is applied across the length of the channel. The movement of a mercury slug in electrolyte-filled channel or tube when electric potential is applied across the length of the channel. The movement of a mercury slug in electrolyte is due to the local change of surface tension.

Figure 1.3 shows a state of electric charge distribution at the mercury-electrolyte interface, which is responsible for surface tension gradient according to Lippman's equation, and the motion induced by it. The electric potential across the electrical double layer becomes higher as x -coordinate increases. The surface tension decreases as the electric potential increases and the motion occurs to the right where the surface tension is lower. Movement of the mercury to the lower surface-tension area can be interpreted as the tendency to minimize the energy by wetting low surface tension region more than the higher one.

Using the enabling technologies developed to make microscale mercury droplets on lithographically defined spots and to encapsulate electrolyte in lithographi-

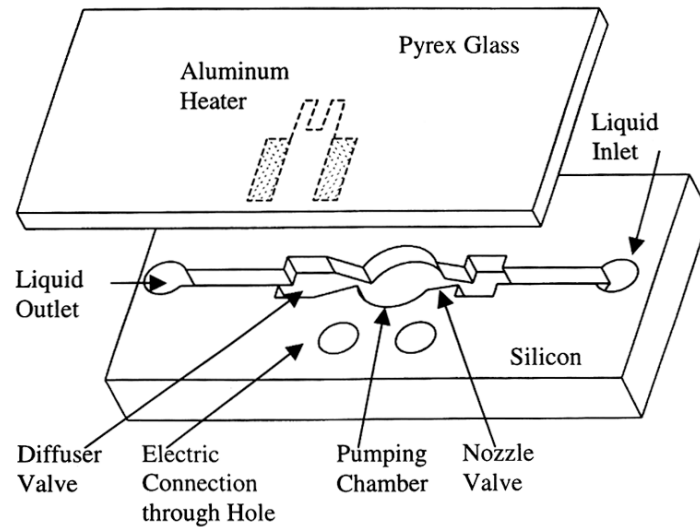


Figure 1.4: Schematic drawing of the nozzle-diffuser based bubble pump (Tsai & Lin, 2002)

cally defined region, CEW effect has been realized with MEMS. Although the moving distance of the liquid metal is found limited for microscale devices due to the severe polarization effect caused by the unusually small size of the electrode, a long-range movement can still be obtained by alternating the polarity to the overlapping electrodes. The application of long-distance travel strategy to a loop of channel results in indefinite circular motion of a liquid metal droplet, which is called a *liquid micromotor*.

Tsai and Lin (2002) reported that it becomes significantly difficult to further miniaturize the diaphragm-based pumps because the large force is required to deflect the diaphragms for pumping. They proposed a new design based on the piezoelectric actuated nozzle-diffuser valveless pump. The piezoelectric actuator was replaced with the bubble pumping chamber. They used isopropanol as the working fluid for its easy access and low boiling temperature. Figure 1.4 shows the schematic of their micropump. They listed the advantages of thermal-bubble-actuated micronozzle-diffuser pump;

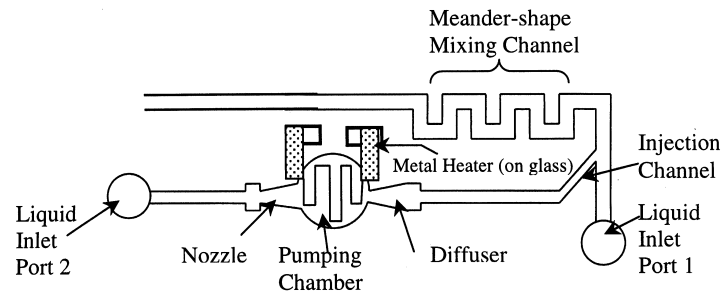


Figure 1.5: Schematic drawing of the exemplary integrated system of a micropump and a mixing channel.

1. thermal bubbles can be easily generated even when the pump is further miniaturized,
2. thermal bubble can sweep across most of the pumping chamber for optimal efficiency, and
3. the concern of complicated fabrication process for micro valves is alleviated because there are no moving mechanical parts in the micropump.

They applied the micropump to assist mixing of liquids. With proper microchannel design, the oscillatory flows generated by micropump can be used to induce a wavy interface between two liquids to enlarge the contact surface and accelerate the mixing process (see Fig. 1.5).

Ink-Jet printing head. The majority of activity in ink jet printing today is in the drop-on-demand methods. Most of the drop-on-demand ink-jet printers on the market today are using either the thermal or piezoelectric principle.

Figure 1.6 shows a novel droplet ejection mechanism that uses the flow-blocking effect of bubbles in microchannels. Due to the large surface tension in microscale, the bubble in microchannel functions as a check valve, which can be created thermally by a patterned resistor and eliminated by conductive heat dissipation. With a bubble in place (i.e., virtual check valve closed), a droplet can be ejected with high pressure without the problem of chamber-to-chamber cross talk. With the

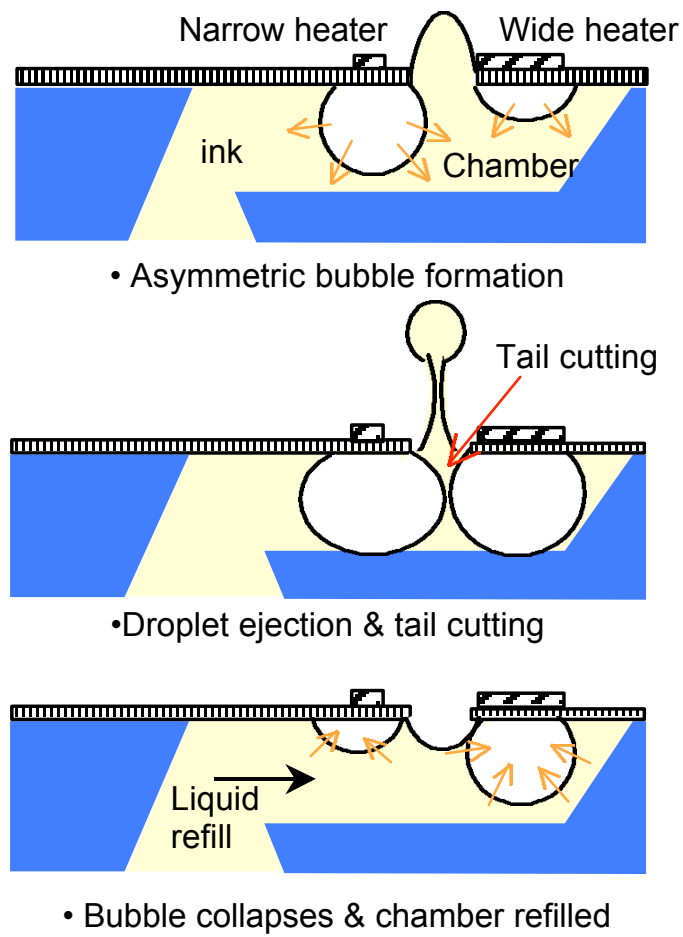


Figure 1.6: Principle of bubble valve for micro-injector (Kim, 1999)

bubble collapsed (i.e., valve open), ink refills the microchamber quickly without much restriction in the flow path. The result is a high frequency droplet ejection without any microvalve fabricated. The device demonstrated an ejection frequency several folds higher than commercial inkjet printers (e.g., from 5 kHz to 35 kHz), not to mention the complete elimination of the so-called satellite droplet, with no added fabrication complexity.

Capillary gating valve. A passive micro-fluidic capillary-driven valve that exploits the surface tension force to stop flows in micro-channels recently has attracted considerable attention and has strong appeal for applications to various microfluidic systems. These valves have the advantage of not requiring moving parts. They are not sensitive to the properties of buffer/samples pumped or the presence of trapped air bubbles. They also alleviate problems associated with Joule heating that occur in electro-kinetic systems that demand high field strengths. The principle of operation is based on the pressure barrier that develops when the cross section of the capillary expands abruptly. As the meniscus (interface) area/volume enlarges with increasing driving pressure, the increase in interfacial surface energy appears as an equivalent capacitance in the fluidic circuit. This fluidic capacitance relates meniscus area to driving pressure in a similar way as electrical capacitance relates charge to voltage. Such a capacitance model requires the relation between the charge (driving pressure) and response (area of the meniscus). When the driving pressure exceeds a specific breaking point - the maximum capillary barrier - a fluid flow will be established through this microfluidic valve shorting the fluidic capacitance. The maximum capillary barrier defines the ceiling criterion of the capacitance working relation, another essential component of the fluidic capacitance model (Zeng).

Heat exchanger. Recent results in the microfluidics group at the Berkeley Sensor and Actuator Center and the Air Force Research Laboratory have shown that a micro-capillary pumped loop (micro-CPL) can move extreme amount of heat

(< 200 W/cm^2) to provide integral cooling to electronics or MEMS type devices without optimizing process (Trebotich et al., 2001).

Micro-cooler based MEMS technologies provide the three advantages:

1. precise temperature control at the chip level,
2. the overall cooling is more efficient because specific heat sources within the electronics package may be targeted, and
3. the overall size of the electronic system can be kept small.

1.3.3 Momentum and Heat Transfer in Microchannels

The compactness and high surface-to-volume ratios of microscale fluid devices make them attractive alternatives to conventional flow systems for heat transfer augmentation, chemical reactor or combustor miniaturization, aerospace technology implementations, and biomedical applications, such as drug delivery, DNA sequencing, and bio-MEMS, to name a few.

While experimental evidence indicates that fluid flow in microchannels, especially in terms of wall friction, differs from macrochannel flow behavior, laboratory observations are often inconsistent and contradictory. Thus, theoretical microfluidics investigations are necessary; however, for any computational analysis of microchannel flow, some pertinent questions have to be considered (Gad-el Hak, 1999; Pfahler et al., 1990): Is the continuum assumption still valid? For example, the gas flow Knudsen number, $Kn = \lambda/L$, should be very small, i.e., $Kn < 0.1$, for the Navier-Stokes equations to hold. Kleinstreuer (2003) discussed alternative Knudsen numbers for liquid and two-phase flows. Are entrance effects persuasive in light of the typically short channel length? Microchannel inlet configurations, flow inlet conditions, and flow developments all have to be considered as entrance effects. Is the onset of instabilities affected by the small size of the conduits? For example, complex inlet geometries, significant wall roughness as well as interactions of large fluid molecules and micro-particle suspensions may trigger or modulate local flow instabilities, including possible transition to turbulence.

Theories have been well developed for gas flow in microchannels, and they have shown good agreements with experimental observations (Gravesen et al., 1993; Beskok and Karniadakis, 1994, 1999; Harley et al., 1995; Chen et al., 1998). For example, Gravesen et al. (1993) highlighted wall-slip and compressibility phenomena in microchannels as important causes for deviations from macroscale gas flows. For liquid flows, Gravesen et al. (1993) emphasized the importance of existing bubbles in a channel, the independence of viscosity on the characteristic dimensions, and the channel length effect. If bubbles are present, they increase the pressure drop, due to the surface tension effect. Bubbles are hard to eliminate

completely; they may entrain when first filling a channel. Gravesen et al. (1993) found no microfluidic device that works in the fully-developed (turbulent) regime, and many devices are so short that the pressure drop is dominated by inertial losses. Elwenspoek et al. (1994) mentioned the entrance effect as a possible cause for the deviation of published experimental results from the conventional theory applied to macroscale systems. They observed that contamination of liquids by particles occurs very often, and their origin is quite unclear. Without filtering, they never would have obtained reproducible results, and if they reproduced, they were in accordance with theoretical expectations. They also emphasized the effect of bubbles trapped in the microchannels and the importance of mixing in microscale devices. Ho and Tai (1998) pointed out the necessity to re-examine the surface forces in the momentum equation. It was found that the frictional force between their rotor and the substrate is a function of the contact area. This result departs from the traditional friction law, which states that the friction force is linearly proportional to the normal force only. They took this as an example for the importance of surface forces in microscale devices such as the van der Waals force, electrostatic force, and steric force. They concluded that an apparent viscosity would represent the integral effects of these surface forces.

Sobhan and Garimella (2001) reviewed published experimental data on fluid flow and heat transfer in microchannels, and summarized that the possible causes of the discrepancies in prediction could be entrance and exit effects, differences in surface roughness in the different microchannels investigated, non-uniformities in channel dimensions, nature of the thermal and flow boundary conditions, as well as uncertainties and errors in instrumentation, measurement, and measurement location. Morini (2004) added electro-somotic effects (EDL) to the list of possible causes.

In addition to surface roughness, wall-slip and possible two-phase effects in microchannels were discussed by several researchers. For example, Trethewey and Mainhart (2002) observed a wall-slip velocity for water flow on hydrophobic walls, while Wu and Cheng (2003) measured a decrease of Nusselt number for flows in hydrophobic channels and an increase in channels of high relative surface roughness. Tyrrell and Attart (2001) reported the exist-

tence of 20-30 [*nm*] thick air bubble gaps between wall and bulk water using atomic force microscopy, and Tretheway and Mainhart (2004) calculated the necessary air gap thickness to yield the velocity slip they observed. As expected, the existence of an air gap will decrease the heat transfer performance in channels.

Clearly, momentum and heat transfer in microchannels are results of complex physical phenomena.

1.4 Numerical Solution Techniques

By definition, *fluids* deform continuously under (shear) stress ignoring molecular effects that, for example, may be important in microfluidics (Gad-el Hak, 1999) when the *continuum mechanics* assumption is violated. The continuum hypothesis postulates that fluid elements, actually material points, are distributed continuously. It implies that the mean-free-path, λ , between fluid (gas) molecules is much less than an appropriate minimum length-scale L of the flow system, as expressed with the Knudsen number

$$Kn = \frac{\lambda}{L} \quad (1.15)$$

For example, $L = \rho/|\partial\rho/\partial y|$ to calculate the *local* Kn-number, or $L = l_{device}$ for the *global* Kn-number (Kleinstreuer, 2003).

1.4.1 Molecular Dynamics (all Knudsen numbers)

Introduction

The information provided in this section is based on the works by ? and Binder et al. (2004). Applications to microfluidics employing molecular dynamics (MD) are presently quite impossible. The typical time scale to simulate a system's dynamics ranges from 0.1 s to 10^3 s. Hence, for a chemically realistic molecular dynamics simulation, with a necessary time step in the range of 1 fs ($= 1 \times 10^{-15}$ s) to 10 fs, the task is quite taxing, considering that one would have to simulate over a range of 10^{15} time steps which is many orders of magnitude more than what is feasible nowadays.

Molecular dynamics (MD) is a computer simulation technique where the time evolution of a set of interacting atoms is followed by integrating their equations of motion. In molecular dynamics we follow Newton's law, i.e., for each atom i in a system consisting of N atoms,

$$F_i = m_i a_i \quad (1.16)$$

Here, m_i is the atom mass, a_i its acceleration, and F_i the force acting upon it, due to the interactions with other atoms. Therefore, in contrast with the Monte Carlo method, molecular dynamics is a deterministic technique: given an initial set of positions and velocities, the subsequent time evolution is in principle completely determined. In more pictorial terms, i.e., in virtual reality, atoms will “move” around, bumping into each other, oscillating in waves in concert with their neighbors, perhaps evaporating away from the system if there is a free surface, mimicing what atoms in a real substance would do. The computer calculates a trajectory in a $6N$ -dimensional phase space ($3N$ positions and $3N$ momenta). However, such trajectories are usually not particularly relevant by themselves. Thus, molecular dynamics brought a statistical mechanics to keep solutions managable. Like Monte Carlo, it is a way to obtain a set of configurations distributed according to some statistical distribution functions, or statistical ensembles. An example is the microcanonical ensemble, corresponding to a probability density in phase space where the total energy is a constant E :

$$\delta(H(\Gamma) - E) \tag{1.17}$$

Here, $H(\Gamma)$ is the Hamiltonian, and Γ represents the set of positions and momenta; δ is the Dirac function, selecting only those states which have a specific energy E . Another example is the canonical ensemble, where the temperature T is constant and the probability density is the Boltzmann function

$$\exp(-H(\Gamma)/\kappa_B T) \tag{1.18}$$

According to statistical physics, physical quantities are represented by averages over configurations distributed according to a certain statistical ensemble. A trajectory obtained by molecular dynamics (see Eq. (1.16)) provides such a set of configurations. Therefore, a measurement of a physical quantity by simulation is simply obtained as an arithmetic average of the various instantaneous values assumed by that quantity during the numerical MD simulation run. Statistical physics is the link between the microscopic behavior and thermodynamics. In the limit of very long simulation times (and high N -values), one could

expect the phase-space to be fully sampled, and in that limit this averaging process would yield the thermodynamic properties. In practice, the runs are always of finite length, and one should exert caution to estimate when the sampling may be good (“system at equilibrium”) or not. In this way, MD simulations can be used to measure thermodynamic properties and therefore evaluate, say, the phase diagram of a specific material. Beyond this “traditional” use, MD is nowadays also used for other purposes, such as studies of non-equilibrium processes, and as an efficient tool for optimization of structures overcoming local energy minima (e.g., simulated annealing).

Applications (Ercolessi, 1997)

- *Liquids*: Availability of new realistic interaction models allows to study new systems, elemental and multicomponent. Through non-equilibrium techniques, transport phenomena such as viscosity and heat flow have been investigated.
- *Defects*: Defects in crystals—crucial for their mechanical properties and therefore of technological interest—remain a favoured topic. The focus shifted perhaps from point defects (vacancies, interstitials) to linear (dislocations) and planar (grain boundaries, stacking faults) defects. Again, improved realism thanks to better potentials constitutes a driving force.
- *Fracture*: Under mechanical action, solids break into two or more pieces. The fracture process can occur in different ways and with different speeds depending of several parameters. The technological importance is obvious, and simulation is providing insight.
- *Surfaces*: Surface physics had a boom starting in the 80s, thanks to the availability of new wonderful experimental tools with microscopic resolution (scanning tunneling microscopy, high resolution electron microscopy, several scattering-based techniques). Simulation is still playing a big role in understanding phenomena such as surface

reconstructions, surface melting, faceting, surface diffusion, roughening, etc, often requiring large samples and simulation times.

- *Friction*: Even more recent are investigations of adhesion and friction between two solids, propelled by the development of the atomic force microscope (AFM). The body of “macroscopic” knowledge is being revised and expanded on microscopic grounds.
- *Clusters*: Clusters—conglomerates of a number of atoms ranging from a few to several thousands—constitute a bridge between molecular systems and solids, and exhibit challenging features. Frequently, an astonishingly large number of different configurations have very similar energies, making it difficult to determine stable structures. Their melting properties can also be significantly different from those of the solid, due to the finite size, the presence of surfaces and the anisotropy. Metal clusters are extremely important from the technological point of view, due to their role as catalysts in important chemical reactions (for instance, in catalytic exhaust pipes of cars).
- *Biomolecules*: MD allows to study the dynamics of large macromolecules, including biological systems such as proteins, nucleic acids (DNA, RNA), membranes. Dynamical events may play a key role in controlling processes which affect functional properties of the biomolecule. Drug design is commonly used in the pharmaceutical industry to test properties of a molecule on the computer without the need to synthesize it (which is far more expensive).
- *Electronic properties and dynamics*: The development of the Car-Parrinello method, where the forces on atoms are obtained by solving the electronic structure problem instead of by an interatomic potential, allows to study electronic properties of materials fully including their dynamics (and, therefore, phase transitions and other temperature-dependent phenomena). This important work gave rise to a very successful research line during the last decade.

Limitations

Typical MD simulations can be performed on systems containing thousands – or, perhaps, millions – of atoms, and for simulation times ranging from a few picoseconds to hundreds of nanoseconds. While these numbers are certainly respectable, it may happen to run into conditions where time and/or size limitations become important. A simulation is “safe” from the point of view of its duration when the simulation time is much longer than the relaxation time of the quantities we are interested in. However, different properties have different relaxation times. In particular, systems tend to become slow and sluggish in the proximity of phase transitions, and it is not uncommon to find cases where the relaxation time of a physical property is orders of magnitude larger than times achievable by simulation. A limited system size can also constitute a problem. In this case one has to compare the size of the MD cell with the correlation lengths of the spatial correlation functions of interest. Again, correlation lengths may increase or even diverge in proximity of phase transitions, and the results are no longer reliable when they become comparable with the box length. This problem can be partially alleviated by a method known as finite size scaling. This consist of computing a physical property A using several box with different sizes L , and then fitting the results on a relation

$$A(L) = A_0 + \frac{c}{L^n} \quad (1.19)$$

using A_0 , c , n as fitting parameters. A_0 then corresponds to $\lim_{L \rightarrow \infty} A(L)$, and should therefore be taken as the most reliable estimate for the “true” physical quantity. Compared with other applications in today’s computational condensed matter physics, MD simulations using classical potentials are not particularly demanding, unless one’s goal is to treat systems of the order of 10^6 atoms. For a typical system containing 10,000 atoms—a size suitable to tackle a large variety of problems—and involving short-range potentials, one can estimate a total memory occupation of the running program between 8 and 16 megabytes (MB). This could fit well in a typical current workstation with a RISC processor, including entry-level

machines. Using code which scales linearly with the number of particles (as described later), a RISC CPU can yield a total simulation time of “*hundred of picoseconds or perhaps a few nanoseconds in a week of production*”, which is a reasonable rate for productive work.

Application to microfluidics

The typical time scale to simulate a system’s dynamics ranges from 0.1 s to 10^3 s. Hence, for a chemically realistic molecular dynamics simulation, with a necessary time step in the range of 1 fs ($= 1 \times 10^{-15}$) to 10 fs, the task is quite taxing, considering that one would have to simulate over a range of 10^{15} time steps which is many orders of magnitude more than what is feasible nowadays.

1.4.2 Direct Simulation Monte Carlo ($0.1 \leq \text{Kn} \leq 10$)

Introduction

Direct Simulation Monte Carlo (DSMC) method was introduced by G.A. Bird in 1978. *Direct Simulation* means the method models physical phenomena using kinetic theory, and *Monte Carlo* implies that the scheme adopts random numbers. The use of random numbers is the distinguishing feature of a Monte Carlo procedure, and the essentially probabilistic nature of a gas flow at the molecular level makes it an obvious subject for a simulation approach based directly on the physics of the individual molecular interactions (Bird, 1994). Using each simulated molecule to represent a large number of actual molecules reduces computational requirements to a manageable level but introduces statistical error which is inversely proportional to the square root of the total number N of simulated particles. The simplicity of the algorithm allows for straightforward incorporation of higher-order physical models and for application to complex geometries.

The direct-simulation method is similar to the molecular-dynamics method in that a large number of simulated molecules are followed simultaneously. The essential difference is that

the intermolecular collisions are dealt with on a probabilistic rather than a deterministic basis. This requires the assumption of *molecular chaos* and restricts the method to *dilute gas flows* in which the mean spacing between the molecules is large in comparison with the molecular diameter. When the ratio of the mean molecular spacing δ to the molecular diameter d is large (δ/d), the fluid becomes *dilute*. The DSMC method may be used for dilute fluids when the ratio of the mean-free-path to the molecular diameter is at least $\lambda/d \geq 10$. DSMC is a statistical method that can be used very efficiently in the transition regime, where $\mathcal{O}(0.1) < Kn (= \lambda/L, \text{ or } \delta/L) < \mathcal{O}(10)$. DSMC remains valid, though extremely expensive to use, for much lower values of Kn .

Another computational approximation involves the time interval over which molecular motions and collisions are *uncoupled*. The effect of this step are negligible if the global timestep is smaller than the mean collision time. Particle motions are modeled deterministically, while the collisions are treated statistically.

The primary drawback of using DSMC is its cost. Whereas idealized calculations are possible on small computers, significant computational resources are required to simulate somewhat realistic flows.

Applications

The application of DSMC has been restricted to flows with high (δ/d)-ratio. In other words, DSMC is applicable to low-density-large-scale flows such as atmospheric gas dynamics and thin film processing, and high-density-small-scale flows like flows in MEMS devices.

Examples for low-density-large-scale flows are:

- the nonequilibrium flows around spacecrafts and re-entry craft;
- plume impingement on satellites and satellite instrumentation, as well as plume-plume interactions, which are generic problems for space shuttles and space stations;
- aerodynamics and real-gas effects of reentry vehicles used in space transportation

systems; and

- controlling the transport of gases to the substrate in Chemical Vapor Deposition (CVD) and Physical Vapor Deposition (PVD) processes under low pressure condition

Applications of the DSMC method to high-density-small-scale flows include:

- understanding and prediction of the properties of flows in fundamental components of microsystems such as channels, diffusers and nozzles
- prediction of pressure distribution around head and platter in hard disk

Advancements

Over time many new concepts which extend the DSMC application to more realistic and useful areas, have been introduced. For example, *Variable Hard Sphere* (VHS), *Variable Soft Sphere* (VSS), and *Generalized Hard Sphere* (GHS) models have been introduced to take the short range forces effect on the collision into consideration (Koura and Matsumoto, 1991; Hassan. and Hash, 1993). Furthermore, physical models, such as rough-sphere model and weighted-sphere model, can be used in the DSMC method; however, they require huge amounts of computer resources. The difficulties associated with the physical models have led to the development of phenomenological models such as the Larsen & Borgnakke model (Bird, 1994).

The classical collision theory for chemical reaction rates is based on kinetic theory and is well established in physical chemistry. It is essentially a phenomenological approach based on steric factors or reactive cross sections and is readily incorporated into direct-simulation methods.

It has been thought that the DSMC method is restricted to dilute gases because, while the molecular size is taken into account in determining the collision rate, the actual collision algorithm employs point molecules. Recently, it was reported (Bird, 1994) that, if space

occupied by the molecules is taken into account when determining the rate and the molecular trajectories are displaced by the appropriate amount during collisions, the hard-sphere equation of state for moderately dense gases is correctly reproduced.

There are situations with curved or time-changing obstacles and boundaries for which a different grid is necessary to produce an accurate solution. A new effort to expand the scope of DSMC to allow more grid adaptation, including moving internal and external boundaries, involves combining DSMC with the monotonic Lagrangian grid (MLG) (Oran et al., 1998). Most efforts to reduce DSMC computation times have involved optimizing the DSMC procedures on a particular type of computer (Oran et al., 1998). Parallelization of DSMC has become a focus of recent research efforts. The sorting and indexing processes in DSMC require intensive interprocessor communication and account for 30-60 % of total computation time. In the most efficient sorting procedure, the computational time is directly proportional to the total number N of simulated particles. The optimization of sorting and indexing processes, and load balancing among the processors are the main challenges in this area.

The development of hybrid algorithms which uses different models to describe the physics in different regimes of physical time or space, such as combining Boltzmann, Navier-Stokes, DSMC, and/or molecular dynamics solutions for various regions of space, depending on the properties of flow in the different regimes are ongoing (Oran et al., 1998).

Development of filters and other ways to increase the signal-to-noise ratio is one major branch. Information Preserving (IP) method is developed to reduce the noise occurs in the DSMC solutions when it deals with low-speed flows. Some researchers even use the Navier-Stokes equation as a filter to reduce the noise.

Application to microfluidics

The Navier-Stokes equations are valid for low Kn -number flows at high enough densities. DSMC can be used for high- Kn -number flows, and it is still possible to use DSMC for the regimes which overlap with Navier-Stokes, where $Kn \simeq 0.1$ and $\delta/d \simeq 10$; but, the

computations become quite expensive. Molecular dynamics, however, becomes expensive for low-density problems because the computational time step is limited by the time scales of the interaction potential and the method of solution. In the regime of parameter space in which $Kn^{-1} = L/\delta \simeq 100$, there are few particles per volume element and, therefore, few collisions. When this is the case, large fluctuations occur in the calculations of the mean properties of the system, such as density, pressure, and temperature. A DSMC calculation would require many ensembles to get good statistics.

There is an important physical problem for which the limit of $L/\delta \simeq 100$ becomes a serious practical issue. Currently, basic experiments and practical microdevices involve flows characterized by high Kn numbers and very low velocities. In a typical case, for example, the channel dimensions are $1.2 \mu\text{m}$ high by $5 \mu\text{m}$ wide by $3000 \mu\text{m}$ long. The undisturbed helium gas pressure and temperature might be 1 atm and 298 K, respectively, and the inflow velocity might be $\simeq 20 \text{ cm/s}$. In this case, $Kn \approx 0.13$ and DSMC is a possible solution method.

However, DSMC cannot be used for reasons involving both the number of time steps and the resolution required. Because of the relatively high number density at 1 atm, the mean collision time is very small (approximately 10^{-10} s). In DSMC, the computational time step must be less than the mean collision time. The particle transit time, which is the time that a flow with speed 20 cm/s takes to pass through the channel, is 10^{-2} s . Therefore, to reach the steady-state flow condition requires 10^8 time steps. A fully three-dimensional simulation of these experiments would also be impractical because of the large number of computational cells required (the limit of memory). One condition that must be satisfied during a DSMC procedure is that the smallest dimension of the computational cells must not be greater than one half of the mean-free-path. For the microchannel described above, a minimum of 500,000 cells would be required. Considering that each cell contains a certain number of particles (at least 20), a total of 10^7 particles would be required. Such a calculation is certainly beyond the capabilities of current computers. There is also the problem that statistical scatter due to small perturbations increases as the flow velocity becomes

very subsonic, that is, when $V_f \ll V_{th}$, where V_f and V_{th} are flow and mean molecular thermal velocities, respectively. In the example above, the thermal speed is approximately 1000 m/sec. With 0.2 m/sec flow, the statistical noise is four orders of magnitude greater than the required signal. The solution of microchannel flow at 0.2 m/s would require over 10^8 samples in a time averaged steady flow because the statistical fluctuations decrease with the square root of the sample size. A general method that will solve problems for flows in the low-speed, high Kn -number regime is still needed.

Application examples

The direct simulation Monte Carlo method has been applied to dilute ideal gas flows in a two-dimensional micro-channel of constant wall temperature. Particular emphasis has been placed on the development of constant wall temperature. Shear-driven and pressure-driven flow has been modeled to thoroughly investigate the abilities of the DSMC method. The entire DSMC process occurs in a well-defined sequence that has four main steps. Figure 1.7 shows the flowchart for the DSMC method. After setting the constraints, boundary conditions, and initializing the molecules (position (x, y, z) , velocity (v_x, v_y, v_z) , internal energy), the first step is to move the simulated molecules based on their prescribed trajectories for the given time step. Interactions with the boundaries are also considered during this step. The surface reflections may be considered as specular or diffusive, and the velocities of the molecules leaving the wall are assigned according to a biased Maxwellian distribution. The second step indexes the particles and sorts them within the computational cells. This step is important for controlling molecular collisions and calculating the flow field properties efficiently, especially for large systems. After the molecules have been properly tracked, the intermolecular collisions can be simulated in the third step. The fourth step of the DSMC algorithm is to sample the microscopic properties of the particles in each cell. These microscopic states are then used to determine the macrostate of each cell. The sample rate can be adjusted to compute the flow properties at defined iteration intervals to minimize computational demand. The DSMC method can model steady flow systems

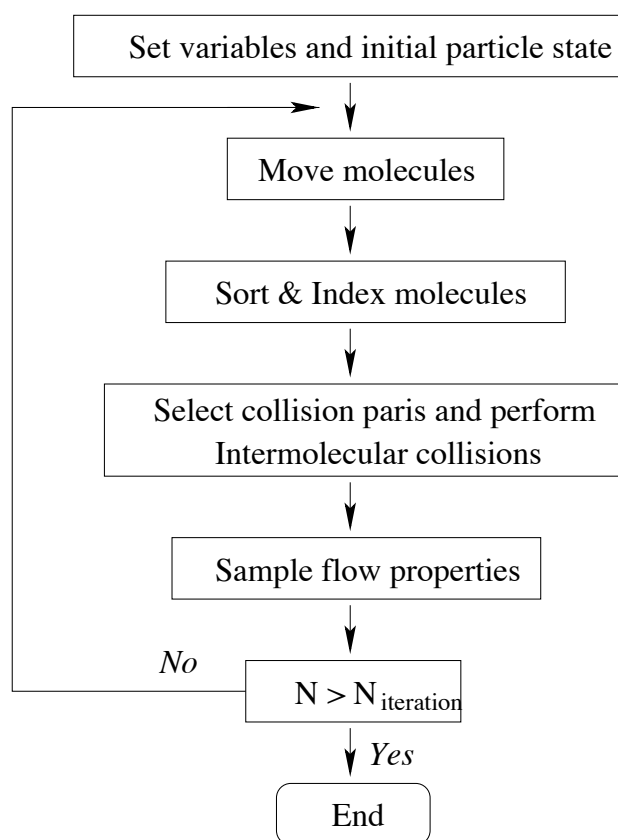


Figure 1.7: DSMC flowchart

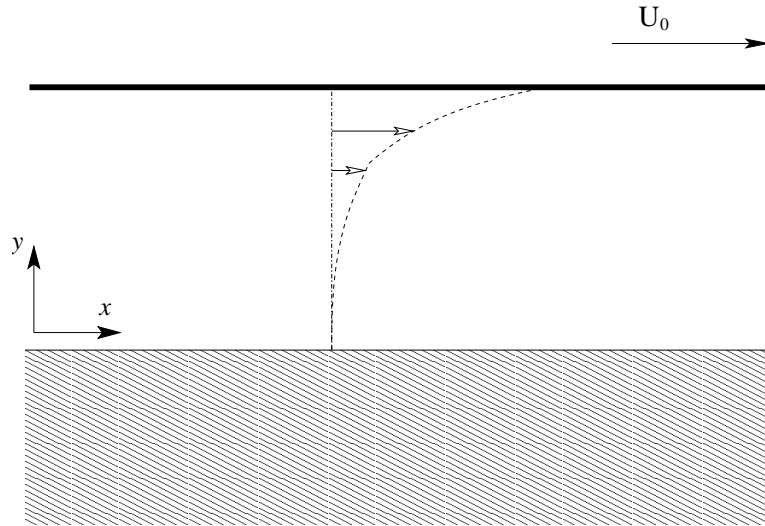


Figure 1.8: System sketch of shear-driven flow; U_0 is the moving wall velocity.

by time averaging flow properties once a steady output is achieved, and an *ensemble* of unsteady solutions can represent unsteady flows with an associated statistical accuracy. For the shear-driven configuration (see Fig. 1.8), both low ($U_0=9.23$ m/sec, $Ma=0.03$, $Re\approx 0.33$) and high ($U_0=615$ m/sec, $Ma=2.0$, $Re\approx 22$) relative wall speeds were utilized. Figure 1.9 indicates that the steady-state solution obtained from the simulation satisfactorily models the linear velocity profile associated with simple Couette flow. Interestingly, the case for high wall speed was characterized by significantly lower statistical fluctuations due to a higher signal-to-noise ratio. In addition, as Kn was increased from the slip-flow to the transition regime, the uncertainty in the data exhibited a corresponding increase and deviated from the continuum solution, as expected. The final case, supersonic pressure-driven flow, was carried out with steady state velocities exhibiting the classical parabolic profile as shown in Fig. 1.10 and 1.11. Due to the supersonic condition, the fully developed profiles had very small fluctuations, and the velocity slip condition at the channel walls was observed. Figure 1.12 indicates strong compressibility effect on the flow.

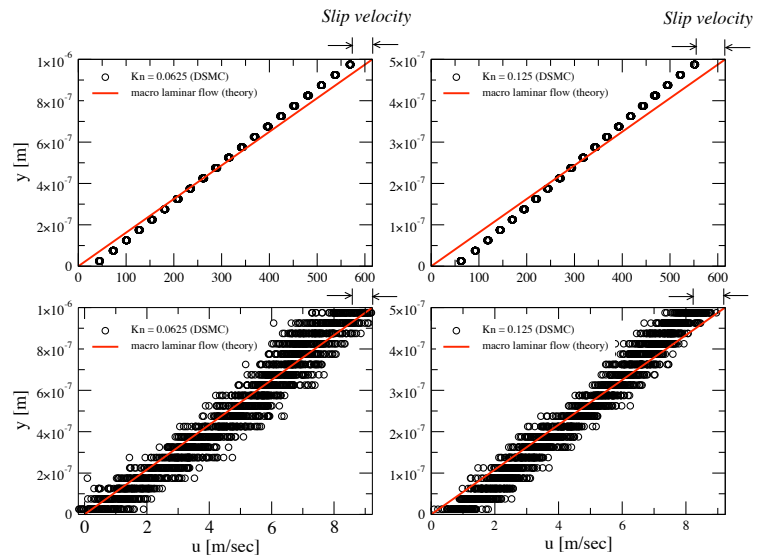


Figure 1.9: Comparison of velocity profiles obtained with DSMC and conventional laminar flow theory. The velocity differences at the walls show the slip velocity, which increases with Kn . The slower flows show higher velocity fluctuations.

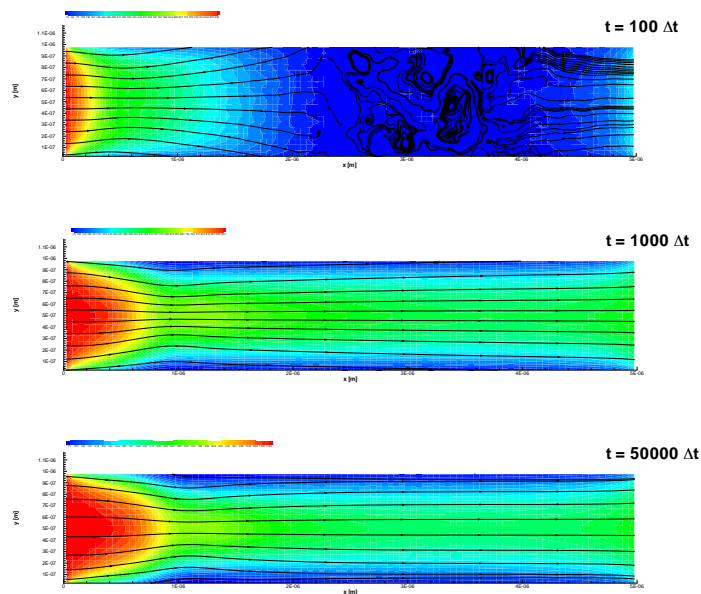


Figure 1.10: Two-dimensional axial velocity contours for the pressure-driven flow case with an inlet velocity of 1,000 m/sec

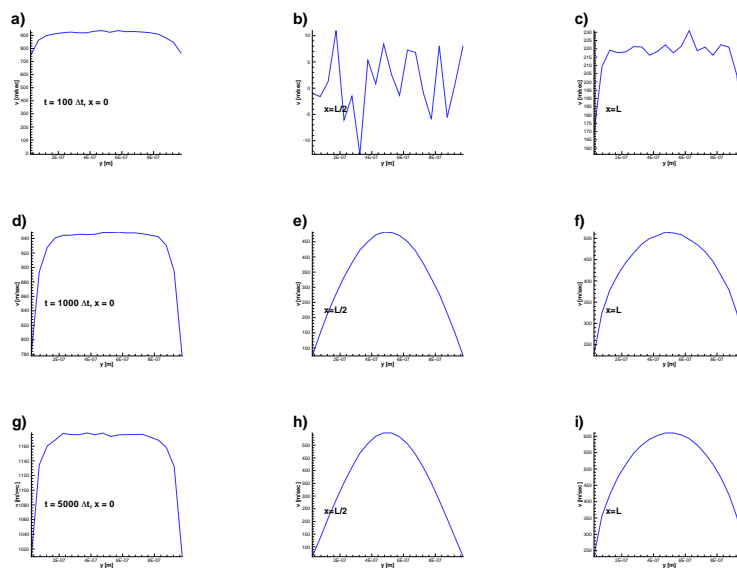


Figure 1.11: Axial velocities at the entrance, mid-point, and exit of a two-dimensional channel for the pressure-driven flow case with an inlet velocity of 1,000 m/sec

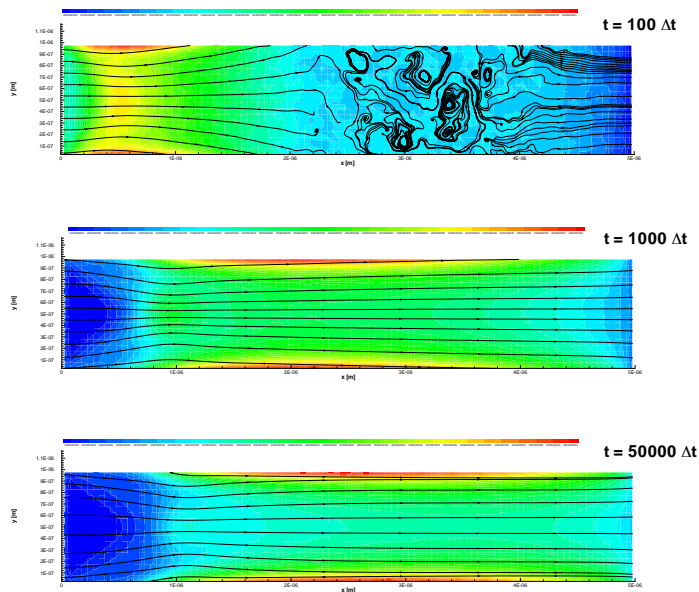


Figure 1.12: Two-dimensional number density contours for pressure-driven flow with an inlet velocity of 1,000 m/sec

1.4.3 Direct Numerical Simulation ($\text{Kn} \leq 0.1$)

Introduction

Direct numerical simulation of solid-liquid flows is a way of solving the initial value problem for the motion of particles in fluids exactly, without approximation. The particles are moved by Newton's laws under the action of hydrodynamics forces computed from the numerical solution of the fluid equations. One must simultaneously integrate the Navier-Stokes equations (governing the motion of the fluid) and the equations of rigid-body motion (governing the motion of the particles). *These equations are coupled through the no-slip condition at the particle boundaries, and through the hydrodynamic forces and torques that appear in the equations of rigid-body motion.* These hydrodynamic forces and torques must be those arising from the computed motion of the fluid, and so are not known in advance, but only as the integration proceeds. It is crucial that no approximation of these forces and torques be made other than that due to the numerical discretization itself so that the overall simulation will yield a solution of the exact coupled initial value problem up to the numerical truncation error. Joseph (2002) clearly mentioned their goal to be doing direct numerical solutions with *many thousands* of particles in three dimensions, with *large volume fractions*, for various kinds of suspensions and slurries. Particle tracking methods take into account the particles and the fluid motion to understand particulate flow. Particle tracking methods move the particles by Newton's equations for rigid-bodies using forces that are modeled from single particle analysis or from empirical correlation rather than from forces which are obtained by direct computation from the fluid motion. Joseph (2002) mentioned that the approximate methods include simulations based on potential flow, Stokes flow, and point-particle approximations so that they all simplify the computation by ignoring some possible important effects like *viscosity* and *wakes* in the case of potential flow, *inertial forces* which produce lateral migration and across-the-stream orientations in the case of Stokes flow; and the effect of *stagnation* and *separation points* in the case of point-particle approximations.

Equations of Motion

For the fluid phase we have

$$\nabla \cdot \vec{u} = 0 \quad (1.20)$$

and

$$\rho_f \left(\frac{\partial \vec{u}}{\partial t} + (\vec{u} \cdot \nabla) \vec{u} \right) = \rho_f \vec{g} - \nabla p + \eta \nabla^2 \vec{u} \quad (1.21)$$

The particle equations of motion, where \vec{u} is the particle velocity and the mass center of each particle is at $\vec{X}(t)$, reads:

$$M \frac{d\vec{U}}{dt} = M\vec{g} + \vec{F}(\vec{u}) \quad (1.22)$$

$$I \frac{d\omega}{dt} = \vec{T}(\vec{u}) \quad (1.23)$$

$$\frac{d\vec{X}}{dt} = \vec{U} \quad (1.24)$$

$$\frac{d\vec{\theta}}{dt} = \vec{\omega} \quad (1.25)$$

where M is particle mass, I is particle inertia of rotation, θ is angular position of a particle, ω is particle rotational velocity, $\vec{F}(\vec{u})$ is the force and $\vec{T}(\vec{u})$ the torque on the particle. The fluid velocity is the same as the particle velocity at the surface of the particle

$$\vec{u} = \vec{U} + \vec{\omega} \times \vec{r} \quad (1.26)$$

The fluid force $\vec{F}(\vec{u})$ acting on the boundary of the particle is the integral over the body surface of the traction

$$\vec{\sigma} \cdot \vec{n} = -p\vec{n} + 2\eta \vec{D}(\vec{u}) \cdot \vec{n} \quad (1.27)$$

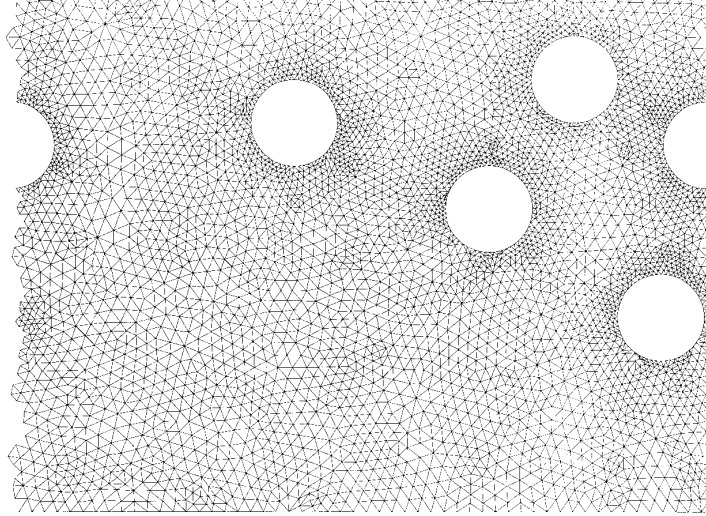


Figure 1.13: Unstructured grid for the ALE method

where $\vec{D} = \frac{1}{2}(\nabla\vec{u} + \nabla\vec{u}^T)$ is the rate of strain and \vec{n} is the outward normal and $\vec{T}(\vec{u})$ is the integral of the moment of the traction vector.

Joseph (2002) introduced three ways of simulating moving particles using DNS: Arbitrary Lagrangian-Eulerian (ALE) particle mover, a projected particle mover, and Distributed-Lagrange-Multiplier (DLM) particle mover. A projected particle mover improved the convergency, scalability and efficiency of ALE mover (see Fig. 1.13.). DLM is a completely different scheme. It assumes there is fluid inside the particle which behaves like a rigid body (see Fig. 1.14.). It uses a simple time-independent regular mesh, which means it does not need any mesh updates. For the velocity field inside particles, one can either use

$$\vec{u}(\vec{x}, t) = \vec{U} + \vec{\omega} \times \vec{r}, \quad \vec{x} \in P(t) \quad (1.28)$$

or

$$\vec{D}(\vec{u}) = 0, \quad \vec{x} \in P(t) \quad (1.29)$$

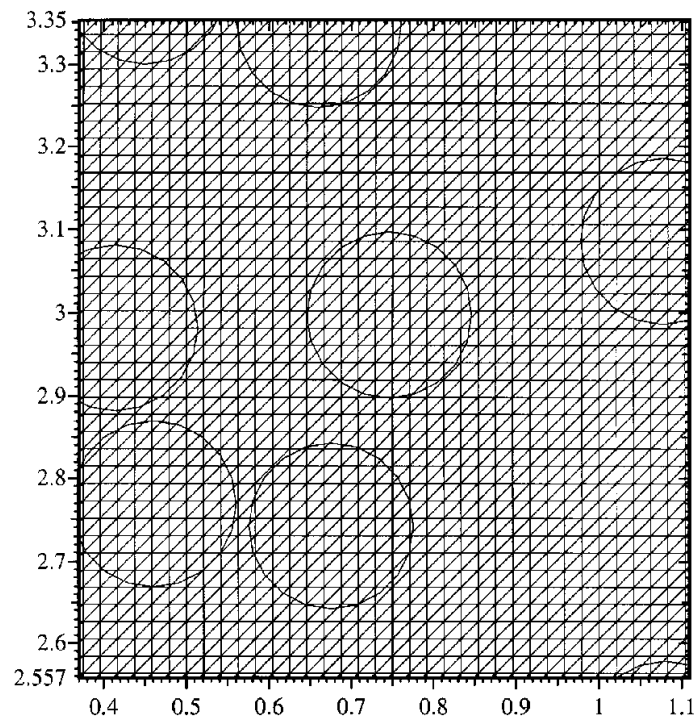


Figure 1.14: Fixed triangular grid used in DLM computation. The same grid covers the fluid and solid. The fluid in the circles is bordered by Lagrange multipliers to move the particles (circles) as a rigid bodies.

where $\vec{D}(\vec{u})$ is the symmetric part of $\nabla\vec{u}$.

1.4.4 Approximate Methods ($Kn \leq 0.5$)

In micro-scales the characteristic dimension of the flow conduits are comparable to the mean-free-path of the *gas* media they operate in. Under such conditions the “continuum hypothesis” may break down. Constitutive laws that determine stress tensors and heat flux vectors for continuum flows have to be modified in order to incorporate the rarefaction effects. The very well known “no-slip” boundary conditions for velocity and temperature of the fluid on the walls are subject to modifications in order to incorporate the reduction of momentum and energy exchange of the molecules with the surroundings. Deviation from continuum hypothesis is identified by the Knudsen number, which is the ratio of the mean-free-path of the molecules to a characteristic length scale, i.e., $Kn = \lambda/L$. This length scale L should be chosen in order to include the gradients of density, velocity and temperature within the flow domain. For example for external flows boundary layer thickness, and for internal fully developed flows channel half thickness should be used as the characteristic length scale. According to the Knudsen number the flow can be divided into various regimes. These are: continuum, slip, transition and free-molecular flow regimes.

A discrete particle or molecular based model is the Boltzmann equation. The Boltzmann equation is an integro-differential equation and solutions of this equation are limited. The continuum based models are the Navier-Stokes equations. A special case is the Euler equation corresponding to the inviscid continuum limit, which shows a singular limit since the fluid is assumed to be inviscid and non-conducting. Euler flow corresponds to $Kn=0.0$. The Navier-Stokes equations can be derived from the Boltzmann equation using the Chapman-Enskog expansion. When the Knudsen number is larger than 0.1, the Navier-Stokes equations *break down* and a higher level of approximation is obtained by carrying second order terms (in Kn) in the Chapman-Enskog expansion. A special form of such an equation is called the *Burnett equations*, for which the solution requires second-order accurate slip boundary conditions in Kn . The Burnett equations and consistent second-order slip bound-

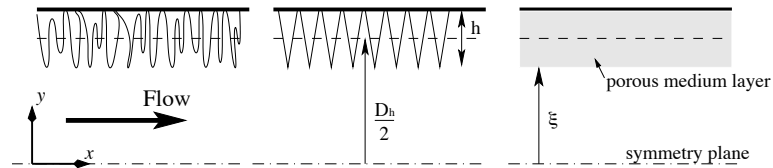


Figure 1.15: Porous medium layer equivalent to surface roughness and simple microchannel geometry: a) real surface roughness; b) homogeneous distribution of identical roughness elements; and c) mid-plane view of conduit with idealized roughness layer, or porous medium layer (PML)

ary conditions is subject to some controversy and a better way of solving high-Knudsen-number flows is through molecular based direct simulation techniques such as the Direct Simulation Monte Carlo method (DSMC). Microflows are typically in the slip and early transitional flow regimes. Therefore, Navier-Stokes equations with appropriate slip boundary conditions govern these gas flows (Beskok and Karniadakis, 1994).

However, slip velocity is negligible for liquid flows in microchannels. Surface phenomena, i.e., surface roughness effect and viscous dissipation effect, which were assumed to be unimportant for liquid flows in macrochannels turn out to be important (Koo and Kleinstreuer, 2003). To simulate the surface roughness effect, a Porous Medium Layer (PML) model was introduced (Kleinstreuer, 2003). The PML model complements the Navier-Stokes equations by adding the Darcy plus Brinkman term, the latter representing the resistance force, or friction force, proportional to the speed of the flow, and the Forchheimer term which is caused by the form drag and proportional to the square of the flow velocity.

For steady, 2D and fully-developed flow in an open channel as well as through an isotropic medium, the Navier-Stokes equations reduces to (Koo and Kleinstreuer, 2003; Kleinstreuer and Koo, 2004)

$$0 = -\frac{dp^*}{dx^*} + \frac{4}{Re_{D_h}} \frac{d^2u^*}{dy^*} + \left\{ \underbrace{-\frac{4u^*}{Da_{H/2} Re_{D_h}}}_{\text{Brinkman term}} - \underbrace{\frac{C_f u^{*2}}{Da_{H/2}^{1/2}}}_{\text{Forchheimer term}} \right\}_{PML} \quad (1.30)$$

where $p^* = \frac{p}{\rho U_0^2}$, $u^* = \frac{u}{U_0}$, $x^* = \frac{x}{H/2}$, $y^* = \frac{y}{H/2}$, $Da_{H/2} = \frac{\kappa}{(H/2)^2}$, $Re_{D_h} = \frac{\rho U_0 2H}{\mu}$, H is the channel height and $C_f (\approx 0.55)$ is drag coefficient. The terms in braces $\{\}_{PML}$ are effective only in the PML, i.e., the roughness region.

The boundary conditions are no-slip velocity at the wall, and the same velocity gradient at the interface between open and porous regions.

1.4.5 Summary

In the preceding sections, various methods to simulate flow in microscale conduits have been reviewed. The continuum assumption in conjunction with appropriate closure models were to simulate and analyze *microscale* effects, such as surface roughness and nanofluids selected. Of special consideration were;

- computational costs,
- close packing nature of liquids,
- Stokesian nature of flow around nanoparticles,
- and high number density of nanoparticle inclusion in nanofluids.

Chapter 2

THEORY and METHODS

2.1 Introduction

The deviations from the conventional theory observed by experimentalists and possible methods of simulating flows in micro-conduits were listed and reviewed in the previous chapter. To select a proper approach, the Knudsen number ($Kn = \lambda/L$) appeared to be the critical parameter, which is usually used for gas flows. It seems to be very hard to define a length scale to replace λ in the Knudsen number for liquid flows (see Kleinstreuer, 2003). However, it was reviewed that molecular dynamics (MD) simulation is not possible even for micro-scale flows, direct simulation Monte Carlo (DSMC) is just for gas flows where the intermolecular interaction is negligible, and direct numerical simulation (DNS) is still inadequate for nanoparticle suspensions where the ratio between channel size and particle size is large.

The close spacing and the strong interactions between liquid molecules support the use of the continuum approach for liquid flow even on a smaller scale down to $\mathcal{O}(1 [nm])$, where it approaches that of $\mathcal{O}(0.1 [\mu m])$ for gas flow. Thus, the conventional continuum mechanics assumption was chosen, which has been supplemented with sub-models to consider micro-scale effects.

In this chapter, the theoretical background and derivations of the sub-models are presented. The validation and detail investigations are contained in the next chapter.

2.2 Governing Equations for Microchannel Flow

The governing equation for a general flow model, which is an extension of the Navier-Stokes equations, can be written in generic form as (Kleinstreuer, 2003):

$$\frac{\partial}{\partial t}(\alpha\rho\Phi) + \nabla \cdot (\rho\vec{K} \cdot u\vec{\Phi}) = \alpha S \quad (2.1a)$$

where α is the porosity, \vec{K} is an area porosity tensor, \vec{u} is the velocity vector, ρ is the fluid density, Γ is the fluid diffusivity (viscosity), S is a source term, and Φ is an arbitrary transport quantity.

For example the corresponding continuity and momentum equations, i.e., $\Phi = 1$, $S = 0$ and $\Phi = \vec{u}$, $S = \vec{S}$, respectively, are:

Continuity equation:

$$\frac{\partial}{\partial t}(\alpha\rho) + \nabla \cdot (\rho\vec{K} \cdot \vec{u}) = 0 \quad (2.1b)$$

Momentum equation:

$$\frac{\partial}{\partial t}(\alpha\rho\vec{u}) + \nabla \cdot (\rho(\vec{K} \cdot \vec{u}) \otimes \vec{u}) - \nabla \cdot (\eta_{eff}\vec{K} \cdot (\nabla\vec{u} + \nabla\vec{u}^T)) = -\alpha\vec{S} - \alpha\nabla p \quad (2.1c)$$

Energy equation:

$$\frac{\partial}{\partial t}(\alpha\rho c_p T) + \nabla \cdot (\rho(\vec{K} \cdot \vec{u}) \otimes c_p T) - \nabla \cdot ((k_{eff})\vec{K} \cdot (\nabla T)) = \eta_{eff}\Phi + \dot{q} \quad (2.1d)$$

Partical transport equation:

$$\frac{\partial\alpha_d}{\partial t} + \nabla \cdot (\vec{u}\alpha_d) = \nabla \cdot \left[\left(D + \frac{\nu_t}{Sc} \right) \nabla\alpha_d \right] \quad (2.1e)$$

For steady, incompressible and constant fluid property flows in an isotropic medium

$$\nabla \cdot \vec{u} = 0 \quad (2.2a)$$

$$(\vec{u} \cdot \nabla)\vec{u} = -\alpha\vec{S} - \alpha\nabla p + \nu_{eff}\nabla \cdot (\nabla\vec{u} + \nabla\vec{u}^T) \quad (2.2b)$$

$$(\vec{u} \cdot \nabla)T = \nabla \cdot ((\alpha_{eff}) \cdot (\nabla T)) + \frac{\eta_{eff}}{\rho c_p} \Phi \quad (2.2c)$$

and

$$\nabla \cdot (\vec{u}\alpha_d) = \nabla \cdot \left[\left(D + \frac{\nu_t}{Sc} \right) \nabla \alpha_d \right] \quad (2.2d)$$

where p is the pressure, η_{eff} is the effective viscosity, ν_{eff} is the effective kinematic viscosity, which is the sum of molecular kinematic viscosity and turbulent viscosity, \vec{S} is the source term which becomes the resistance vector for flow in a porous medium layer (see Sect. 3.3.1), Φ is the viscous dissipation function, \dot{q} is a possible heat source/sink, α_d is the particle concentration, D is the particle diffusion coefficient, ν_T is the turbulent viscosity, and Sc is the Schmidt number.

On the left-hand side of Eq. 2.1c, the first term is the time derivative or local time variation of momentum, the second term represents the spatial momentum convection, and the third term stands for viscous diffusion of momentum. On the right-hand side, the first term captures the augmented surface forces induced by the scale-down of the system, and the last term is the pressure force acting on the fluid. Similarly, for RHS of Eq. 2.1d, the first term is the transient term, the second is the convective heat transfer, the third one represents the thermal diffusion. The first term in the LHS represents the viscous dissipation, and the last term represents possible internal heat generation.

The low-Reynolds number $k - \omega$ model (Wilcox, 1998; Zhang and Kleinstreuer, 2003) is used to investigate turbulent flow effects. The governing equations are: LRN $k - \omega$ model:

$$u_j \frac{\partial k}{\partial x_j} = \tau_{ij} \frac{\partial u_i}{\partial x_j} - \beta^* k \omega + \frac{\partial}{\partial x_j} \left[(\nu + \sigma_k \nu_T) \frac{\partial k}{\partial x_j} \right] \quad (2.3a)$$

$$u_j \frac{\partial \omega}{\partial x_j} = \alpha \frac{\omega}{k} \tau_{ij} \frac{\partial u_i}{\partial x_j} - \beta^* \omega^2 + \frac{\partial}{\partial x_j} \left[(\nu + \sigma_\omega \nu_T) \frac{\partial \omega}{\partial x_j} \right] \quad (2.3b)$$

where the turbulent viscosity is given as $\nu_T = c_\mu f_\mu k / \omega$, and the function f_μ is defined as

$$C_\mu = 0.09, \alpha = 0.511, \beta = 0.8333, \beta^* = 1, \sigma_k = \sigma_\omega = 0.5 \quad (2.3c)$$

The equations are discretized using a central difference scheme except for the convective terms, which are discretized by using a second-order upwind scheme, and are integrated by means of a commercial code (AEA Technology, 2001) enhanced with our Fortran programs for pre- and post-processing. For a simplified microchannel flow system, reduced ordinary differential equations (Sect. 3.3.1) are integrated using the modules provided in MATLAB 6 (Mathworks, 2002). Results from computer experiments focusing on different effects potentially important in microchannel flow are discussed in the next sections.

2.3 Nanofluid Property Models

Mills (1992) stated that on a microscopic level, the physical mechanisms of conduction are very complex, encompassing such varied phenomena as molecular collisions in gases, lattice vibrations in crystals, and flow of free electrons in metals. The movement of particles does not contribute to the fluid body at rest. Although there exist micro-convections due to the particles and surrounding fluid motion, that random motion contributes to heat conduction instead of forced convection from a macroscopic point of view. In contrast, thermo-phoretic motion should be classified as a convection phenomenon because it induces an ordered bulk fluid motion. *Alternatively, the effect could be incorporated in a resulting effective thermal conductivity.* To obtain the effective thermal conductivity due to nanoparticle motion induced micro-convection, a new model was developed and used as a constitute equation to close the problem.

2.3.1 Effective Thermal Conductivity Model

It is postulated that the enhanced thermal conductivity of a nanofluid, when compared to conventional predictions, is mainly due to Brownian motion which produces micro-mixing. This effect is additive to the thermal conductivity of a *static* dilute suspension, i.e.,

$$k_{eff} = k_{static} + k_{Brownian} \quad (2.4)$$

where, for example, according to Maxwell (1904) (see Table 1.1)

$$\frac{k_{static}}{k_c} = 1 + \frac{3\left(\frac{k_d}{k_c} - 1\right)\alpha_d}{\left(\frac{k_d}{k_c} + 2\right) - \left(\frac{k_d}{k_c} - 1\right)\alpha_d} \quad (2.5)$$

Here α_d is the particle volume fraction, k_c is thermal conductivity of the carrier fluid, and k_d is that of the particles. Since the speed of thermal wave propagation is much faster than

the particle Brownian motion, the static part cannot be neglected.

Concerning temperature dependence, Patel et al. (2003) performed experiments with suspensions of very small volume fractions, i.e., $\alpha_d < 0.001$ %, where the static part of the thermal conductivity is negligible. They observed a measurable increase of thermal conductivity even when the volume fraction was as low as 0.00013 %. They also found that the thermal conductivity of the nanofluids increases with fluid temperature, which supports the importance of the Brownian motion effect (see Eq. (4.71)). Das et al. (2003) also observed the temperature dependence of the thermal conductivity for different types of nanofluids. For the derivation of $k_{Brownian}$, we consider two nanoparticles with translational time-averaged Brownian motion, \bar{v} , in two different temperature fields (or cells) of extent l , where l is the average distance for a particle to travel in one direction, without changing its direction, due to the particle's Brownian motion. Figure 2.1 shows the key parameters and schematic diagram illustrating the Brownian-motion induced micro-mixing mechanism. Hence, the travel time is $\Delta t = l/\bar{v}$, where \bar{v} is the translational time-averaged speed due to the Brownian effect (Probstein, 2003):

$$\bar{v} = \sqrt{\frac{18\kappa T}{\pi\rho_d D^3}} \quad (2.6)$$

Here, κ is the Boltzmann constant, T is the fluid temperature, ρ_d is the particle density, and D is its diameter. Table 2.1 lists typical values of particle traveling speeds and corresponding Reynolds numbers.

Defining p as the probability for a particle to travel along any direction, and assuming that each of the two particle cells are in thermal equilibrium at temperatures T_1 and T_2 , respectively, these particles moving to neighboring cells will carry energy across the interface, i.e.,

$$q_{net} = \frac{\Delta Q}{A\Delta t} \approx \frac{(pNm_d)c_v(T_1 - T_2)}{A\Delta t} = -\frac{pNm_dc_v\bar{v}\frac{\Delta T}{l}l}{A\bar{v}dt} \quad (2.7a)$$

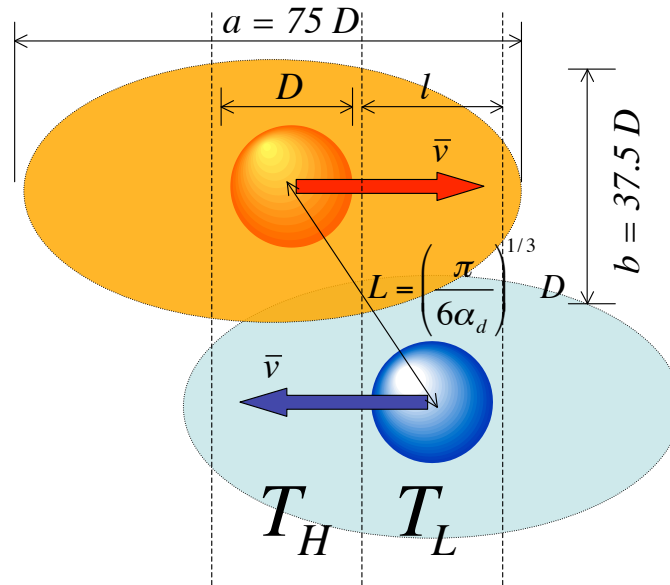


Figure 2.1: Illustrative schematic explaining the particles' Brownian-motion effect on micro-mixing

Table 2.1: Particle speed due to the Brownian effect and corresponding particle Reynolds number of Cu-nanoparticle-water suspensions

Particle size [nm]	Traveling speed [m/sec]	Re_D [-]
10	1.63	1.87×10^{-2}
100	5.15×10^{-2}	5.90×10^{-3}
1000	1.63×10^{-3}	1.87×10^{-3}

Here, $\frac{\Delta T}{l} \rightarrow \nabla T$, N is the total particle number in a cell, m_d is the particle mass, ρ_d is its density, and c_v is its specific heat, $m_d = \rho_d V_d$, V_d is the particle volume, A is the cross-sectional area of the system normal to the x -direction, $A\bar{v}\Delta t = V$, and $\frac{NV_d}{V} = \alpha_d$. Now we can write

$$q_{net} \approx -p\alpha_d\rho_dc_v\bar{v}D\nabla T \quad (2.7b)$$

or

$$q_{net} = -\hat{k}_{Brownian}\nabla T \quad (2.7c)$$

Here, $\hat{k}_{Brownian}$ is the added thermal conductivity due to Brownian motion of a given nanosphere. Thus, with Eq. (2.6)

$$k_{Brownian} = \sqrt{\frac{18}{\pi}}p\alpha_d\rho_dc_v\sqrt{\frac{\kappa T}{\rho_d D}} \frac{l}{D} \quad (2.8)$$

This approach is quite similar to the kinetic theory to estimate the gas material properties. Krieger (1972) stated that the common structural feature unifying the rheologically interesting class of fluids is the presence of flow units, either colloidal particles or macromolecules, whose dimensions are large compared with molecules of the suspending medium, while still small enough to exhibit significant rotatory and translatory Brownian movement. The structure of the fluid resembles a gas of large molecules, with the void space replaced by a Newtonian continuum. The newly developed effective thermal conductivity and dynamic viscosity model well complies his statement by applying the kinetic theory for the gas-like behavior and considering the induced liquid motion considering the Newtonian continuum replacing the void space.

As the nanoparticles move *randomly*, a portion of the surrounding fluid is affected, i.e., fluid motion and interaction occurs, leading to micro-scale mixing and heat transfer. For a quantitative assessment, we can assume steady flow in the Stokes regime (see Table 2.1) so

that for the axial velocity field surrounding a sphere of radius R we can write

$$\frac{v_x}{\bar{v}} = 1 - \left[1 - \frac{3R}{2r} + \frac{1}{2} \left(\frac{R}{r} \right)^3 \right] \cos^2 \theta - \left[1 - \frac{3R}{4r} - \frac{1}{4} \left(\frac{R}{r} \right)^3 \right] \sin^2 \theta \quad (2.9)$$

The validity of this assumption is two-fold;

1. The particle Reynolds number $Re_D = \frac{\rho_l \bar{v} D}{\mu}$ is very small due to the small particle size and the time scale for a nanoparticle.
2. The response time for a nanoparticle ($\sim 6 \times 10^{-2}$ nsec) in a fluid is much smaller than the required time for a nanoparticle to move a distance of its diameter (~ 6 nsec). Therefore, the steady state assumption could be applied.

Equation (2.9) can be employed to estimate the region of influence of a creeping sphere, i.e., with the 99 % criterion of vanishing impact, the affected fluid volume is

$$V_f = \frac{\pi}{6} a^2 b \quad (2.10)$$

where $a \approx 37.5D$ is the short axes and $b \approx 75D$ is the long axes of a spheroidal body of fluid (see Fig. 2.2). Clearly, shape and size of the affected fluid volume depend on the particle shape as well as the interparticle distance. In any case, not just nanoparticles move around due to the Brownian effect but actually significantly larger fluid bodies, which may interact and lead to vigorous micro-mixing. Thus, for isolated particles Eq. (2.8) has to be multiplied by $\left(\frac{a}{D}\right)^2 \times \frac{b}{D} = 105,470$ in order to encapsulate the extended Brownian motion effect. Therefore, neglecting the energy transport by particles due to its negligible volume compared to the carrier fluid volume traveling with it, Eq. (2.8) reads

$$k_{Brownian} = 37.5^2 \times 75 \sqrt{\frac{18}{\pi}} p \beta \alpha_d \rho_l c_v \sqrt{\frac{\kappa T}{\rho_d D}} \frac{l}{D} \quad (2.11)$$

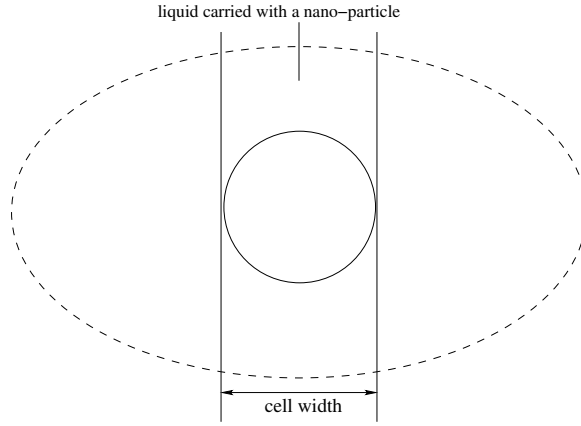


Figure 2.2: A traveling particle carries fluid around it due to viscous effect. For a low Reynolds number flow, the amount of fluid travel with a particle could be obtained by using Eq. (2.9).

where ρ_l is the liquid density. Actually, only a fraction of V_f (see Eq. (2.10)) will travel with the particles due to the hydrodynamic interaction among affected fluid volumes for cases where the interparticle distance is not long enough for neighboring affected volumes to travel independently. Here, β represents the fraction of the liquid volume V_f which travels with a particle. It will decrease with volume fraction α_d due to the viscous effect of other moving particles.

Equation (2.11) is a result obtained from basic kinetic theory without considering the interparticle interaction. Referring to Deen (1998), it has been reported that a simple model indicating $k_{Brownian} \sim T^{1/2}$ does remarkably well in predicting the main features of the transport properties of gases, although real gas conductivities show a stronger dependence on the temperature, i.e., $k_{gas} \sim T$ instead of \sqrt{T} . He reported this discrepancy is largely corrected with the kinetic theory of Chapman and Enskog (Chapman and Cowling, 1951), which considers in some detail the effect of intermolecular potential energy on the interactions between colliding molecules.

For liquid-solid suspensions, the effect of interactions between solid particles are much stronger than between gas molecules, since the interparticle potential is proportional to

d^{-1} , where d is the interparticle distance, while it is d^{-6} for intermolecular potential, which decays very fast with distance. As it is observed in gases, the thermal conductivity dependence on temperature in liquids should be greater than what is predicted with the simple model. Based on this statement, a function $f(T, \alpha_d, \text{fluid and particle properties})$ is introduced in Eq. (2.8) to result in

$$k_{Brownian} = 37.5^2 \times 75 \sqrt{\frac{18}{\pi}} p \beta \alpha_d \rho_l c_v \sqrt{\frac{\kappa T}{\rho_d D}} \frac{l}{D} f(T, \alpha_d, \text{etc.}) \quad (2.12)$$

The function $f(T, \alpha_d, \text{etc.})$ should depend on properties of the intervening fluid, and hence particle interactions. Traditionally, the interparticle potential can be used to take interparticle interaction into consideration, i.e., it is given as

$$w(d) = -\frac{AR}{6d} \quad (2.13)$$

where A is the Hamaker constant, R is the particle radius, and d is the surface distance. The Hamaker constant A for two identical phases 1 interacting across medium 3 can be described as (Israelachvili, 1992):

$$A = \frac{3}{4} \kappa T \left(\frac{\epsilon_1 - \epsilon_3}{\epsilon_1 + \epsilon_3} \right)^2 + \frac{3h\nu_e}{16\sqrt{2}} \frac{(n_1^2 - n_3^2)^2}{(n_1^2 + n_3^2)^{3/2}} \quad (2.14)$$

where ϵ is the electric dipole constant, n is the refractivity, h is the Planck constant, and ν_e is the frequency where the dielectric medium has the strong absorption peak (see Table 2.2). For dilute cases, the thermal conductivity of the nanofluids is expected to show a relatively low dependence on particle interactions due to the retardation effect of the interparticle potential, i.e., it is the dispersion energy that suffers retardation. The complexities of the involved phenomena make it difficult to obtain the function f theoretically, if not impossible. Therefore, we decided to determine the function f from experimental data, and check whether the experimentally determined function shows the same trend with the

Table 2.2: Parameter values for different materials (see Eq. (4.75))

Phase material	ϵ	n	A_0^*
<i>Cu</i>	∞		3.11×10^{-21}
<i>Al₂O₃</i>	4.5	1.761	2.48×10^{-21}
<i>CuO</i>	18.1	2.6	1.24×10^{-21}
<i>TiO₂</i>	86	2.6	4.06×10^{-24}
Water	80.4	1.33	
Ethylene glycol	37.0		
Decene	2.2	2.2	

* A_0 is the first term in Eq. (4.75).

theory, to confirm the validity of the new model. Furthermore, molecular dynamics simulations considering particle-particle, and particle-liquid interactions should be performed to determine the average traveling distance without changing travel direction $\frac{l}{D}$. Here, it is assumed that $\frac{l}{D} = 1$ and the experimentally determined function f contains its effect.

Since all three directions have equal probability for a particle to travel, roughly one-sixth of total particles travel in the positive x -direction during $\Delta t = l/\bar{v}$. To be more precise, a numerical simulation was performed to evaluate the expectation for a particle to travel in the x -direction. The dashed circles in Fig. 2.3 indicate possible locations of a particle starting at the origin after an elapsed time of $\Delta t = D/\bar{v}$. Generating 10,000 random numbers to simulate particle motions and calculating the fraction of spheres moving in the positive x -direction, the probability of a particle to move in the x -direction was 0.197.

Now, with the expectation value of particles to move in one direction being 0.197, Eq. (2.8) can be rewritten as

$$k_{Brownian} = 5 \times 10^4 \beta \alpha_d \rho_l c_l \sqrt{\frac{\kappa T}{\rho_d D}} f(T, \alpha_d, \text{etc.}) \quad (2.15)$$

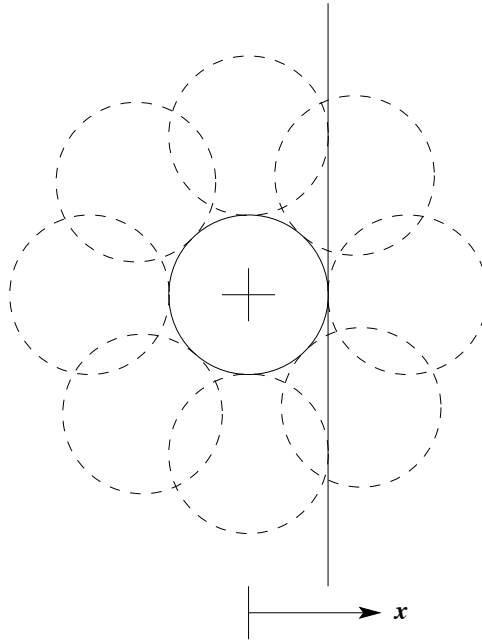
Figure 2.3: Expectation for a particle to travel in the x -direction

Table 2.3: Comparison of augmented thermal conductivities

Type of particles	β	Condition
<i>Au</i> -citrate, <i>Ag</i> -citrate and <i>CuO</i>	$\beta = 0.0137(100\alpha_d)^{-0.8229}$	$\alpha_d < 1\%$
<i>CuO</i>	$\beta = 0.0011(100\alpha_d)^{-0.7272}$	$\alpha_d > 1\%$
<i>Al</i> ₂ <i>O</i> ₃	$\beta = 0.0017(100\alpha_d)^{-0.0841}$	$\alpha_d > 1\%$

Determination of the functions β and f

Since β is related to the particle motion, it should depend not only on volume fraction but also temperature, particle shape as well as material properties of particles and carrier fluid. Here, we assumed that β is a function of volume fraction only, since all other dependencies can be covered with the function f . The function β can be determined with ease under the assumption that f is unity for the given system conditions, because most experimental data available in the literature have been obtained at a fixed temperature. Figure 3.27 and Table 2.3 show the results obtained for water-based nanofluids. For the

cases of small volume fractions, $\alpha_d < 1\%$, where the particle interaction effect is relatively insignificant, due to both the long interparticle distance and the potential retardation effect, the function β is independent of the type of particle. In contrast, the function β depends on the type of particle in high concentration cases, $\alpha_d > 1\%$, which is found to be the result of interparticle interactions. As was expected, the function β decreased with the volume fraction α_d in most cases. This will be discussed in more detail in the next section.

There are not many data sets available for determining the function f . Das et al. (2003) and Patel et al. (2003) observed that their experimentally measured thermal conductivity increased with temperature. Specifically, the thermal conductivity enhancement increased by 7% for the 1% water- Al_2O_3 nanofluid, and by 15% for the 4% water- Al_2O_3 nanofluid for a temperature rise of 30 [K]. It increased by 20% for the 1% and 4% water- CuO nanofluid for the same temperature rise. Patel et al. (2003) did experiments with very low concentration nanofluids and they observed about 5% increase of thermal conductivity enhancement for a 30 [K] temperature rise. Specifically, an expression for $f(T, \alpha_d, \text{properties of particles and carrier fluid})$ in Eq. (4.73) was obtained from the CuO -nanofluids experimental data of Das et al. (2003). The function was assumed to vary continuously with the particle volume fraction because data for two volume concentration cases were available.

$$f(T, \alpha_d) = (-6.04\alpha_d + 0.4705)T + (1722.3\alpha_d - 134.63) \quad (2.16)$$

It should be noted that the function is a linear equation because of the Taylor series truncation; but, that functional dependence can be confirmed with Eqns (4.74) and (4.75) as well. Equation (4.77) is valid for the given experimental conditions in the ranges $1\% < \alpha_d < 4\%$

and $300 < T < 325$ [K]. The change of $k_{Brownian}$ with α_d is given as

$$\begin{aligned} \frac{dk_{Brownian}}{d\alpha_d} = & 1.9318\rho_l c_l \sqrt{\frac{\kappa T}{\rho_d D}} \left\{ 0.2728\alpha_d^{-0.7272} ((-6.04\alpha + 0.4705)T \right. \\ & \left. + (1722.3\alpha_d - 134.63)) + \alpha_d^{0.2728} (-6.04T + 1722.3) \right\} \end{aligned} \quad (2.17)$$

The last term in the equation becomes negative and its magnitude increases with temperature, which explains the thermal conductivity reduces near $x = 1$ [m], as discussed in the next section.

We investigated other transport mechanisms, such as thermophoresis and fluid thermal energy, potentially contribution to enhanced thermal conductivities of nanofluids, and found that they are negligible (Koo and Kleinstreuer, 2005b).

The effect of particle size on the Brownian motion induced thermal conductivity is shown in Fig. 2.4. The Brownian motion induced thermal conductivity decreases with particle size, hence the new effective thermal conductivity model in Eq. (4.71) reduces to the conventional relation for large particle cases.

2.3.2 Thermal conductivity due to thermo-phoresis

Using the equi-partition theorem Schroeder (2000), at temperature T the average energy of any quadratic degree of freedom is $\frac{1}{2}\kappa T$, and the force on a particle in the direction of the temperature gradient could be obtained

$$F_{TP} = \frac{1}{2}\kappa \nabla T|_p \quad (2.18)$$

where F_{TP} is the thermo-phoretic force and $\nabla T|_p$ is the temperature gradient in the particle. According to Hamilton and Crosser Hamilton and Crosser (1962), the temperature gradient

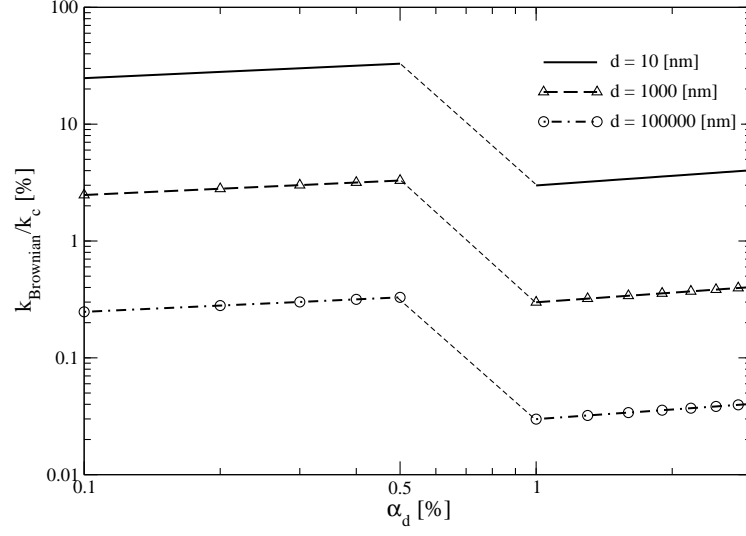


Figure 2.4: The particle size effect on k_{eff} .

in a particle has a relation with the base liquid temperature gradient as

$$\frac{\nabla T|_p}{\nabla T} = \frac{3k_c}{k_d + 2k_c} \quad (2.19)$$

where ∇T is the temperature gradient in the base liquid, k_c and k_d are the thermal conductivities of continuous and discrete phases respectively, and n is a shape factor which is 3 for a spherical particle. For steady-state in the Stokes regime, the thermo-phoretic and drag forces should be in balance, i.e.

$$\frac{1}{2}\kappa T \nabla(\log T) \frac{3k_c}{k_d + 2k_c} = 3\pi\mu_c D \bar{u} \quad (2.20)$$

After rearranging, the thermo-phoretic velocity can be expressed as

$$\bar{u} = \frac{1}{6\pi} \frac{\kappa}{\mu_c} \frac{3k_c}{k_d + 2k_c} \frac{\nabla T}{D} \quad (2.21)$$

which shows that the thermo-phoretic migration velocity is proportional to D^{-1} for a given temperature gradient field.

Using kinetic theory, the net heat flux has the proportionality

$$q_{net} \sim -n\bar{u}m_d c_d \nabla T D \quad (2.22)$$

where n is the number density. Hence, the thermo-phoretic thermal conductivity k_{TP} can be represented as

$$k_{TP} \sim n\bar{u}m_d c_d D = \frac{1}{6\pi} \frac{\alpha_d \kappa}{\mu_c} \frac{3k_c}{k_d + 2k_c} \rho_d c_d \nabla T \quad (2.23a)$$

Again, as particles travel, they carry the surrounding fluid with them due to viscous effects. When this effect is taken into consideration, Eq. (2.23a) becomes

$$k_{TP} \sim n\bar{u}m_d c_d = \frac{1}{6\pi} \frac{\alpha_d \kappa}{\mu_c} \frac{3k_c}{k_d + 2k_c} (1 \times 10^5 \rho_l c_l) \nabla T \quad (2.23b)$$

2.3.3 Thermal conductivity due to the osmo-phoresis

When there is a temperature gradient in a solution, a suspended particle experiences a net force because the molecules arriving from the high temperature level have greater momentum than the ones from the colder direction. Analogous to *van't Hoff's equation* Probstein (2003) for the osmotic pressure, it is postulated a relation between temperature gradient and pressure in the form,

$$\nabla p = n\kappa(\nabla T|_p) \quad (2.24)$$

The pressure gradient works as an impetus for a particle to move under a temperature gradient. The temperature gradient acting on a particle relates to the fluid temperature gradient as expressed in Eq. (2.19). This is due to the fact the particles have different amount of thermal energy in different temperature.

The force exerted by a pressure gradient can be obtained as Crowe et al. (1998),

$$F_p = \int_{cs} p \vec{n} dS = \int_{cv} \nabla p dV = \nabla p V_d \quad (2.25)$$

Therefore, the force due to osmotic pressure can be written as

$$F_{OS} = n \kappa \nabla T|_p V_d \quad (2.26)$$

Again, the osmotic pressure force should balance with the drag force, so that the migration velocity is

$$\bar{u} = \frac{1}{3\pi} \frac{\alpha_d \kappa}{\mu_c D} \frac{3k_c}{k_d + 2k_c} \nabla T \quad (2.27)$$

The heat flux due to this cause of migration can be expressed as given with Eq. (2.22), so that

$$k_{OS} = \frac{1}{3\pi} \frac{\alpha_d^2 \kappa}{\mu_c} \frac{3k_c}{k_d + 2k_c} \rho_d c_d \nabla T \quad (2.28)$$

With viscous effects, Eq. (2.28) reads

$$k_{OS} = \frac{1}{3\pi} \frac{\alpha_d^2 \kappa}{\mu_c} \frac{3k_c}{k_d + 2k_c} (1 \times 10^5 \rho_l c_l) \nabla T \quad (2.29)$$

2.3.4 Comparisons

The three mechanisms of nanoparticle motion on a micro-scale are compared for typical nanoparticles (CuO , $D=10$ [nm], $\alpha_d = 1$ %) suspended in water. The results are

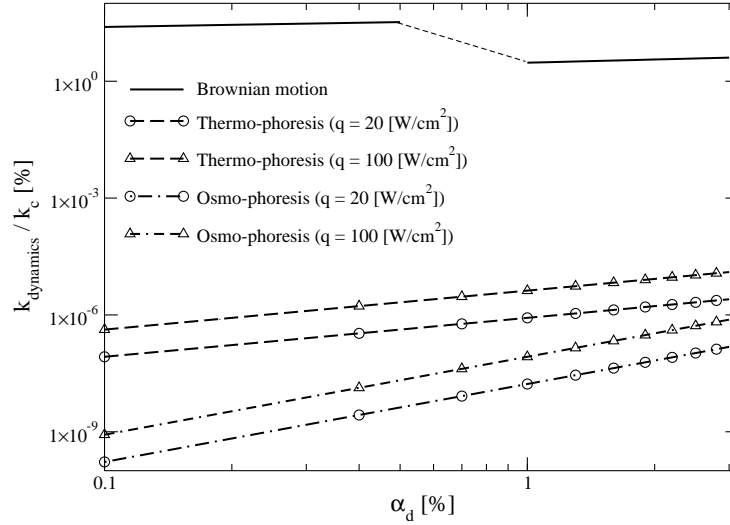


Figure 2.5: Comparison of three different particle dynamics effects on the thermal conductivity enhancement

shown in Fig 2.5. The Brownian motion effect is most important when compared to the other two mechanisms.

Thermo-phoresis and osmo-phoresis are ordered movements of particle complexes, and their effects are different from that of Brownian motion because the whole movement is in the same direction as the temperature gradient. Furthermore, the effect of each particle motion is additive since the momentum equations for the Stokesian flow is linear, which means no β -function is needed to consider the hydrodynamic interaction, so, i.e., $\beta \equiv 1$. Furthermore, thermo-phoresis and osmo-phoresis induced thermal conductivity relations are independent of particle size.

As a sample case, consider a copper-water nanofluid suspension with 1 % concentration of $D = 10$ [nm] particles. For this case, $k_{TP} \approx 5.1 \times 10^{-10}$ [W/mK] which is 8.4×10^{-8} % of the conductivity of water under the condition of $\nabla T = 3.2 \times 10^5$ which is obtained for

a typical heat flux for electronics cooling $q = 20 [W/cm^2]$ and the thermal conductivity of water, $k = 0.611 [W/mK]$.

The effect of osmo-phoresis was found to be negligible, i.e., typically, $k_{OS} \approx 1 \times 10^{-10} [W/mK]$ which corresponds to $1.7 \times 10^{-8} \%$ of the thermal conductivity of water. However, the temperature gradient would be much smaller when the convective transfer mode is active.

The effect of particle volume concentration on the effective thermal conductivities are compared in Fig. 2.5. For a given particle size, the thermal conductivity increases with particle volume concentration. The dotted line for the Brownian motion induced thermal conductivity graph indicates the transitional behavior of two different regimes; specially, the increase of thermal conductivity is relatively independent of particle interaction for the low concentrations, i.e., $\alpha_d < 0.5 \%$, while it is strongly dependent on the particle interaction for high concentrations, i.e., $\alpha_d > 1.0 \%$. The transition-start and -end points depend on the properties of both particle and base fluid. The effect of heat flux on the thermo- and osmo-phoresis induced thermal conductivity increases are also depicted in Fig. 2.5. The lines with circles show the case of low heat flux, i.e., $q'' = 20 [W/cm^2]$, while those with triangles show the case of high heat flux, i.e., $q'' = 100 [W/cm^2]$. Strong heat fluxes result in higher thermal conductivities due to the larger temperature gradients across the bulk fluid.

2.3.5 Effective Dynamic Viscosity Model

Choi (1995) reported that the influence of particle loading and size on the pressure drop of slurry is negligible for solids suspensions even in the 20 % volume fraction range. However, Pak and Cho (1998), Li et al. (2002), and Xuan and Li (2003) reported measurable, sometimes anomalous increase of driving force. In this section, a new effective viscosity model, which considers the particle Brownian motion effects, will be derived by using the kinetic theory.

Using the same concept with the derivation of the effective thermal conductivity, the addi-

tional viscosity due to the Brownian motion can be estimated as below:

$$\mu_{Brownian} = 37.5^2 \times 75 \sqrt{\frac{18}{\pi}} p \beta \alpha_d \rho_l \sqrt{\frac{\kappa T}{\rho_d D}} f(T, \alpha_d, etc.) \quad (2.30)$$

Comparing with the Brownian motion induced thermal conductivity,

$$k_{Brownian} = 37.5^2 \times 75 \sqrt{\frac{18}{\pi}} p \beta \alpha_d \rho_l c_v \sqrt{\frac{\kappa T}{\rho_d D}} \frac{l}{D} f(T, \alpha_d, etc.) \quad (2.31)$$

$$\frac{k_{Brownian}}{\mu_{Brownian}} = c_l \quad (2.32)$$

$$\frac{k_{Brownian}}{k_l} = \frac{c_l \mu_{Brownian}}{k_l} \quad (2.33)$$

$$\frac{k_{Brownian}}{k_l} = \frac{c_l \mu_l}{k_l} \frac{\mu_{Brownian}}{\mu_l} \quad (2.34)$$

$$\frac{k_{Brownian}}{k_l} = Pr_l \frac{\mu_{Brownian}}{\mu_l} \quad (2.35)$$

$$\frac{\mu_{Brownian}}{\mu_l} = \frac{k_{Brownian}}{k_l} \times \frac{1}{Pr_l} \quad (2.36)$$

Therefore, the effect of Brownian motion on the effective fluid viscosity is less significant than that on the effective thermal conductivity, since $Pr_l > 1$ for liquids. At room temperature, the Prandtl number is about 5, 100, and 5000 for water, ethylene glycol, and engine oil, respectively. It should be noted that the Prandtl numbers decrease with temperature, so that they become 2.3, 34.6, and 546 at $T = 350$ [K].

2.3.6 The effect of particle-wall interaction

Not only particles and liquid interact with each other but also particles, liquid and the wall. In a quiescent environment such as in the experimental apparatus to measure the effective thermal conductivity of nanofluids, the wall effect might be not so significant if the size of the vessel is large. However, the particle-liquid-wall interaction becomes impor-

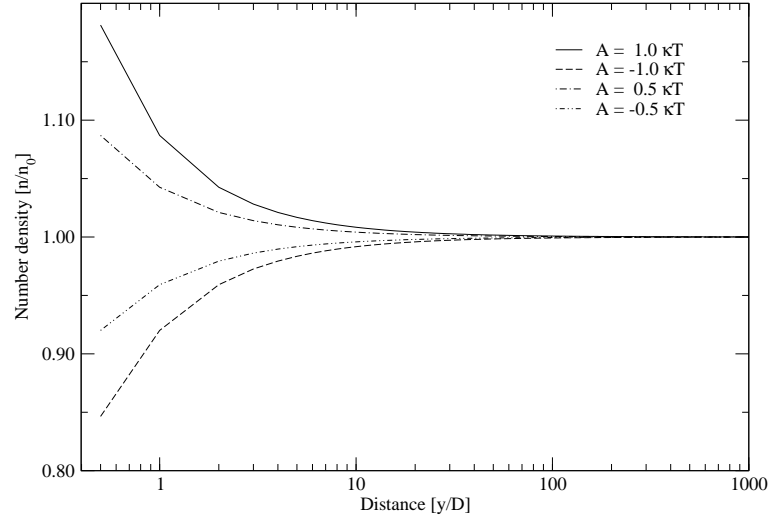


Figure 2.6: The particle-liquid-wall interaction effect on nanoparticle distribution near the wall

tant for flows in microchannels where the surface area of the wall is relatively large. The equilibrium nanoparticle distribution was derived considering the particle-liquid-wall attraction ($= \frac{AD}{12y^2}$, Israelachvili (1992)) and the thermal Brownian forces ($= \kappa T \nabla \ln n$, Probst (2003)) as

$$n(y) = C \exp\left(\frac{A}{12\kappa T} \frac{D}{y}\right) \quad (2.37)$$

where y is the distance from the wall. The nanoparticle distribution depends on the particle size D , and the Hamaker constant A which is a function of the material properties of the particle, wall, and carrier fluid. Figure 4.14 shows the effect of particle-liquid-wall interaction on the nanoparticle distribution near the wall for different nanofluids, where n_0 is the centerline number density. When particles and the wall attract each other, i.e., $A > 0$, the concentration near the wall increases as it approaches the wall. In contrast, it decreases when particles and the wall repulse each other, i.e., $A < 0$. The concentration

can change near the wall up to 18 % due to the interaction.

Chapter 3

LIQUID FLOW in MICROCHANNELS

3.1 Introduction

The model configurations, laboratory conditions and experimental findings for liquid flow in microchannels are summarized in Table 3.1. The first two groups in Table 3.1 list contributors who measured microfluidics deviations when compared with conventional, or macro-scale, theory. Group I emphasizes possible occurrence of *flow instabilities* and Group II points out *viscosity changes* as the causes of discrepancies in friction factor values when compared to conventional theory. Group III did not detect any measurable differences between micro- and macro-scale fluid flow behaviors. Specifically, the experimental findings discussed by the individual research teams of Groups I to III are as follows:

Group I Peng et al. (1994), Peng and Peterson (1996) and Xu et al. (1999) observed the increase and decrease of friction factor/pressure gradient compared to conventional theory, and they attributed this to an early onset of laminar-to-turbulent flow transition.

Group II Pfahler et al. (1990, 1991), Urbanek et al. (1993), Mala and Li (1999), Qu et al. (2000), Papautsky et al. (1999), and Ren et al. (2001) assumed the deviation would originate from surface phenomena such as surface roughness, electrokinetic forces, temperature effects, and microcirculation near the wall. Most results indicate that the friction factor/pressure gradient would increase due to effects of surface phenomena.

Group III Tuckerman and Pease (1981), Xu et al. (2000), Sharp (2001), and Judy et al. (2002) insisted that the friction factor/pressure gradient results are the same as the values predicted by conventional theory. They claimed that the deviations which other researchers had observed (see Groups I and II), might have originated from measurement errors of channel size, experimental uncertainties, and by overlooking the entrance effect.

Thus, the use of the Navier-Stokes equations appears to be appropriate for microchannel flows of liquids as long as $l_{system} \geq 0.1 [\mu m]$ for conduits filled with, say, water

Table 3.1: Experimental observations of fluid flow characteristics in microchannels

Reference	System configuration	Nature of work	Observations/conclusions	Class
Tuckerman and Pease (1981)	Rectangular; $W=50 [\mu m]$; $H=300 [\mu m]$; $Q=4.7, 6.5, 8.6 [cm^3/s]$; Water; Silicon substrate, pyrex cover	Experiments on integral heat sink for silicon integrated circuits	Flow rate obeyed Poiseuille equation	III
Pfhaler et al. (1990)	Rectangular; $W=53, 100 [\mu m]$; $H=135, 1.7, 0.8 [\mu m]$; $Re \approx 300$; N-propanol; Silicon substrate, pyrex cover	Deviation of friction factor prediction from that of classical theory	Error in channel height measurements was around 20 %; absolute value of the friction factor was meaningless. Smaller channel higher friction factor; Dependence on Re number; FC: Increase and decrease	II
Pfhaler et al. (1991)	Trapezoidal; $D_h=0.48-40 [\mu m]$; Silicone oil, iso-propanol; Relative roughness 1%; Silicon substrate, pyrex cover	Comparison between polar and non-polar liquids	Lower friction factor; Friction factor of polar liquid (iso-propanol) depended heavily on channel size; FC: Increase and decrease (mainly a decrease)	II
Urbanek et al. (1993) (Neglected the entrance effect and minor loss)	Triangular, trapezoidal; $D_h=5, 12, 25 [\mu m]$; 0-85 [°C]; 1-, 2-Propanol, 1-, 3-Pentanol; Silicon substrate, pyrex cover	Effects of fluid temperature and channel size on friction factor	Deviation from classical theory; Temperature dependence of friction factor; FC: Always increases with temperature $\approx 35\%$	II
Peng et al. (1994) and Peng and Peterson (1996) (Neglected the entrance effect and minor loss)	Rectangular; $D_h=133-367 [\mu m]$, $L=50 [mm]$; water; $Re = 50-4000$, Surface roughness 0.6-1 [%]; Stainless steel substrate, fiberglass plastic cover	Effects of channel size and shape on friction factor	Laminar to turbulent transition at $Re = 200 - 700$; Geometric parameters such as hydraulic diameter and H/W ratio are important.; FC: Increase and decrease (mainly increase) ≈ 300 [%]	I
Mala and Li (1999) (Neglected the entrance effect)	Circular $D = 50 - 254 [\mu m]$; $Re = 50 - 2500$; Stainless steel/fused silica; Mean roughness height = 1.75 $[\mu m]$ (Relative roughness ≈ 3.5 [%])	Development of a "roughness-viscosity" model	Significant increase in pressure gradient compared to that predicted by Poiseuille flow theory; at higher Re number, the deviation is greater and the difference increases as the diameter of the tube decreases.	I,II
Papautsky et al. (1999)	Rectangular; $W=50-600 [\mu m]$, $H=20-30 [\mu m]$; $Re \approx 20$; Water; relative roughness ≈ 2 [%]; silicon substrate	Development of a model using micropolar fluid theory	Micro-rotational effects of fluid molecules on the continuum and variations in the apparent fluid viscosity in the region close to the walls; Friction increased with Re number; FC: Max 20 [%] increase of friction factor; Micropolar theory predicted the trend well.	II
Xu et al. (1999)	Rectangular; $D_h = 50 - 300 [\mu m]$; $Re = 50 - 1500$; Water; Roughness $\approx 0.5 [\mu m]$ (Relative $\approx \max. 1$ [%])	Effect of channel size	Reduction of friction factor; Slip boundary effect; Early laminar to turbulent transition; 100 $[\mu m]$ is the limit of the continuum assumption; FC : mainly decrease	I,II
Xu et al. (2000) (Neglected the entrance effect)	Rectangular; $D_h = 30 - 344 [\mu m]$; $Re = 20 - 4000$; Water; Surface roughness (A) 0.5 $[\mu m]$ (max. ~ 1.7 [%]) (S) 20 $[nm]$; A : aluminum, S : silicon	Effect of channel size and surface roughness	Dimensional error caused by gluing the channel to the glass cover can cause an error in measuring the friction factor; FC: no deviation from classical theory	III
Qu et al. (2000) (Neglected the entrance effect)	Trapezoidal; $D_h = 51 - 169 [\mu m]$; $Re \approx 1500$; Roughness ≈ 1.6 [%]; Silicon substrate, pyrex cover	Development of a roughness-viscosity model	Reynolds number dependency; FC : increase (~ 40 [%])	I,II
Ren et al. (2001)	Rectangular; $W=5 [mm]$; $H=14.1-40.5 [\mu m]$; KCl solution in water; roughness $\sim 20 [nm]$; Silicon	The effect of electrical double layer (EDL)	Theoretical model using electro-viscous effect predicted electrokinetic effect on friction factor well.; FC: increase	I,II
Sharp (2001)	Circular; $D=50-250 [\mu m]$; $Re = 50 - 3000$; Deionized water, 1-propanol, 20 [%] solution of glycerol	Study of electro-viscous effect, and size of tube effect on friction factor; PIV measurements of velocity profiles	Obeyed classical theory; Capacitance effect (long transient time); No early laminar to turbulent flow transition; No electro-viscous effect; No polarity effect; FC : no deviation from classical theory	III
Judy et al. (2002)	Circular and square; $D=15-150 [\mu m]$; $Re = 8 - 2300$; Fused silica, stainless steel	Effect of polarity of liquids, channel size, entrance effects, viscous heating effect, wall roughness effects (FS,SS); FS : fused silica SS : Stainless steel (rougher)	Neglecting viscous heating effect gave 7-10 [%] lower fe values.; More viscous heating with decreasing channel size and increasing velocity.; No evidence of flow regime transition.; Fluid polarity didn't affect the friction factor.; Flow in fused silica channel showed better matching with classical theory. ; FC : no deviation from classical theory	III

Table 3.2: Classification of experimental observations

I	Peng et al. (1994); Peng and Peterson (1996), Mala and Li (1999), Xu et al. (1999), Qu et al. (2000)	$D_h : 0.48 \sim 367 [\mu m]$, $Re_D : 50 \sim 4000$, Rectangular, trapezoidal, circular conduits	Liquid: Water Stainless steel, Aluminum, steel substrate, fiberglass plastic cover	Enhanced surface phenomena due to increased surface-to-volume ratio and flow instability effects	Flow instability effect	Friction factor increases or decreases
II	Pfhaler et al. (1990, 1991), Yang and Li (1998), Mala and Li (1999), Li (2001), Papautsky et al. (1999), Qu et al. (2000), Ren et al. (2001), Urbanek et al. (1993)	$D_h : 5-254 [\mu m]$ $Re_{D_h} : 8 \sim 4,000$ Rectangular, trapezoidal, circular, triangular conduits	Liquid: Iso-propanol, n-propanol, 1-, 2-Propanol, 1-, 3-Pentanol, KCl solution in water Material: Stainless steel substrate, fiberglass plastic cover	Apparent viscosity effects	Friction factor increase	
III	Tuckerman and Pease (1981), Elwenspoek et al. (1994), Xu et al. (2000), Sharp (2001), Judy et al. (2002)	$D_h : 15-344 [\mu m]$ $Re_{D_h} : 84,000$ Rectangular, circular conduits	Liquid: Deionized water, 1-propanol, 20 % solution of glycerol Material: Fused silica, stainless steel, silicon substrate, pylex cover	No deviation from conventional theory	→	Same as macrochannel flow data

at standard conditions. This condition is based on the global Knudsen number for liquids, $\text{Kn}(= \lambda_{IM}/l_{system})$, which is very small, where the intermolecular length for water molecules is $\lambda_{IM} = 3 \text{ \AA}$ (Kleinstreuer, 2003). Nevertheless, as the system size decreases, surface phenomena, such as near-wall forces and relative roughness, become more and more important, and hence the Navier-Stokes equations have to be augmented as shown in the next sections.

3.2 Friction Factor Analysis

Based on the continuum mechanics assumption, the continuity equation and equation of motion (or the Navier-Stokes equations for constant-fluid-property cases) are being solved in the conventional theory approach. With the resulting information, the friction factors for various internal and external flow systems can be calculated. The friction factor is defined as the ratio between the wall shear stress and the dynamic pressure, i.e.,

$$f = \frac{\tau_w}{\frac{1}{2}\rho\bar{u}^2} \quad (3.1a)$$

where \bar{u} is the mean fluid velocity. The friction factor defined in Eq. (3.1a) is called the Fanning friction factor, or skin-friction coefficient. There is another commonly used friction factor called the Darcy friction factor, which is four times greater than the Fanning friction factor (Kleinstreuer, 1997):

$$f_D = \frac{4\tau_w}{\rho\bar{u}^2} = 4f \quad (3.1b)$$

Friction factor deviations can be expressed as percentage change

$$\Delta f^* = \frac{f_{observed} - f_{base}}{f_{base}} \quad (3.1c)$$

where f_{base} (see Eqs. (3.1a), (3.2), (3.3a) or (3.4)) is the theoretical friction factor value and $f_{observed}$ is the experimental or computational microchannel value.

Friction factor relationships for turbulent fully-developed flow through macrochannels are typically expressed as a function of the Reynolds number and relative roughness height. For example, Colebrook combined the surface roughness and Reynolds number effects in an interpolation formula, expressed as (White, 1999):

$$\frac{1}{f_{D,turb}^{1/2}} = -2.0 \log\left(\frac{\epsilon/d}{3.7} + \frac{2.51}{Re_{D_h} f_{D,turb}^{1/2}}\right) \quad (3.2)$$

where $Re_{D_h} = \frac{\bar{U}D_h}{\nu}$ and D_h is the hydraulic diameter.

For laminar pipe flow, $Re_D < 2,300$, the friction factor is given by

$$f_{D,lam} = \frac{C_f}{Re_D} \quad (3.3a)$$

or

$$f_{D,lam}Re_D = C_f \quad (3.3b)$$

where $C_f = 64$ for circular tubes, and for rectangular channels, C_f will have different values that are determined by the aspect ratio b/a , knowing the hydraulic diameter (White, 1991).

The friction factor in the entrance region of any conduit is always larger than that for fully-developed flow; the difference increases with the Reynolds number for a given channel length and decreases as the channel length increases. Shah and London (1978) suggested an experimentally validated formula for the laminar friction factor, which is valid within 2.4 percent for many macro-scale duct shapes (White, 1991):

$$f_{app}Re \approx \frac{3.44}{\sqrt{\zeta}} + \frac{f_p Re + K_\infty/4\zeta - 3.44/\sqrt{\zeta}}{1 + c/\zeta^2} \quad (3.4)$$

with $Re_D = \frac{U_0 D_h}{\nu}$ where $f_p Re = 14.23$, $K_\infty = 1.43$, $c = 0.00029$ and ζ is a Graetz-type variable defined as $\zeta = (x/D_h)/Re_{D_h}$ for channels, where x is the distance from the inlet.

3.3 Surface Roughness Effect

3.3.1 Effects on momentum transfer

The effect of surface roughness on flow characteristics was investigated by Mala and Li (1999) and Qu et al. (2000), who proposed a roughness-viscous model (RVM). It assumes that the roughness-viscosity is a function of y , the distance from the wall. The viscosity introduced by surface roughness has a finite value at the wall and zero at the channel center, and is proportional to the Reynolds number. Sharp (2001) claimed that the RVM does not fully explain friction factor trends at high Reynolds numbers referring to their experimental results.

In this study, surface roughness effects are investigated with a thin porous medium layer (PML) on the walls for which the Brinkman-Forchheimer extended Darcy equation holds. Thus, the effects of surface roughness on the friction factor, pressure gradient and flow structures in microchannel flow are elucidated. Generally, the PML results show that surface roughness may increase or decrease the friction factor, depending upon the roughness-equal-PML permeability, i.e., if the Darcy number, $Da = \kappa/D_h^2$, approaches ∞ , then the PML resistance vanishes and when $Da \rightarrow 0$, the PML acts like a solid coating, reducing the cross-sectional flow area.

The PML, or surface roughness, effects on the pressure gradient and friction factor are analyzed using a steady fully-developed flow model. Typical relative surface roughness values, which depend on the wall material and machining process, are listed in Table 3.3. Generally, micromachining results in higher roughness than etching processes, and microchannels made out of stainless steel have higher values of surface roughness than those of silicon. A typical roughness value for etching processes was found to be 20 [nm], which is negligible in most microchannels where $D_h > 10$ [μm]. However, considering flow in channels with $D_h \leq 10$ [μm], the effect of surface roughness should be taken into account.

The source term in the momentum equations, Eq. (2.2), simulating the resistance in the

Table 3.3: Typical values of relative surface roughness($h/D_h \times 100[\%]$)

Author	Relative surface roughness [%]	Material
Pfhaler et al. (1991)	~ 1 [%]	Silicon
Peng et al. (1994)	$\sim 0.6 - 1$ [%]	Silicon
Mala and Li (1999)	~ 3.5 [%]	Stainless steel, fused silica
Papautsky et al. (1999)	~ 2 [%]	Silicon
Xu et al. (1999, 2000)	$\sim 1 - 1.7$ [%]	Aluminum, silicon

porous medium is the resistance vector, \vec{R} , which can be represented as (Bear, 1972):

$$\vec{R} = (R_C + R_F|\vec{u}|^\beta)\vec{u} \quad (3.5)$$

where R_C is a resistance constant, R_F is the resistance speed factor, and β is a resistance speed power (usually 1.0). The quadratic drag term ($R_F u^2$) in Eq. (3.5) is dominant for relatively high-Reynolds number flows (Nield and Bejan, 1992).

For steady ($\partial/\partial t = 0$), 2-D ($\partial/\partial z = 0$), and fully-developed flow ($\partial/\partial x = 0$) in an open channel as well as through an isotropic medium, Eq. (2.1c) reduces to the Brinkman-Forchheimer extended Darcy equation, which can be readily solved using MATLAB. Specially, for the channel (or parallel-plate) case:

$$0 = -\frac{dp^*}{dx^*} + \frac{4}{Re_{D_h}} \frac{d^2 u^*}{dy^{*2}} + \left\{ \underbrace{-\frac{4u^*}{Da_{H/2} Re_{D_h}}}_{\text{Brinkman term}} - \underbrace{\frac{C_f u^{*2}}{Da_{H/2}^{1/2}}}_{\text{Forchheimer term}} \right\}_{PML} \quad (3.6)$$

where $p^* = \frac{p}{\rho U_0^2}$, $u^* = \frac{u}{U_0}$, $x^* = \frac{x}{H/2}$, $y^* = \frac{y}{H/2}$, $Da_{H/2} = \frac{\kappa}{(H/2)^2}$, $Re_{D_h} = \frac{\rho U_0 2H}{\mu}$, H is the channel height, and $C_F (\approx 0.55)$ is drag coefficient.

Table 3.4: Typical PML parameters.

Symbol	Meaning	Typical values/formats
α	(Volume) porosity	$0 \leq \alpha \leq 1.0$
κ	Permeability	$10^{-4}[cm^2] \leq \kappa < \infty$
K	Area porosity tensor	For isotropic porous media, $K_{ij} = \alpha\delta_{ij}$
Γ	Fluid diffusivity	For laminar flow, $\Gamma \equiv \mu$
R_C	Resistance constant	$R_C = f(Da, Re)$
R_F	Resistance speed factor	$R_F = f(Da, \vec{u})$
β	Resistance speed power	$\beta \approx 1.0$

For the tubular case:

$$0 = -\frac{dp^*}{dx^*} + \frac{2}{Re_D} \left(\frac{d^2u^*}{dr^{*2}} + \frac{1}{r^*} \frac{du^*}{dr^*} \right) + \left\{ -\frac{2u^*}{Da_R Re_D} - \frac{C_F u^{*2}}{Da_R^{1/2}} \right\}_{PML} \quad (3.7)$$

where $x^* = \frac{x}{R}$, $r^* = \frac{r}{R}$, $Da_R = \frac{\kappa}{R^2}$, $Re_D = \frac{\rho U_0 D}{\mu}$, R is the tube radius and U_0 is the average velocity. The relative roughness layer thickness was calculated based on the pipe diameter, i.e., $D = 2R$. The terms in braces $\{\}_{PML}$ are effective only in the PML, i.e., the roughness region. Typical values of model parameters are listed in Table 3.4.

The boundary conditions are no-slip velocity ($u = 0$) at the wall, and velocity gradient at the interface, $r^* = \xi$, between open and porous regions, i.e., $\frac{du^*}{dr^*}|_{r^*=\xi} = \frac{Re_D}{2} \frac{dp^*}{dx^*} \xi$. The interface velocity gradients should be obtained by iteration.

Figure 3.1 shows the Darcy number effect on the axial velocity profile. When decreasing the Darcy number, the maximum velocity at the pipe center increases, while the velocity profiles near the wall flattens. As expected, the velocity profile in the PML is a function of the Darcy number. It is found that the effect of the Forchheimer term on the friction factor is much more significant in tubes when compared to the parallel-plate case (see Fig. 3.2). This can be explained by the fact that the surface area increases with the radius, attaining a maximum at the shell where the roughness layer lies. Increasing surface area causes an increase in the effects of surface phenomena, e.g., surface roughness effect in this study, while

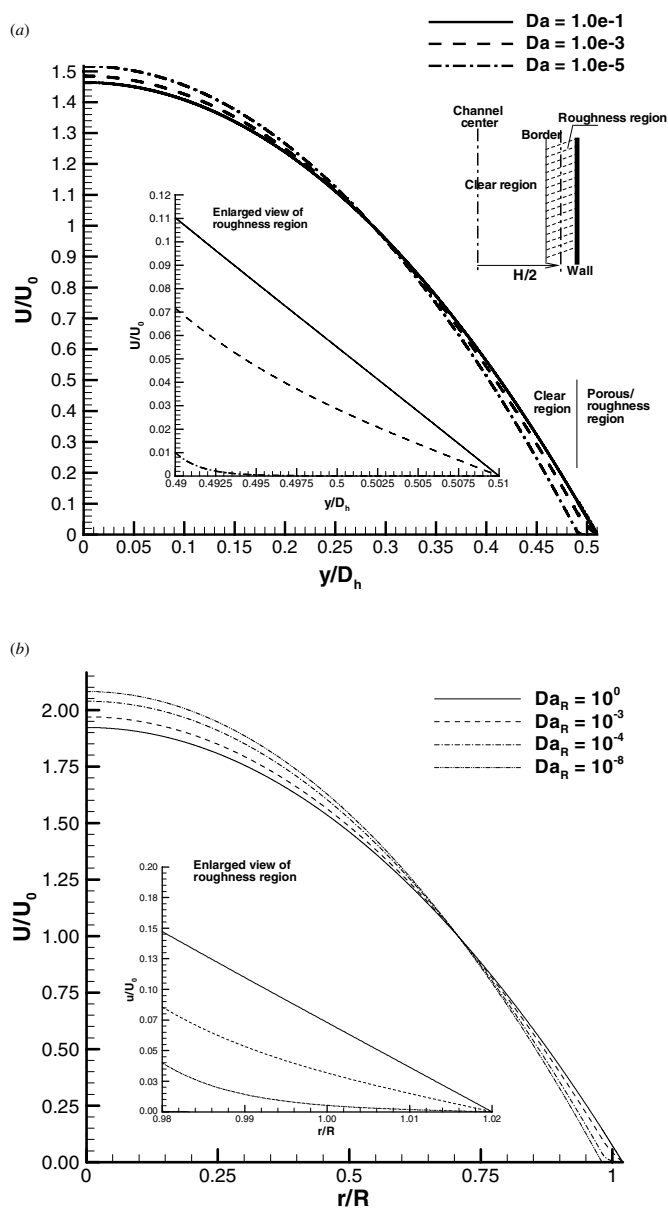


Figure 3.1: Effect of the Darcy number on steady 2-D fully-developed flows (Brinkman term only): (a) parallel-plate case and (b) circular tube case.

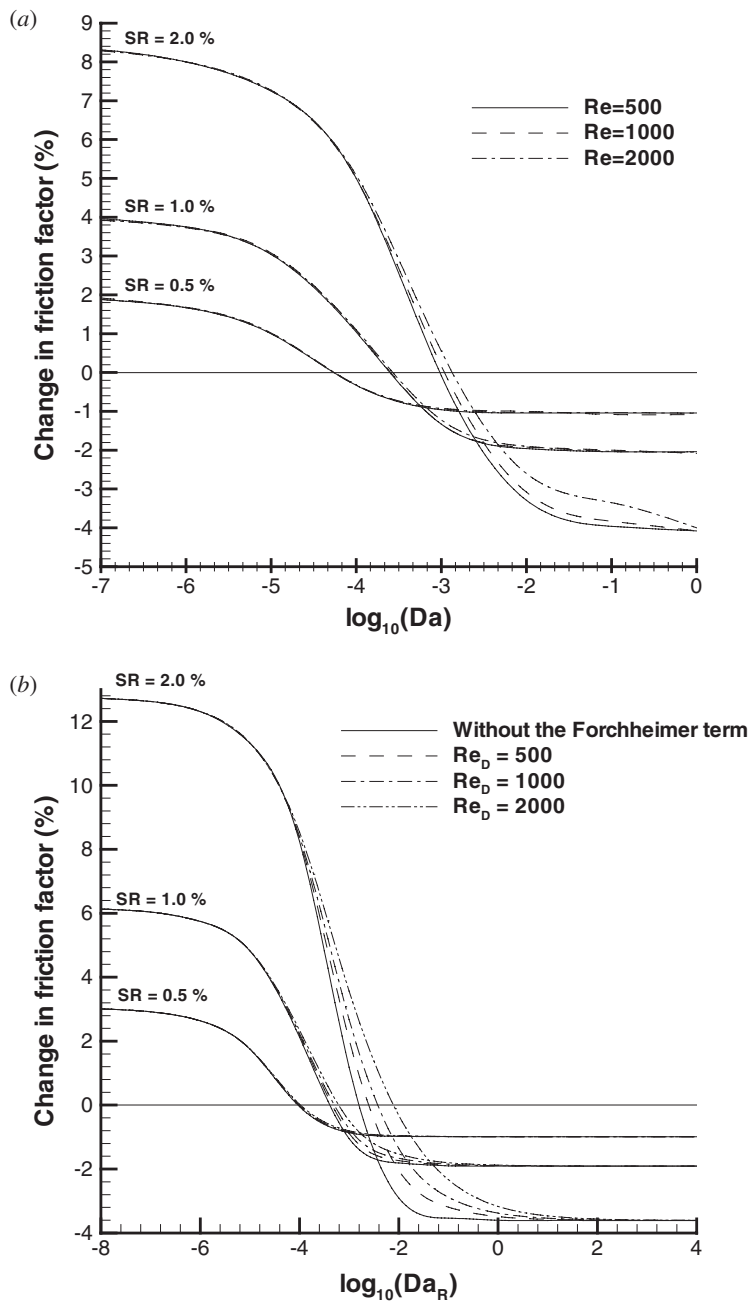


Figure 3.2: Effect of the Darcy number on steady 2-D fully-developed flows (Brinkman term only): (a) parallel-plate case and (b) circular tube case.

it is maintained to be constant for the parallel-plate case. Figure 3.3 shows comparisons between the PML model predictions and selected experimental results. Specifically, the experimental results of Mala and Li (1999), which fall into the region predicted by the PML model, indicate a strong $f^*(Re_D)$ dependence (Figure 3.3(a)). The experimental data sets of Guo and Li (2003) are well matched with those of the PML model (Figure 3.3(b)). Clearly, roughness elements of the 179.8 [μm] diameter tube have a higher Darcy number when compared to the 128.8 [μm] diameter tube. The $f^*(Re_D)$ data for the 179.8 [μm] diameter tube seem to indicate the effect of laminar-to-turbulent transition, when $Re_D = 1700$. They claimed that ‘*the form drag resulting from the roughness is one reason leading to the increased friction factor*’; the form drag is captured by the Forchheimer term in the PML model.

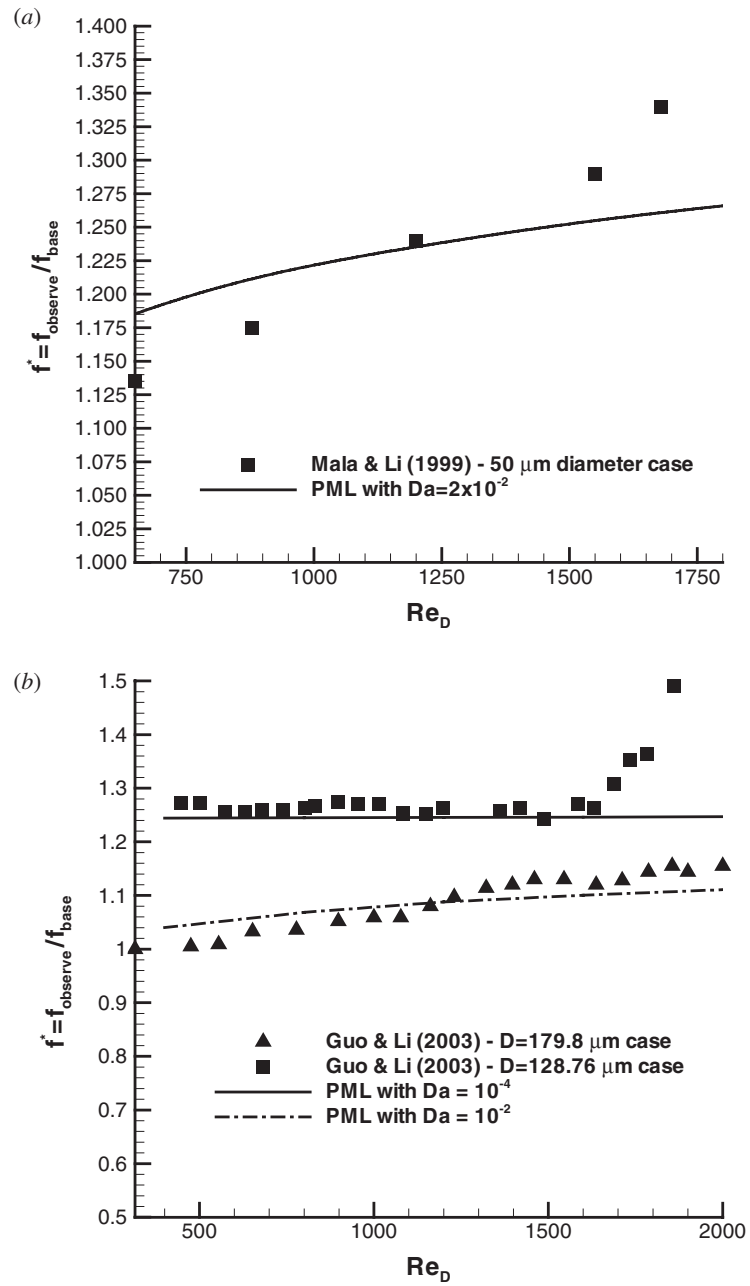


Figure 3.3: Comparisons of porous medium layer (PML) model predictions with experimental data: (a) Mala and Li (1999) and (b) Guo and Li (2003)

3.3.2 Effects on energy Transfer

Kleinstreuer and Koo (2004) introduced the porous medium layer (PML) model to model the surface roughness effect on friction factor. The friction factor could either increase or decrease depending on the surface roughness characteristics. In this study the PML model will be expanded to explain the surface roughness effect on heat transfer phenomena (Koo and Kleinstreuer, 2005a).

Kuznetsov and Xiong (2000) observed that the Nusselt number was a function of Darcy number, Forchheimer number, Reynolds number and interface position. Kuznetsov (2001) reported that during forced convection or strong natural convection in porous media, there may be significant heat transfer due to hydrodynamic mixing of the interstitial fluid at the pore scale in addition to the molecular diffusion of heat. This effect is called thermal dispersion. The importance of the thermal dispersion in PML was re-evaluated in the current study.

Governing Equations

The general governing equations for momentum and energy transfer in conduits with PMLs read:

$$\rho \frac{D\vec{u}}{Dt} = -\nabla p + \nabla \cdot \tau_{ij} - \{(R_C + R_F|\vec{u}|)\vec{u}\}_{PML} \quad (3.8)$$

$$\rho c_p \frac{DT}{Dt} = \{\nabla \cdot (k_f \nabla T)\}_{clear} + \left\{ \nabla \cdot \left(\left(k_m + C k_f Pr \frac{\rho_f u_f d_p}{\mu_f} \right) \nabla T \right) \right\}_{PML} \quad (3.9)$$

Assuming steady laminar fully-developed viscous flow in a parallel-plate microchannel with porous medium layer, the governing equations can be presented as:

$$-\frac{dp}{dx} + \mu_f \frac{d^2 u_f}{dy^2} = 0 \quad 0 \leq y \leq \xi \quad (3.10)$$

$$-\frac{dp}{dx} + \mu_{eff} \frac{d^2 u_f}{dy^2} - \frac{\mu_f}{\kappa} u_f - \frac{\rho_f c_F}{\kappa^{1/2}} u_f^2 = 0 \quad \xi \leq y \leq \xi + s \quad (3.11)$$

$$\rho_f c_f u_f \frac{\partial T}{\partial x} = k_f \frac{\partial^2 T}{\partial y^2} \quad 0 \leq y \leq \xi \quad (3.12)$$

$$\rho_f c_f u_f \frac{\partial T}{\partial x} = \frac{\partial}{\partial y} \left[\left(k_m + C k_f Pr \frac{\rho_f u_f d_p}{\mu_f} \right) \frac{\partial T}{\partial y} \right] \quad \xi \leq y \leq \xi + s \quad (3.13)$$

Equation (3.10) is the momentum equation for the clear fluid region while Eq. (3.11) holds for the porous region (i.e., the Brinkman-Forchheimer-extended Darcy equation). Equations (3.12) and (3.13) are the energy equations for the clear fluid and porous region, respectively. The energy equation for the porous region accounts for transverse thermal dispersion, while longitudinal thermal dispersion is neglected. This is consistent with the assumption of longitudinal conduction, $k_x \partial^2 T / \partial x^2$ being negligible in comparison with $k_y \partial^2 T / \partial y^2$.

The thermal dispersion term $C k_f Pr \frac{\rho_f u_f d_p}{\mu_f}$ can be rewritten as

$$C k_f Pr \frac{\rho_f u_f d_p}{\mu_f} = C k_f Pr Re_p = C k_f Pr Re_{D_h} \frac{u_f}{U_0} \frac{d_p}{D_h} \quad (3.14)$$

Equations (3.10) to (3.13) are subject to the following boundary conditions:

$$\frac{\partial u_f}{\partial y} = 0 \quad \text{at} \quad y = 0 \quad (3.15)$$

$$\frac{\partial T}{\partial y} = 0 \quad \text{at} \quad y = 0 \quad (3.16)$$

$$u|_{y=\xi-0} = u|_{y=\xi+0} \quad \text{at} \quad y = \xi \quad (3.17)$$

$$\mu_{eff} \frac{\partial u_f}{\partial y} |_{y=\xi+0} - \mu_f \frac{\partial u_f}{\partial y} |_{y=\xi-0} = \beta \frac{u_f}{\kappa^{1/2}} u_f |_{y=\xi} \quad \text{at} \quad y = \xi \quad (3.18)$$

$$T|_{y=\xi+0} = T|_{y=\xi-0} \quad \text{at} \quad y = \xi \quad (3.19)$$

$$\left(k_m + Ck_f Pr \frac{\rho_f u_f d_p}{\mu_f} \right) \frac{\partial T}{\partial y} |_{y=\xi+0} = k_f \frac{\partial T}{\partial y} |_{y=\xi-0} \quad \text{at} \quad y = \xi \quad (3.20)$$

$$u_f = 0 \quad \text{at} \quad y = \xi + s \quad (3.21)$$

$$\left(k_m + Ck_f Pr \frac{\rho_f u_f d_p}{\mu_f} \right) \frac{\partial T}{\partial y} = q'' \quad \text{at} \quad y = \xi + s \quad (3.22)$$

For the mean (or effective) PML conductivity, Kuznetsov and Xiong (2000) used the relation

$$k_m = \phi k_f + (1 - \phi) k_s \quad (3.23)$$

In the current study, β the slip coefficient was assumed to be zero.

After non-dimensionalization, the governing equations read:

$$u^* Nu = -4 \frac{d^2 \theta}{dy^{*2}} \quad (3.24)$$

$$u^* Nu = -4 \left[\left(\frac{k_m}{k_f} \right) + CPrRe_p \right] \frac{d^2 \theta}{dy^{*2}} \quad (3.25)$$

where $u^* = u_f/U_0$, $Nu = h \cdot 2H/k_f$, $\theta = (T_m - T)/(T_m - T_w)$, $Pr = \mu/\rho\alpha$, and $Re_p = \rho_f u_f d_p/\mu$. Here, U_0 is the mean velocity, h is the heat transfer coefficient, and d_p represents the equivalent hydraulic diameter of the surface roughness elements. For a porous-medium

free, i.e., clear part of the microchannel

$$u^*(y^*) = \frac{Re_{D_h}}{4} \frac{dp^*}{dx^*} (y^{*2} - \xi^{*2}) + u_{int}^* \quad (3.26)$$

where ξ^* is the non-dimensionalized coordinate for the open channel-porous medium interface, and u_{int}^* is the flow velocity at the interface, which depends on the iterative solution to the PML-flow problem.

The dispersion term was found to be negligible because the velocity in the surface roughness region is very small, implying very low particle Reynolds numbers. Referring to Kleinstreuer and Koo (2004), typical values of $\frac{u_f}{U_0}$ and $\frac{d_p}{D_h}$ are in the order of $\mathcal{O}(10^{-1})$ and $\mathcal{O}(10^{-2})$, respectively. Considering typical values of C , Pr and Re_{D_h} to be 0.1, 5 and 2000, respectively, the order of magnitude of the thermal dispersion term is in the order of k_f , which can be usually neglected due to high k_s/k_f ratios and hence high k_m/k_f values. According to Kuznetsov (2001), the thermal dispersion effect is negligible for $Re_p < 100$. for the present case, $Re_{p,max} = 1$ and hence the thermal dispersion effect will be neglected. However, it becomes important for fluid flows of high Prandtl numbers, such as oils ($Pr \sim 1000$).

For the clear region, Eq. (3.24) can be integrated with the given parabolic velocity profile to:

$$\theta = \left\{ \frac{Re_{D_h}}{4} \frac{dp^*}{dx^*} \left(\frac{1}{12} y^{*4} - \frac{1}{2} y^{*2} \xi^{*2} + \frac{5}{12} \xi^{*4} \right) + \frac{1}{2} u_{int}^* (y^{*2} - \xi^{*2}) \right\} Nu + \theta_{int} \quad (3.27)$$

The velocity profiles were obtained in the same way as introduced in Kleinstreuer and Koo (2004), and the Nusselt numbers were iteratively obtained to meet the energy balance at the interface. 300 elements were evenly distributed in the porous medium layer and 2,000 elements in the open region. The equations were solved using a boundary-value-problem ordinary differential equation solver routine that is provided in MATLAB 7.0.

In order to gain a better understanding of convective heat transfer in microchannels with measurable surface roughness, $SR \equiv s/D_h$, the dependence of the Nusselt number on SR

is established. By definition,

$$Nu = \frac{hD_h}{k_f} \quad (3.28a)$$

where

$$h = \frac{q''}{T_w - T_m} = \frac{k_m(dT/dy)|_{wall}}{T_w - T_m} \quad (3.28b)$$

For a given relative surface roughness, Eqs. (3.28a) and (3.28b) are combined into

$$Nu \sim \frac{k_m}{k_f} \frac{d\theta}{dy^*}|_{wall} \quad (3.28c)$$

which can be rewritten for a given thermal conductivity ratio in the form:

$$Nu \sim \frac{k_m}{k_f} \frac{d\theta}{dy^*}|_{\xi^*=0} \frac{1}{Re_{D_h} f / 6(1 - SR/2)^3} \quad (3.28d)$$

Of interest are the effects of SR characteristics in terms of the Darcy number, $Da = \frac{\kappa}{(H/2)^2}$ (or, $Da = \frac{\kappa}{R^2}$ for tubes), thermal conductivity ratio and Reynolds number on the Nusselt number, considering first parallel plates and then tubes.

Parallel Plates

Effects of Darcy number and PML thermal conductivity The effect of PML thermal conductivity on the temperature profile in a channel is shown in Fig. 3.4, where $\theta \equiv \frac{T_m - T}{T_m - T_w}$. The higher the PML thermal conductivity is, the lower is the centerline temperature to yield higher Nusselt numbers. The temperature profiles in the PML are affected by the thermal conductivity ratio more significantly at relatively low values compared to those at high ones. Figure 3.5 illustrates the Darcy number effect on the temperature profiles, which turned out to be minimal. Clearly, the PML thermal conductivity affects temperature profiles more strongly than the Darcy number.

Figure 3.6 shows the effects of PML Darcy number and thermal conductivity on

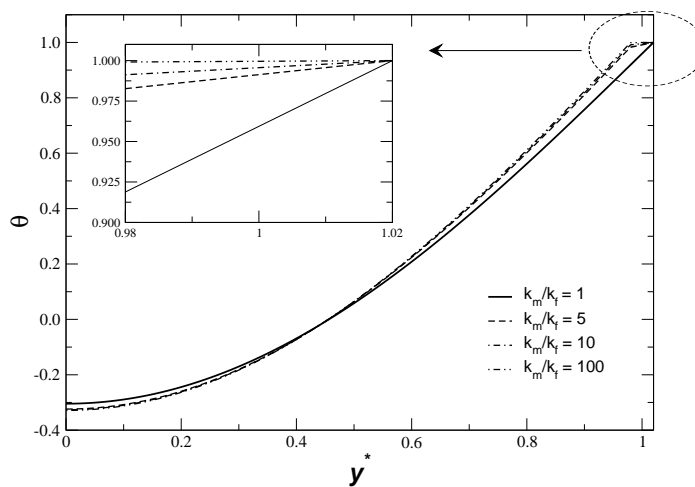


Figure 3.4: PML thermal conductivity effect on the temperature profiles between parallel plates ($Da=10^{-3}$, $SR = 2$ [%])

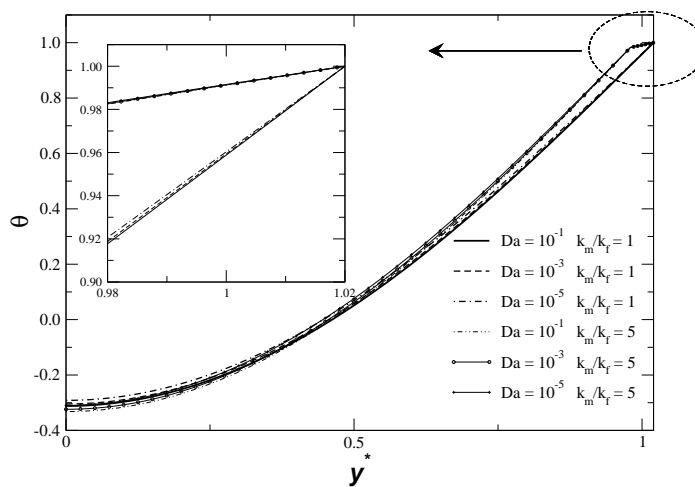


Figure 3.5: Darcy number effect on the temperature profiles between parallel plates ($SR = 2$ [%])

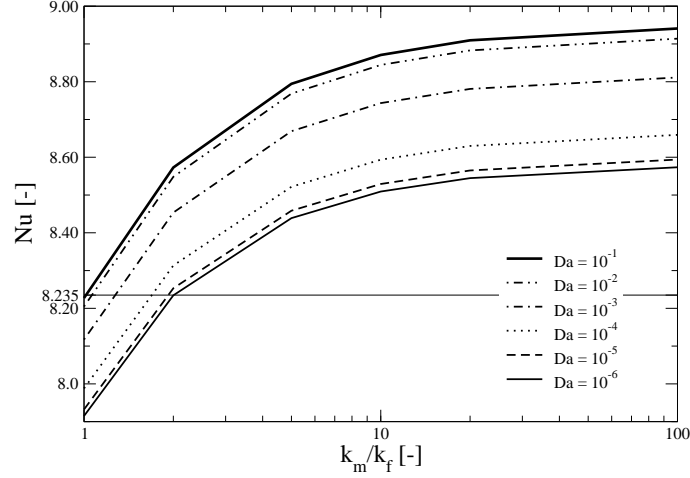


Figure 3.6: Effects of PML Darcy number and thermal conductivity on the Nusselt number for parallel plates ($Re = 1000$, $SR = 2$ [%])

the Nusselt number for the case of $SR = 2$ [%] and $Re_{D_h} = 1000$. As expected, the Nusselt number increased with an increase in PML conductivity. The Nusselt number showed deviations from the conventional laminar flow result ($Nu = 8.235$) between -4 [%] and 9 [%] depending on the PML characteristics. Specifically, the Nusselt number is lower than the conventional result, for low Darcy number and low thermal conductivity conditions, and it increases with elevated PML Darcy number and thermal conductivity values. The Nusselt number change is observed to be sensitive in the mid-range regime, i.e., $Da = 10^{-3}$ to 10^{-4} . Indeed, there is a relationship between the Darcy number and thermal conductivity, since the PML thermal conductivity depends on the void fraction which is directly related to the Darcy number. For certain types of porous media, the *Kozeny-Carman* equation could be used as the relation with void fraction, ϕ , i.e., $\kappa = \frac{d^2 \phi^3}{180(1-\phi)^2}$, although the surface roughness elements forming the PML are not exactly homogeneous and isotropic. The Reynolds number dependence is stronger in the mid-Darcy number range compared to that in

low- and high-Darcy number ranges. The Nusselt number increases rapidly for low PML thermal conductivities, and it increases slowly under high thermal conductivity conditions. This indicates that there exists a limiting Nusselt number when increasing the PML thermal conductivity.

Judging from Figs. 3.5 and 3.6, the Darcy number influences convection more in the clear region than conduction in the surface roughness region for a given k_m/k_f -ratio. Specifically, the temperature profiles in Fig. 3.5 do not change much with the Darcy number in contrast to the Nusselt number (see Fig. 3.6).

As indicated in Eq. (3.28c), the Nusselt number is a function of the conductivity ratio and the temperature gradient at the wall. In Fig. 3.4, it was shown that the temperature gradient is greater for the lower conductivity cases, and it decreases fast with the thermal conductivity ratio; that explains the high rate of the Nusselt number increase at low thermal conductivity ratios. The temperature gradient at the wall increases with the Darcy number; thus, the Nusselt number increases with the Darcy number as shown in Fig. 3.6.

Reynolds number effect Conventionally, the Nusselt number for laminar flow is independent of the Reynolds number. However, a weak Reynolds number dependence is observed for microchannels with PMLs, as shown in Fig. 3.7. Although the Reynolds number dependence is stronger in the Darcy number mid-range, overall its influence is usually negligible for $1 \leq SR \leq 4$ [%].

Effect of relative surface roughness Figure 3.8 shows the SR effect, i.e., thickness of the PML, on the Nusselt number, where the Reynolds number is 1000 for all cases. The Nusselt number as a function of k_m/k_f varies only from 8.0927 to 8.5822 for $SR = 1$ [%], while it changes from 7.6378 to 9.6486 for $SR = 4$ [%]. As the PML-thermal conductivity and surface roughness increase, the Nusselt number quickly exceeds the conventional value of 8.235. In more detail, for any given SR value, the thermal conductivity ratio decreases with the Darcy number for the cross-over point when

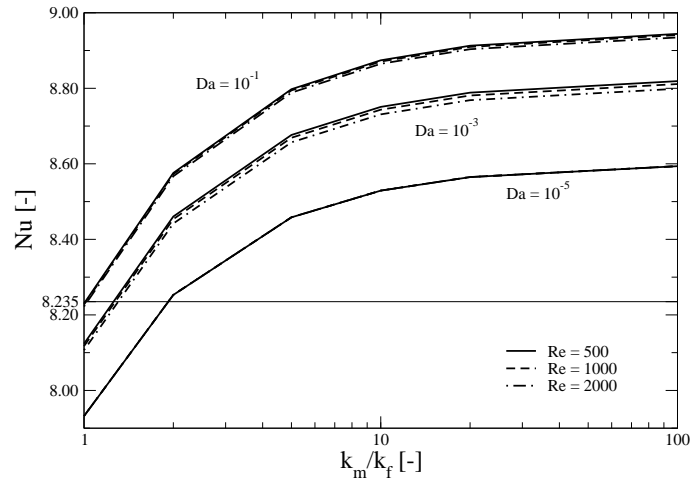


Figure 3.7: Effect of the Reynolds number on the Nusselt number for different Darcy numbers and the conductivity ratios (SR = 2 [%])

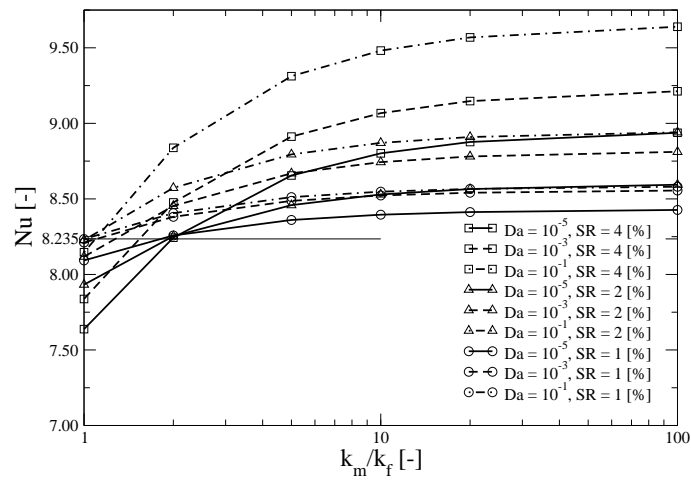


Figure 3.8: Effects of PML thickness on the Nusselt number ($Re = 1000$)

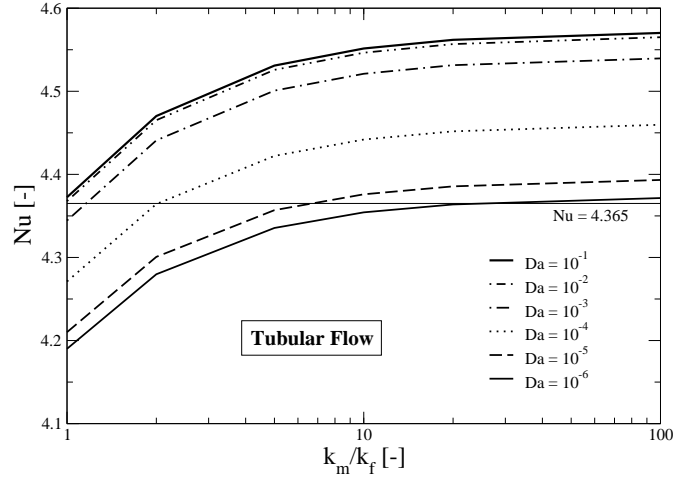


Figure 3.9: Effects of PML Darcy number and thermal conductivity on the Nusselt number ($Re = 1000$, $SR = 2$ [%])

$$Nu \geq 8.235.$$

When inspecting Eq. (3.28d), it is evident that the conductivity ratio and the temperature gradient have opposite impacts, assuming a constant relative surface roughness. In summary, the Nusselt number increases with relative surface roughness and decreases with the product of Reynolds number and friction factor.

Tubular flow

Effects of Darcy number and PML thermal conductivity Compared to the parallel plate cases, the Nusselt number for tubes exceeds the conventional value of 4.365 at higher thermal conductivity ratios, as shown in Fig. 3.9. Specifically, the thermal conductivity ratio has to be increased by a factor of 10 to achieve the same Nusselt number improvement at low Darcy numbers. This could explain why most experimental Nusselt number data fall below the conventional value. For example, Croce

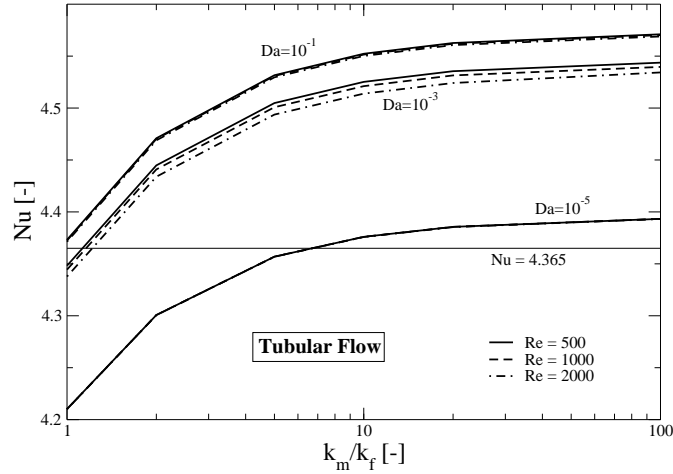


Figure 3.10: Effect of the Reynolds number on the Nusselt number ($SR = 2$ [%])

and D'Agaro (2004) reported that Nusselt number is less sensitive to the roughness height with respect to the friction factor. Considering the friction factor changes with surface roughness as reported by Koo and Kleinstreuer (2003) and the Nusselt number changes now given in Fig. 3.9, the observation of Croce and D'Agaro (2004) can be confirmed. Furthermore, Croce and D'Agaro (2004) reported an increase in Nusselt number for parallel plate flow and a decrease for tubular flow, which is evident when comparing Figs. 3.6 and 3.9.

Reynolds number effect A small-influence of the Reynolds number on the Nusselt number for flow in tubes (see Fig. 3.10) is very similar to the parallel plate cases.

Effect of relative surface roughness As it was observed for the parallel plate cases, the Nusselt number changes in tubes are greater for the high relative surface roughness cases, as shown in Fig. 3.11. The PML thickness effect can be understood in the same way as for the parallel plate cases. One minor difference is that the Darcy number effect for $SR = 1$ and 2 [%] on the Nusselt number is smaller for tubular flow. This is

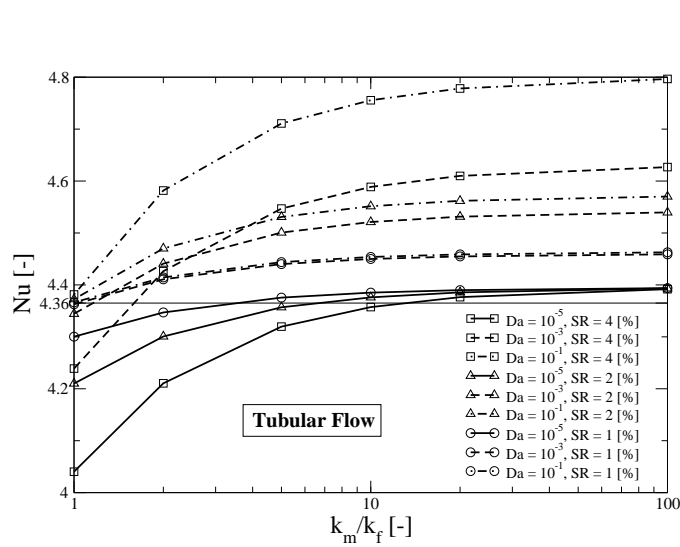


Figure 3.11: Effect of PML thickness on the Nusselt number ($Re = 1000$)

due to the definition of the relative surface roughness ($SR = \frac{s}{D_h}$). In this study, we adopted the hydraulic diameter as the system length scale. The height of the surface roughness layer in parallel-plate channels is twice thicker than that in tubes resulting in a small difference in Nusselt number.

Thermal dispersion effect

Kuznetsov and Xiong (2000) and Kuznetsov (2001) investigated the thermal dispersion effect and concluded that it is negligible for low Reynolds number flows. However, they considered only low Prandtl number fluids, i.e., $Pr = 0.25$ and 0.7 . Referring to Eq. (3.24), the thermal dispersion effect is a function of both Reynolds number and Prandtl number. Therefore, for high Prandtl number (e.g., $Pr_{oil} \sim 1000$) in a PML region of low thermal conductivity ratio, the thermal dispersion effect could become a very important part of the heat transfer mechanism. Fortunately, thermal dispersion affects the Nusselt number in the same way as the PML thermal conductivity ratio. Hence, the effect could

be simply absorbed in the thermal conductivity ratio term.

3.3.3 Summary

The relative surface roughness and the Darcy number are functions of parameters such as wall material, way of micro-cutting processes, and they affects both momentum and energy transport in microchannels. The PML model has been developed to simulate the effect of the surface roughness on the momentum and energy transports. Focusing on steady laminar fully-developed flow of a liquid in different micro-conduits, relative surface roughness and actual diameter (or channel height) variations are captured in terms of a porous medium layer (PML) model. The new approach allows the evaluation of microfluidics variables as a function of PML characteristics, i.e., layer thickness and porosity, uncertainties in measuring hydraulic diameters, as well as the inlet Reynolds number.

For momentum transport phenomena, it was observed that

- *Surface roughness effects* are a function of the Darcy number, the Reynolds number, and cross-sectional configurations.
- The friction factor f can either increase or decrease depending on the conditions of wall surface.
- The Forchheimer term produces the Reynolds number dependence of friction factor, and the effects of the term increases with Reynolds number.
- The surface roughness effect is more important for tubes than it is for parallel plates.

For energy transport phenomena, the results could be summarized:

- The Nusselt number can be either higher or lower than the conventional value depending on the actual surface roughness conditions, i.e., PML characteristics.
- However, the surface roughness effect on heat transfer is less significant than on momentum transfer.

- The most important parameter affecting heat transfer performance for a given relative surface roughness is the thermal conductivity ratio k_m/k_f , i.e., between PML and bulk fluid.
- The Nusselt number increases with the Darcy number, $Da = \frac{\kappa}{(H/2)^2}$ or $\frac{\kappa}{R^2}$.
- The Reynolds number effect on the Nusselt number is negligible compared to its effect on the friction factor. Hence any Reynolds number dependence observed in experimentally obtained Nusselt number correlations has to originate from effects other than surface roughness.
- Relative to the thermal parallel-plate cases, the Nusselt number for tubular flow is typically lower than the conventional value .
- For high Prandtl number fluid flow in microchannels with low PML thermal conductivity ratios, thermal dispersion may greatly influence the heat transfer mechanism.

3.4 Viscous Heating Effect

3.4.1 Viscous dissipation effect

Except for very viscous fluids at relatively high speed, viscous dissipation effects are typically ignored in macro-conduits. In contrast, even for common fluids at laminar Reynolds numbers, frictional effects in micro-size conduits may change the temperature fields measurably. As a result, the local viscosity, friction factor, flow structure and scalar transport variables may be affected. Applications include micro heat exchangers for cooling electronic systems (Tuckerman and Pease, 1981) and valveless pumping mechanisms (Jun and Kim, 1998).

For example, when the water temperature rises from 300 to 310 K, say, due to viscous dissipation, the kinematic-viscosity decreases by 20 % which results in a 25 % increase of the local Reynolds number. Thus, fluid temperature changes in microchannels may affect the friction factor and hence all transport phenomena (Urbanek et al., 1993). Toh et al. (2002) investigated numerically transport phenomena in heated microchannels. As expected, they found that heat input lowers the frictional losses, particularly at low Reynolds numbers. Judy et al. (2002) observed measurable liquid flow temperature rises (e.g., 6.2 K for isopropanol in a long square fused-silica channel of 74.1 μm diameter for $\text{Re} \approx 300$) and related this to viscous dissipation. They suggested that the viscosity change due to temperature changes should be taken into account to estimate the friction factor. Pfahler et al. (1991) attributed viscosity changes to the channel size, and defined a viscosity ratio as $C^* = \frac{\mu_{exit}}{\mu_{inlet}}$, or $\frac{\mu_{mean}}{\mu_{inlet}}$, a parameter used in this study as well.

Tunc and Bayazitoglu (2001) investigated the viscous dissipation effect in rarefied gas flow by varying the Brinkman number ($Br = \frac{\text{viscous dissipation term}}{\text{thermal diffusion term}}$) in their non-dimensionalized governing equations, and concluded that it plays an important role in heat transfer. Tso & Mahulikar Tso and Mahulikar (1998, 1999, 2000) published three papers regarding the Brinkman number effect on convective heat transfer and flow transition. They stated that *“the problem of heat dissipation accompanied by reducing the future size of IC chips cannot*

be solved by indefinitely reducing the microchannel dimensions without considering the effect of the Brinkman number, as this will lead to the same problem of viscous heat dissipation in the fluid which will offset the gains of high heat transfer coefficient associated with a reduction in channel size”.

In this study, viscous dissipation effects on the evolution of temperature distributions are investigated, employing scale analyses and numerical solutions (Koo and Kleinstreuer, 2004b). Such considerations are important in microfluidics in order to develop correct mathematical models for computer simulations. It should be noted that in all previous studies the viscous dissipation effect was just a minor part of the overall heat transfer process. Here, the importance of viscous dissipation is analyzed separately employing the experimental systems of Pfahler et al. (1991) and Judy et al. (2002). Three common working fluids, i.e., water, methanol and iso-propanol, as well as Reynolds number and channel geometry effects are considered.

3.4.2 Governing equations and scale analyses in tubes

Tubular flow To assess the possible impact of temperature changes due to viscous dissipation on the velocity profile in Poiseuille-type flows, the x-momentum equation reads:

$$0 = -\frac{\partial p}{\partial x} + \frac{1}{r} \frac{\partial}{\partial r} \left(r \mu \frac{\partial u}{\partial r} \right) \quad (3.29)$$

Non-dimensionalization of Eq. (3.29) and replacing the net pressure force term with the net shear force evaluated at the tube wall yields

$$\mu \frac{\partial^2 u^*}{\partial r^{*2}} + \left(\frac{\mu}{r^*} + \frac{d\mu}{dT} \frac{\partial T}{\partial r^*} \right) \frac{\partial u^*}{\partial r^*} - 2 \left\{ \mu \frac{\partial u^*}{\partial r^*} \right\}_{r^*=1} = 0 \quad (3.30)$$

where $r^* = \frac{r}{R}$ and $u^* = \frac{u}{U_{ave}}$.

For a typical radial temperature difference of $0 \leq \Delta T \leq 20$ K in iso-propanol, which, of the three fluids, has a viscosity most sensitive to temperature changes, the velocity

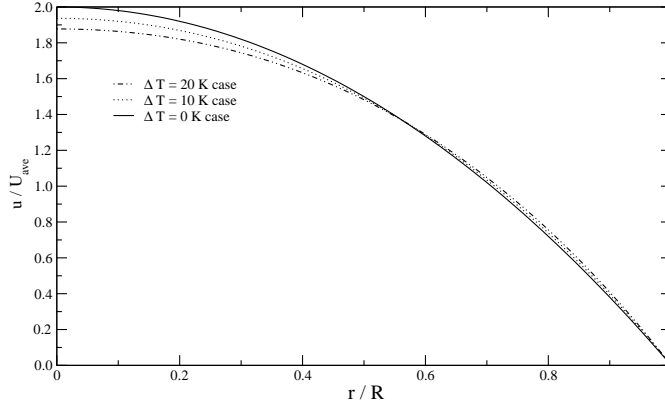


Figure 3.12: Effects of viscosity changes for different radial temperature distributions ΔT on tubular velocity profiles

profiles based on Eq. (3.30) are shown in Fig. 3.12. Although the velocity change is measurable in the range $0 \leq r^* \leq 0.4$, the effect on the viscous dissipation term in the energy equation (see Eq. (3.31)) is minimal. Specifically, the impact on the viscous dissipation term (see Eq. (3.31)) is only 0.15 % for $\Delta T = 10$ K and 0.61 % for $\Delta T = 20$ K.

Tubular heat transfer The energy equation can be expressed as:

$$\rho C_p \left(u \frac{\partial T}{\partial x} + v_r \frac{\partial T}{\partial r} \right) = \frac{\partial}{\partial x} \left(k_x \frac{\partial T}{\partial x} \right) + \frac{1}{r} \frac{\partial}{\partial r} \left(k_r r \frac{\partial T}{\partial r} \right) + \mu \Phi \pm \dot{q} \quad (3.31a)$$

where $\mu \Phi$ is the viscous dissipation term and \dot{q} is a possible heat source/sink. Specifically,

$$\mu \Phi = \mu \left\{ 2 \left[\left(\frac{\partial v_r}{\partial r} \right)^2 + \left(\frac{\partial u}{\partial x} \right)^2 \right] + \left(\frac{\partial v_r}{\partial x} + \frac{\partial u}{\partial r} \right)^2 \right\} \quad (3.31b)$$

Thus, with the stated assumption of hydrodynamically fully-developed flow, Eq. (3.31) reduces to

$$\rho C_p \left(u \frac{\partial T}{\partial x} \right) = \frac{\partial}{\partial x} \left(k \frac{\partial T}{\partial x} \right) + \frac{1}{r} \frac{\partial}{\partial r} \left(kr \frac{\partial T}{\partial r} \right) + \mu \left(\frac{\partial u}{\partial r} \right)^2 \quad (3.32)$$

where, $Re_D = \frac{\rho U_{mean} D}{\mu} = \frac{\rho U_{max} R}{\mu}$. The axial velocity can be written as

$$u(r) = \frac{Re_D \mu}{\rho R} (1 - (r/R)^2) \quad (3.33)$$

The boundary conditions associated with Eq. (3.32) for a tube with, say, L/D=800 are:

$$T = 300K \quad \text{at } x=0 \quad (3.34a)$$

$$\frac{\partial T}{\partial r} = 0 \quad \text{at } r=0 \quad (3.34b)$$

$$T = 300K \quad \text{at } r=R \text{ for constant temperature case} \quad (3.34c)$$

$$\frac{\partial T}{\partial r} = 0 \quad \text{at } r=R \text{ for adiabatic case} \quad (3.34d)$$

$$\frac{\partial}{\partial x} \left(\frac{T - T_w}{T_m - T_w} \right) = 0 \quad \text{at the exit} \quad (3.34e)$$

The material of micro-conduits, e.g., in MEMS devices, affects the type of thermal boundary condition. If the conduit is made of fused silica, as in the case reported by Judy et al. (2002), the channel wall would work as an insulator due to the low heat conductivity of fused silica.

Scale analysis is performed to investigate the conduit size-effect on the relative magnitude of the viscous dissipation term with respect to other terms in the energy equation, assuming constant properties. Again, the axial diffusion term is negligible compared to radial diffusion. Hence, substituting Eq. (3.33) into Eq. (3.32) yields after non-

dimensionalization with $T^* = \frac{T-T_w}{T_m-T_w}$, $r^* = r/R$, and $x^* = x/L$:

$$\begin{aligned} & \frac{C_p Re_D \mu}{RL} (1 - r^{*2}) \frac{\partial [T^* (T_m(x) - T_w(x))]}{\partial x^*} \\ &= \frac{k}{R^2 r^*} (T_m(x) - T_w(x)) \frac{\partial}{\partial r^*} \left(r^* \frac{\partial T^*}{\partial r^*} \right) + 4 \frac{\mu^3 Re_D^2}{\rho^2} \frac{r^{*2}}{R^4} \end{aligned} \quad (3.35)$$

The convective term should balance with the diffusion term and the viscous dissipation term. If the flow is thermally fully developed for a constant heat flux boundary condition, then $T_m(x) - T_w(x) = \text{const.}$ Comparing the two terms on the RHS, the diffusion term is inversely proportional to R^2 while the viscous dissipation term is inversely proportional to R^4 for a given fluid and Reynolds number. Thus, when the tube radius decreases, the viscous dissipation term increases much faster than the diffusion term. When ignoring the viscous dissipation term, there is a growing importance of the diffusion term ($\sim \frac{1}{R^2}$) in microtubes when compared to the convection term ($\sim \frac{1}{R}$). Furthermore, the Reynolds number effect on the viscous dissipation term is more important than on the convection term. While traditionally the Brinkman number is employed to describe the effect of viscous dissipation, we analyzed the temperature rise of a given working fluid as a function of the geometric ratio, $\left(\frac{L}{R}\right)$, the Reynolds number, and the Eckert number. Thus Eq. (3.35) is rewritten as

$$\begin{aligned} & \frac{(1 - r^{*2})}{(T_m(x) - T_w(x))} \cdot \frac{\partial [T^* (T_m(x) - T_w(x))]}{\partial x^*} \\ &= \frac{1}{Pr \cdot Re_D} \left(\frac{L}{R}\right) \frac{\partial}{\partial r^*} \left(r^* \frac{\partial T^*}{\partial r^*} \right) + 32 \frac{Ec}{Re_D} \left(\frac{L}{R}\right) r^{*2} \end{aligned} \quad (3.36)$$

Clearly, for a given Pr and $\Delta T = (T_m - T_w)$, the Eckert number is proportional to the square of the Reynolds number. In turn, for a given set of fluid properties, the temperature rise is proportional to the Reynolds number. The impact of fluid temperature rise on the tube friction factor is as follows. By definition, $f \equiv \frac{8\tau_w}{\rho U_{ave}^2} = \frac{8\tau}{\rho U_{ave}^2} \frac{R}{r}$ and the friction head loss is $h_f \equiv f \frac{L}{D} \frac{U_{ave}^2}{2g}$; now, the pressure change in a

tube can be written as $\Delta p = \frac{2\tau}{r}\Delta x = \rho gh_f = f\rho\frac{L}{D}\frac{U_{ave}^2}{2}$, where $\tau = \mu(T)\frac{\partial u}{\partial r}$. For an incompressible fluid, the density variation with temperature is negligible compared to the viscosity variation. Hence, the friction factor is proportional to the fluid viscosity which is a function of temperature only, and so the viscous dissipation effect on the friction factor can be analyzed by investigating variations in fluid temperature.

3.4.3 Numerical solution for rectangular ducts

Two thermal flow cases for rectangular microchannels were considered in order to validate the computational approach and to assess the impact of the thermal entrance length on the fluid temperature development. In order to test the merits of a one-dimensional analysis, the effect of viscosity changes on the temperature rise was estimated for the cross-sectional mean temperature of iso-propanol flow. The energy equation was solved for the laboratory system of Judy et al. (2002), i.e.,

$$\rho C_p U_{ave} A \frac{dT_m}{dx} = kA \frac{d^2 T_m}{dx^2} + \mu \iint_A \Phi dA \quad (3.37)$$

where A is the cross sectional area of the channel. The data point (Judy et al., 2002) was obtained at the highest Reynolds number (Re=300), so that the entrance effect should be the most significant compared to other cases considered in this study. The equation was solved using MATLAB[®].

To investigate the thermal entrance effect, the full heat transfer equation was solved for hydraulically fully-developed flow and constant fluid properties except for the viscosity which was assumed to vary only with the (mean) flow temperature. Thus, Eq. (3.32) was discretized using a central difference scheme except for the convection term, which was discretized by using a first-order upwind scheme. The equation was integrated explicitly with the simple explicit method. The computational domain was refined until no mesh dependence of the results was observed. It took about 24 hours to obtain a solution on a

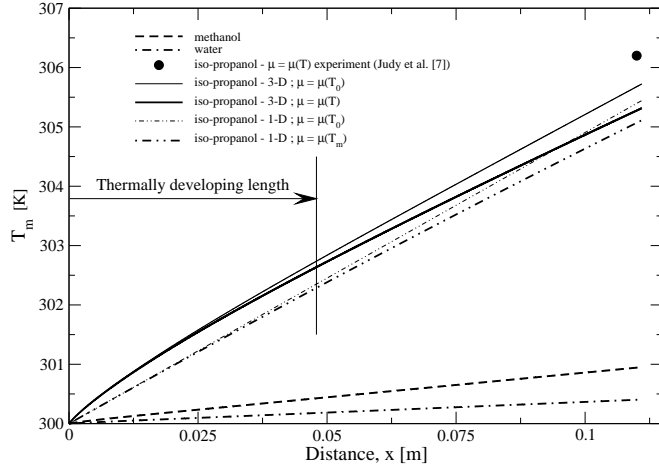


Figure 3.13: Working fluid effect on mean temperature rise ($L/D=1500$, $Re=300$)

Linux box with dual Pentium 4, 2.0 GHz processors and 4 GB of memory.

3.4.4 Model validations

The computer simulation model was validated with experimental data sets of Judy et al. (2002) and Pfahler et al. (1991). In the case of Judy et al. (2002), the flows of iso-propanol, methanol and water in a $74.1 \mu\text{m}$ square channel were simulated where the channel length was 1500 times the hydraulic diameter. The velocity profile and its gradient were calculated using the information given by White (1991). Because of the varying surface temperature, a mean wall temperature was used for T_w in Eq. (3.34e). The predicted iso-propanol temperature rise is close to the experimental data point of Judy et al. (2002) as indicated in Fig. 3.13. Specifically, the dynamic viscosity of iso-propanol decreases about 20 % per 10 K temperature change (MicroFab, 1999). Hence, if the viscosity change due to viscous dissipation is neglected, then the Reynolds number will be underestimated by about 25 %, which measurably affects the friction factor.

Table 3.5: Mechanical and thermodynamic properties of various working fluids at 298K (Zabransky, 1996; MatWeb, 1999)

Working fluid	Density [kg/m^3]	Dynamic viscosity [Pa/sec]	Thermal conductivity [$W/m \cdot K$]	Specific heat [$J/kg \cdot K$]	Pr
water	996	8.67×10^{-4}	0.611	4178	5.9
iso-propanol	779	1.95×10^{-3}	0.135	2606	37.6
methanol	792	8.17×10^{-4}	0.200	2531	10.3

The thermal entrance length is much longer than the hydraulic entrance length due to the high Prandtl number (see Table 3.5). Figure 3.13 shows that the thermal entrance for iso-propanol flow ($Re=300$), is about half of the channel length. The thermal entrance behavior generates about a 1 K-difference at the exit compared to the non-thermal entrance case. However, for low Reynolds number flows, $Re < 1$, like those investigated by Pfhaler et al. (1991), the thermal entrance behavior can be neglected. The experimental data of Pfhaler et al. (1991) for iso-propanol flow in trapezoidal channels was compared with theoretical results obtained from a one-dimensional analysis. Figure 3.14 shows the calculated temperature rise in the channels for various Reynolds numbers, which cover the experimental Reynolds number range. The actual trapezoidal channels ($D_h \approx 16, 30$ and $40 \mu m$) were simulated as rectangular conduits with the same hydraulic diameters and the same aspect ratios (i.e., average width/depth). Figure 3.15 depicts comparisons between the theoretical results and the experimental data, where the latter were not interpreted in light of the viscous dissipation effects. In small and narrow channels, the dimensionless viscosity parameter, $C^* = \frac{\mu_{exit}}{\mu_{inlet}}$, decreases rapidly as the Reynolds number increases even in the very low Reynolds number range (i.e., $Re \ll 1$). Noticing that the graph has a logarithmic scale as the x-axis, a small error in evaluating the Reynolds number can induce a large shift in experimental data. Indeed, Pfhaler et al. (1991) observed large error bounds for the C^* -data in the smallest channels which may also imply (unreported) errors with respect to the observed Reynolds numbers. Figure 3.15 indicates that the simulations reproduce the experimental data trend except for the case of the $47.5 \times 10 \mu m$ channel, for which C^* appears to be independent of the Reynolds number. The dotted-line graphs represent the average effect of viscous dissipation on C^* , which were obtained using half the temperature

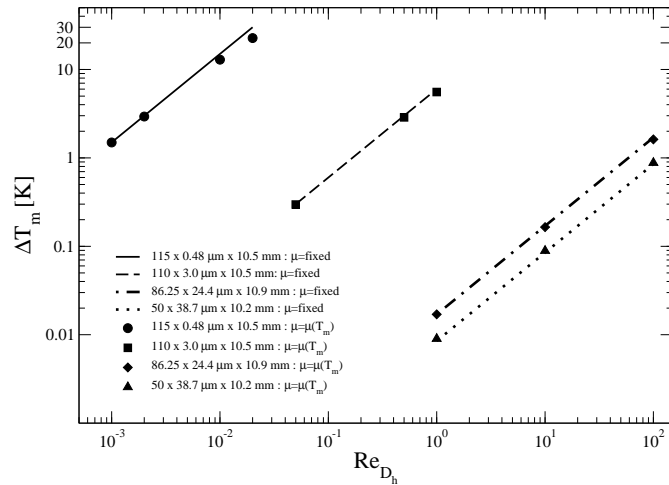


Figure 3.14: Comparison of temperature rises in rectangular channels (Pfhaler et al., 1991). Note : the experimental trapezoidal channels of hydraulic diameter 30 and 40 μm were modeled as rectangular channels of the same hydraulic diameters and the same aspect ratio

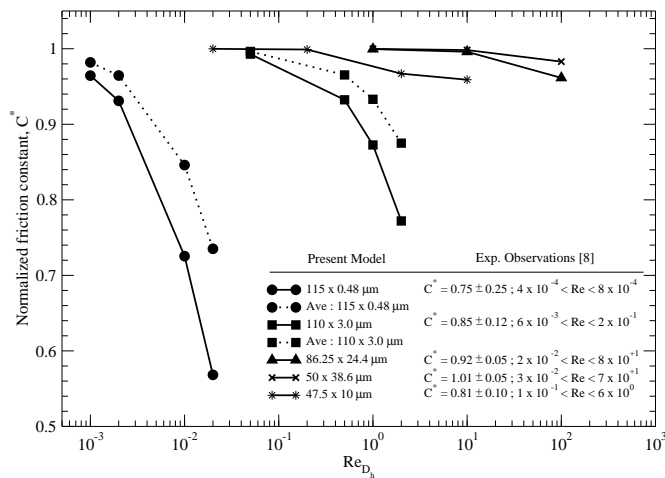


Figure 3.15: Comparison between experimental data (Pfhaler et al., 1991) and computational results

rises in the channels.

3.4.5 Results and Discussion

Viscous dissipation, influencing the fluid temperature and ultimately the friction factor in micro-conduits, was investigated for a simplified case, geometric effects, flow regime effects, and fluid property effects. The impact of viscous dissipation for a basic convection heat transfer case is also discussed.

One-dimensional case Revisiting Fig. 3.13, the results obtained from one-dimensional and three-dimensional analyses are compared. The slopes are identical for both cases after the flow is fully developed. The difference between the 1-D approximation and the 3-D analysis is the entrance effect. The axial temperature gradient near the inlet of the conduit is higher than that of the exit. Hence, the simple and robust one-dimensional analysis can be used to investigate thermally fully-developed and low-Reynolds number cases where entrance effects are negligible.

Geometric effects

Conduit size and thermal boundary effects. Figure 3.16 shows the effect of tube size on the fluid temperature changes between inlet and exit of the channels. The temperature rise is a strong function of pipe size. It is more significant for the adiabatic wall case. In the $20\ \mu\text{m}$ channel, the temperature rises by 20 K, resulting in a reduction of the dynamic viscosity by 33 %. Assuming the Reynolds number at the inlet to be 2000, it increases to 2985 at the exit. This implies that the effect of the temperature change due to viscous dissipation should be taken into account for micro-channels. For the constant-wall-temperature case, the fluid temperature rises by 4.5 K which reduces the dynamic viscosity of the fluid by 9 % in the $20\ \mu\text{m}$ channel.

Aspect ratio effect. Figure 3.17 shows the effect of channel aspect ratio on the temperature change in a channel of $D_h = 6\ \mu\text{m}$, which corresponds to the $110 \times 3.0\ \mu\text{m}$ channel case of Pfahler et al. (1991). As the aspect ratio deviates from unity,

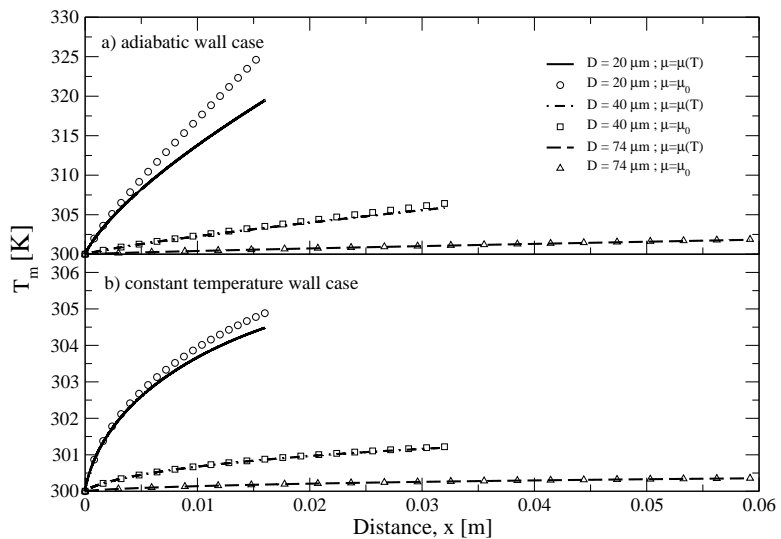


Figure 3.16: Tube size effect on temperature change, i.e., viscous dissipation (water, $Re=2,000$): a) adiabatic wall case; b) constant wall temperature case

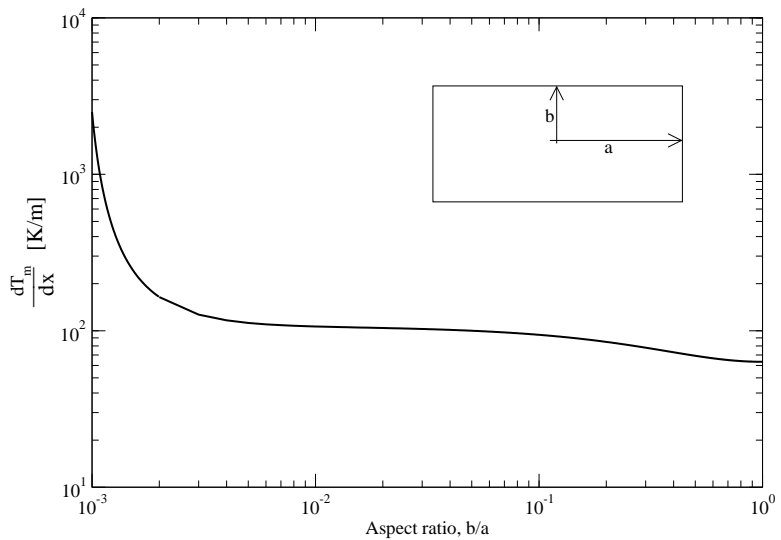


Figure 3.17: Effect of channel aspect ratio on temperature change due to viscous dissipation for iso-propanol flows in channels of $D_h = 6 \mu\text{m}$ with $Re=0.2$

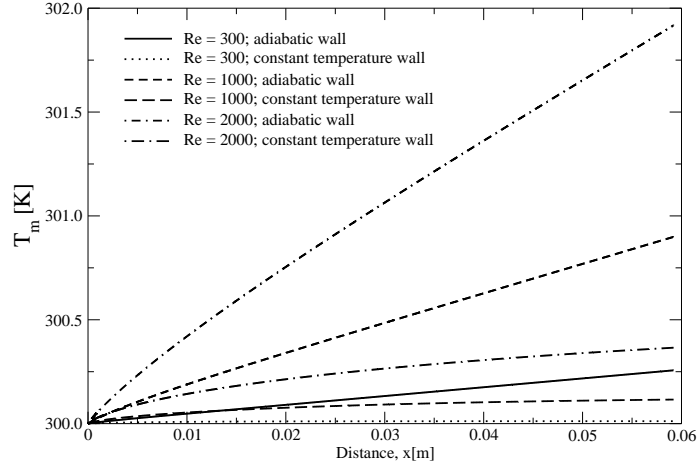


Figure 3.18: Reynolds number effect on mean temperature rise (water, $D_h=74 \mu m$)

the effect of viscous dissipation increases. In rectangular channels, viscous dissipation increases the fluid temperature even for low Reynolds numbers (i.e., $Re_{D_h} \approx 0.2$).

Reynolds number effect Investigating Eq. (3.35), the viscous dissipation term is proportional to the square of the Reynolds number. The effect of the Reynolds number on the temperature rise is shown in Fig. 3.18. The Reynolds number effect on viscous dissipation is stronger for the constant wall temperature case.

Using the property data of water at 300 K and assuming the $(T_m - T_w)$ -effect to be $\mathcal{O}(1)$, the relative magnitude of each coefficient in Eq. (3.35) has been calculated for $Re=20, 200, 2000$ (see Table 3.6). For higher Reynolds numbers, the relative magnitude of the dissipation term increases drastically with a decrease in channel size.

Varying viscosity effect The temperature effect on viscous dissipation was observed by investigating the last term in Eq. (3.35). Expanding the Reynolds number using the definition, $Re_D = \frac{\rho U_0 2R}{\mu}$, the last term is proportional to $\frac{\mu U_0^2}{R^2}$, where the dynamic

Table 3.6: Magnitude comparisons between convective, diffusion and dissipation terms in tubes

R [m]	Re=20		Re=200		Re=2000	
	$\frac{CONV^*}{DISS}$	$\frac{DIFF}{DISS}$	$\frac{CONV}{DISS}$	$\frac{DIFF}{DISS}$	$\frac{CONV}{DISS}$	$\frac{DIFF}{DISS}$
10^{-3}	$3.45 \times 10^{+4}$	$5.81 \times 10^{+5}$	$3.45 \times 10^{+3}$	$5.81 \times 10^{+3}$	$3.45 \times 10^{+2}$	$5.81 \times 10^{+1}$
10^{-4}	$3.45 \times 10^{+2}$	$5.81 \times 10^{+3}$	$3.45 \times 10^{+1}$	$5.81 \times 10^{+1}$	$3.45 \times 10^{+0}$	5.81×10^{-1}
10^{-5}	$3.45 \times 10^{+0}$	$5.81 \times 10^{+1}$	3.45×10^{-1}	5.81×10^{-1}	3.45×10^{-2}	5.81×10^{-3}
10^{-6}	3.45×10^{-2}	5.81×10^{-1}	3.45×10^{-3}	5.81×10^{-3}	3.45×10^{-4}	5.81×10^{-5}

* $CONV \triangleq$ convection term; $DIFF \triangleq$ diffusion term; $DISS \triangleq$ dissipation term

viscosity of water changes with temperature, according to White (1999), as:

$$\ln \left(\frac{\mu [kg/(m \cdot sec)]}{1.788E - 3} \right) \approx -1.704 - 5.306 \left(\frac{273}{T} \right) + 7.003 \left(\frac{273}{T} \right)^2. \quad (3.38)$$

For iso-propanol, a relation from Perry and Green (1984) was used for $293 < T < 333$ K:

$$\mu(T) \approx 4.266 \times 10^{-7} T^2 - 3.016 \times 10^{-4} T + 5.398 \times 10^{-2}. \quad (3.39)$$

As mentioned, the dynamic viscosity of water reduces by about 20 % for a temperature increase of 10 K, which implies that the viscous dissipation effect decreases downstream of the channel. With reference to Fig. 3.16, curves depicted with symbols represent mean fluid temperature changes under the assumption of constant viscosity, i.e., μ is evaluated at $\mu(T_0)$, while the line curves are the fluid temperatures taking viscosity changes into account, i.e., $\mu = \mu(T)$. Clearly, the variable viscosity effect is strongest for the smallest microtube subject to the adiabatic wall condition. Numerically, with respect to the inlet temperature of 300 K, the exit temperature decreased by 24 % in the 20 μm , 9 % in the 40 μm , and 3 % in the 74 μm tube (Fig. 3.16a). The temperature changes are 8 % in the 20 μm , 2 % in the 40 μm , and 0.8 % in the 74 μm tube for the constant temperature wall case (Fig. 3.16b).

Fluid properties effect In order to investigate the effect of viscous dissipation on the temperature rise in a tube, the temperature distributions in a hydraulically fully-

developed flow field was simulated for water, methanol and iso-propanol (see Table 3.5). Revisiting Fig. 3.13, the effect of working fluid, and hence implicitly the Eckert number ($Ec = Br/Pr$), on the axial temperature profile can be seen. Because the Eckert number is inversely proportional to the specific heat capacity of the working fluid, the mean temperatures of methanol and iso-propanol increase more, due to viscous dissipation, than the water temperature. For example, when comparing methanol and iso-propanol for the same Eckert number, the temperature rise for iso-propanol would be higher because of its higher dynamic viscosity and lower heat capacity; as a result, the average velocity would be higher for a given Reynolds number.

Effect on heat transfer It has been shown that significant temperature increases may occur due to viscous dissipation even for a fluid with high viscosity and low heat capacity, subjected to very low Reynolds number flow. For example, the smallest micro-channel of Pfahler et al. (1991), when assuming the inlet coolant temperature to be 20 °C, the exit temperature was $T_{exit} \approx 50$ °C. It is evident, from Eq. (3.31), that a heated boundary can be regarded as a source term as viscous dissipation term works, as a heat source inside the domain. Adopting the 74 μm square channel of Judy et al. (2002), the strengths of the source terms due to viscous dissipation and a thermal boundary condition are compared (Fig. 3.19). The viscous dissipation source term increases with the Reynolds number, while the heat transfer source term is kept constant. The fraction of viscous dissipation decreases with the heat transfer rate. In a smaller channel, the heat transfer source term will decrease linearly with channel width, while viscous dissipation will increase inversely proportional to the quadruple of the channel width size. Hence, the fraction of the heat dissipation source term increases rapidly.

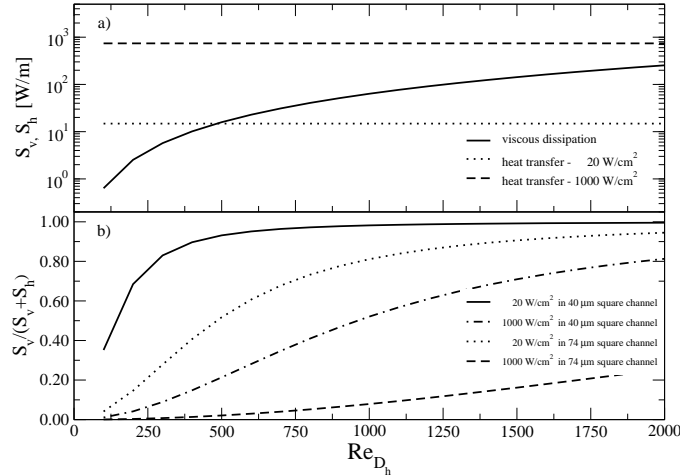


Figure 3.19: Comparison of heat source term impact due to viscous dissipation, S_v , and thermal boundary, S_h , for $100 \leq Re \leq 2000$: a) in a $74 \mu m$ square channel; and b) Fractions of source terms in $40 \mu m$ and $74 \mu m$ square channels

3.4.6 Summary

The following conclusions can be drawn from this validated computer simulation study:

- By comparing the magnitude of each term in the governing heat transfer equation, the viscous dissipation effect on the friction factor was found to increase as the system size decreases. Specifically, for water flow in a tube with $D < 50 \mu m$, viscous dissipation becomes significant and hence should be taken into consideration for all experimental and computational analyses.
- Channel size, the Reynolds number and the Brinkman number (or the Eckert number and the Prandtl number) are the key factors which determine the impact of viscous dissipation. Viscous dissipation effects may be very important for fluids with low specific heat capacities and high viscosities, even in relatively low Reynolds number

flows.

- The effect of viscosity change, caused by variations in fluid temperature, on viscous dissipation was found to be measurable for flows in a long channel with a small hydraulic diameter. For liquids, the viscous dissipation effect decreases as the fluid temperature increases.
- The aspect ratio of a channel, i.e., height vs. width, plays an important role in viscous dissipation. Specifically, as the aspect ratio deviates from unity, the viscous dissipation effect increases.
- Viscous dissipation increases rapidly with a decrease in channel size and hence should be considered along with imposed boundary heat sources.
- Ignoring the viscous dissipation effect could ultimately affect friction factor measurements for flows in micro-conduits.

3.5 Entrance and other Microchannel Effects

3.5.1 Entrance effect

The other microchannel effects influencing the friction factor and ultimately the liquid flow behavior analyzed and discussed include: channel entrance, fluid power-law, wall slip, and entrance geometry effects. Starting with the friction factor in macrochannels, Fig. 3.20 shows a comparison between Eq. (3.4) and computer simulation results, i.e., a solution to the reduced momentum equation, i.e., Eq. (3.40):

$$(\vec{u}^* \cdot \nabla^*) \vec{u}^* = -\nabla p^* + \frac{1}{Re_{D_h}} \nabla^{*2} \vec{u}^* \quad (3.40)$$

where $p^* = \frac{p}{\rho U_0^2}$, $\vec{u}^* = \frac{\vec{u}}{U_0}$, $x^* = \frac{x}{D_h}$, $y^* = \frac{y}{D_h}$, $Re_{D_h} = \frac{\rho U_0 D_h}{\mu}$, and U_0 is the inlet or average flow velocity. The boundary conditions are uniform velocity at the inlet and constant pressure at the channel exit.

As the height-to-width ratio of a channel changes from a square (1.0) to a parallel plate (0.0), the friction factor increases for any given Reynolds number (Fig. 3.21). This implies that square channels have the lowest friction factor among the rectangular channel family for a given Reynolds number. The reason is that the maximum centerline velocity decreases with decreasing height-to-width ratio and hence the pressure gradient needed to accelerate the inviscid core is less.

3.5.2 Non-Newtonian fluid effects

In order to evaluate a non-Newtonian fluid effect on the friction factor, Eq. (3.40) is solved where with under the assumption of steady, laminar, incompressible flow. The effect depends highly on the exponent n of the power law where $n = 1$ implies Newtonian fluid. By varying it within reasonable bounds, i.e., $0.9 \leq n \leq 1.1$, the friction factor decreases by 50 [%] and increases by around 100 [%] as shown in Fig. 3.22. Relatively low-Reynolds-number

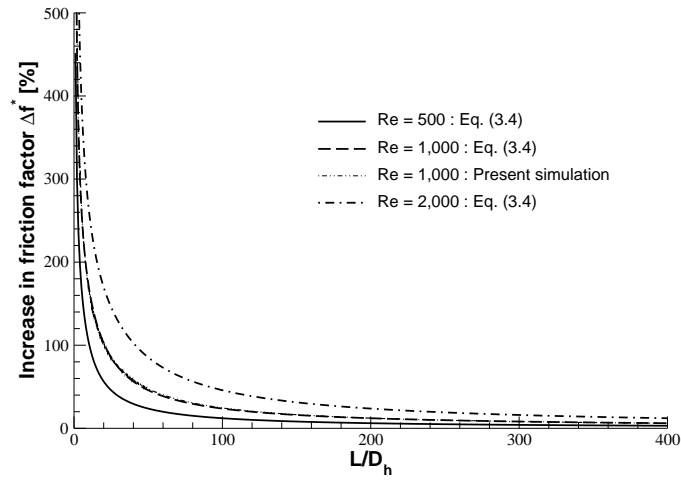


Figure 3.20: Comparison of friction factor deviations in a channel entrance ($h/w=1.0$) based on experimental observations (Eq. (3.4)) and computer simulation results for various Reynolds numbers

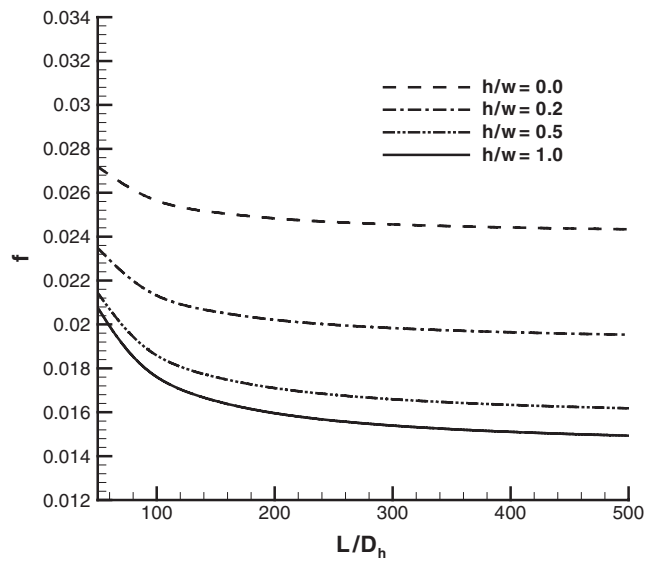


Figure 3.21: Effect of height-to-width ratio on apparent friction factor for $Re=1,000$

flows are more affected than high-Reynolds-number flows. Despite the dramatic impact of n , ordinary liquids in microchannels do not turn suddenly into non-Newtonian fluids. Sharp (2001) brought the possibility of the effect of high shear rate on the change of viscosity into question, saying that high shear rates, as high as $10,000 [s^{-1}]$, do not cause water to behave like a non-Newtonian fluid. The flow may only show non-Newtonian behavior when there exist long chain polymers or when fine particle suspension are being considered. However, if liquids obey the power law, it greatly affects the friction factor.

3.5.3 Wall slip effects

From the numerical experiments for a $200 \times 200 [\mu m]$ square channel and using Maxwell equation, $u_{slip} = l \left(\frac{du}{dy} \right)_{y=0}$, where $l = 3 [\text{Å}]$ for water, the maximum possible slip velocity is found to be about $14 [\mu m/sec]$ where the average velocity is $105 [\mu m/sec]$, i.e., it is only $0.0014 [\%]$ of the average velocity. Thus, in general, the effect of wall slip on the friction factor is negligible for liquid flows in microchannels. However, as Tyrrell and Attart (2001), Tretheway and Mainhart (2002) and Tretheway and Mainhart (2004) reported, there could exist an air gap between the wall and bulk fluid in channels of hydrophobic wall, resulting in measurable velocity slip.

3.5.4 Channel entry geometry effect

In general, when designing flow systems, operation in the transitional laminar-to-turbulent regions should be avoided because of highly non-linear flow instabilities and the difficulty of predicting flow characteristics. In the 1990s (see Table 3.1), different researchers observed an increase in the friction factor for microchannels, and tried to explain the phenomenon by virtue of early laminar-to-turbulent flow transition (c.f., Peng et al. (1994), Peng and Peterson (1996); Mala and Li (1999); Xu et al. (1999); Qu et al. (2000). Sharp (2001) performed bulk-flow resistance experiments and micro-PIV measurements to investigate the validity of this early laminar-to-turbulent transition hypothesis. She did not detect

any deviation from the conventional theory and concluded that the laminar-to-turbulent transition theory is invalid. However, the graphs in her dissertation, showing centerline velocities for various Reynolds numbers and microtube diameters, seem to indicate turbulence effects for Reynolds numbers around 1,800. On the other hand, Judy et al. (2002) measured the friction factor in microtubes and rectangular channels, and confirmed that the friction factor can be predicted using laminar theory as long as $Re_{D_h} \leq 2,300$. In contrast, Xu et al. (2001) developed a model to predict friction factors for turbulent flows in microtubes using a one-equation model, which improved the accuracy for low-Reynolds number flows (Wilcox, 1998). They modified a constant, which controls the mixing length increase with distance from the wall, to fit their experimental data. They claimed that microtubes smaller than 130 [μm] show turbulent flow characteristics different from macrochannels. By adjusting a constant in their turbulence model equation, they obtained turbulent velocity profiles for microchannels smaller than 130 [μm]. However, their results show a somewhat strange behavior in terms of the turbulence kinetic energy (TKE) distribution in radial direction (see their Figs. 9-14). Zhang and Kleinstreuer (2003) performed a comparison study to select a low-Reynolds number (LRN) turbulence model suitable for the human oral airways, which are composed of unique area constrictions and expansions. For medium inhalation rates ($Q \approx 30$ [l/min]), they observed a sudden TKE increase after the major constriction. They concluded that a modified LRN $k - \omega$ model (Wilcox, 1998) is suitable for simulating laminar-transitional-turbulent flows in constricted tubes, such as the human upper airways, stenosed blood vessels, obstructed pipes, or engine inlet ducts (c.f., Kleinstreuer & Zhang 2003). Similar non-uniform geometries can be found in many microchannels which, for example, have sumps or 90 bends before their actual inlets. Such sudden contractions and bends cause the flow to have strong radial velocity components, which may increase the TKE and induce local instabilities to elongate the entrance length at relatively low Reynolds numbers. Considering a typical step contraction as given in Fig. 3.23, it is assumed that the incompressible Newtonian fluid flow is steady and axi-symmetric values for a uniform velocity, u_{in} , TKE, k , and pseudo-vorticity, ω , were prescribed at the inlet. Specially, at

the inlet (AEA Technology, 2001; Zhang and Kleinstreuer, 2003)

$$k = 1.5(I \times u_{in})^2 \quad (3.41a)$$

and

$$\omega = \frac{k^{0.5}}{0.3D} \quad (3.41b)$$

where u_{in} is the mean velocity ($Re_D = 1000$), I is the turbulence intensity, usually taken as 0.037, and D is the diameter of the inlet tube. The length of the intake part was determined for the flow to be fully developed.

Figure 3.24 shows cross-sectional views of various flow characteristics at different locations. The axial velocity profile (Fig. 3.24(a)) is laminar and fully-developed before the sudden contraction, and changes dramatically in the smaller microtube where it eventually fully develops to a turbulent velocity profile. The associated radial velocity component (Fig. 3.24(b)) is zero before the contraction and becomes significant, especially near the wall at and after the contraction. The turbulence kinetic energy, which is set to be uniform at the inlet, is damped out and hence negligible before the contraction (Fig. 3.24(c)). It has a peak near the contraction and evolves into a near uniform profile with a maximum between the flow center and the wall. The pressure gradient increases greatly after the contraction (Fig. 3.24(d)). The recirculating zone near the contraction causes a bump just after the contraction. The entrance length, starting at the contraction, is much shorter than for the laminar flow case.

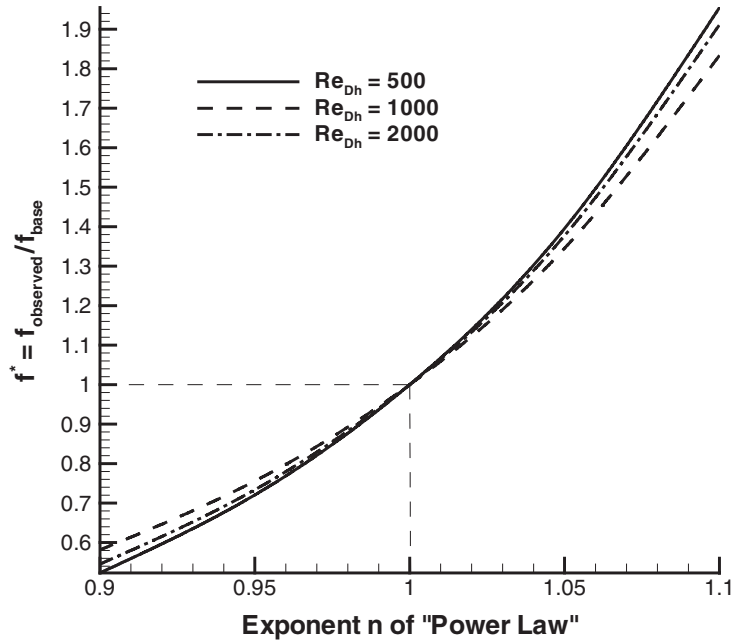


Figure 3.22: Effect of non-Newtonian fluid behavior on the friction factor

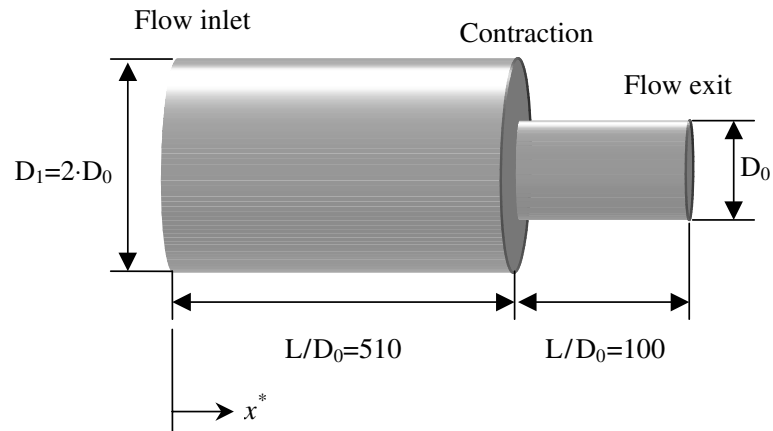


Figure 3.23: Schematic diagram of the geometry used in computing the effect of sudden contraction on laminar-to-turbulent flow transition.

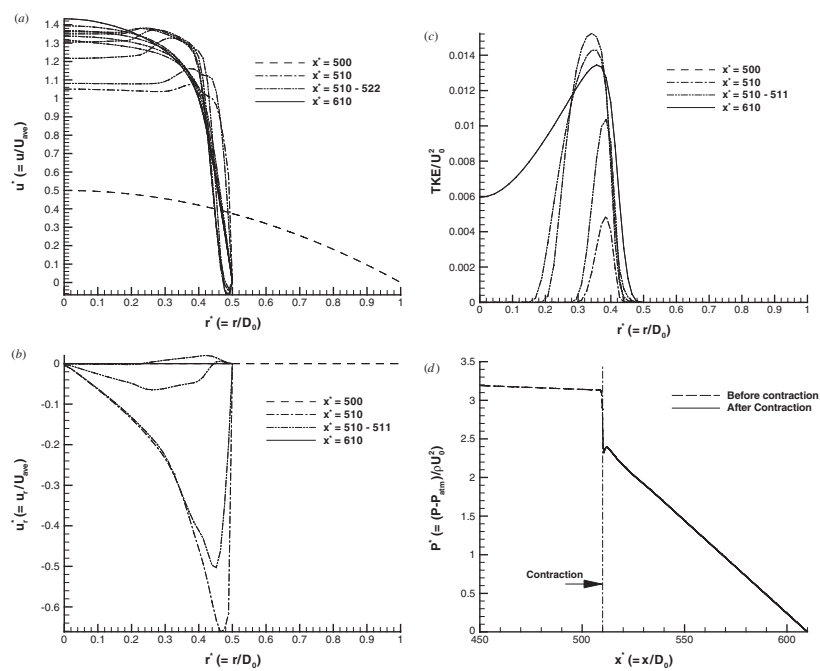


Figure 3.24: Evolution of velocity components, turbulent kinetic energy, apparent viscosity and pressure in a microchannel (50 % contraction, $Re = 2000$): (a) evolution of axial velocity profile, (b) evolution of radial velocity profile, (c) evolution of turbulent kinetic energy and (d) pressure profile in axial direction.

3.5.5 Summary

- The *entrance effect* should be taken into consideration for microfluidic systems; it is a function of channel length, aspect ratio, and the Reynolds number. It becomes more important for the case of flow in short channels with high aspect ratios at high Reynolds number conditions.
- *Non-Newtonian fluid effects* are expected to be important for polymeric liquids and particle suspension flows.
- *Wall slip effects* are negligible for liquid flows in micro-conduits.
- *Channel entry geometry effects* become very important for Reynolds numbers above 1,000, mainly due to geometric non-uniformities. For example, the turbulence kinetic energy has a maximum right after a typical contraction and induces transition to turbulent flow. The peak value is a function of the geometry of the contraction (especially, the diameter ratio).

3.6 Nanofluids Properties Model

3.6.1 Higher thermal conductivities due to Brownian motion effect.

In a quiescent suspension, nanoparticles move randomly and thereby carry relatively large volumes of surrounding liquid with them. This micro-scale interaction may occur between hot and cold regions, resulting in a lower local temperature gradient for a given heat flux compared with the pure liquid case. Thus, as a result of Brownian motion, the effective thermal conductivity, k_{eff} , increases, which results in a lower temperature gradient for a given heat flux. Figures 3.25 and 3.26) show the experimental data and the non-dimensionalized effective thermal conductivity respectively. Furthermore, at elevated suspension temperatures, the Brownian motion effect increases and higher k_{eff} -values arise (see Figs. 3.26 and 3.31) as was experimentally observed by Patel et al. (2003) and Das et al. (2003). As stated in Sect. 1.3.1, Koblinski et al. (2002) argued that the thermal diffusion time scale is much smaller than Brownian diffusion time scale by an order of 10^2 for 10 [nm] particle suspensions. However, considering the effective complex particle-plus-liquid volume to be $\beta 37.5^2 \times 75 \times V_d$ and taking a typical value of β as 0.01 (see Fig. 3.27), the two time scales have about the same order of magnitude, and hence Brownian motion becomes a very important mechanism for augmented heat transfer.

Additional confirmation of the importance of the Brownian effect can be deduced when different carrier fluids and nano-material have been used. For example, Lee et al. (1999) found thermal conductivity improvements in ethylene glycol based nanofluids when compared to water based ones. Xie et al. (2002) observed that the thermal conductivity augmentation ratio decreases with an increase in base liquid thermal conductivity. Xie et al. (2003) compared the effective thermal conductivity of distilled-water(DW)-, ethylene-glycol(EG)-, and decene(DE)-based carbon nanotube-suspensions and observed that:

$$k_{DW} < k_{EG} < k_{DE} \quad (3.42)$$

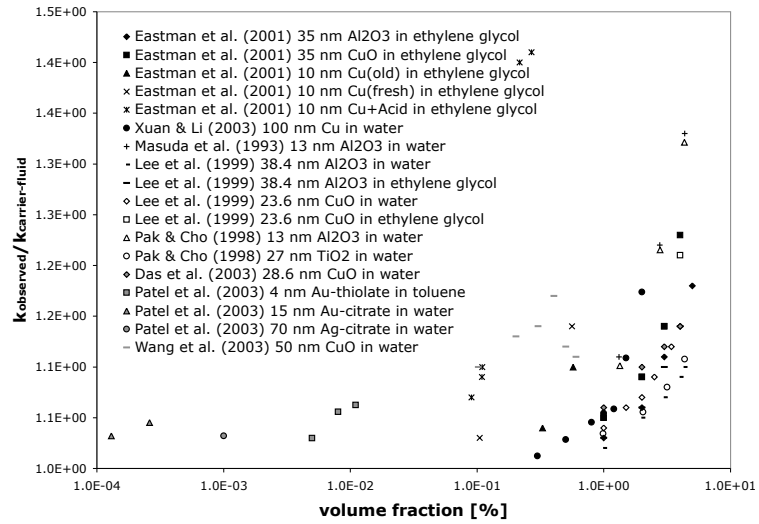


Figure 3.25: Experimental data sets

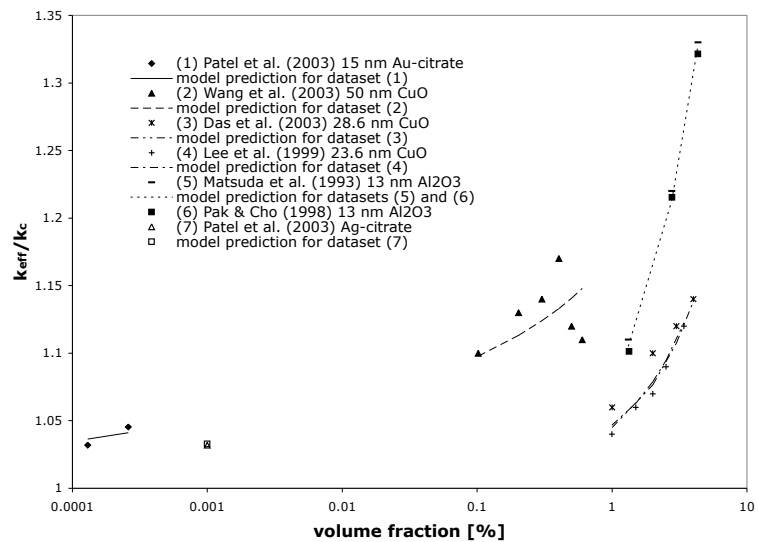


Figure 3.26: Comparison of model predictions with experimental data sets

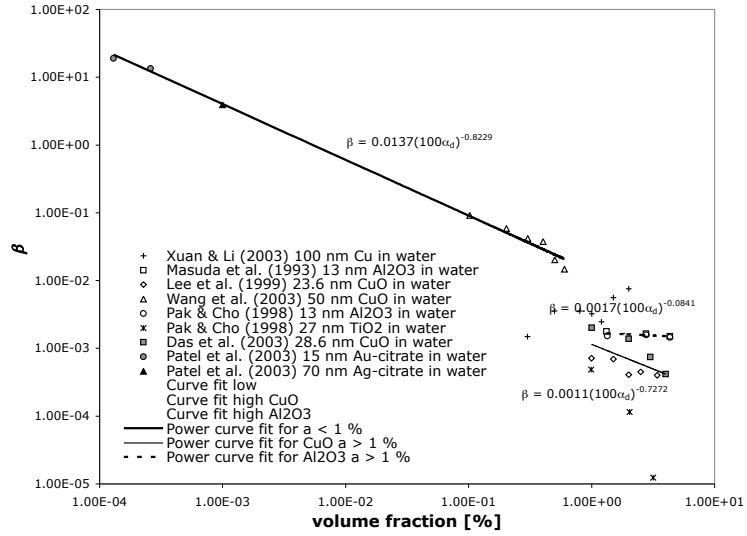


Figure 3.27: Comparison of β -functions obtained from experimental data

Lee et al. (1999) also noticed that the ethylene glycol based nanofluids show higher thermal conductivities than the water based ones.

The thermal conductivity due to Brownian motion is not explicitly related to the fluid thermal conductivity, while the static part of the effective thermal conductivity is strongly dependent on it (see Eq. (4.72)). The thermal conductivity of the three liquids are 0.611, 0.252, and 0.145 [W/mK], respectively. Moreover, their thermal capacities ($\rho_l c_l$), to which the thermal conductivities due to Brownian motion are proportional, are 4153, 2674, and 1700 [kJ/m³K], respectively. Using the fact that

$$\frac{k_{Brownian}}{k_{static}} \sim \frac{\rho_l c_l}{k_c} \tag{3.43}$$

the ratio among the three suspensions is

$$\left(\frac{k_{Brownian}}{k_{static}}\right)_{DW} : \left(\frac{k_{Brownian}}{k_{static}}\right)_{EG} : \left(\frac{k_{Brownian}}{k_{static}}\right)_{DE} = 0.58 : 0.91 : 1 \tag{3.44}$$

which explains the observation that the carrier fluid has an influence and hence merits the inclusion of the of Brownian motion effect.

3.6.2 Interparticle interactions at high concentrations ($\alpha_d > 1 \%$)

As mentioned in the Theory section, the intermolecular interaction becomes more important for suspensions with high particle concentrations. As shown in Fig. 3.27, the β function was independent of the particle material in low concentration region, while it showed strong dependence in high concentration region. The interparticle potentials for suspensions of nanoparticles of the interparticle distance $d > 10$ [nm], the non-retarded part of the potential is most important (Israelachvili, 1992). The induced liquid motion controls the low concentration region, where the interparticle interaction force suffers from the retardation, while the interparticle interaction force governs the high concentration region, where the interparticle distance is so short that the interparticle force is very strong. Table 2.2 shows the Hamaker constants of the non-retarded term(cf. Eq. (4.75)), were $A_0 = \frac{3}{4}\kappa T \left(\frac{\epsilon_1 - \epsilon_3}{\epsilon_1 + \epsilon_3} \right)^2$. Clearly, the β -function when $\alpha_d > 1 \%$ (see Fig. 3.27) for the four particle materials, i.e., *Cu*, *Al₂O₃*, *CuO*, and *TiO₂*, encapsulates the same relative magnitude trend as A_0 (see Table 2.2). This supports our explanation that the effective thermal conductivity for $\alpha_d > 1 \%$ is mainly affected by interparticle interactions. As shown with Eq. (4.75), interparticle interaction becomes more important when the difference in electric dipole constants between particle and carrier fluid increases. It also depends on the volume fraction α_d and the particle size (cf. Eq. (4.74)).

Compared to the potential between (gas) molecules which is inversely proportional to d^6 , the cluster potential impacts long range. Figure 3.28 shows the effect of the exponent in the potential on the impact distance; lower exponent cases show longer impact distance. Especially, the attractive part is inversely proportional to the surface distance itself. Israelachvili (1992) reported that large distance contributions to the interaction disappear only for values of the exponent in the potential greater than 3. But for the exponent smaller than 3, the contribution from more distant molecules will dominate over that of

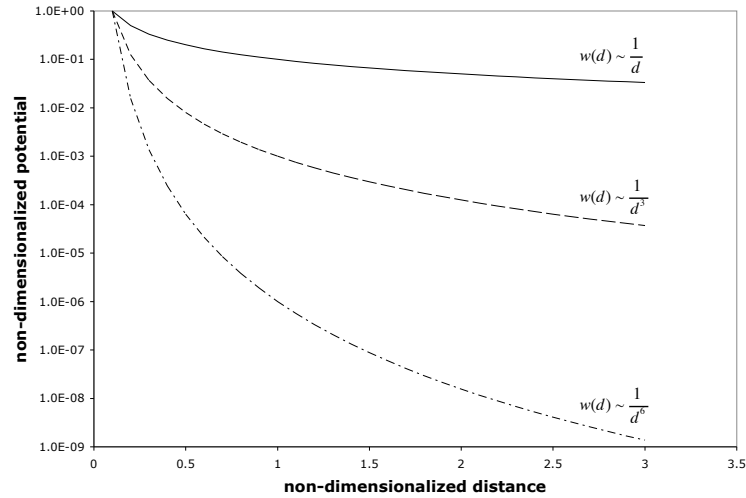


Figure 3.28: Comparison of effect of the exponent in the intermolecular potential on impact distance

near-by molecules. The measured gas thermal conductivities show stronger temperature dependence ($k \sim T$) compared to the predicted values using kinetic theory. More rigorous treatment of kinetic theory including the effect of intermolecular potential energies can correct the discrepancies for gases (Deen, 1998). Stronger temperature dependence compared to gases is expected in liquids due to the far-reaching potential.

3.6.3 Examples of heat conduction in nanofluids.

The model to estimate the nanoparticle Brownian motion effect on the effective thermal conductivity was derived in Sect. 2.3.1. Figure 3.29 shows examples of effective thermal conductivity for water-base CuO nanofluids at constant fluid temperature. The effective thermal conductivity increases with the particle concentration for low particle concentration region ($\alpha_d < 1\%$), while it decreases near $\alpha_d = 1\%$ and it increases again in high particle concentration region ($\alpha_d > 1\%$). This means there is a transition region between low- and high-concentration regions. The β values of the experimental data set from Wang et al. (2003) in Fig. 3.27 shows the same trend. The β drops suddenly near $\alpha_d = 1\%$.

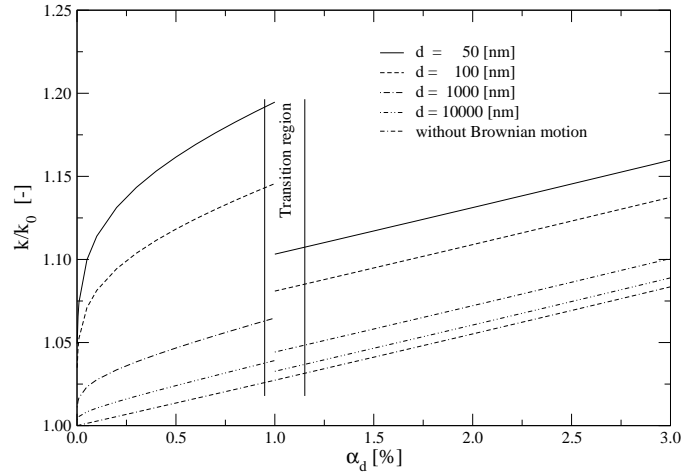


Figure 3.29: The particle size effect on the effective thermal conductivity at $T = 300$ [K]; $f(T, \alpha_d) \equiv 1$

Figure 3.29 also informs that the discontinuity of the effective thermal conductivity between low- and high-concentration regions decreases with particle size increase. Therefore, the new model can be applied for all suspensions of any size of particles. Since the $k_{Brownian}$ term decreases with particle size, it reduces to conventional relations for macro-scale particle suspensions.

Figure 3.30 shows the effect of particle type on effective thermal conductivity. Although no experimental data is available for low concentration region, it was assumed that Al_2O_3 -nanofluid behaves as other nanofluids, since the interparticle potential suffers from the retardation effect and its effect is negligible in low concentration region. Compared to CuO -nanofluids, Al_2O_3 -nanofluids showed higher effective thermal conductivity in high concentration region due to higher value of β -function which is related to the greater interparticle interaction potential. The transition is expected to happen at lower concentration for Al_2O_3 nanofluids than for CuO nanofluids due to higher particle interaction.

Wen and Ding (2004) measured effective thermal conductivity of water-base Al_2O_3 nanoflu-

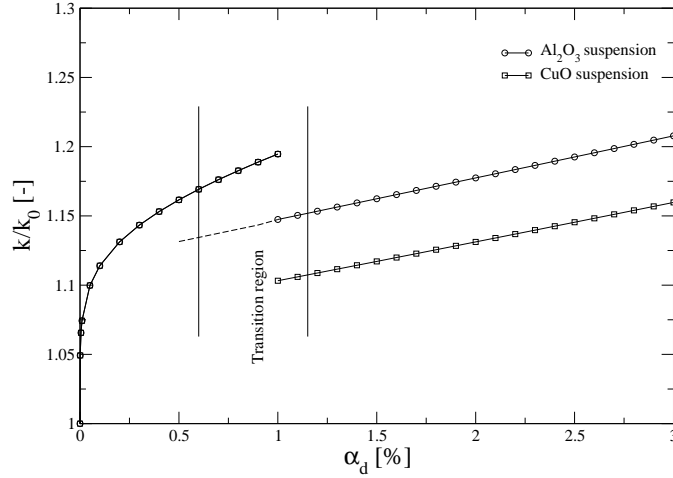


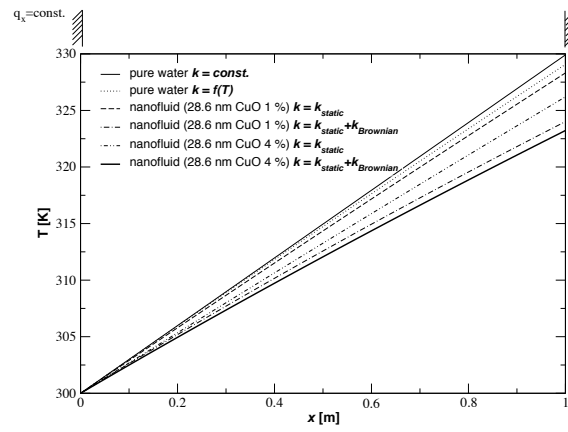
Figure 3.30: The particle type effect on the effective thermal conductivity at $T = 300$ [K]; $f(T, \alpha_d) \equiv 1$

ids for the particle concentration between 0.2 and 1.7 [%] at the constant fluid temperature of 295 [K]. Their data showed relatively lower than the new model predicts. This might be a result due to the effect of dispersant (sodium dodecylbenzene sulfonate) they added to stabilize the nanoparticles since even small amount of dispersant could alter the interparticle potential measurably. However, they did not observe the decrease of effective thermal conductivity which was observed for water-base *CuO* nanofluids by Wang et al. (2003). As explained before, Al_2O_3 nanofluids might have the transition region at a relatively lower concentration than *CuO* nanofluid has, and the effective thermal conductivity change across the transition region is much lower for Al_2O_3 nanofluids (see Fig. 3.30), such that they might not observe it. The axial conduction heat flux component can be expressed as

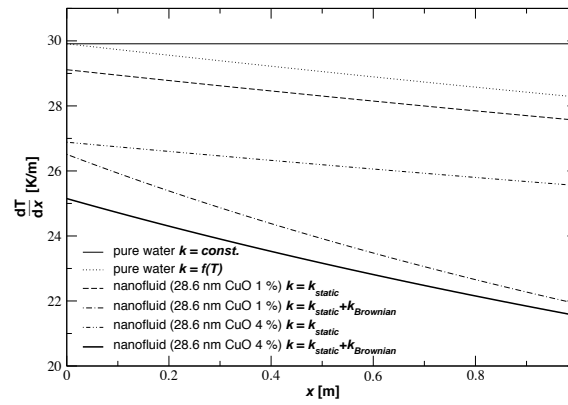
$$q_x = -k_{eff} \frac{dT}{dx} \quad (3.45)$$

A sample problem is solved considering steady-state, no internal heat generation, and a constant heat flux. Figure 3.31 shows the profiles of temperature, temperature gradient, and effective thermal conductivity in pure water and uniform nanofluids of different particle volume fractions for a heat flux of $18 [W/m^2]$ in a 1-D system. The temperature at $x = 1 [m]$ is lower by $7 [K]$ for the 4 % nanofluid case compared to the pure water of constant thermal conductivity case. From the data in Table 2.3, the thermal conductivity due to Brownian effect is proportional to $\alpha_d^{0.2728}$ while the static part is proportional to α_d . The higher contribution of Brownian motion in the nanofluid of $\alpha_d = 1\%$ compared to that of the 4 % case, makes the temperature difference very small. Referring to the temperature gradient and thermal conductivity graphs, the difference between the two nanofluids becomes smaller at higher temperatures due to the Brownian effect. The temperature gradients, considering the temperature dependence of the thermal conductivity, show decreasing trends since the thermal conductivity increases with temperature as indicated in Eq. (4.73).

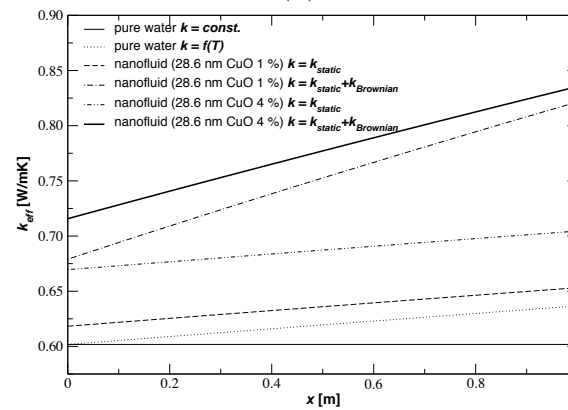
It is possible for particles to have nonuniform distributions due to the interaction between particles and wall. Particles could be denser either near a wall or the center of a conduit. Figure 3.32 shows three different particle distribution profiles with an average volume fraction of 2.5 %. The resulting profiles of temperature, temperature gradient, and the effective thermal conductivity are shown in Fig. 3.33. The temperature profiles for all cases are almost the same, while $\nabla T(x)$ and $k_{eff}(x)$ change and differ significantly. The thermal conductivity with a concave α_d -distribution is higher near $x = 0$, whereas that for the uniform distribution case is highest near $x = 1 [m]$. This is because of the impact of the particle volume fraction on the Brownian-motion part of the effective thermal conductivity (Eq. (4.71)).



(a)



(b)



(c)

Figure 3.31: Comparisons of temperature, temperature gradient, and effective thermal conductivity profiles

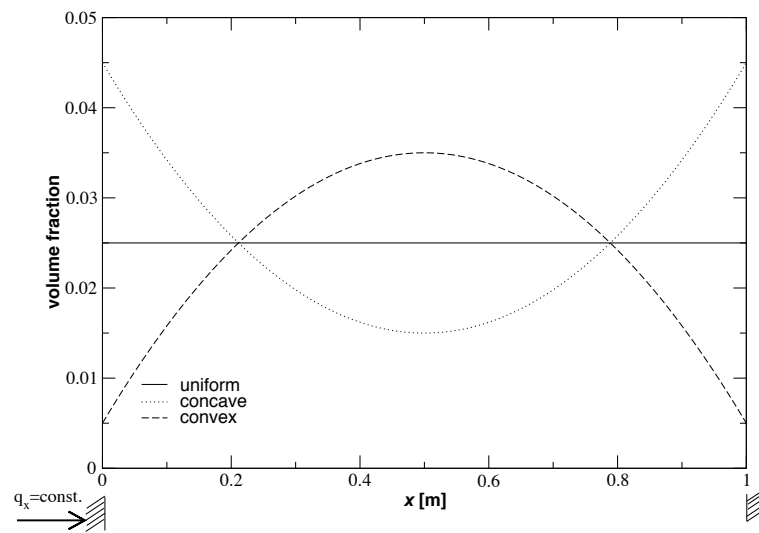
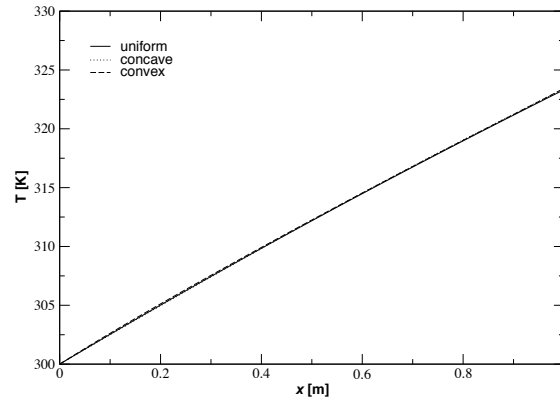
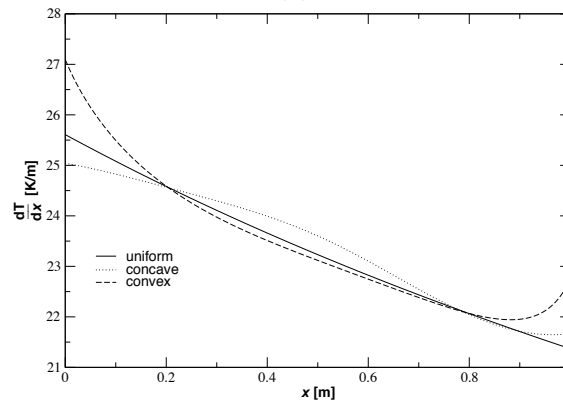


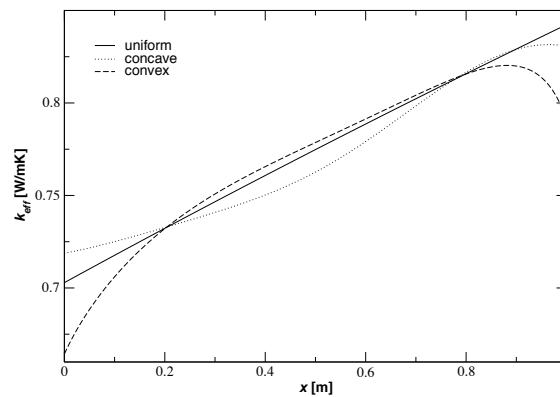
Figure 3.32: Volume fraction profiles



(a)



(b)



(c)

Figure 3.33: Effect of volume fraction change on temperature-, temperature gradient-, and effective thermal conductivity-profiles

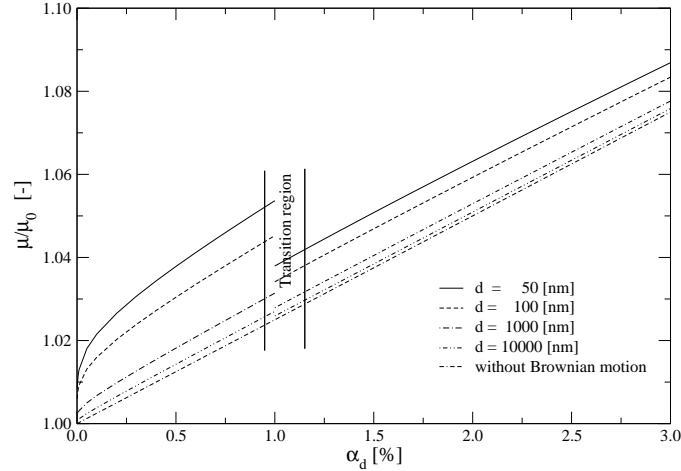


Figure 3.34: The particle size effect on the effective viscosity for water-CuO nanofluids at 300 [K]; $f(T, \alpha_d) \equiv 1$

3.6.4 Brownian motion effect on momentum transfer

The model to estimate the nanoparticle Brownian motion effect on the effective viscosity was derived in Sect. 2.3.5. Figure 3.34 shows examples of the effective dynamic viscosities for water-base *CuO* nanofluid at 300 [K]. The viscosity increases with the particle concentration α_d , and it decreases suddenly at the transition region, then it increases with the particle concentration. As explained for the effective thermal conductivity, the Brownian motion and the induced liquid motion dominates for low concentration condition ($\alpha_d < 1\%$), while the interparticle interaction forces control the particle motion for high concentration region ($\alpha_d > 1\%$). Li et al. (2002) measured the effective dynamic viscosity for water-base *CuO* ($D = 50$ [nm]) nanofluids by measuring the time elapsed for nanofluids to pass through capillary tubes under the gravitational field. They observed that the nondimensional effective viscosities $\frac{\mu}{\mu_0}$ are around 1.2 for $\alpha_d = 0.3\%$, 1.18 for $\alpha_d = 1\%$, and 1.3 for $\alpha_d = 1.7\%$, which confirms the existence of the transition region. They also observed the

effective viscosity increase with fluid temperature, which could be explained as the Brownian motion effect.

Pak and Cho (1998) reported that they observed anomalous increase of the effective dynamic viscosity. Although the new model cannot explain the phenomena in magnitude, it predicts that the interparticle interaction effects will be more significant for Al_2O_3 nanoparticle suspensions compared to TiO_2 suspensions, which will result in higher effective viscosity for Al_2O_3 suspensions.

Contrary to the report of Choi (1995), the driving force increase is not negligible, and the trend could be well understood using the new model.

3.6.5 Particle non-sphericity effect on the thermal conductivity

Taking the same procedure as for the spherical particle case, the nanotubes carry surrounding liquid with them. The effect is expected to be much more significant due to the particle's long aspect ratio and increased degree of freedom (i.e., additional angular rotation).

For example, Choi et al. (2001) used $D_c = 25$ [nm] \times $L = 50$ [μ m] nanotubes of which the hydraulic diameter is 360 [nm]. Due to its extremely high aspect ratio $L/D_c = 2000$, cylinders can be assumed as a prolate. The ratio of drag force becomes

$$\frac{F_{D,s}}{F_{D,c}} = \frac{6\pi\mu\bar{R}_C\bar{U}}{6\pi\mu R_S\bar{U}} = \frac{\bar{R}_C}{R_S} \quad (3.46)$$

where R represent the translation tensor, and \bar{R}_C/R_S is called Perrin factor which is given as (Probstein, 2003):

$$\frac{\bar{R}_C}{R_S} = \frac{(p^2 - 1)^{1/2}}{p^{1/3} \ln[p + (p^2 - 1)^{1/2}]} \quad (3.47)$$

Here, the bar over R_c represents that it is an average value of the all possible flow attack angle to the spheroid, and p is the aspect ratio. For the given case the Perrin factor is estimated to be 19. Thus, the drag force on a cylinder is about 19 times greater than that

on a sphere. Assuming that the influenced liquid mass is proportional to the drag force, the volume of the influencing zone, hence the micro-mixing effect, could be estimated. Then, Eq. (4.73) can be written for nano-cylinders as

$$k_{Brownian} \sim 0.197 \sqrt{\frac{18}{\pi}} 19 \times 37.5^2 \times 75 \alpha_d \rho_l c_l \sqrt{\frac{\kappa T}{\rho_d}} D_h^{-0.5} \quad (3.48)$$

It is evident that a cylindrical particle exerts the same effect on the thermal conductivity as a spherical particle of diameter about 1/360 times that of the given hydraulic diameter of a cylinder. For example, 25 [nm] $D \times 50$ [μm] nanotubes used by Choi et al. (2001) correspond to 1 [nm] spherical nanoparticles. Furthermore, taking the angular motion into account, the effect would be much more significant since the rotating motion enhances in mixing regardless of its direction. The schematic diagram for the effect of particle rotation on the thermal conductivity is shown in Fig. 3.35. A typical value of the Brownian rotational velocity for the given example can be calculated using Eq. (3.49). There are two modes of rotation for a cylinder; one is a rotation about a long axis and the other one is one about a short axis. Since the rotation about the short axis is more important, the energy concerning that Brownian motion is $\frac{1}{2} \kappa T$.

$$\frac{1}{2} I \omega^2 = \frac{1}{2} \kappa T \quad (3.49)$$

$$\omega = \sqrt{\frac{48 \kappa T}{\pi \rho_d D_h^3 L^2}} \quad (3.50)$$

The moment of inertia is $\frac{mL^2}{12}$ for a rod of length L . It was estimated to be about 130 rotations per second. Assuming that the mixing volume due to the motion to be the disc volume spanned by revolving a cylinder about its axis of short symmetry, the heat flux could be estimated as

$$q_{rot} \sim -3 \left(\frac{L}{2} \right)^3 D_c^{-1} \alpha_d \rho_l c_l \omega_{rot} \nabla T \quad (3.51)$$

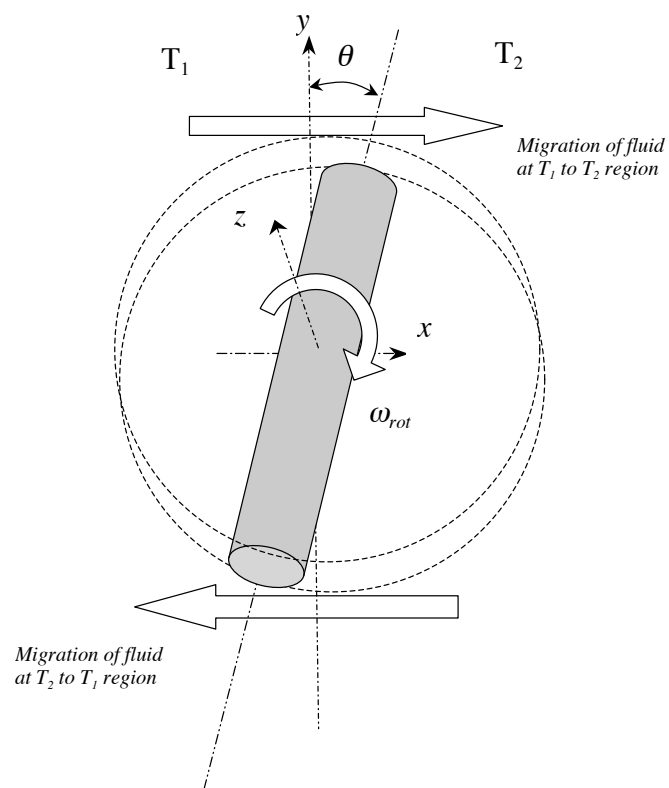


Figure 3.35: Schematic diagram to explain the effect of particle rotation

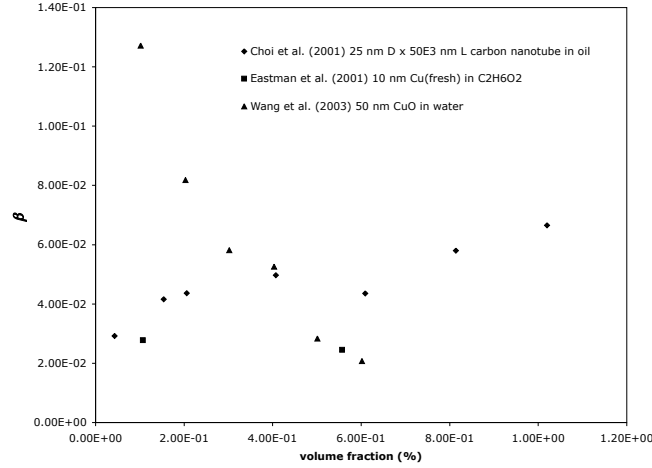


Figure 3.36: Comparison of model constants β among nanotube (Choi et al., 2001), Cu (Eastman et al., 2001), and CuO (Wang et al., 2003) suspensions

where $\omega_{rot} = \omega/2\pi$. It was assumed that the left half volume of disc travels to the right, and the other right half moves to the left per half a rotation (see Fig. 3.35). Assuming that only two directions of rotation out of three contributes to the mixing, the corresponding thermal conductivity can be estimated as

$$k_{rot} \sim 2 \left(\frac{L}{2} \right)^3 D_c^{-1} \alpha_d \rho_l c_l \omega_{rot} \quad (3.52)$$

For the given example with 1 % of nanotubes, the order of magnitude of the rotation effect was estimated to be $k_{rot}/k_{oil} \sim 10$. The result was drawn under the assumption of no interaction among particles. Considering the interaction, the magnitude should be smaller than the above result. However, the effectiveness of rotation motion could be observed.

Figure 3.36 shows comparison of model constant β among nanotube (Choi et al., 2001), Cu (Eastman et al., 2001), and CuO (Wang et al., 2003) suspensions. They have the same range of model constant β . However, β for nanotube suspension shows slight increasing trend different from other suspensions. This might be the effect of rotational mode.

However, the stability, momentum and heat transfer phenomena in nanofluids have been reported to be affected by various factors such as the pH of the suspension, the material selection of particle and base fluid, etc. According to DLVO theory, the electrostatic repulsion potential provides energy for nanoparticles to stay suspended under the influence of attractive van der Waals interaction. To include such effects, other theories concerning various phenomena such as DLVO theory for suspension stability analysis, must be considered, and much more experiment data are required to compare with.

3.6.6 Summary

A new effective thermal conductivity and effective dynamics viscosity model for nanofluids has been developed, which takes the effects of particle size, particle volume fraction and temperature dependence as well as properties of base liquid and particle phase into consideration by considering portions of surrounding liquid traveling with randomly moving nanoparticles and interparticle interaction force.

- It is found that the induced fluid motion is the main mechanism for the thermal conductivity enhancement in low concentration region ($\alpha_d < 1\%$), while the interparticle interaction force introduces the particle material dependence of the thermal conductivity in high concentration region ($\alpha_d > 1\%$).
- There are transition regions for both effective thermal conductivity and effective dynamic viscosity. The transitions are confirmed with experimental data. The discontinuities between low- and high-concentration regions decreases with the particle size increase. Therefore, the model is consistent with the conventional models for macro-scale particle suspensions.
- In the new model, the Brownian motion effect was found to become more effective at higher temperatures as observed experimentally.
- The time scales for such a complex particle-liquid body, creating micro-mixing and

local heat transfer, were found to be of about the same magnitudes, which manifests the efficient energy transport due to Brownian motion.

- The strong temperature dependence was attributed to the long impact range of the interparticle potential.
- The effect of interparticle potential is very important for dense nanofluids, i.e., $\alpha_d > 1$ %, as evident by comparing the experimentally obtained thermal conductivities with the calculated interparticle potentials. The electric dipole constant was observed to be a very important parameter influencing the interparticle potential and hence resulting in a particle-type dependence of the thermal conductivity.

To improve the versatility and accuracy of the k_{eff} model, additional experimental data sets are needed.

Chapter 4

NANOFLUID FLOW APPLICATIONS

4.1 Introduction

From the literature review, scale analysis, analytical and numerical analysis, it was found that the deviations from the conventional theory observed experimentally by other researchers (refer to Table 1.2), could be explained that they are results caused by neglecting micro-phenomena in micro-scale conduits. It was shown that the deviations could be explained with the simulations using conventional approach with added terms to explain the micro-scale phenomena. The particle Brownian motion effect is a completely new way of explaining what happens in nanofluids, which explains macro-scale observations using micro-scale description.

Micro heat-sinks and drug delivery system are selected to apply the models and information, we have. The viscous dissipation, particle Brownian motion, and surface roughness effects on heat transfer phenomena were investigated for micro heat-sink application case, and new designing parameters to be considered in designing and analyzing micro heat-sinks were provided. A new way of designing the channel configuration was developed for drug delivery system and a critical review on the current configuration and a suggested new system design were provided.

4.2 Micro Heat-Sinks

4.2.1 Introduction

In order to cope with ever increasing demands from the electronic, automotive and aerospace industries, cooling devices have to be small in size, light-weight and of high performance. The level and reliability of heat rejection efficiency largely determine the optimal design of cooling devices. Inspired by the microchannel heat-sink idea proposed by Tuckerman and Pease (1981), several new designs and modeling approaches of high performance cooling devices have been proposed, including the fin model and the “porous medium” model. For example, Koh and Colony (1986) introduced the porous medium model, which

Tien and Kuo (1987) expanded by adopting a modified Darcy's law for the momentum equation and volume-averaging for the energy equation. Kim et al. (2000) compared analytically the one-equation and two-equation models for heat transfer in microchannel heat sinks. They reported that the one-equation model is valid only when the fluid phase is in local thermal equilibrium with the solid phase. They investigated parameters such as the Darcy number and conductivity ratio, which influence the validity of local thermal equilibrium, and concluded that the one-equation model is adequate for channels with high aspect ratios as well as for flows of highly conductive fluids. Zhao and Lu (2002) and Kim (2004) compared the fin model and porous medium model. They suggested that the porous medium model is more accurate and more suitable for optimizing microchannels with high aspect ratios. In order to further enhance micro heat-sink performance, the use of nanofluids is proposed.

Nanofluids, as coined by Choi (1995), represent a new class of engineered heat transfer fluids which contain metallic or carbon-based particles with an average size of about 10 [nm]. Specifically, aluminum- and copper-oxide spheres as well as carbon-nanotubes of an average diameter of 30 [nm] were employed with volume concentrations of 0.001 % to 6 %. They generated, under static conditions, elevated thermal conductivities where $k_{nanofluid} < 3k_{carrierfluid}$ (Choi et al., 2001; Eastman et al., 2001; Patel et al., 2003). Thus, the use of nanofluids, for example in heat exchangers, may result in energy and cost savings and should facilitate the trend of device miniaturization.

Traditional theories, such as Maxwell (1904) or Hamilton and Crosser (1962), cannot explain this thermal phenomenon. Thus, new assessments and mathematical models of the new apparent (or effective) thermal conductivity have been proposed. For example, Xuan and Li (2000) summarized previous experimental observations and concluded that $k_{eff} \equiv k_{nanofluid}$ was a function of both the thermal conductivities of the nano-material and carrier fluid, in terms of particle volume fraction, distribution, surface area, and shape. Yu and Choi (2003) and Yu and Choi (2004) modified the Maxwell equation and Hamilton-Crosser relation for k_{eff} of solid-liquid suspensions to include the effect of ordered nano-

layers around the particles. They also matched the model with observed conductivities by adjusting the nano-layer thickness and conductivity. Jang and Choi (2004) suggested an effective thermal conductivity model considering the particles Brownian motion. They focused on the heat transfer between particles and carrier fluid, which is not directly related to the heat transfer phenomena in the fixed reference frame. Furthermore, the validity of their thermal boundary layer thickness, which they defined as $3\delta_{BF}/Pr$, where $Pr \sim \mathcal{O}(10)$ and δ_{BF} is the diameter of the fluid molecule, is questionable when applying the continuum approach together with their Nusselt number correlation. Kumar et al. (2004) developed a new expression for the thermal conductivity, considering the increase of effective heat transfer area and particle motion. However, increasing the particle surface area is merely an indirect mechanism for heat transfer enhancement of the whole system. To consider the impact of particle Brownian motion, they replaced the particle-phase heat conductivity with $c \cdot \bar{u}_p$, which is problematic because the thermal conductivity is a property of the particle material. Koo and Kleinstreuer (2004a) developed a new, experimentally validated thermal conductivity model which takes the effects of particle Brownian motion and induced surrounding fluid motion into account (see Sect. 2.2).

While the previous thermal analyses focused on *quiescent* nanoparticle suspensions, Xuan and Li (2003) studied heat transfer enhancement of water-based *Cu*-nanofluids in turbulent pipe flows. Wen and Ding (2004) performed experiments with water-based Al_2O_3 nanofluids for laminar flow in a tube of 4.6 [mm] inside diameter and 6.4 [mm] outside tube diameter. While both of them reported improvements in heat transfer performances, they under-estimated the heat transfer performance by up to 40 [%], ignoring the important wall conduction effect for microchannels.

In this chapter, considering nanofluid flow in a representative microchannel, conduction-convection heat transfer is analyzed for different base fluids, i.e., water and ethylene glycol with *CuO*-nanoparticles, incorporating new k_{eff} and μ_{eff} models as well as the effect of viscous dissipation.

4.2.2 Theory

Conjugated problem

Figure 4.1 shows a typical micro heat-sink with multi-channels in it. For 2-D ODE solutions, the effect of the conduction through the top and bottom plates cannot be considered, while the 3-D solutions could. The unit element enclosed by the dashed-dot line is selected to be modeled where coolant flows in x -direction which is normal to the figure, q'' is the heat flux from the heat source, q_w is the heat flux from the side walls to the coolant. In the conventional convection problem, heat transfer through the wall is characterized by a thermal boundary condition directly or indirectly specified at the wall-fluid interface. The velocity and forced convection temperature problems are solved only for the fluid region. The solution to the temperature problem for the solid wall is not needed. However, the heat transfer through the duct wall by conduction may have significant normal and/or peripheral as well as axial components; or the fluid heating (or cooling) flux may be nonuniform around the duct periphery; or the duct wall may be of nonuniform thickness. As a result, the temperature problem for the solid wall needs to be analyzed simultaneously with that for the solid wall needs to be analyzed simultaneously with that for the fluid in order to establish the actual wall-fluid interface heat transfer flux distribution. The combination is referred to as the *conjugated problem*. The simultaneous solutions of the energy equations for the solid and fluid media are obtained by considering temperature and heat flux as continuous functions at the solid wall-fluid interface. The velocity distribution for the fluid medium must first be found by solving the applicable continuity and momentum equations. The dimensionless temperature profile is always variant (*never fully developed*) for this class of problems (Shah and London, 1978).

Fin model

The fin model is based on the assumptions of one-dimensional conduction only along the fin height, constant heat transfer coefficient, and uniform fluid temperature. It

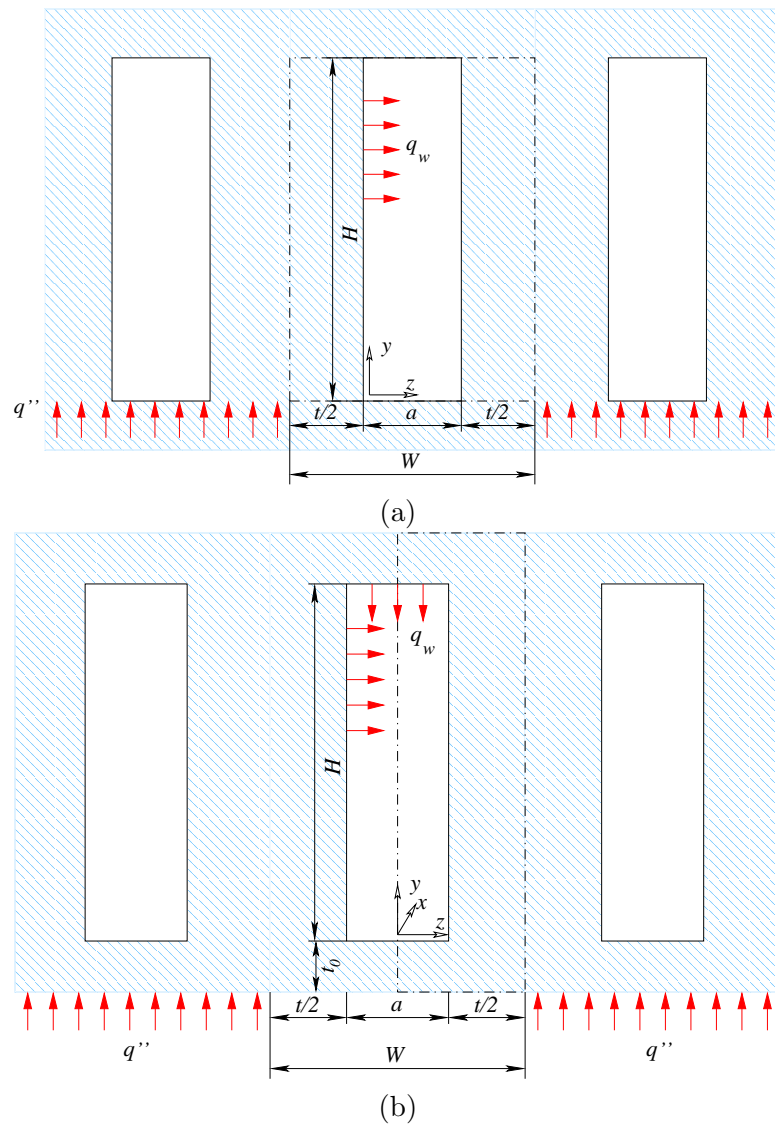


Figure 4.1: Schematic diagrams of (a) 2-D ODE problems and (b) 3-D PDE problems

is assumed that the fluid temperature is averaged over the height of the microchannel, with $T_f = T_f(x)$, so the fluid temperature $T_f(x)$ is the bulk mean fluid temperature over the cross-section. When the flow is fully developed thermally, the temperature difference between the heat sink base and the bulk fluid is the same at any plane in the streamwise direction. The convective resistance can then be expressed as

$$R_{\theta,conv} = \frac{1}{\bar{h}_{base}A_{base} + \eta\bar{h}_{fin}A_{fin}} \quad (4.1)$$

The heat transfer coefficients with reference to the bulk mean temperature of the fluid and the fin efficiency used in Eq. (4.1) are defined as

$$\bar{h}_{base} \equiv \frac{1}{A_{base}} \int_{A_{base}} h_{base} dA \quad (4.2)$$

$$\bar{h}_{fin} \equiv \frac{1}{A_{fin}} \int_{A_{fin}} h_{fin} dA \quad (4.3)$$

$$\eta \equiv \frac{q_{fin,actual}}{q_{fin,ideal}} = \frac{\int_{A_{fin}} h_{fin}(T_{fin} - \bar{T}_f) dA_{fin}}{\bar{h}_{fin}A_{fin}(T_{base} - T_b)} \quad (4.4)$$

where A_{base} and A_{fin} represent the area available for heat transfer between the fins at the base of the microchannel and the fin area, respectively. Assuming $\bar{h} = \bar{h}_{base} = \bar{h}_{fin}$, Eq. (4.1) reduces to

$$R_{\theta,conv} = \frac{1}{\bar{h}A_s} \quad (4.5)$$

The surface area available for heat transfer is determined as

$$A_s = \frac{n}{\Gamma + 1} WL + \eta 2nHL \quad (4.6)$$

where n and Γ are the number of cooling channels and the ratio of the fin thickness to the channel width, respectively, whereas Kim (2004) reported the heat transfer area to be

$$A_s = \frac{nWL}{n + \Gamma(n - 1)}WL + \eta 2(n - 1)HL \quad (4.7)$$

It seems like they neglected the conduction/convection heat transfer from the both two last walls to the channel. The first term is the area available for heat transfer between the fins at the base of the microchannel, and the second term is the effective fin area with the fin efficiency included to account for a finite thermal conductivity of the fin. The heat transfer coefficient, \bar{h} , is obtained from the Nusselt number as follows:

$$\bar{h} = \frac{Nu_{D_h} k_f}{D_h} \quad (4.8)$$

The convective thermal resistance is obtained as follows:

$$R_{\theta,conv} = \frac{4(1 + \Gamma)}{Nu_{D_h} k_f n L \{1 + \eta 2 \frac{H}{W} (1 + \Gamma)\} \{ \frac{W}{H} + 2(1 + \Gamma) \}} \quad (4.9)$$

where Nu_{D_h} is a constant depending on H/a , η is given as $\tanh(mH)/mH$, and mH is defined as $\sqrt{\frac{1+2(\frac{H}{a})}{2} \frac{H}{t} Nu_{D_h} (\frac{k_f}{k_s})} = \sqrt{\frac{hP}{k_s A}} H \cong \sqrt{\frac{2h}{k_s} \frac{H}{t} H}$. mH is a function of the channel geometry, the Nusselt number, and the conductivity ratio. The fin efficiency is shown in Fig. 4.2.

No matter whether the Fin model is right or wrong, the Fin model explains why the channel aspect ratio should be high. The fin effectiveness ϵ_f is the ratio of the fin heat transfer rate to the heat transfer rate that would exist without the fin (Incropera and DeWitt, 1990). Therefore, assuming the heat transfer coefficients h , and \bar{h} are the same, the fin effectiveness

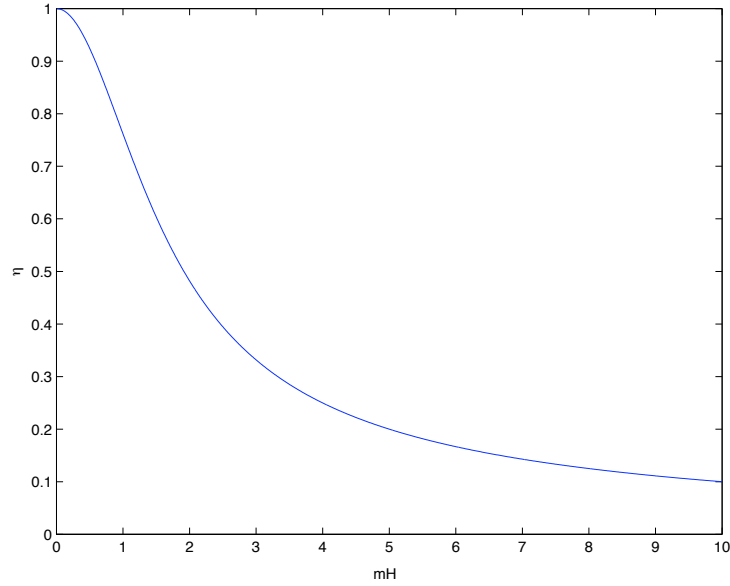


Figure 4.2: Fin efficiency

can be described as:

$$\epsilon_f = \frac{q_f}{hA_{c,b}\theta_b} = \frac{\eta\bar{h}HL\theta_b}{htL\theta_b} \sim \frac{\tanh\sqrt{\frac{2h}{k_s}H}\left(\frac{H}{t}\right)}{\sqrt{\frac{2h}{k_s}H}}\sqrt{\frac{H}{t}} \quad (4.10)$$

Since both $\tanh x$ and \sqrt{x} are increasing function of x , the fin effectiveness ϵ_f increases with the aspect ratio, which explains the need for high channel aspect ratio.

Porous medium model

In the porous medium model, the microchannel heat sink is modeled as a fluid-saturated porous medium, as shown in Fig. 4.3. Mathematically, this is equivalent to averaging the velocity and temperature distributions in the direction parallel to the wall but perpendicular to the flow direction. This approach was applied to the microchannel heat sink by Tien and Kuo (1987) and later extended by Kim et al. (2000, 2002); Kim and

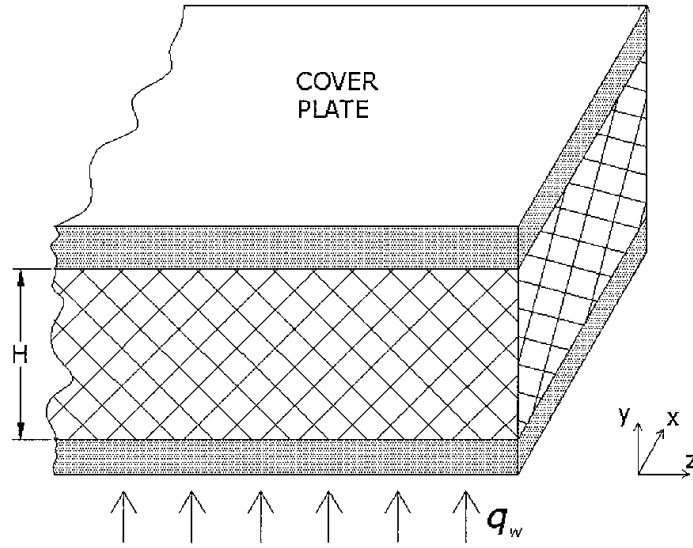


Figure 4.3: Porous medium analogy

Jang (2002); Kim (2004). The governing equations for the velocity and temperature fields in the microstructure are established by applying the volume-averaging technique. The representative element volume (REV) for the volume-averaging is a slender cylinder aligned parallel to the z -axis. The volume-averaged quantities over the fluid and solid phases are defined respectively as follows:

$$\langle \phi \rangle^f = \frac{1}{a} \int_a \phi dz \quad (4.11)$$

$$\langle \phi \rangle^s = \frac{1}{t} \int_t \phi dz \quad (4.12)$$

For hydrodynamically and thermally fully developed flow, the governing equations and boundary conditions are simplified as follows:

$$0 = -\frac{\partial \langle p_f \rangle}{\partial x} + \mu_f \frac{\partial^2 \langle u_f \rangle}{\partial y^2} - \frac{\mu_f}{K} \epsilon \langle u_f \rangle \quad (4.13)$$

$$\epsilon \rho_f c_f \langle u_f \rangle \frac{\partial \langle T_f \rangle}{\partial x} = \frac{\partial}{\partial y} \left(k_{fe} \frac{\partial \langle T_f \rangle}{\partial y} \right) + h_l A_w (\langle T_s \rangle - \langle T_f \rangle) \quad (4.14)$$

$$\frac{\partial}{\partial y} \left(k_{se} \frac{\partial \langle T_s \rangle}{\partial y} \right) = h_l A_w (\langle T_s \rangle - \langle T_f \rangle) \quad (4.15)$$

$$\langle u \rangle^f = \langle v \rangle^f = 0, \quad \langle T_f \rangle^f = \langle T_s \rangle^s = T_w \quad \text{at } y = 0 \quad (4.16)$$

$$\langle u \rangle^f = \langle v \rangle^f = 0, \quad \frac{\partial \langle T_f \rangle^f}{\partial y} = \frac{\partial \langle T_s \rangle^s}{\partial y} = 0 \quad \text{at } y = H \quad (4.17)$$

where ϵ , K , A_w , k_{se} , and k_{fe} are porosity, permeability, wetted area per volume, effective conductivity of the solid and effective conductivity of the fluid, respectively. Equation (4.13) is the extended Darcy equation, which has been developed for describing fluid flow in a porous medium and accounts for the boundary effect. Equations (4.14) and (4.15) are identical to the so-called two-equation model, which treats the solid and the fluid as separate entities. They are used in place of the one equation model because the temperature difference between the solid and the fluid in general cannot be neglected. Kim et al. (2000, 2002) studied the assumption of a local thermal non-equilibrium to present a criterion by which one can determine when to use it. The interstitial heat transfer coefficient h_l is the proportionality constant between the interfacial heat flux and the solid-fluid temperature difference within the REV, and it is further discussed in later section. For the microchannel, the porosity, wetted area per volume, and effective conductivities can be represented as

$$\epsilon = \frac{w_c}{w}, \quad a = \frac{2}{w}, \quad k_{se} = (1 - \epsilon)k_s, \quad k_{fe} = \epsilon k_f. \quad (4.18)$$

To solve the governing equations, K , and h_l should be determined in advance. The permeability K is related to the viscous shear stress caused by the fins, and the interstitial heat transfer coefficient h_l is related to the convective heat transfer from the fins. In porous medium studies, we typically replace the lost information with empirical data for K and h_l . For the present configuration, however, these parameters can be determined analytically through an approximation. For this we assume that the characteristics of pressure drop across and heat transfer from the fins under consideration can be approximated as those found for the Poiseuille flow *between two infinite parallel plates* that are subject to a constant heat flux in the streamwise direction. The velocity and temperature distribution for the Poiseuille flow in this configuration can easily be determined to be

$$\langle u_f \rangle = -\frac{a^2}{12\mu} \frac{dp_f}{dx} \quad (4.19)$$

$$T_w - \langle T_f \rangle = \frac{a^2}{10\alpha} \langle u_f \rangle \frac{d\langle T_f \rangle}{dx} \quad (4.20)$$

Using the definition of the permeability and the interstitial heat transfer coefficient together with Equations above;

$$K = \frac{\epsilon \langle u \rangle_m^f}{-\mu \frac{dp}{dx}} = \frac{\epsilon a^2}{12} \quad (4.21)$$

$$h_l = \frac{q''}{T_w - \langle T_f \rangle_m^f} = \frac{a^2}{10\alpha} \langle u \rangle_m^f \frac{dT_{f,m}}{dx} \quad (4.22)$$

For large values of an aspect ratio α_s in which the influence of the fins on the pressure drop and heat transfer characteristics of a heat sink is significant, an order of magnitude analysis shows that the diffusion of momentum and energy along the fin direction is negligible compared to that in the direction normal to the fin direction. Hence, we can safely assume that the approximation employed in determining K and h_l is valid when the aspect ratio is of the order of one or larger.

From the definition of the bulk mean temperature, the convective thermal resistance of the

microchannel heat sink can be represented by

$$R_{\theta,conv} = -\frac{\theta_{f,b}H}{(1-\epsilon)k_sLW} + \frac{3}{140} \frac{a^2}{k_fL\epsilon A_c} \quad (4.23)$$

where the bulk mean temperature adopted in the porous medium approach is

$$\theta_{f,b} = \int_0^1 U\theta_f dY \quad (4.24)$$

The second term in Eq. (4.23) is included to account for the difference between the conventional bulk mean temperature and the bulk mean temperature defined in Eq. (4.24).

One- and Two-equations models for the energy equation

Kim et al. (2000) compared the one- and two-equation approaches for the energy equation. They identified the Darcy number, and the effective thermal conductivity ratio as important engineering parameters. Bejan (1995) derived the energy equation for a homogeneous porous medium layer by using volume averaging as follows:

$$\rho_f c_{Pf} \left(\sigma \frac{\partial T}{\partial t} + u \frac{\partial T}{\partial x} \right) = k \frac{\partial^2 T}{\partial x^2} + q_s''' + \frac{\mu}{K} \langle u \rangle^2 \quad (4.25)$$

where the capacity ratio σ is $\sigma = \frac{\epsilon \rho_f c_{Pf} + (1-\epsilon) \rho_s c_s}{\rho_f c_{Pf}}$, the internal heat generation rate per unit volume of porous medium q_s''' is defined as $q_s''' = (1-\epsilon)q_s$, and the last term represents the viscous dissipation effect. Kim et al. (2000) used the one-equation model with the assumption of negligible viscous dissipation effect and no internal heat generation. They analyzed the temperature difference between the two phase by the asymptotic method and found that the error induced by the local thermal equilibrium assumption is proportional to $\frac{Da}{C}$, where $Da = \frac{1}{12\alpha_s^2}$, and $C = \frac{\epsilon k_f}{(1-\epsilon)k_s}$. Kim and Jang (2002) also analyzed the error of the local thermal equilibrium assumption.

Analogy with the averaged general governing equation approach

Kim (2004) reported that PMM is mathematically equivalent to averaging the velocity and temperature distributions in the direction parallel to the wall but perpendicular to the flow direction. In this section, the PMM will be derived from the general governing equations.

For steady, fully developed and incompressible fluid flows, the general momentum equations reduces to

$$0 = -\frac{dp}{dx} + \mu \frac{\partial^2 u}{\partial y^2} + \mu \frac{\partial^2 u}{\partial z^2} \quad (4.26)$$

$$0 = -\frac{1}{a} \int_0^a \frac{dp}{dx} dz + \frac{1}{a} \int_0^a \mu \frac{\partial^2 u}{\partial y^2} dz + \frac{1}{a} \int_0^a \mu \frac{\partial^2 u}{\partial z^2} dz \quad (4.27)$$

$$0 = -\frac{dp}{dx} + \mu \frac{d^2 \bar{u}}{dy^2} - \frac{1}{a} 2\tau_w \quad (4.28)$$

Using the definition of the friction factor $f = \frac{\tau_w}{\frac{1}{2}\rho u_m^2}$, the equation becomes

$$0 = -\frac{dp}{dx} + \mu \frac{d^2 \bar{u}}{dy^2} - \frac{1}{a} f \rho u_m^2 \quad (4.29)$$

$$0 = -\frac{dp}{dx} + \mu \frac{d^2 \bar{u}}{dy^2} - \frac{1}{a} \frac{24}{\frac{\rho \bar{u} 2a}{\mu}} \rho \bar{u} \quad (4.30)$$

$$0 = -\frac{dp}{dx} + \mu \frac{d^2 \bar{u}}{dy^2} - \frac{12\mu}{a^2} \bar{u} \quad (4.31)$$

Comparing with PMM, we can get the same permeability value K .

$$\frac{12\mu}{a^2} \bar{u} = \frac{\mu}{K} \epsilon \bar{u} \quad (4.32)$$

$$K = \frac{\epsilon a^2}{12} \quad (4.33)$$

Energy equations for both phases given as:

$$\rho_f c_f u \frac{dT}{dx} = k \frac{\partial^2 T}{\partial y^2} + k \frac{\partial^2 T}{\partial z^2} \quad \text{for the fluid phase} \quad (4.34)$$

$$0 = k \frac{\partial^2 T}{\partial y^2} + k \frac{\partial^2 T}{\partial z^2} \quad \text{for the solid phase} \quad (4.35)$$

For the fluid phase, taking integral from 0 to a and dividing it by a yields

$$\rho_f c_f \frac{1}{a} \int_0^a u dz \frac{dT}{dx} = \frac{k}{a} \int_0^a \frac{\partial^2 T}{\partial y^2} dz + \frac{k}{a} \int_0^a \frac{\partial^2 T}{\partial z^2} dz \quad (4.36)$$

After arranging the equation, we obtain

$$\rho_f c_f \langle u_f \rangle \frac{dT_f}{dx} = k \frac{\partial^2 \langle T_f \rangle}{\partial y^2} + \frac{k}{a} \frac{\partial T}{\partial z} \Big|_0^a \quad (4.37)$$

$$\rho_f c_f \langle u_f \rangle \frac{dT_f}{dx} = k \frac{\partial^2 \langle T_f \rangle}{\partial y^2} + \frac{2q_w}{a} \quad (4.38)$$

For constant heat flux cases,

$$\frac{\partial T}{\partial x} = \frac{\partial \langle T_f \rangle}{\partial x} \quad (4.39)$$

By defining,

$$q_w = h_l (\langle T_s \rangle - \langle T_f \rangle) \quad (4.40)$$

We should note that the definition of the heat transfer coefficient h_l is different from the conventional definition, and using the relation

$$\epsilon = \frac{a}{W} \quad (4.41)$$

$$\rho_f c_f \langle u_f \rangle \frac{dT}{dx} = k \frac{\partial^2 \langle T_f \rangle}{\partial y^2} + \frac{2h_l (\langle T_s \rangle - \langle T_f \rangle)}{\epsilon W} \quad (4.42)$$

Multiplying ϵ to each term, and using the definition of the effective fluid conductivity, $k_{fe} = \epsilon k_f$,

$$\epsilon \rho_f c_f \langle u_f \rangle \frac{dT}{dx} = k_{fe} \frac{\partial^2 \langle T_f \rangle}{\partial y^2} + h_l \frac{2}{W} (\langle T_s \rangle - \langle T_f \rangle) \quad (4.43)$$

For the solid phase, taking integral over half the wall thickness $t/2$,

$$0 = k \frac{1}{t/2} \int_0^{t/2} \frac{\partial^2 T_s}{\partial y^2} dz + k \frac{1}{t/2} \int_0^{t/2} \frac{\partial^2 T_s}{\partial z^2} dz \quad (4.44)$$

$$0 = \frac{1}{t/2} \int_0^{t/2} \frac{\partial^2 T_s}{\partial y^2} dz + \frac{2}{t} \frac{\partial T_s}{\partial z} \Big|_0^a \quad (4.45)$$

$$0 = \frac{\partial^2 \langle T_s \rangle}{\partial y^2} + \frac{2}{kt} (0 - q_w) \quad (4.46)$$

$$\frac{\partial^2 \langle T_s \rangle}{\partial y^2} = \frac{2}{kt} q_w \quad (4.47)$$

Using the relation, $t = (1 - \epsilon)W$, and Eq. (4.40),

$$\frac{\partial^2 \langle T_s \rangle}{\partial y^2} = \frac{2}{kt} q_w \quad (4.48)$$

$$\frac{\partial^2 \langle T_s \rangle}{\partial y^2} = \frac{2h_l}{k(1 - \epsilon)W} (\langle T_s \rangle - \langle T_f \rangle) \quad (4.49)$$

$$k_{se} \frac{\partial^2 \langle T_s \rangle}{\partial y^2} = \frac{2}{W} h_l (\langle T_s \rangle - \langle T_f \rangle) \quad (4.50)$$

The energy equations are exact up to this point. The heat transfer coefficient h_l should be provided to close the problem. Assuming the side walls as parallel plate, the energy equation for the fluid phase reduces to

$$\rho_f c_f u \frac{\partial T}{\partial x} = k \frac{\partial^2 T}{\partial z^2} \quad (4.51)$$

The velocity profile between parallel plates is given as

$$u = 6u_m(z^2 - az) \quad (4.52)$$

Integrating Eq. (4.51) about z with the velocity profile,

$$\rho_f c_f u_m \frac{\partial \langle T_s \rangle}{\partial x} \int_0^a (z^2 - az) dz = \int_0^a k \frac{\partial^2 T}{\partial z^2} dz \quad (4.53)$$

After integration and averaging over z direction, we obtain

$$T_w - \langle T_f \rangle \cong \langle T_s \rangle - \langle T_f \rangle = \frac{u_m}{10\alpha} \left(\frac{d \langle T_f \rangle}{dx} \right) a^2 \quad (4.54)$$

From the energy balance,

$$2q_w HL = \rho_f c_p \Delta T_f \quad (4.55)$$

$$\frac{d \langle T_f \rangle}{dx} = \frac{2q_w}{\rho_f u_m a c_f} \quad (4.56)$$

Therefore,

$$h_l = \frac{5k_f}{a} \quad (4.57)$$

All the equations derived above are the same as those in Kim (2004). Then, what would be the advantage of PMM over the averaged general governing equations? The closed set of the averaged general governing equations could be obtained for the simple geometry. When there exist fins and obstacles in channels to enhance the heat transfer rate, it would be very difficult, if not possible, to derive a closed set of governing equations. However, the permeability K and interstitial heat transfer coefficient, h_l could be determined experimentally, PMM has more flexibility. For this stage of industrial micro heat sink applications, mostly clear straight channels are used for which we can simply use the averaged general governing

equations approach.

Comparison between one- and two-equation models

Kim (2004) reported that the the solid temperature obtained from Fin model deviated noticeably from the numerical solution for the cases of increase of any one of channel aspect ratio α_s , porosity ϵ , and conductivity ratio k_f/k_s . He confirmed that the Porous Medium Model is superior to the Fin model. He also reported that the conductivity ratio has a more profound effect on the dimensionless solid temperature distribution than the porosity and the aspect ratio. He stressed that the Fin model is not adequate for the thermal designing tool since it failed to capture the minimum thermal resistance, whereas the Porous Medium Model and Numerical Model could. He attributed this to the assumption of constant heat transfer coefficient with reference to the bulk mean temperature.

Governing equations and boundary conditions for PDE analyses

A typical multi-microchannel heat exchanger is depicted in Fig. 4.1, where the channel length is 1 [cm] with $a=50$ [μm], $H=300$ [μm], $t_0=25$ [μm], and $W=100$ [μm]. Focusing on the representative microchannel in the center, the coolant, i.e., liquid plus nanoparticles, flows in the x -direction and the heat flux from the source, q'' , causes via conduction a wall heat flux, q_w , to the fluid. Assuming steady laminar flow of a dilute uniform suspension, and constant heat flux q'' , the governing equations for this conjugated heat transfer problem can be written as follows.

Continuity:

$$\nabla \cdot \vec{u} = 0 \quad (4.58)$$

Momentum equation:

$$(\vec{u} \cdot \nabla)\vec{u} = -\frac{1}{\rho}\nabla p + \frac{\mu_{eff}}{\rho}\nabla^2\vec{u} \quad (4.59)$$

Energy equation for fluid:

$$(\vec{u} \cdot \nabla)T = \frac{k_{eff}}{\rho c_p} \nabla^2 T + \frac{\mu_{eff}}{\rho c_p} \Phi \quad (4.60)$$

where

$$\Phi = \left(\frac{\partial u_i}{\partial x_j} + \frac{\partial u_j}{\partial x_i} \right) \frac{\partial u_i}{\partial x_j} \quad (4.61)$$

Energy equation for solid:

$$0 = \nabla^2 T \quad (4.62)$$

The associated boundary conditions are:

$$u = U_0 \text{ at } x=0 \quad (4.63)$$

$$\vec{u} = 0 \text{ at the wall} \quad (4.64)$$

$$\frac{\partial u}{\partial z} = 0 \text{ at } z=0 \quad (4.65)$$

$$T_f = T_0 \text{ at } x=0 \quad (4.66)$$

$$T_s = T_0 \text{ at } x=0 \quad (4.67)$$

$$q'' = 0 \text{ at } x = 0, x = L, z = \frac{W}{2} \text{ and } y = H + 2 \cdot t_0 \quad (4.68)$$

$$k_s \frac{\partial T}{\partial y} = q'' \text{ at } y = 0 \quad (4.69)$$

$$k_s \nabla^2 T_s|_n = k_{eff} \nabla^2 T_f|_n \text{ at wall-fluid interfaces} \quad (4.70)$$

As alluded to in Sec. 4.2.1, the presence of nanoparticles at volume fractions $1 \leq \alpha_d \leq 4$ [%] alter the mixture properties, i.e., $k_{liquid} \rightarrow k_{effective}$ and $\mu_{liquid} \rightarrow \mu_{effective}$. While $\mu_{liq.}$ does not differ measurably from μ_{eff} for $Pr > 1$, major heat transfer improvements center around k_{eff} for which a new model has been proposed. Specifically, the k_{eff} -model for nanofluids considers the impact of particle Brownian motion and that of the particle interaction potential (Koo and Kleinstreuer, 2004a). The new model is composed

of two parts, the conventional static part as well as a dynamic part which originates from the particle Brownian motion.

$$k_{eff} = k_{static} + k_{Brownian} \quad (4.71)$$

where, for example, according to Maxwell (1904)

$$\frac{k_{static}}{k_c} = 1 + \frac{3\left(\frac{k_d}{k_c} - 1\right)\alpha_d}{\left(\frac{k_d}{k_c} + 2\right) - \left(\frac{k_d}{k_c} - 1\right)\alpha_d} \quad (4.72)$$

Here, α_d is the particle volume fraction, k_c is the thermal conductivity of the carrier fluid, and k_d is that of the particles.

The $k_{Brownian}$ term was developed using kinetic theory together with Stokes' flow approximation to estimate the size of the affected fluid-parcel moving with each particle.

$$k_{Brownian} = 5 \times 10^4 \beta \alpha_d \rho_l c_l \sqrt{\frac{\kappa T}{\rho_d D}} f(T, \alpha_d, \text{etc.}) \quad (4.73)$$

The two modeling functions β and f were introduced to consider the hydrodynamic interaction among the Brownian motion induced (moving) fluid parcels, and the particle interaction due to the particle interaction potential to encapsulate the strong temperature dependence, respectively. Specifically, the function f depends on properties of the intervening fluid, and hence particle interactions. Traditionally, the interparticle potential, $w(d)$, can be used to take that into consideration, i.e.,

$$w(d) = -\frac{AR}{6d} \quad (4.74)$$

where A is the Hamaker constant, R is the particle radius, and d is the surface distance. The Hamaker constant A for two identical phases 1 interacting across medium 3 can be

expressed as (Israelachvili, 1992):

$$A \approx \frac{3}{4} \kappa T \left(\frac{\epsilon_1 - \epsilon_3}{\epsilon_1 + \epsilon_3} \right)^2 \quad (4.75)$$

where ϵ is the electric dipole constant. Based on experimental evidence, for water-based *CuO*-nanofluids, β and f were estimated as (Koo and Kleinstreuer, 2004a):

$$\beta = 0.0137(100\alpha_d)^{-0.8229} \quad \text{for } \alpha_d < 1[\%] \quad (4.76a)$$

$$\beta = 0.0011(100\alpha_d)^{-0.7272} \quad \alpha_d > 1[\%] \quad (4.76b)$$

and

$$\begin{aligned} f(T, \alpha_d) = & (-6.04\alpha_d + 0.4705)T \\ & + (1722.3\alpha_d - 134.63) \quad \begin{array}{l} 1 < \alpha_d < 4[\%] \\ 300 < T < 325[K] \end{array} \end{aligned} \quad (4.77)$$

It should be noted that the function f is a linear equation because of the Taylor series truncation; but, that functional dependence can be confirmed with Eqns (4.74) and (4.75) as well. It is observed that β is quite independent of the particle type for low concentration cases (say, $\alpha_d < 1$ [%]), while it exhibits a strong particle material dependence for relatively high concentration cases (say, $\alpha_d > 1$ [%]).

Employing the same concept for the derivation of the effective viscosity due to Brownian motion, it can be stated that:

$$\mu_{eff} = \mu_{static} + \mu_{Brownian} \quad (4.78a)$$

where

$$\mu_{Brownian} = \frac{k_{Brownian}}{k_l} \times \frac{\mu_l}{Pr_l} \quad (4.78b)$$

Thus, the effect of Brownian motion on the effective fluid viscosity is less significant than that on the effective thermal conductivity, since $Pr_l > 1$ for liquids. At room temperature, the Prandtl number is about 5, 100, and 5000 for water, ethylene glycol, and engine oil, respectively, while for $T \equiv 350$ [K], the values are 2.3, 34.6, and 546.

Krieger (1972) stated that the common structural feature unifying rheologically interesting class of fluids is the presence of constituents, either colloidal particles or macromolecules, whose dimensions are large compared with molecules of the suspending medium, while still small enough to exhibit significant rotatory and translatory Brownian movement. The structure of the fluid resembles a gas of large molecules, with the void space replaced by a Newtonian continuum. The newly developed effective thermal conductivity and dynamic viscosity models well comply with his statement by applying the kinetic theory for the gas-like behavior and considering the induced liquid motion considering the Newtonian continuum replacing the void space.

4.2.3 Results and Discussion

Comparison of ODE and PDE analyses

To compare the temperature profiles of ODE and PDE solutions, PDE solutions were obtained first and ODE solutions were obtained for the given effective thermal conductivity. Figures 4.4 and 4.5 show the comparisons of temperature profiles obtained from PDE and ODE. The non-dimensional temperature profiles obtained from ODE solutions are always lower than those of PDE solutions. The difference comes mainly from the different boundary conditions. Adiabatic condition was used for the upper interface between the fluid phase and the solid phase, while the heat flux balance condition is enforced for

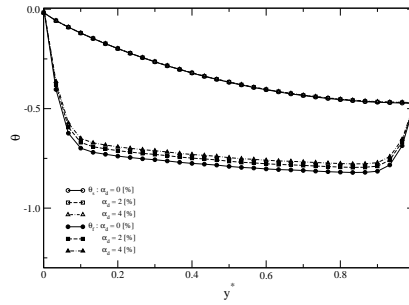
PDE solutions which facilitates the heat transfer from the top plate to the fluid domain. Therefore, the temperature gradients at the upper interface are zero for ODE solutions and become negative for PDE solutions to make the temperature profiles of ODE solutions be lower than those of PDE counterparts.

The non-dimensionalized temperature difference between ODE and PDE solutions is smaller for water based nanofluids. This is due to the thermal entrance effect. The inlet Reynolds number is much higher for water based nanofluids ($Re_{WT} = 222$) compared to ethylene glycol based ones ($Re_{EG} = 16.6$) due to higher dynamic viscosity of ethylene glycol. Hence, the hydraulic entrance length ($L_{hydraulic\ entrance} \approx 0.06Re \cdot D_h$) is much longer for the water based nanofluids. However, the thermal entrance length ($L_{thermal\ entrance} \approx Pr \cdot L_{hydraulic\ entrance}$) is much longer for ethylene glycol based nanofluids due to the high Prandtl number of ethylene glycol ($Pr \approx 150$). For the given case, the thermal entrance length for ethylene glycol based nanofluids is longer than the system length L , so that ethylene glycol-based nanofluids are affected more by the developing region, although the temperature profiles of both cases are always developing throughout the channel for conjugate heat transfer problems as discussed in Sect. 4.2.2. Figure 4.4(a) and 4.5(a) shows the temperature profiles near the channel inlet. This explains why the fluid temperature profiles at $x = 0.008$ [m] of PDE and ODE solutions are closer to each other for water based nanofluids than those for ethylene glycol based nanofluids.

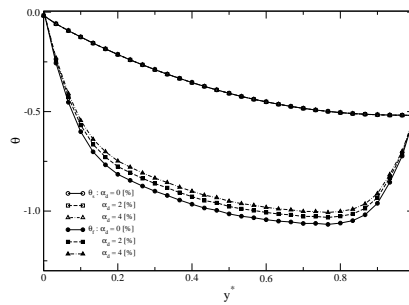
Otherwise than that, they show good match each other. As a result, we could conclude that the ODE model provides a conservative tool to design and analyze the heat transfer phenomena in micro heat-sinks.

Nanofluids effects on momentum and energy transports

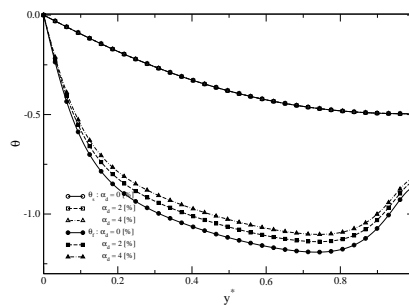
The thermal nanofluid flow results, focus on four aspects: hydrodynamics, temperature gradients, Nusselt numbers, and wall effects (Koo and Kleinstreuer, 2005c). It should be noted that the results for ethylene glycol based nanofluids do not contain the impact of the function f due to the lack of experimental data. Therefore, comparisons between



(a)

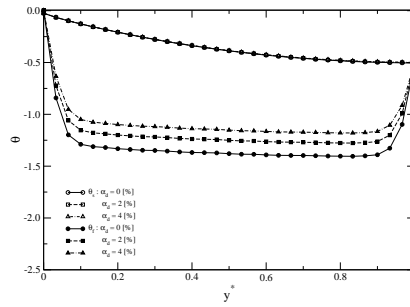


(b)

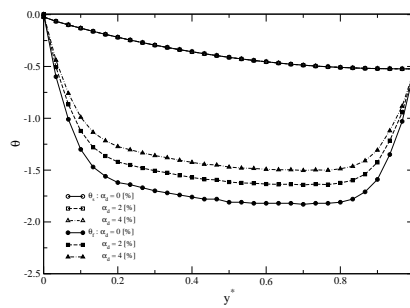


(c)

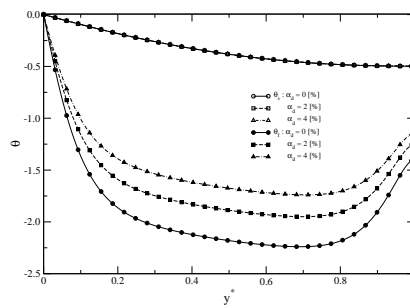
Figure 4.4: Comparison between the full partial-differential-equation solution ((a) at $x = 0.0006$ [m] and (b) at $x = 0.008$ [m]) and (c) the reduced ordinary-differential-equation solution for the water based CuO nanofluid under the heat flux of 100 [W/cm^2]



(a)



(b)



(c)

Figure 4.5: Comparison between the full partial-differential-equation solution ((a) at $x = 0.0006$ [m] and (b) at $x = 0.008$ [m]) and (c) the reduced ordinary-differential-equation solution for the Ethylene Glycol based CuO nanofluid under the heat flux of 100 [W/cm^2]

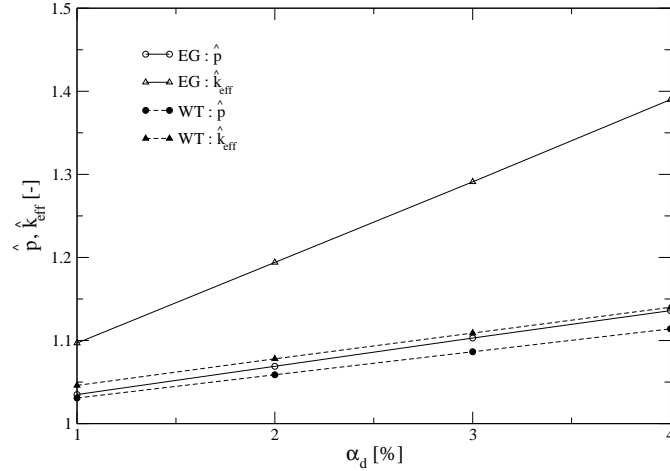


Figure 4.6: Comparison of the pressure gradient increase, and effective thermal conductivity between ethylene glycol- and water-base *CuO* nanofluids

ethylene glycol- and water-based nanofluids are performed by setting $f = 1$.

Nanofluid flows

Setting $f \equiv 1$ for both test fluids, so that any additional temperature influence is ignored, Fig. 4.6 summarizes the impact of nanofluids with different particle concentrations on the effective thermal conductivity, $\hat{k}_{eff|_{x=8 \text{ [mm]}}} = k_{eff}/k_l$, and the necessary pressure gradient, $\hat{p} = (p_{in} - p_{exit})/(p_{in, \alpha_d=0} - p_{exit, \alpha_d=0})$, to maintain the mixture flow rate.

Although the changes in \hat{p} are slightly higher for ethylene glycol-based nanofluids, the thermal conductivity increases significantly due to the higher Prandtl number. This was confirmed by Lee et al. (1999), Xie et al. (2002) and Xie et al. (2003) who reported that ethylene glycol-based nanofluids showed a larger increase in thermal conductivity than water-based ones. Indeed, by comparing $k_{Brownian}/k_{static} \sim \rho_l c_l / k_l$, which is the ratio of dynamic part and static part of the effective thermal conductivity (see Eq. (4.73)), Koo and Kleinstreuer (2004a) showed that this is a result of Brownian motion

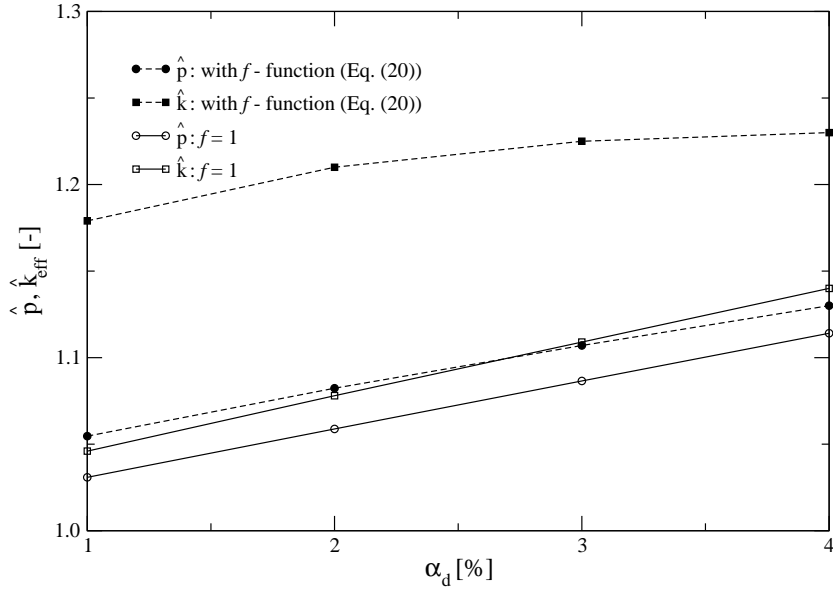


Figure 4.7: Influence of temperature-function f on dimensionless pressure gradient and effective thermal conductivity for water-based CuO nanofluids

of the nanoparticles.

Due to the lack of published experimental data to estimate the function f for different carrier fluids, its influence could only be analyzed for water-based CuO -nanofluids (c.f. Eq. (4.77)). Figure 4.7 shows the effect of f on the driving force and the effective thermal conductivity. Clearly, the improvement in heat transfer performance outweighs the inherent cost of higher \hat{p} -values. Future work will consider the impact of f on enhanced heat transfer performance of ethylene glycol-based nanofluids as well.

Temperature profiles

In this section, the effects of nanofluids and viscous dissipation on temperature profiles

are discussed in terms of non-dimensional temperatures.

Solid phase:

$$\theta_s = \frac{\bar{T}_s - \bar{T}_w}{\frac{\bar{q}_w H}{(1-\epsilon)k_s}} \quad (4.79)$$

Fluid phase:

$$\theta_f = \frac{\bar{T}_f - \bar{T}_w}{\frac{\bar{q}_w H}{(1-\epsilon)k_s}} \quad (4.80)$$

where all variables are locally averaged. T_w is the heat-capacity-averaged temperature at $y = 0$.

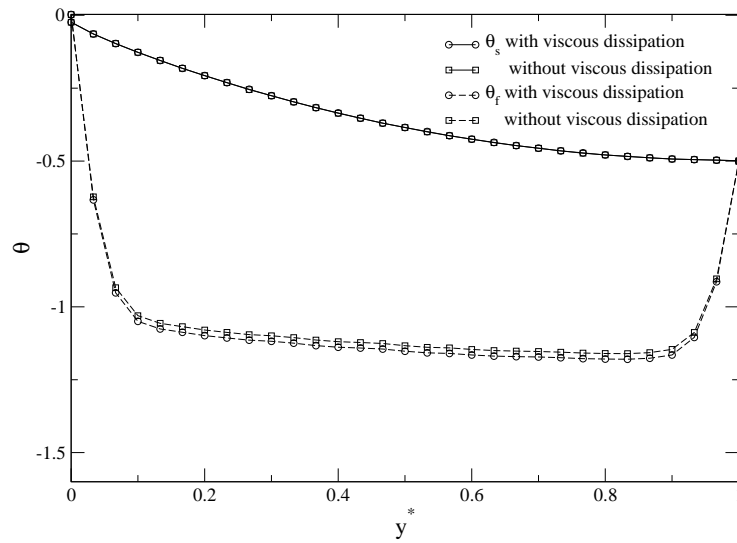
Effects of base fluid and viscous dissipation

Figures 4.8 and 4.9 compare the dimensionless temperature variations across the microchannel, $0 \leq y \leq H$, for ethylene glycol- and water-based nanofluids. The temperature difference between the solid and liquid phases is greater for ethylene glycol due to its lower thermal conductivity. The solid-phase temperature profiles are not affected by viscous dissipation. That effect is more pronounced for ethylene glycol(EG)-based nanofluids due to its higher dynamic viscosity and lower heat capacity compared to water-based ones. For EG-based nanofluids, the fluid temperature profiles without the viscous dissipation term are always higher, which potentially incorrectly leads to higher Nusselt numbers.

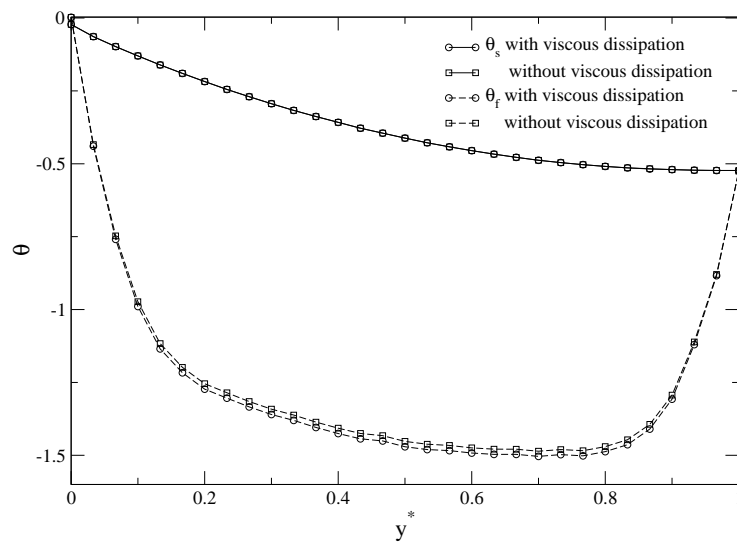
Reducing the channel width by half (now $a = 25 \text{ } [\mu\text{m}]$), the resulting influence on the temperature profile of the EG-nanofluid is given in Fig. 4.8. The inlet velocity was kept at $2.2 \text{ } [m/s]$, because the total mass flow rate in the system is the same due to the increase of the number of channels.

Comparison of cooling performance between pure fluid and nanofluid

In order to assess the impact of the channel inlet velocity on solid- and fluid-phase temperature profiles of pure ethylene glycol and EG-based nanofluids (Fig. 4.10), the pressure drop requirement was kept the same for the cases $U_0 = 2.2$

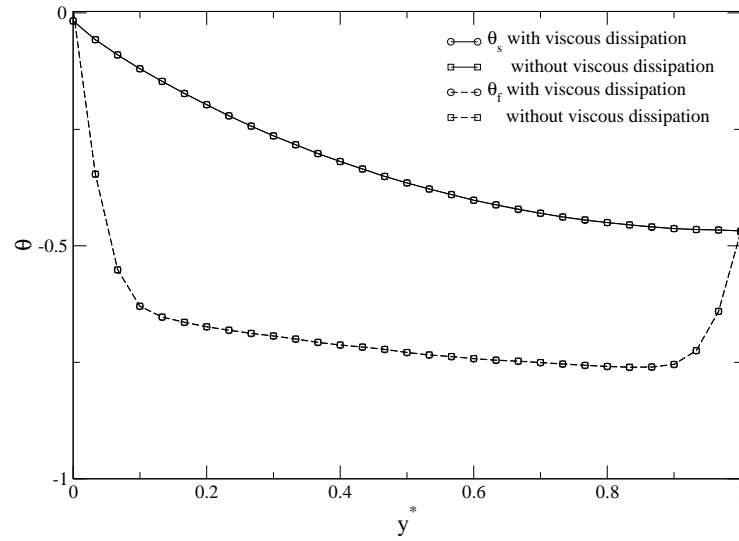


(a)

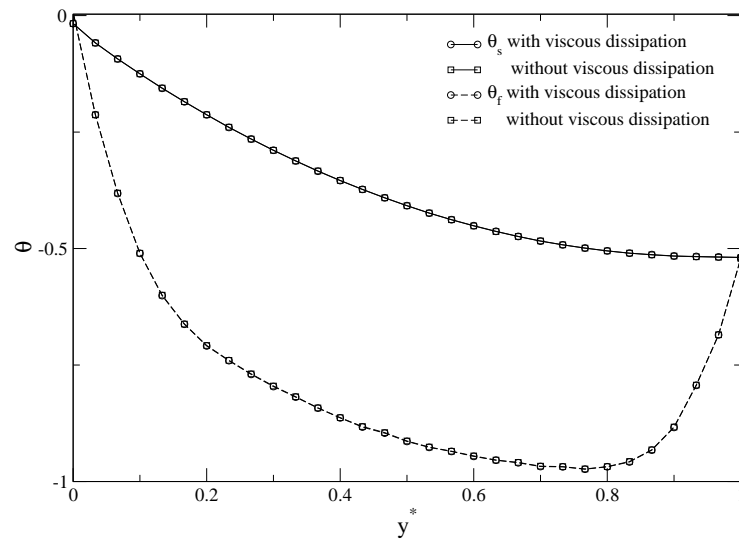


(b)

Figure 4.8: The viscous dissipation effect on non-dimensional temperature profiles for ethylene glycol-based CuO nanofluids ($\alpha_d = 4$ [%], $y^* = y/H$, $f \equiv 1$); (a) $x = 0.0006$ [m], and (b) $x = 0.008$ [m]



(a)



(b)

Figure 4.9: The viscous dissipation effect on non-dimensional temperature profiles for water-based CuO nanofluids ($\alpha_d = 4$ [%], $f \equiv 1$); (a) $x = 0.0006$ [m], and (b) $x = 0.008$ [m]

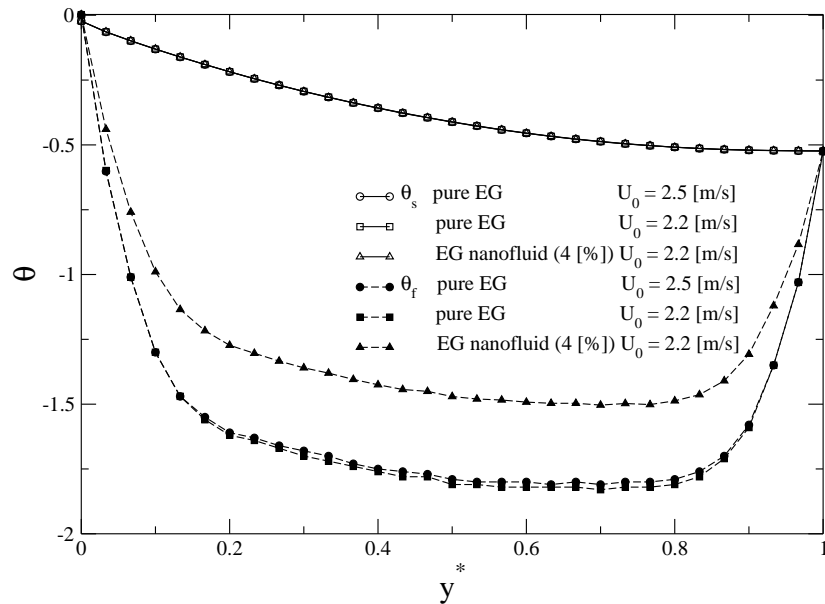


Figure 4.10: Comparison of temperature profiles of pure-fluid cooling and nanofluid cooling cases ($f \equiv 1$)

$[m/s]$ and $U_0 = 2.5 [m/s]$ as well as $\alpha_d = 0 [\%]$ and $4 [\%]$. While the impact of $\Delta U_0 = 0.3 [m/s]$ is negligible, the influence of the presence of CuO -particles is significant.

Impact of the f -function

Turning again to water-based nanofluids, the influence of the augmenting temperature-function f (see Eq. (4.77)) can be evaluated. As shown in Fig. 4.12, the f -function improves heat transfer performance. However, the temperature difference is less for the cases considering the f -function compared to those without it, because the slope of the f -function decreases with particle concentration for the given carrier fluid of the mixture.

The Nusselt number

Base fluid effect

Nusselt number comparisons for the two nanofluids are shown in Fig. 4.11. The Nusselt numbers ($Nu = \frac{hD_h}{k_{eff}}$) were calculated at stations $x = 0.0006, 0.005,$ and $0.008 [m]$. The heat transfer coefficient h was calculated as:

$$h = \frac{\bar{q}_w}{\bar{T}_w - T_m} \quad (4.81)$$

where $\bar{q}_w = q'' \frac{W}{2 \cdot (H+a)}$ and q'' is the heat flux from the bottom plate, T_w is the averaged wall temperature, and T_m is the mass-flux-averaged fluid temperature. The effect of axial conduction heat transfer along the wall was found to be negligible for the given configuration. The Nusselt numbers for EG-based nanofluids are always higher than for the water-based ones. This is due to the fact that EG-based nanofluids are experiencing stronger thermal flow development effects.

For a given location, the Nusselt number decreases with the volume fraction α_d , where the effect is more profound for EG-based nanofluids. This is attributed mainly to both different increase rates of the effective thermal conductivity k_{eff} and the heat transfer coefficient h , and the heat generation due to viscous dissipation. The effective thermal conductivity and dynamic viscosity increase is proportional to the particle concentration α_d . The heat transfer coefficient h is proportional to $Re^m \cdot Pr^n$, where m and n are $1/3$ for laminar flows, so it is proportional to $\alpha_d^{-1/3}$. Therefore, the Nusselt number decreases proportional to $\frac{Pr^{1/3}}{\alpha_d^{4/3}}$. The Nusselt number of ethylen glycol-based nanofluids decreases more with particle concentration α_d due to the higher Prandtl numbers.

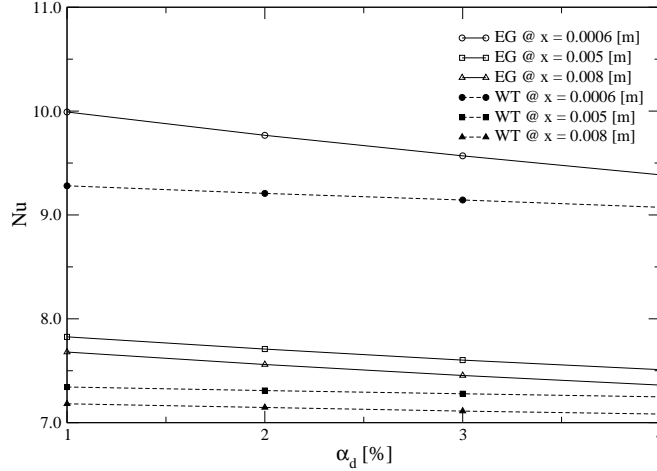


Figure 4.11: Nusselt number comparisons for ethylene glycol- and water-based nanofluids with different CuO -volume fractions ($q'' = 100 [W/cm^2]$, $f \equiv 1$)

Viscous dissipation effect

As indicated in Fig. 4.11, the Nusselt numbers are higher by 2.2 [%] for the base configuration ($a = 50 [\mu m]$) (see Fig. 4.8). Although this is not a significant increase, it implies that the viscous dissipation effect affects the thermal performance of ethylene glycol-based nanofluids, which is not the case for water-based ones.

It is observed that the Nusselt number is 12.93 with viscous dissipation and 13.93 without it. The difference is 7.7 [%] which is about 3.5 times that for the base case. Clearly, the viscous dissipation effect becomes more important for flows in very narrow channels. Thus, the heat transfer performance cannot be endlessly improved by simply adopting narrow channels. The increase in Nusselt number is due to the higher aspect ratios.

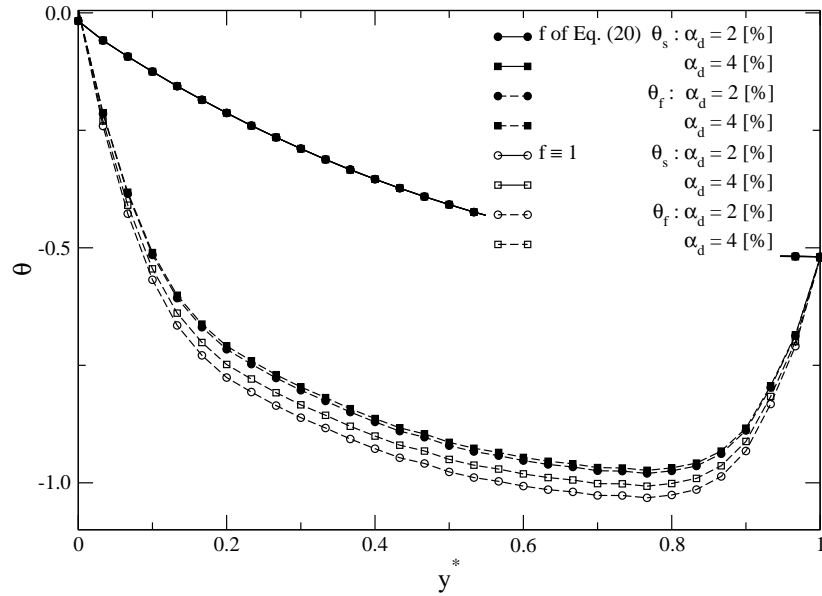


Figure 4.12: The effect of function f on temperature profiles

Influence of the f -function

The non-dimensional fluid temperature is higher for the cases considering the influence of the function f as shown in Fig. 4.12, which implies that the actual temperature dependence of nanofluids improves heat transfer performance. However, the Nusselt number decreases slightly when considering the f -function (Fig. 4.13). This is due to the fact that the effective thermal conductivity increases at a higher rate than the heat transfer coefficient does ($\Delta h \sim \Delta Re^{1/3} \sim \Delta \nabla_x p^{1/3}$).

Particle-particle and particle-wall interactions

As discussed by Koo and Kleinstreuer (2004a), the particle interaction plays an important role in high concentration suspensions. Without the help of either electrostatic stabilization or steric stabilization, particles will flocculate or coagulate when they

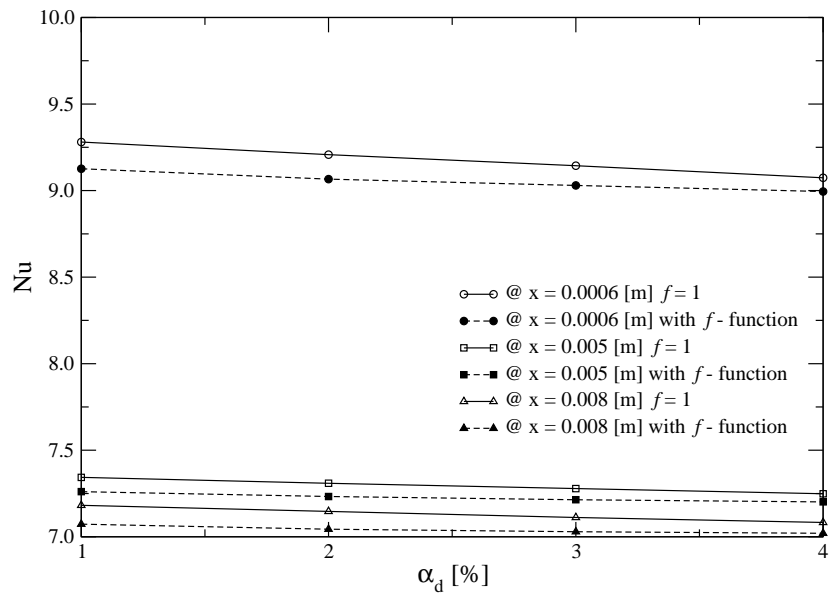


Figure 4.13: The effect of function f on the Nusselt number

are brought together via Brownian motion. For example, most metal oxides have a surface layer of the metal hydroxide which is amphoteric in nature and can become either positively or negatively charged, depending on the pH to generate the electrical double layer (Hunter, 2003). Particles will flocculate when the energy of the electrostatic barrier is not greater than the particle kinetic energy, such that the particle can overcome the energy barrier (Probstein, 2003). In reality, the speed of particles shows a Maxwellian distribution (Schroeder, 2000), and there always exists a fraction of particles which have enough kinetic energy to overcome the energy barrier resulting in flocculation. That possible increase in average particle size might diminish the benefits of nanofluids.

Interactions between wall and particle could be even more problematic. In a quiescent environment, such as in an experimental apparatus to measure the effective thermal conductivity of nanofluids, the wall effect might be not so significant if the size of the vessel is large. However, the particle-liquid-wall interactions become important for flows in microchannels where the surface area of the wall is relatively large. Assuming a much smaller impact region of the double-layer than that of particle attraction, and no flocculation, the equilibrium nanoparticle distribution was derived considering the particle-liquid-wall attraction ($= \frac{AD}{12\eta^2}$, Israelachvili (1992)) and the thermal Brownian forces ($= \kappa T \nabla \ln n$, Probstein (2003)) as:

$$n(y) = C \exp\left(-\frac{A}{12\kappa T} \frac{D}{y}\right) \quad (4.82)$$

where y is the distance from the wall. The nanoparticle distribution depends on the particle size D , and the Hamaker constant A (see Eq. (4.75)) which is a function of the material properties of the particle, wall, and carrier fluid. Figure 4.14 shows the effect of particle-liquid-wall interactions on the nanoparticle distribution near the wall for different nanofluids, where n_0 is the centerline number density. When particles and the wall attract each other, i.e., $A > 0$, the concentration near the wall increases

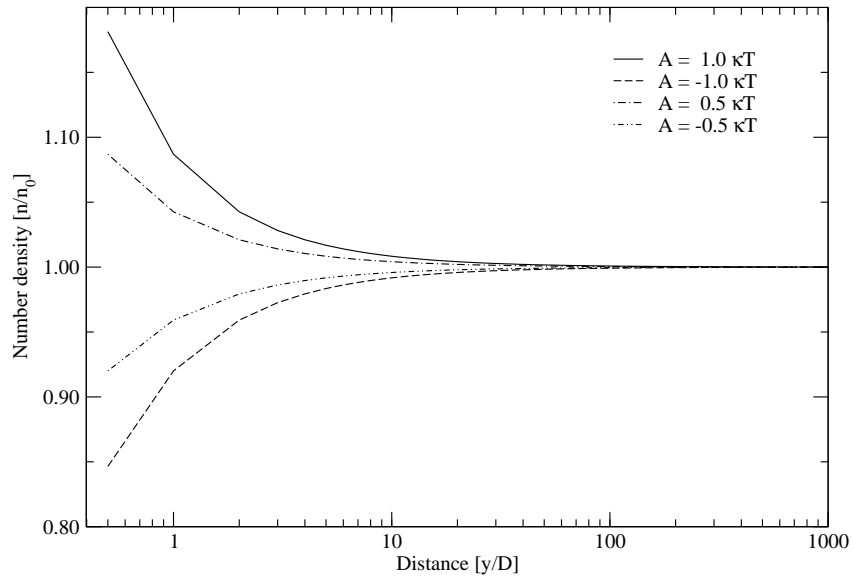


Figure 4.14: The particle-liquid-wall interaction effect on nanoparticle distribution near the wall

as it approaches the wall. In contrast, it decreases when particles and the wall repulse each other, i.e., $A < 0$. The concentration can change near the wall up to 18 % due to the interaction. If the wall material is such that there exists a strong attractive force between particle and wall surface, particles would deposit on the wall forming a layer. In turn, particles would deposit on the mono-layer due to the strong attraction between the particle layer and approaching particles.

The newly developed thermal conductivity and dynamic viscosity model indicates ways to avoid this problem. The strength of the attraction is proportional to the Hamaker constant (see Eq. (4.75)). Therefore, the problem could be resolved by selecting appropriate particle-fluid and particle-solid pairs to minimize the Hamaker constant.

4.2.4 Summary

To optimize the overall cooling performance of nanofluids, the combination of nanoparticle, base fluid and wall, and the channel aspect ratio should be examined thoroughly not to suffer from the anomalous driving force increase. It is recommended

- to use base fluid of high Prandtl number, e.g. Ethylene Glycol and oils;
- with nanoparticles of which the dielectric constant difference with base fluid is large;
- in a channel of high aspect ratio.

to maximize the merits of adding nanoparticles.

4.3 BioMEMS

4.3.1 Introduction

Part of the advanced endeavors in biomedical engineering in the development of integrated neurofunctionomics (NF)/nano-drug delivery (ND) systems, of interest is the easily monitored and controlled target-cell response to stimuli and drugs to facilitate drug development processes. Usually, an integrated NF/ND system is composed of drug preparation, feeding, sensing (test), and feedback parts. The type and dose of drugs are selected in the drug preparation part, while the feeding system guides drugs and buffer fluids into the test part. Test cells are placed into the test section, where they act to drugs and response signals are monitored via the feedback part.

In this study, the governing mechanism of drug delivery are identified, and a methodology to design mixture flow channels and analyze drug delivery processes are presented. One idea is to use multi-stream perfusion systems where drug streams are guided by buffer streams. The potential problems of multi-stream perfusion design are investigated, and remedies are proposed. A new design to avoid the problems is discussed as well.

4.3.2 Theory

The process whereby one phase is distributed into a second one is termed miscible dispersion (Probstein, 2003). In laminar flow, both convection and molecular diffusion will contribute to this dispersion process. Other factors can also enter, including the geometry and any forced unsteadiness. Figure 4.15 shows the effect of convection on dispersion. Drug enters from the left at a constant concentration c_0 , and the flow field is fully developed. Since there is no radial velocity component, drug can never be delivered to the wall by means of convection alone. The drug concentration decreases linearly with distance. As time elapses, the axial concentration gradient becomes flatter. However, the concentration at the wall stays zero. The mechanism by which drug is delivered to the wall is due to radial diffusion.

There are three time scales to be considered for nanofluid system design. The first one is the drug supply cycle time (~ 10 sec), another one is the drug supply convection time (L/U), and the third one is the radial diffusion time (a^2/D), where L is the system length, U is the convection speed or average velocity, a is the half channel depth, and D is the diffusion coefficient. The time scales for a channel design were selected as:

$$t_1 \quad (\text{cycle time scale}) \quad = 10 \text{ [sec]} \quad (4.83)$$

$$t_2 \quad (\text{convection time scale}) \quad < 1 \text{ [sec]} \quad (4.84)$$

$$t_3 \quad (\text{radial diffusion time scale}) \quad = 1 \text{ [sec]} \quad (4.85)$$

Assuming the system length to be 2 [cm], the average velocity of each stream was set at 6 [cm/sec]. The diffusivity of drug was calculated as (Probstein, 2003):

$$D = \frac{\kappa T}{6\pi\mu a} \approx \frac{1.38 \times 10^{-23} \times 300}{6 \times \pi \times 10^{-3} \times 10^{-10}} = 4 \times 10^{-9} \text{ [m/sec]} \quad (4.86)$$

Therefore, the channel depth can be obtained from the relation,

$$t_3 = 1 \text{ [sec]} = \frac{a^2}{D} = \frac{a^2}{4 \times 10^{-9}} \quad (4.87)$$

i.e., in this case $a = 60 \text{ [\mu m]}$.

Boundary conditions

The governing equations are presented in Sect. 2.2. For the current design analysis, uniform inlet velocity conditions for drug and guiding fluid inlets, and ambient pressure condition for the outlet were applied. 0.1 % concentration drug was assumed to enter at the drug supply inlet, and the zero flux condition was used for the walls. For the plenum chamber analysis, a uniform inlet velocity condition was applied to the inlet, while the

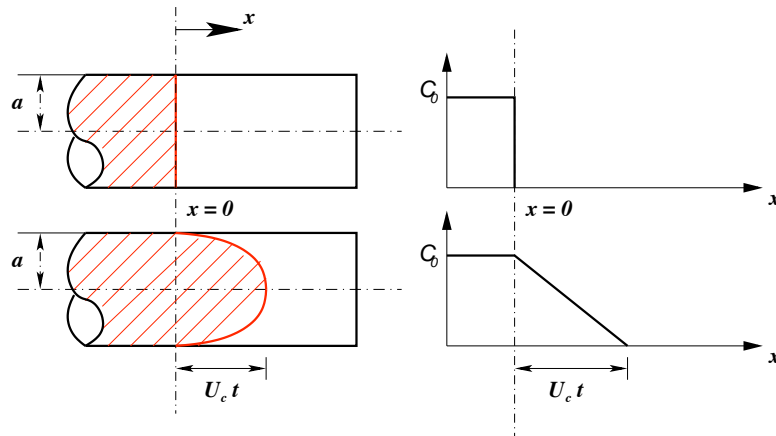


Figure 4.15: Dispersion by convection; (Top) at $t=0$, (Bottom) at time t (sec) (Probstein, 2003)

ambient pressure condition was assumed for the branch-outlets. For the switching channel operation analysis, the pressure boundary conditions for purging fluid and drug supply inlet were implemented. The pressure for the purging fluid was kept at $75 [Pa]$, while the drug supply pressure varied between 60 and $95 [Pa]$, depending on the operation mode.

4.3.3 Results

Analysis of current design

Figure 4.16 shows the velocity distribution at the mid-plane ($Z = 0$). It was found that the velocity profile reached steady state much faster than the concentration profile did. This can be explained in terms of time scales. The time scale for velocity field development is proportional to a^2/ν where that of concentration field is proportional to a^2/D . Since the kinematic viscosity ν of water is about 1000 times greater than the diffusivity, the velocity field develops 1000 times faster. Tracking the residuals during the simulation, this was confirmed.

Comparing Figs. 4.17(a) and 4.18(a), it was found that the concentration field at the mid-plane develops very fast since it develops via convection mechanism. Furthermore, it was

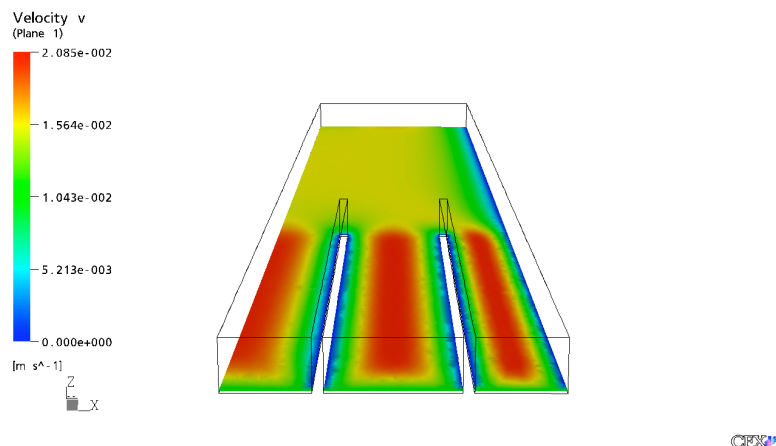


Figure 4.16: Velocity distribution in two-drug-stream system

observed that the concentration profile diffused out and deflected. The deflection is due to the acceleration of the guiding fluid from the right channel. Due to the low Reynolds number of the flow, the velocity field develops in almost no distance. Since the inlet velocities of all branches have the same value, the fluid supply per width is the same at the merging point. However, after fully developed, the fluid supply per width increases approaching the channel center (left side in Figs. 4.17(a) and 4.18(a)). Therefore, the guiding fluid in the right channel expands into the channel center, and it deflects the drug supply stream. *This informs us that we should take care of the diffusion in transverse direction and flow rate of each branch to control the drug supply, which makes the design complicated.* Comparing Figs. 4.17(b) and 4.18(b), it was found that the controlling mechanism of drug delivery is radial diffusion in the given system so that it takes much longer for the drug to be delivered in radial direction than in axial direction. Therefore, *it is necessary to use very shallow channel for the drug to be delivered in desired time.* Figures 4.19 and 4.20 show preliminary layout of the drug delivery system. If a system shown in Fig. 4.19 is used, it is impossible to keep the same flow rate for the 8 streams and it is very difficult to control the concentration for branches near side-walls, because the diffusion becomes more

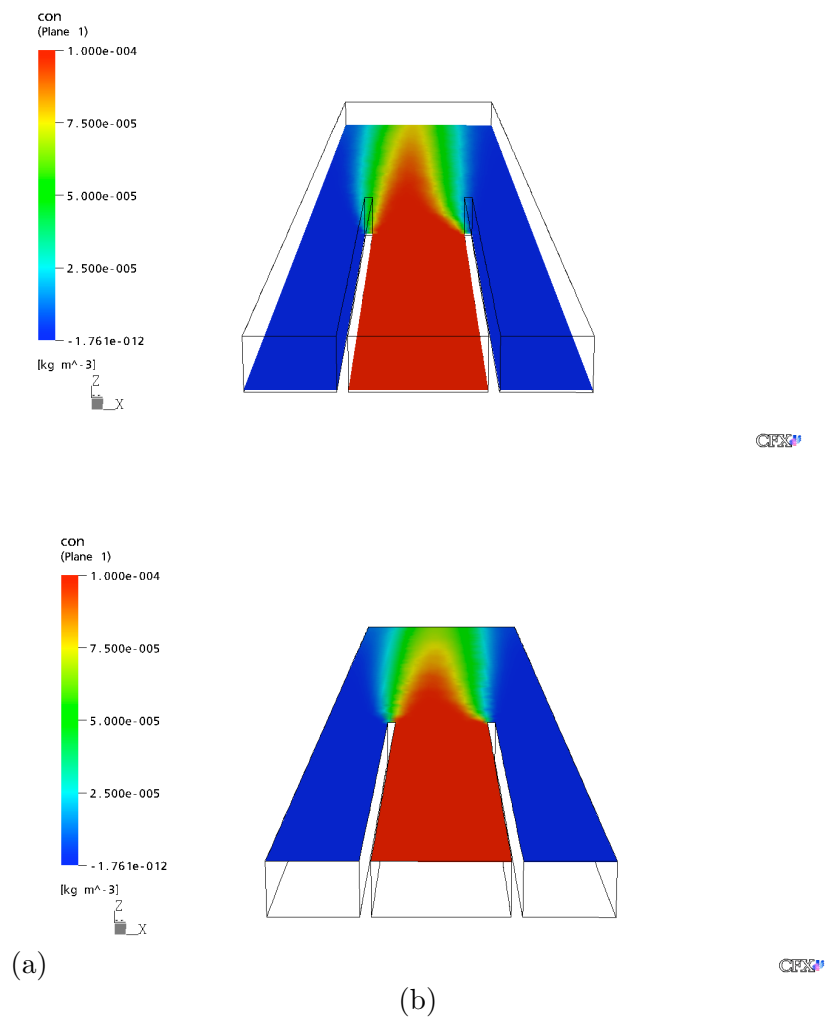


Figure 4.17: Concentration distribution at (a) the mid-plane ($Z=0$) and (b) at the wall ($Z=200 \text{ } [\mu\text{m}]$) at $t = 10 \text{ [sec]}$

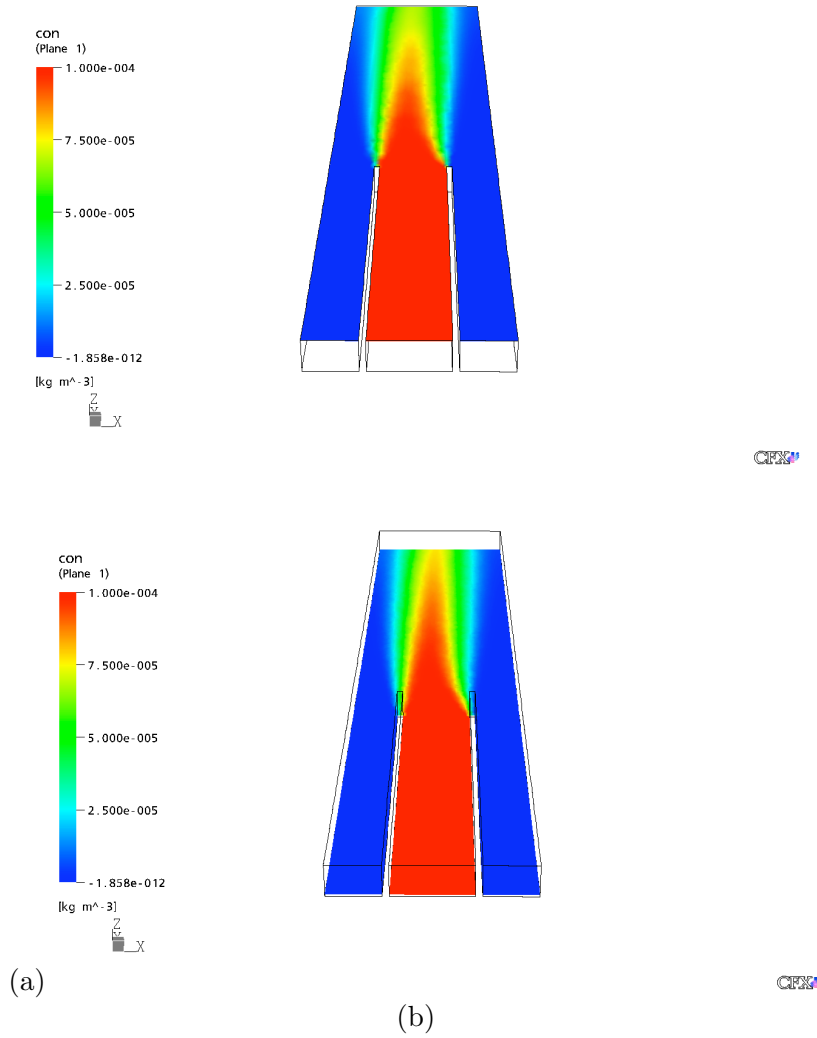


Figure 4.18: Concentration distribution at (a) the mid-plane ($Z=0$) and (b) at the wall ($Z=200 \mu\text{m}$) at $t = 130 \text{ [sec]}$

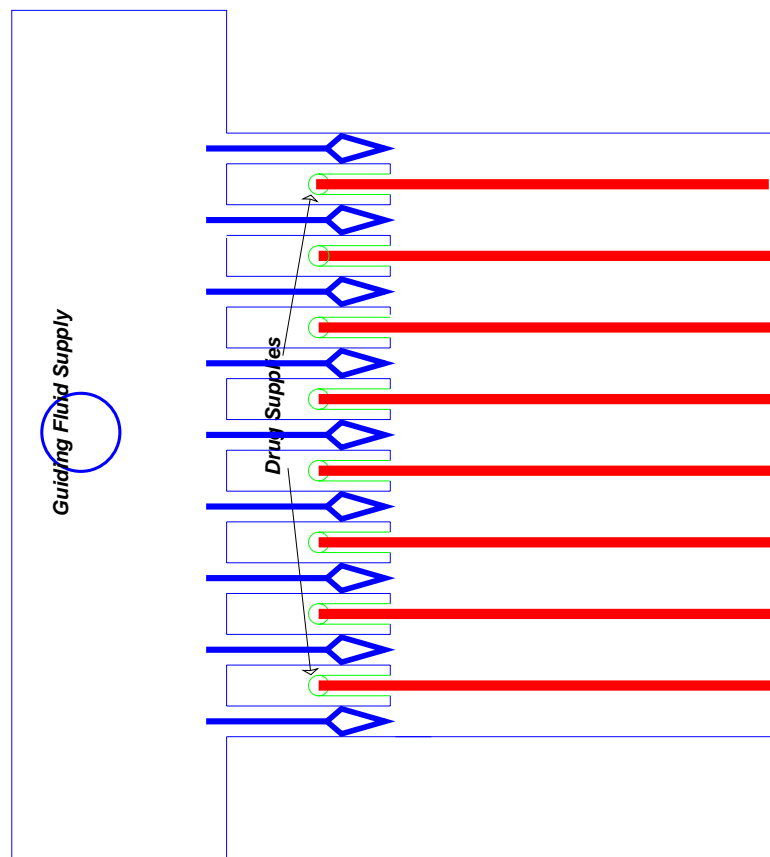


Figure 4.19: Preliminary schematic sketch of the drug delivery channel (1)

important due to the slow flow velocity. Hence, the concentration changes significantly in both transverse and longitudinal directions.

Remedies to the current design

To avoid this problem, a new design is proposed in Fig. 4.20. Only center part of the flow field is used where flow velocity is fast and flow field changes slowly so that we can keep the flow rate differences and concentration change minimal.

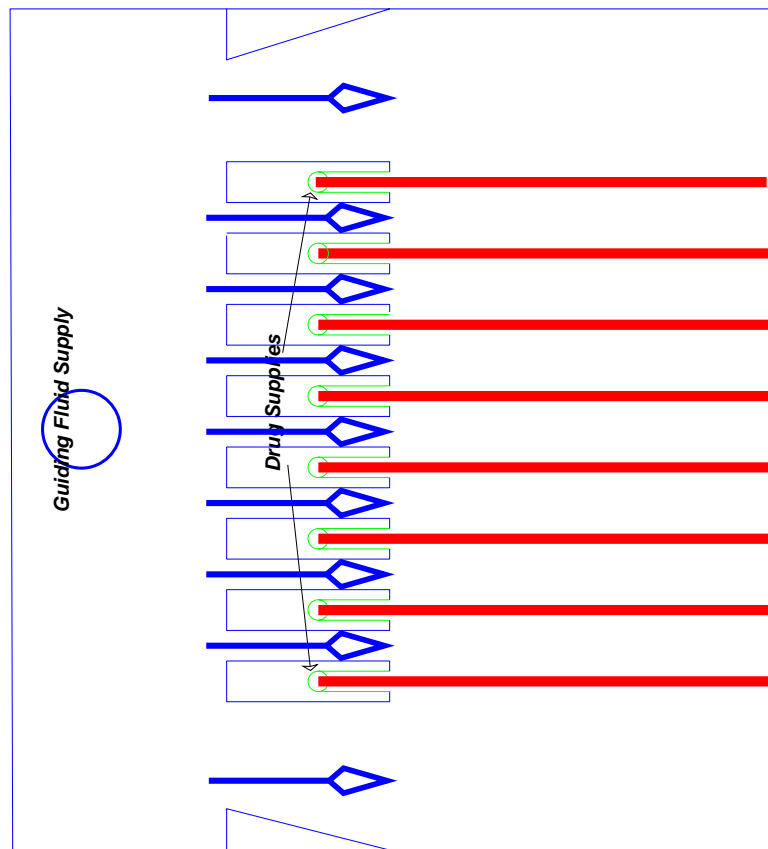


Figure 4.20: Preliminary schematic sketch of the drug delivery channel (2)

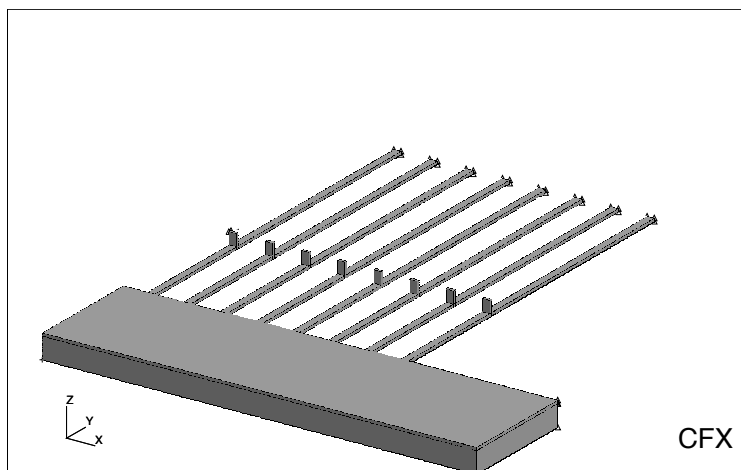


Figure 4.21: Sketch of the new system

A new system design

An alternative design was prepared to avoid the difficulties encountered with the current design. The biggest difference is the existence of walls to divide 8 streams. One of the problems for the current design arises from the fact that there still exists concentration gradient between the drug and guiding streams, which results in change of the concentration in the axial direction. In the new design, the concentration can be kept constant through the testing sections.

Figure 4.21 shows the sketch of the new system. A plenum chamber sits in the inlet section. It maintains the inlet velocity much lower than those in branches owing to its large cross-sectional area, which allow the pressure drop in it to be negligible. Figures 4.22-4.24 shows the pressure and velocity distributions in the plenum chamber and channels. The pressure was kept uniform throughout the chamber, which results in the same pressure gradients in all branch channels.

The switching branches can alter the incoming fluid to the test section by adjusting drug inlet pressure; setting the drug supply pressure higher than that of purging fluid supply-side, drugs can be supplied, while the purging fluid can go through the testing section by

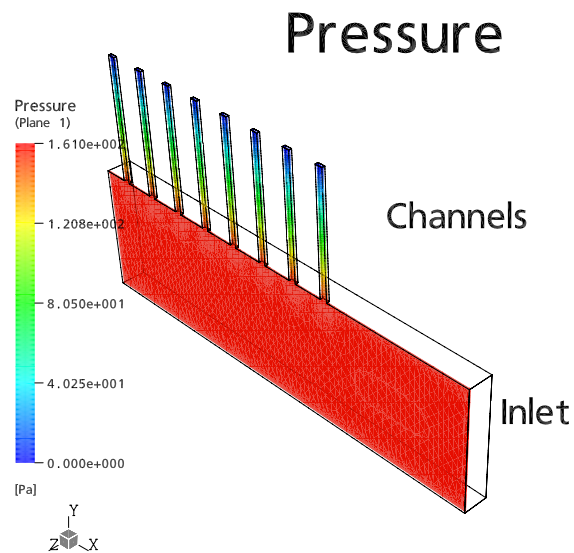


Figure 4.22: The function of a plenum chamber (top-view); the pressure gradients are uniform for all branches.

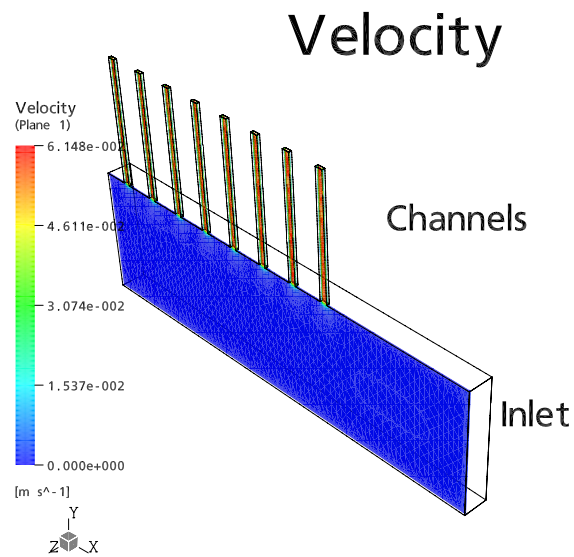


Figure 4.23: The function of a plenum chamber (top-view); the velocity fields are uniform for all branches.

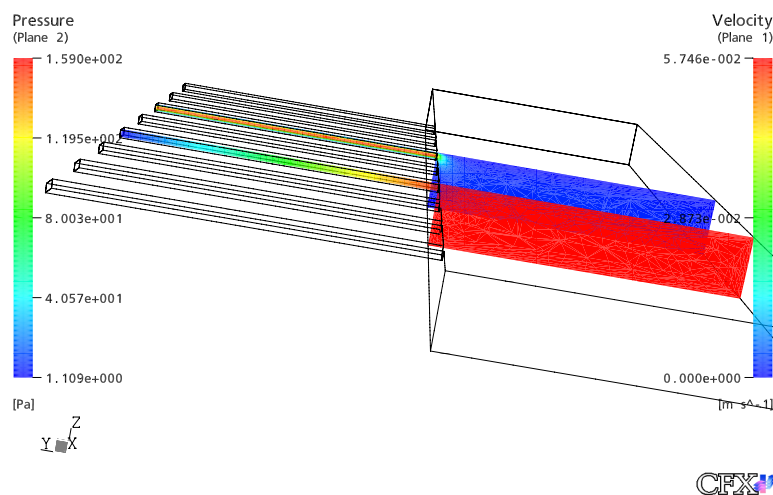


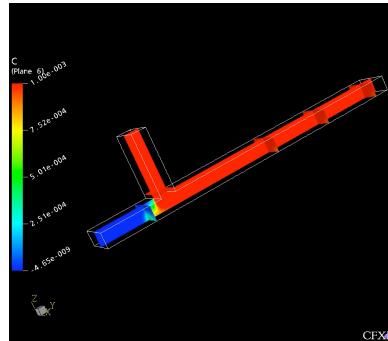
Figure 4.24: The function of a plenum chamber (side-view)

lowering the drug supply pressure. Figures 4.25-4.27 shows the snapshots of the operations. The pressure of the guiding fluid inlet side was kept to be 75 [Pa], while that of the drug inlet side varied from 60 [Pa] during purging process to 95 [Pa] during drug supply process. When the pressure at the drug supply inlet is lower than 60 [Pa], the contact line between the drug and guiding fluid rises in the +z-direction, whereas the drug leaks into the testing section when the pressure level is higher than that.

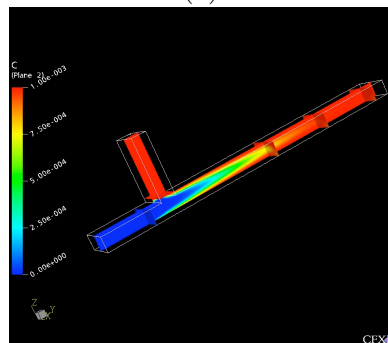
Figure 4.26 informs that the velocity field develops much faster than the concentration field; the velocity field development was completed in less than 0.001 [sec], while it takes less than 1 [sec] for the concentration to fully develop. In contrast to the current design, the new design ensures that the concentration field is very uniform and develops very fast.

The effect of drug particle concentration on mass flow rate

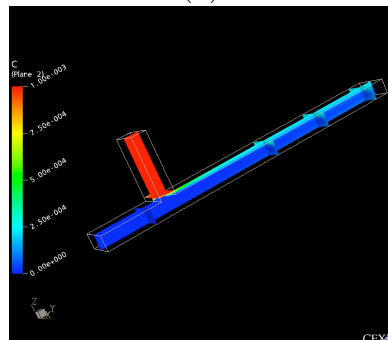
Analyses up to this point did not consider the effect of particle concentration on effective dynamic viscosity. The effective dynamic viscosity change affects the mass flow



(a)



(b)



(c)

Figure 4.25: Snapshots of concentration distributions during purging process; (a) 0.001 [sec]; (b) 0.017 [sec]; (c) 0.041 [sec]

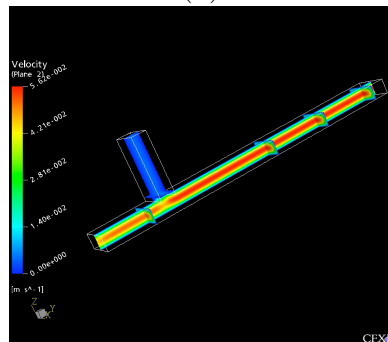
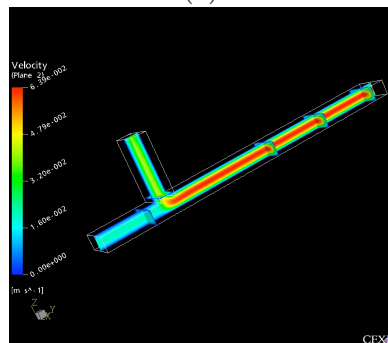
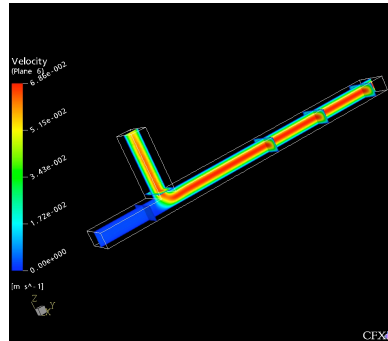
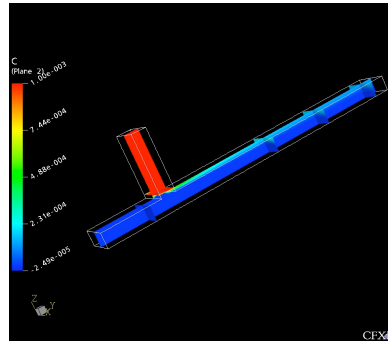
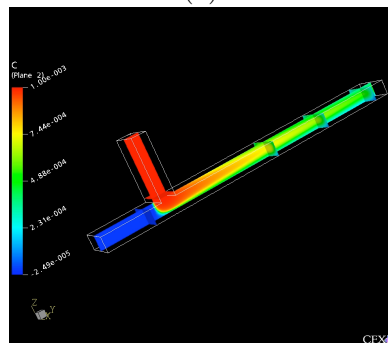


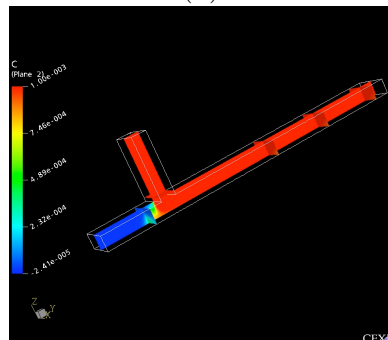
Figure 4.26: The snapshots of velocity fields during purging process; (a) 0.001 [sec]; (b) 0.003 [sec]; (c) 0.009 [sec]



(a)



(b)



(c)

Figure 4.27: The snapshots of concentration distributions during drug supply process; (a) 0 [sec]; (b) 0.05 [sec]; (c) 1 [sec]

rate of the drug for the given operating pressure condition. Therefore, the prediction of the effective dynamic viscosity of the drug fluid is important. The material of nanoparticles and nanospheres used for drug delivery is well documented in Kumar (2000). As explained, the function β and f should be determined experimentally since they depend on the particle type and shape. Unfortunately, no experimental data is available for the nanoparticle suspensions for the nanoparticle materials listed in Kumar (2000). The concentration of nanoparticles depends on the dosage of drug, and it could vary from very low ~ 1 [%] to relatively high ~ 30 [%]. Since the effective dynamic viscosity model was originally developed for nanofluids where the particle concentration is usually less than 4 [%], the model might not work for the high particle concentration cases, where other effects could arise. For conventional microparticles, the shear induced particle collision effect greatly increases the effective dynamic viscosity, which might not be important for nanoparticle suspensions, since the particles are more subject to the Brownian motion compared to the flow shear.

In this study, the particle Brownian motion effect is neglected due to the shortage of the information.

$$\frac{\mu_{eff}}{\mu_0} = 1 + 2.5\alpha_d \quad (4.88)$$

where μ_{eff} is the effective dynamic viscosity, and μ_0 is the dynamic viscosity of pure liquid.

The particle concentration was considered up to 10 [%], since, conventionally, the Einstein model is considered to hold for dilute case ($\alpha_d < 0.1$). Figure 4.28 shows the effect of particle concentration on the mass flow rate of the drug delivery side. The non-dimensional flow rate represents the ratio of the inlet drug flow rate with particles to that without particles. The pressure at the drug inlet was kept at 95 [Pa], and 60 [Pa] at the purging flow inlet. The mass flow rate decreases linearly with particle concentration α_d . It was observed that the mass flow rate decreased to 80 [%] compared to the pure liquid case, which means the mean flow velocity decreases correspondingly. With the particle Brownian motion, it could

be worse than that. The most important thing is to meet the requirement that the drug supply should be completed in a given time. For the given design, the system should work since the concentration gradient developed within 1 [sec] without particles, and it would increase to 1.2 [sec], while the cycle time is 10 [sec].

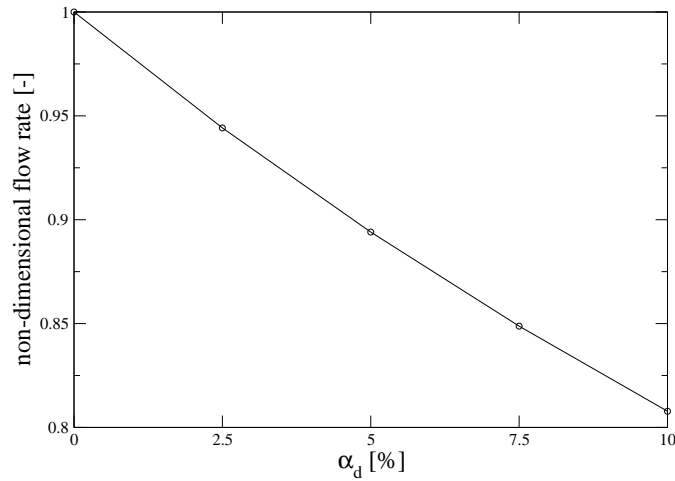


Figure 4.28: Effect of particle concentration on mass flow rate supplied to the testing section

4.3.4 Summary

From the investigations to design an efficient drug delivery system, the following results were obtained;

- Time and length scale comparisons provide very useful criteria for the system design.
- Open 8 stream-design could suffer from the non-uniform concentration and difficulty in controlling drug supply and purging processes.
- Plenum chamber design enables uniform pressure and flow rate distributions for sub-branch channels.

- Wall guided design provides uniform concentration and ease of operation.
- The contact line between drug and purging fluid can be adjusted by manipulating the pressure of the drug and purging fluid supplies.

Chapter 5

CONCLUSIONS and FUTURE WORK

5.1 Conclusions and Novel Contributions

The following conclusions can be drawn from this study.

- *The continuum approach is still valid in micro-conduits with complementary sub-models to take key micro-scale effects into considerations.*

1. The deviations from conventional theory were found to be the results of micro-scale phenomena such as surface roughness, viscous dissipation, and inlet geometry effects, which could be neglected in macro-scale conduits.
2. The porous medium layer model was developed to consider the surface roughness effect on momentum and heat transfer.
3. Using scale analysis, viscous dissipation was found to become more important in smaller channels.
4. The sudden contraction in the entry of the micro-conduit to connect with macro-conduit was observed to cause local flow instabilities to elongate the entrance length.

- *Particle Brownian motion is the key mechanism to increase the effective thermal conductivity and dynamic viscosity.*

1. A new effective thermal conductivity and dynamic viscosity model has been developed to consider the particle Brownian motion and induced fluid motion. It is composed of static and dynamic parts, i.e., $k_{eff} = k_{static} + k_{dynamic}$.
2. The particle Brownian motion effect is a function of particle concentration, particle size, particle shape, particle properties, the particle-and-liquid combination, and liquid properties.
3. The interparticle interaction effect becomes dominant at high concentrations ($\alpha_d > 1$ [%]), while it is negligible for low concentrations ($\alpha_d < 1$ [%]) due to the retardation effect of the interparticle interaction.

4. The Hamaker constant A is a very important parameter for particle interaction as it is related to the dielectric constant difference between particle and base liquid.
 5. The new k_{eff} -model is consistent with conventional models. The dynamic, $k_{dyn.}$, part becomes negligible as the particle size increases.
- *The application of nanofluids to micro heat-sinks for performance enhancement seems to be promising.*

Model comparisons:

1. The fin model, the porous medium model, and full-equation model including viscous dissipation effect, were compared, and the fin model was found to be inadequate for micro heat-sinks.
2. The porous medium model was derived directly from the full equation model. The porous medium model is a result of one integration of the full equation model under the assumptions of fully developed flows between parallel plates.
3. The porous medium model can provide a very conservative design for micro heat-sinks.
4. In reality, the temperature profiles do not fully develop for conjugate heat transfer problems as Shah and London (1978) reported, which means that the porous medium model yields only very conservative results.

Nanofluids

1. Nanofluids are suitable for micro heat-sink performance improvement.
2. Ethylene glycol-base nanofluids showed greater performance improvement than water-based ones.
3. Viscous dissipation effect becomes very important as the channel size decreases, and it is more important for ethylene glycol-base nanofluids compared to water-based ones.

4. The function f to capture the particle interaction effect greatly improves the thermal conductivity, and it should be obtained experimentally for nanofluids under consideration.
 5. The information on the interparticle potential provides a guideline to select the the particle-liquid-wall combination. The dielectric constant difference should be great between particle and base fluid, while it should be small between particle and wall material to avoid clogging.
- *A new methodology to design a drug delivery system was developed.*
 1. The main mechanism for drug delivery was identified as slow radial diffusion, and the time scale for it should be kept well below drug delivery duration to achieve well controlled drug delivery.
 2. A wall guided drug delivery system is superior to an open multi-stream design which suffers from uncontrollable radial diffusion, in terms of uniform drug delivery and ease of operation.
 3. A plenum chamber design ensures uniform pressure and flow distributions for sub-branch channels.

5.2 Future Work

As outlined, different physical phenomena govern on different scales. The most important thing to be successful in micro- and nano-scale engineering, is the determination and understanding of the governing forces to activate and control the dynamics on such scales. Some suggestions are made here to improve the understanding of micro- and nano-scale phenomena investigated in this study:

- The newly developed effective thermal conductivity and dynamic viscosity model should be expanded to consider other effects such as fluid pH, addition of dispersants and ions, external electromagnetic forces, etc.
- The functions $\beta(\alpha_d)$ and $f(T, \alpha_d)$ are related to each other and are not well defined yet. The origin and role of the functions are completely different: β arises from the hydrodynamic interaction of the fluid cells, while f originates from particle interactions in the carrier fluid. As Chapman-Enskog expansion considers intermolecular interaction for gas flows, a new theory could be provided to determine the functions β and f analytically. To achieve this, large amounts of information on intermolecular, interparticular, ion-particle interaction have to be provided, and a molecular level approach might be necessary.

Bibliography

- Inc. AEA Technology. *CFX-4.4: Solve CFX International*. AEA Technology, Inc., Oxfordshire, UK, 2001.
- J. Barrat and F. Chiaruttini. Kapitza resistance at the liquid-solid interface. *Molecular Physics*, 101(11):1605–1610, 2003.
- J. Bear. *Dynamics of fluids in porous media*. American Elsevier publishing company, Inc., New York, NY, 1972.
- A. Bejan. *Convection Heat Transfer*. John Wiley & Sons, Inc., New York, second edition, 1995.
- A. Beskok and G.E. Karniadakis. Simulation of heat and momentum transfer in complex micro-geometry. *Journal of Thermophysics and Heat Transfer*, 8:355–370, 1994.
- A. Beskok and G.E. Karniadakis. A model for flows in channels, pipes and ducts at micro and nano scales. *Microscale Thermophysical Engineering*, 3:43–77, 1999.
- K. Binder, J. Horbach, W. Kob, W. Paul, and F. Varnik. Molecular dynamics simulations. *Journal of Physics: Condensed matter*, 16:S429–S453, 2004.
- G. A. Bird. *Molecular gas dynamics and the direct simulation of gas flows*. Clarendon Press, New York, NY, 1994.

- S. Chapman and T. G. Cowling. *Mathematical Theory of Non-Uniform Gases*. Cambridge University Press, Cambridge, UK, 2nd edition, 1951.
- C.S. Chen, S.M Lee, and J.D. Sheu. Numerical analysis of gas flow in microchannels. *Numerical Heat Transfer, A*, 33:749–762, 1998.
- S.U.S. Choi. Enhancing thermal conductivity of fluids with nanoparticles. *FED*, 231:99–103, 1995.
- S.U.S. Choi, Z.G. Zhang, W. Yu, F.E. Lockwood, and E.A. Grulke. Anomalous thermal conductivity enhancement in nanotube suspensions. *Applied Physics Letters*, 79(14): 2252–2254, 2001.
- G. Croce and P. D’Agaro. Numerical analysis of roughness effect on microtube heat transfer. *Superlattices and Microstructures*, 35:601–616, 2004.
- C. Crowe, M. Sommerfeld, and Y. Tsuji. *Multiphase Flows with droplets and particles*. CRC Press, Boca Raton, FL., 1998.
- S.K. Das, N. Putra, P. Thiesen, and W. Roetzel. Temperature dependence of thermal conductivity enhancement for nanofluids. *Journal of Heat Transfer*, 125:567–574, 2003.
- W. M. Deen. *Analysis of Transport Phenomena*. Oxford Univ. Press, New York, NY, 1998.
- J.A. Eastman, S.U.S. Choi, S. Li, W. Yu, and L.J. Thompson. Anomalous increased effective thermal conductivities of ethylene glycol-based nanofluids containing copper nanoparticles. *Applied Physics Letters*, 78:718–720, 2001.
- W. Ehrfeld. Electrochemistry and microsystems. *Electrochimica Acta*, 48:2857–2868, 2003.
- M. Elwenspoek, T.S. Kannerubj, R. Miyake, and J.H.J. Fluitman. Towards integrated microliquid handling systems. *Journal of Micromechanics and Microengineering*, 4:227–245, 1994.

- M. Gad-el Hak. The fluid mechanics of microdevices-the freeman scholar lecture. *Journal of Fluid Engineering*, 121:5–33, 1999.
- P. Gravesen, J. Branebjerg, and O.S. Jensen. Microfluidics-a review. *Journal of Micromechanics and Microengineering*, 3:168–182, 1993.
- Z. Guo and Z. Li. Size effect on microscale single-phase flow and heat transfer. *International Journal of Heat and Mass Transfer*, 46:149–159, 2003.
- R.L. Hamilton and O.K. Crosser. Thermal conductivity of heterogeneous two-component systems. *I and EC Fundamentals*, 125(3):187–191, 1962.
- J.C. Harley, Y. Huang, Bau H.H., and J.N. Zemel. Gas flow in micro-channels. *Journal of Fluid Mechanics*, 285:257–274, 1995.
- H.A. Hassan. and D.B. Hash. A generalized hard-sphere model for monte-carlo simulation. *Physics of Fluids A-Fluid dynamics*, 5:738–744, 1993.
- C.M. Ho and Y.C. Tai. Micro-electro-mechanical systems (mems) and fluid flow. *Annual Review of Fluid Mechanics*, 30:579–612, 1998.
- Z. S. Hu and J. X. Dong. Study on antiwear and reducing friction additive of nanometer titanium oxide. *Wear*, 216:92–96, 1998.
- R. J. Hunter. *Introduction to Modern Colloid Science*. Oxford Science Publications, Oxford, UK, 2003.
- F. P. Incropera and D. P. DeWitt. *Fundamentals of heat and mass transfer*. John Wiley & Sons, Inc., New York, third edition edition, 1990.
- J. Israelachvili. *Intermolecular and Surface Forces*. Academic press, Amsterdam, second edition edition, 1992.
- S. P. Jang and S. U. S. Choi. Role of brownian motion in the enhanced thermal conductivity of nanofluids. *Applied Physics Letters*, 84(21):4316–4318, 2004.

- D. Joseph. Interrogations of direct numerical simulation of solid-liquid flow, 2002. URL <http://efluids.com/efluids/books/joseph.htm>.
- J. Judy, D. Maynes, and B.W. Webb. Characterization of frictional pressure drop for liquid flows through microchannels. *International Journal of Heat and Mass Transfer*, 45(17): 3477–3489, 2002.
- T.K. Jun and C.J. Kim. Valveless pumping using traversing vapor bubbles in microchannels. *Journal of Applied Physics*, 83(11):5658–5664, 1998.
- P. Keblinski, S.R. Phillpot, S.U.S. Choi, and J.A. Eastman. Mechanisms of heat flow in suspensions of nano-sized particles (nanofluids). *International Journal of Heat and Mass Transfer*, 45:855–863, 2002.
- C. J. Kim. Mems devices based on the use of surface tension, 1999. URL http://cjmems.seas.ucla.edu/papers/CJ_ISDRS_99.pdf.
- S. J. Kim and S.P. Jang. Effects of the darcy number, the prandtl number, and the reynolds number on local thermal non-equilibrium. *International Journal of Heat and mass Transfer*, 45:3885–3896, 2002.
- S. J. Kim, D. Kim, and D. Lee. On the local thermal equilibrium in microchannel heat sinks. *International Journal of Heat and mass Transfer*, 43:1735–1748, 2000.
- S. J. Kim, J. W. Yoo, and S. P. Jang. Thermal optimization of a circular-sectored finned tube using a porous medium approach. *International Journal of Heat and mass Transfer*, 124:1026–1033, 2002.
- S.J. Kim. Methods for thermal optimization of microchannel heat sinks. *Heat Transfer Engineering*, 25:37–49, 2004.
- C. Kleinstreuer. *Engineering Fluid Dynamics*. Cambridge University Press, New York, 1997.

- C. Kleinstreuer. *Two-Phase Flow: Theory and Applications*. Taylor & Francis, New York, NY, 2003.
- C. Kleinstreuer and J. Koo. Computational analysis of wall roughness effects for liquid flow in micro-conduits. *Journal of Fluids Engineering*, 126:1–9, 2004.
- J.C.Y. Koh and R. Colony. Heat transfer of microstructures for integrated circuits. *International Communication of Heat and mass Transfer*, 13:89–98, 1986.
- J. Koo and C. Kleinstreuer. Liquid flow in microchannels: experimental observations and computational analyses of microfluidics effects. *Journal of Micromechanics and Micro-engineering*, 13:568–579, 2003.
- J. Koo and C. Kleinstreuer. A new thermal conductivity model for nanofluids. *Journal of Nanoparticle Research*, in press, 2004a.
- J. Koo and C. Kleinstreuer. Viscous dissipation effects in microtubes and microchannels. *International Journal of Heat and mass Transfer*, 47:3159–3169, 2004b.
- J. Koo and C. Kleinstreuer. Analysis of surface roughness effects on heat transfer in micro-conduits. *International Journal of Heat and Mass Transfer*, in press, 2005a.
- J. Koo and C. Kleinstreuer. Impact analysis of nanoparticle motion mechanisms on the thermal conductivity of nanofluids. *International Communications in Heat and Mass Transfer*, submitted, 2005b.
- J. Koo and C. Kleinstreuer. Laminar nanofluid flow in micro heat-sinks. *International Journal of Heat and Mass Transfer*, in press, 2005c.
- K. Koura and H. Matsumoto. Variable soft sphere molecular model for inverse-power-law or lennard-jones potential. *Physics of Fluids A-Fluid dynamics*, (2459-2465), 1991.
- I. M. Krieger. Rheology of monodisperse latices. *Advances in Colloid and Interface Science*, 3:111–136, 1972.

- D. H. Kumar, H. E. Patel, V. R. R. Kumar, T. Sundararajan, T. Pradeep, and S. K. Das. Model for heat conduction in nanofluids. *Physical review letters*, 93(14):175–180, 144301(1)-144301(4) 2004.
- M. N. V. Kumar. Nano and microparticles as controlled drug delivery devices. *Journal of pharmacy and Pharmaceutical Sciences*, 3:234–258, 2000.
- A. V. Kuznetsov. Influence of thermal dispersion on forced convection in a composite parallel-plate channel. *Z. angew. Math. Phys.*, 52:135–150, 2001.
- A. V. Kuznetsov and M. Xiong. Numerical simulation of the effect of thermal dispersion on forced convection in a circular duct partly filled with a brinkman-forchheimer porous medium. *International Journal of Numerical Methods for Heat and Fluid Flow*, 10:488–501, 2000.
- P. C. Lee, F. G. Tseng, and C. Pan. Bubble dynamics in microchannels. part i: single microchannel. *International Journal of Heat and Mass Transfer*, 47:5575–5589, 2004.
- S. Lee, S.U.S. Choi, S. Li, and J.A. Eastman. Measuring thermal conductivity of fluids containing oxide nanoparticles. *Journal of Heat Transfer*, 121:280–289, 1999.
- D. Li. Electro-viscous effects on pressure-driven liquid flow in microchannels. *Colloids and Surfaces, A*, 195:35–57, 2001.
- H. Y. Li, F. G. Tseng, and C. Pan. Bubble dynamics in microchannels. part ii: two parallel microchannels. *International Journal of Heat and Mass Transfer*, 47:5591–5601, 2004.
- J. Li, Z. Li, and B. Wang. Experimental viscosity measurements for copper oxide nanoparticle suspensions. *Tsinghua Science and Technology*, 7:198–201, 2002.
- K. V. Liu, S. U. S. Choi, and K. E. Kasza. Measurements of pressure drop and heat transfer in turbulent pipe flows of particulate slurries. Technical Report ANL-88-15, Argonne National Laboratory, 1988.

- G. M. Mala and D. Li. Flow characteristics of water in microtubes. *International Journal of Heat and Mass Transfer*, 20:142–148, 1999.
- H. Masuda, A. Ebata, K. Teramae, and N. Hishinuma. Alteration of thermal conductivity and viscosity of liquid by dispersion ultra-fine particles (dispersion of $\gamma\text{-Al}_2\text{O}_3$, SiO_2 , and TiO_2 ultra-fine particles). *Netsu Bussei (Japan)*, 4(43):227–233, 1993.
- Inc. Mathworks. *Using Matlab 6*. The Mathworks, Inc., Natick, MA, 2002.
- MatWeb. Matweb-material property data, 1999. URL <http://www.matweb.com>.
- J.C. Maxwell. *A treatise on electricity and magnetism*. Oxford Univ. Press, Cambridge, UK, 2nd edition, 1904.
- MicroFab. Fluid properties effects on ink-jet device performance. Technical Report 99-02, MicroFab Technologies, Inc., 1999. URL www.microfab.com/technotes/technote99-02.PDF.
- A. F. Mills. *Heat transfer*. Irwin, Inc., Homewood, IL, international student edition, 1992.
- G. L. Morini. Single-phase convective heat transfer in microchannels:a review of experimental results. *International Journal of Thermal Sciences*, 43:631–651, 2004.
- D.A. Nield and A. Bejan. *Convection in Porous Media*. Springer-Verlag, New York, NY, 1992.
- T. Ohara and D. Suzuki. Intermolecular energy transfer at a solid-liquid interface. *Microscale Thermophysical Engineering*, 4:189–196, 2000.
- E.S. Oran, C.K. Oh, and Cybyk B.Z. Direct simulation monte carlo: Recent advances and applications. *Annual Review of Fluid Mechanics*, 30:403–441, 1998.
- B.C. Pak and Y.I. Cho. Hydrodynamic and heat transfer study of dispersed fluids with submicron metallic oxide particles. *Experimental heat transfer*, 11:151–170, 1998.

- I. Papautsky, J. Brazzle, T. Ameel, , and A. B. Frazier. Laminar fluid behavior in microchannels using micropolar fluid theory. *Sensors and Actuators*, 73:101–108, 1999.
- H. Patel, S. Das, T. Sundararajan, A. Sreekumaran, B. George, and T. Pradeep. Thermal conductivities of naked and monolayer protected metal nanoparticle based nanofluids: Manifestation of anomalous enhancement and chemical effects. *Applied Physics Letters*, 83(14):2931–2933, 2003.
- X. F. Peng and G. P. Peterson. Convective heat transfer and flow friction for water flow in microchannel structures. *International Journal of Heat and Mass Transfer*, 39:2599–2608, 1996.
- X. F. Peng, G. P. Peterson, and Wang B. X. Frictional flow characteristics of water flowing through rectangular microchannels. *Experimental heat transfer*, 7:249–264, 1994.
- R.H. Perry and D. Green. *Perry's Chemical Engineers' Handbook*. McGraw-Hill, New York, NY, sixth edition, 1984.
- J. Pfahler, J. Harley, and H. Bau. Liquid transport in micron and submicron channels. *Sensors and Actuators*, A21-A23:431–434, 1990.
- J. Pfahler, J. Harley, H. Bau, and J.N. Zemel. Gas and liquid flow in small channels. *Micromechanical Sensors, Actuators, and Systems*, DSC 32:49–60, 1991.
- R.F. Probstein. *Physicochemical hydrodynamics*. Wiley Interscience, Hoboken, NJ., second edition, 2003.
- W. Qu, G. M. Mala, and D. Li. Pressure-driven water flows in trapezoidal silicon microchannels. *International Journal of Heat and Mass Transfer*, 43:353–364, 2000.
- L. Ren, W. Qu, and D. Li. Interfacial electrokinetic effects on liquid flow in microchannels. *Int. J. Heat Mass Trans.*, 44:3125–3134, 2001.
- D.V. Schroeder. *An introduction to thermal physics*. Addison Wesley Longman, San Francisco, CA, 2000.

- L.M. Schwartz, E.J. Garboczi, and D.P. Bentz. Interfacial transport in porous media: Application to dc electrical conductivity of mortars. *Journal of applied physics*, 78(10): 5898–5908, 1995.
- R. K. Shah and A. L. London. *Laminar Flow Forced Convection in Ducts*. Academic Press, New York, 1978.
- K. Sharp. *Experimental investigation of liquid and particle laden flows in microtubes*. PhD thesis, University of Illinois at Urbana-Champaign, Urbana-Champaign, IL, 2001.
- C. B. Sobhan and S. V. Garimella. A comparative analysis of studies on heat transfer and fluid flow in microchannels. *Microscale Thermophysical Engineering*, 5:293–311, 2001.
- C. L. Tien and S. M. Kuo. Analysis of forced convection in microstructures for electronic system cooling. In *Proc. Int. Symp. Cooling Technology for Electronic Equipment*, pages 217–226, Honolulu, HI, 1987.
- K.C. Toh, X.Y. Chen, and J.C. Chai. Numerical computation of fluid flow and heat transfer in microchannels. *International Journal of Heat and Mass Transfer*, 45:5133–5141, 2002.
- D. Trebotich, J. Jirshberg, J. Teng, and D. Liepmann. Optimization of a mems based micro capillary pumped loop for chip-level temperature control. *Technical Proceedings of the 2001 International Conference on Modeling and Simulation of Microsystems*, pages 262–265, March 2001.
- D. C. Tretheway and C. D. Mainhart. Apparent fluid slip at hydrophobic microchannel walls. *Physics of Fluids*, 14(3):9–12, 2002.
- D. C. Tretheway and C. D. Mainhart. A generating mechanism for apparent fluid slip in hydrophobic microchannels. *Physics of Fluids*, 16(5):1509–1515, 2004.
- W. Trimmer and R. H. Stroud. *The MEMS Handbook, Chapter 2: Scaling of Micromechanical Devices*. CRC Press, Boca Raton, FL., 2002.

- J. Tsai and L. Lin. A thermal-bubble-actuated micronozzle-diffuser pump. *J. Microelectromech. S.*, 11:665–671, 2002.
- C.P. Tso and S.P. Mahulikar. The use of the Brinkman number for single phase forced convective heat transfer in microchannels. *International Journal of Heat and Mass Transfer*, 41:1759–1769, 1998.
- C.P. Tso and S.P. Mahulikar. The role of the Brinkman number in analysing flow transitions in microchannels. *International Journal of Heat and Mass Transfer*, 42:1813–1833, 1999.
- C.P. Tso and S.P. Mahulikar. Experimental verification of the role of Brinkman number in microchannels using local parameters. *International Journal of Heat and Mass Transfer*, 43:1837–1849, 2000.
- D.B. Tuckerman and R.F.W. Pease. High-performance heat sinking for VLSI. *IEEE Electron Device Letter*, EDL-2(5):126–129, 1981.
- T. Tunc and Y. Bayazitoglu. Heat transfer in microtubes with viscous dissipation. *International Journal of Heat and Mass Transfer*, 44:2395–2403, 2001.
- J. W. G. Tyrrell and P. Attart. Images of nanobubbles on hydrophobic surfaces and their interactions. *Physical Review Letters*, 87(17):1–4, 2001.
- W. Urbanek, J.N. Zemel, and H.H. Bau. An investigation of the temperature dependence of Poiseuille numbers in microchannel flow. *Journal of Micromechanics and Microengineering*, 3:206–208, 1993.
- B. Wang, L. Zhou, and X. Peng. A fractal model for predicting the effective thermal conductivity of liquid with suspension of nanoparticles. *International Journal of Heat and Mass Transfer*, 46:2665–2672, 2003.
- D. Wen and Y. Ding. Experimental investigation into convective heat transfer of nanofluids at the entrance region under laminar flow conditions. *International Journal of Heat and Mass Transfer*, 47:5181–5188, 2004.

- F.M. White. *Viscous fluid flow*. McGraw-Hill, Singapore, second edition edition, 1991.
- F.M. White. *Fluid Mechanics*. McGraw-Hill, Boston, MA, fourth edition, 1999.
- D. C. Wilcox. *Turbulence Modeling for CFD*. DCW Industries, La Canada, CA, 1998.
- H. Y. Wu and P. Cheng. An experimental study of convective heat transfer in silicon microchannels with different surface conditions. *International Journal of Heat and Mass Transfer*, 46:2547–2556, 2003.
- H. Xie, H. Lee, W. Youn, and M. Choi. Nanofluids containing multiwalled carbon nanotubes and their enhanced thermal conductivities. *Journal of applied physics*, 94(8):4967–4971, 2003.
- H. Xie, T. Wang, J. Xi, Y. Liu, F. Ai, and Q. Wu. Thermal conductivity enhancement of suspensions containing nanosized alumina particles. *Journal of applied physics*, 91(7):4568–4572, 2002.
- B. Xu, K. T. Ooi, N. T. Wong, and W. K. Choi. Liquid flow in microchannels. In *Proc. 5th ASME/JSME Joint Thermal Engineering Conference*, San Diego, CA, 1999.
- B. Xu, K. T. Ooi, N. T. Wong, and W. K. Choi. Experimental investigation of flow friction for liquid flow in micro channels. *International Communication of Heat and Mass Transfer*, 27:1165–1176, 2000.
- D. Xu, T. Y. Ng, L. S. Pan, K. Y. Lam, and H. Li. Numerical simulations of fully developed turbulent liquid flows. *Journal of Micromechanics and Microengineering*, 11:175–180, 2001.
- Y. Xuan and Q. Li. Heat transfer enhancement of nanofluids. *International Journal of Heat and Fluid Flow*, 21:58–64, 2000.
- Y. Xuan and Q. Li. Investigation on convective heat transfer and flow features of nanofluids. *Journal of Heat Transfer*, 125:151–155, 2003.

- Y. Xuan and W. Roetzel. Concepts for heat transfer correlation of nanofluids. *International Journal of Heat and Mass Transfer*, 43(43):3701–3707, 2000.
- Q.Z. Xue. Model for effective thermal conductivity of nanofluids. *Physics Letters A*, 307: 313–317, 2003.
- C. Yang and D. Li. Analysis of electrokinetic effects on the liquid flow in rectangular microchannels. *Colloids and Surfaces, A*, 143:339–353, 1998.
- W. Yu and S.U.S. Choi. The role of interfacial layers in the enhanced thermal conductivity of nanofluids: A renovated maxwell model. *Journal of Nonoparticle research*, 5:167–171, 2003.
- W. Yu and S.U.S. Choi. The role of interfacial layers in the enhanced thermal conductivity of nanofluids: A renovated hamilton-crosser model. *Journal of Nanoparticle Research*, in press, 2004.
- M. Zabransky. *Heat capacity of liquids : critical review and recommended values*. American Chemical Society, Washington D.C., 1996.
- J. Zeng. Modeling of multi-phase flows in mems world. URL http://www.coventor.com/media/papers/dropsim{_}app{_}note.pdf.
- Z. Zhang and C. Kleinstreuer. Modeling of low reynolds number turbulent flows in locally constricted conduits: a comparison study. *AIAA*, 41:831–840, 2003.
- C. Y. Zhao and T. J. Lu. Analysis of microchannel heat sinks for electronics cooling. *International Journal of Heat and mass Transfer*, 45:4857–4869, 2002.